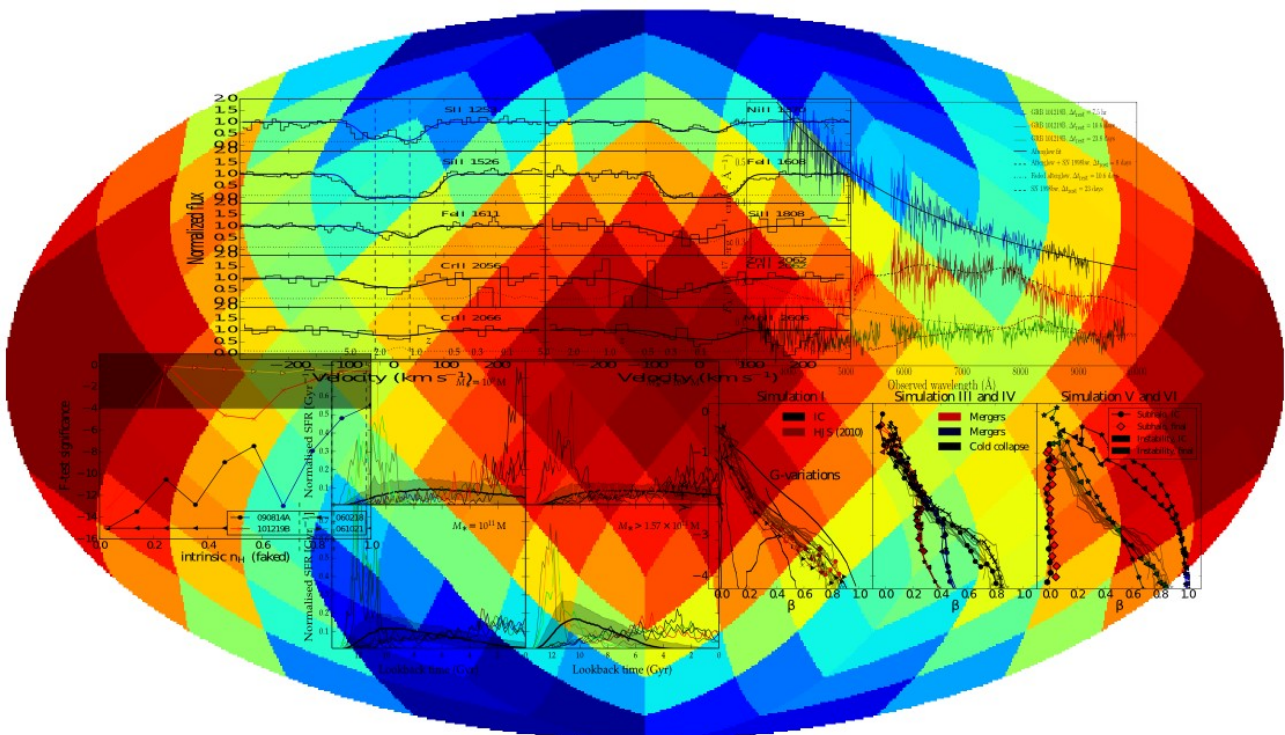


This thesis has been submitted to the PhD School
of The Faculty of Science, University of Copenhagen



Galaxy formation: observations and simulations of galaxies



Dissertation submitted for the degree

Doctor of Philosophy

Submission: 30/09/2014
Defence: xx/xx/2014
Supervisor: Prof. Johan Peter Uldall Fynbo
Opponents: Dr. Lise Christensen
Prof. Jürg Diemand
Prof. Martin Haehnelt

Abstract

Galaxy formation is an enormously complex discipline due to the many physical processes that play a role in shaping galaxies. The objective of this thesis is to study galaxy formation with two different approaches: First, numerical simulations are used to study the structure of dark matter and how galaxies form stars throughout the history of the Universe, and secondly it is shown that observations of gamma-ray bursts (GRBs) can be used to probe galaxies with active star formation in the early Universe.

A conclusion from the hydrodynamical simulations is that the galaxies from the state-of-the-art cosmological simulation, *Illustris*, follow a tight relation between star formation rate and stellar mass. This relation agrees well with the observed relation at a redshift of $z = 0$ and $z = 4$, but at intermediate redshifts of $z \simeq 2$ the normalisation is lower than in real observations. This is highlighted as an important problem to solve in future cosmological simulations. Another important result from this thesis is that abundances of different chemical elements (e.g. Fe, S, and Ni) can be measured out to $z \simeq 5$ with GRB host observations. Pushing the observations of chemical abundances to higher redshift is important, since it helps constraining chemical evolution models at high redshift.

A new project studying how the population of galaxies hosting GRBs relate to other galaxy population is outlined in the conclusion of this thesis. The core of this project will be to quantify how the stellar mass function of GRB host galaxies is affected by the fact that GRBs appear mainly to happen in low-metallicity galaxies. Solving this problem will make it possible to derive the total cosmic star formation rate more reliably from number counts of GRBs.

Opsummering (danish)

Galakser er komplekse systemer bestående af stjerner, gas og mørkt stof. I denne afhandling studeres bl.a. hastighedsfordelingen af mørkt stof partikler (afsnit 2 og 3), hvordan stjerner bliver dannet i store computersimuleringer af galaksedannelse (afsnit 4) og observationer af gamma-glimt. Kapitel 2-7 er hver baseret på en artikel. Nedenfor er en opsummering for hvert af de forskellige emner, som studeres i denne afhandling:

- I kapitel 2 og 3 studeres computersimuleringer af strukturer af mørkt stof. De to kapitler fokuserer på hastighedsfordelingerne af mørkt stof partikler. En speciel egenskab ved mørkt stof partikler er, at hastighedsdispersionen ikke nødvendigvis er den samme i alle retninger i modsætning til normale gas-partikler, som har en isotrop hastighedsfordeling. Hvis σ_{rad} er hastighedsdispersionen målt i den radiale retning af en mørkt stof hob, og σ_{tan} er den totale hastighedsdispersion i tangentielle retninger, så kan man definere hastighedsanisotropien som

$$\beta(r) = 1 - \frac{\sigma_{\text{tan}}^2}{2\sigma_{\text{rad}}^2}, \quad (1)$$

hvor r er strukturens radius. Med denne definition så har strukturer med en dominerende radial hastighedsdispersion $\beta > 0$, og strukturer med dominerende tangentiell dispersion $\beta < 0$. I simuleringerne, som præsenteres i kapitel 2 og 3, studeres opførslen af $\beta(r)$. I stedet for at udregne $\beta(r)$ ved hjælp af sfærisk midling over hele strukturen (som det oftest gøres i litteraturen), så måles $\beta(r)$ i forskellige kegler ud igennem de analyserede strukturer. Det vises, at strukturer der har gennemgået et galakse-sammenstød, har meget forskellige β -profiler i forskellige retninger. Strukturer der er dannet i idealiserede simuleringer ved hjælp af et sfærisk kollaps har derimod sfærisk symmetriske β -profiler. For galakser i det virkelige univers er galaksesammenstød hyppige, så derfor forventes det at haloer i virkeligheden også vil have β -profiler, som ikke er sfærisk symmetriske. Derimod er det mere sandsynligt at β -profilerne bestemmes af de seneste galaksesammenstød samt af strukturer, der er faldet ind i galakser.

- Illustris-simuleringen (www.illustris-project.org) er en af verdens største og mest præcise simuleringer af galaksedannelse. I kapitel 4 studeres det hvordan og hvornår galakser danner deres stjerner i Illustris. Et af Hovedresultaterne for dette studie er at der eksisterer en tæt sammenhæng mellem en galakses stjernedannelsesrate og den totale masse af stjerner i galaksen. Ved rødforskydning $z = 0$ og $z = 4$ stemmer den simulerede relation overens med observationer, men ved $z = 2$ er normaliseringen af den simulerede relation for lav. Dette problem fremhæves som værende et vigtigt problem at løse for galaksedannelsesmodeller. For at løse

dette problem er det sandsynligvis nødvendigt at lave nye modeller for hvordan stjerner dannes i galakser.

- I sektion 5, 6 og 7 præsenteres tre studier af observationer af gamma-glimt, som er korte intense udbrud af gamma-stråling. I afsnit 5 præsenteres en observation af et gamma-glimt, som viser sig at stamme fra en stjerne, der er kollapsed og derefter eksploderer som en supernovae. I kapitel 7 bliver gamma-glimt brugt til at studere dannelsen af grundstoffer 1.2 milliarder år efter big bang (dvs., for 12.6 milliarder år siden). Observationerne viser at det totale metalindhold er lavere end i Solen i dag, men et bemærkelsesværdigt resultat er forholdet mellem mængden af forskellige tunge grundstoffer (S, Fe, Ni) er identiske dem forholdene fra Solen. Dette er en indikation af at grundstofferne, som var til stede 1.2 milliarder år efter big bang, er dannet på samme måde som grundstofferne i Solen.

Acknowledgement

It is a pleasure to thank my PhD advisor, Johan Fynbo, for enormous support and many interesting discussions (about astronomy, and many others topics as well). I would also like to thank Steen H. Hansen for his enthusiastic supervision during both my PhD and undergraduate studies. Also thanks to other people I have collaborated closely with on various projects; especially I would like to thank Rhaana (Starling), Olga (Hartoog), Chris (Hayward) and Volker (Springel). Also thanks to everybody at DARK.

List of papers

Here is a list of the first-author papers I wrote during my PhD. These are the papers my PhD thesis consists of.

Paper 1.

Sparre, M., Sollerman, J., Fynbo, J. P. U., Malesani, D. et al. 2011,
Spectroscopic Evidence for SN 2010ma Associated with GRB 101219B,
The Astrophysical Journal Letters, 735, L24.

Paper 2.

Sparre, M. & Hansen, S. H. 2012,
Asymmetric velocity anisotropies in remnants of collisionless mergers,
Journal of Cosmology and Astro-Particle Physics, 7, 42.

Paper 3.

Sparre, M. & Hansen, S. H. 2012,
The behaviour of shape and velocity anisotropy in dark matter haloes,
Journal of Cosmology and Astro-Particle Physics, 10, 49.

Paper 4.

Sparre, M. & Starling, R. L. C. 2012,
A search for thermal X-ray signatures in gamma-ray bursts - II. The Swift sample,
Monthly Notices of the Royal Astronomical Society, 427, 2965.

Paper 5.

Sparre, M., Hartoog, O. E., Krühler, T., Fynbo, J. P. U. et al. 2014,
The Metallicity and Dust Content of a Redshift 5 Gamma-Ray Burst Host Galaxy,
The Astrophysical Journal, 785, 150.

Paper 6.

Sparre, Martin; Hayward, Christopher C.; Springel, Volker; Vogelsberger, Mark; Genel, Shy; Torrey, Paul; Nelson, Dylan; Sijacki, Debora; Hernquist, Lars. 2014,
The star formation main sequence and stellar mass assembly of galaxies in the Illustris simulation,
submitted to *Monthly Notices of the Royal Astronomical Society*,
available as Arxiv preprint, arXiv: 1409.0009

Contents

1	Introduction	1
1.1	Dark matter and collisionless dynamics	1
1.2	Galaxy formation and hydrodynamical simulations	2
1.3	Introduction to gamma-ray bursts and their host galaxies	3
1.3.1	The progenitors of gamma-ray bursts	3
1.3.2	X-ray observations of gamma-ray burst afterglows	4
1.3.3	Probing star formation at high redshift	4
2	Collisionless dynamics I: mergers between dark matter halos	7
2.1	Introduction	7
2.2	The merger simulations	9
2.2.1	Initial conditions	9
2.2.2	Simulation details	9
2.3	Analysing particles in cones	10
2.3.1	Major mergers	10
2.3.2	The effect of an impact parameter	13
2.3.3	Major mergers with Osipkov-Merritt haloes	14
2.3.4	Minor mergers	14
2.4	The effect of an accretion process	15
2.5	Skymaps of the anisotropies	17
2.6	β - γ relations	20
2.7	Pseudo-phase-space density profiles	20
2.8	The shape of the haloes	21
2.9	Conclusion	22
3	Collisionless dynamics II: more idealized simulations of dark matter halos	25
3.1	Introduction	26
3.2	Simulations	27
3.2.1	Simulation code	27
3.2.2	Simulation I – An instantaneous change in the potential	27
3.2.3	Simulation II – Exchange of energy	29
3.2.4	Simulation III – A cold collapse experiment with substructure	30
3.2.5	Simulation IV – Major mergers	30
3.2.6	Simulation V – Unstable Osipkov-Merritt models	31
3.2.7	Simulation VI – A halo and its subhaloes	31
3.3	Analysis methods	31
3.3.1	Analysing particles in cones	31
3.3.2	Determination of halo shapes	31

3.4	The behaviour of velocity anisotropy and halo shape	32
3.4.1	Category 1: Haloes with well-behaved β -profiles	32
3.4.2	Category 2: Haloes with complex β -profiles	32
3.4.3	Category 3: The spherically symmetric haloes	33
3.4.4	A summary of the categories	33
3.5	Relating the results to cosmological haloes	35
3.5.1	Comparison with a cosmological halo	35
3.5.2	Spatial anisotropy of galaxy kinematics in galaxy clusters	36
3.6	Spherically averaged profiles	36
3.6.1	Velocity anisotropy profiles	39
3.6.2	γ -profiles	39
3.6.3	Halo shapes	39
3.7	Comparison with the attractor	40
3.7.1	Motivation for the attractor	40
3.7.2	Comparing haloes with the attractor	40
3.7.3	An overview: which structures are on the attractor?	43
3.7.4	The relevance of the attractor	44
3.8	Summary	44
4	Star formation in a hydrodynamical galaxy formation simulation	48
4.1	Introduction	49
4.2	The Illustris simulation	51
4.3	The star formation main sequence	52
4.3.1	The scatter in the main sequence	54
4.3.2	Star formation above the main sequence relation	54
4.3.3	The choice of SFR indicator	55
4.4	Halo mass and star formation properties of galaxies	56
4.4.1	Halo and stellar masses of star-forming galaxies	56
4.4.2	Build up of stellar components at different halo masses	60
4.5	Star formation histories of galaxies	61
4.5.1	Outliers from the average star formation histories	61
4.5.2	Modes of star formation in a principal component analysis	61
4.5.3	Assessing the SFH variability timescale	65
4.5.4	Relations between the SFH main mode and galaxy properties	66
4.6	Discussion	68
4.6.1	The normalisation of the star formation main sequence	68
4.6.2	The paucity of starbursts in Illustris	69
4.7	Conclusions	70
5	The origin of gamma-ray bursts: the explosion of a massive star at $z \simeq 0.55$	77
5.1	Introduction	77
5.2	Observations and data reduction	78
5.3	Results	79
5.3.1	Redshift measurement	79
5.3.2	The first epoch afterglow	80
5.3.3	Detection of a supernova	81
5.3.4	Dust extinction and host galaxy continuum	81
5.3.5	Mg absorption in the host galaxy	83

5.4	Discussion	84
6	The X-ray afterglow of gamma-ray bursts	89
6.1	Introduction	89
6.2	Fitting models with black body components to a sample of GRBs	90
6.2.1	A sample of <i>Swift</i> bursts	90
6.2.2	Spectral modelling	91
6.2.3	Selecting candidates with the F-test	92
6.3	Recovering a black body component in mock spectra of GRB 101219B	92
6.3.1	The role of column densities	92
6.3.2	Redshift and afterglow parameters	93
6.4	Selecting Candidates	94
6.4.1	Ruling out candidates with uncertain n_H	94
6.4.2	Candidates at high and low redshift	97
6.4.3	Approach I: Fitting with 5 free parameters	98
6.4.4	Approach II: Breaking N_H -degeneracies with the late time spectrum	99
6.5	The final candidates and potential caveats	102
6.5.1	The Redshifts	102
6.5.2	Light curves and spectral evolution	102
6.5.3	Contribution from the prompt emission	102
6.5.4	Is it a black body component?	107
6.6	Properties of the black body components	107
6.6.1	The fraction of bursts with black body components	107
6.7	Conclusion	108
7	Probing high-redshift galaxies with gamma-ray bursts	112
7.1	Introduction	113
7.2	Observations	114
7.2.1	X-shooter spectroscopy	114
7.2.2	GMOS spectroscopy	114
7.2.3	GROND photometry	115
7.3	The GRB host absorber	115
7.3.1	The chemical composition	116
7.3.2	Fine-structure lines	119
7.4	Determining the dust extinction	121
7.5	The intervening system at $z = 4.6$	121
7.6	Searching for emission from the host and from the intervening absorber	124
7.7	Dust-to-metals ratio	125
7.8	Discussion	126
7.8.1	The GRB host galaxy	126
7.8.2	The intervening DLA	129
7.9	Summary	129
7.10	APPENDIX: The issue of saturation for the S II 1253-transition	135
7.10.1	The effect a third absorption component	135
7.11	APPENDIX: The X-shooter spectrum	137
8	Conclusions and perspectives for further research	140
A	Author statements	144

Chapter 1

Introduction

This thesis is a collection of the first-author articles I have done during my PhD. The articles span a wide variety of subjects, including studies of the dynamics of dark matter systems (collisionless dynamics), star formation in galaxy formation simulations, and the progenitors and galaxy-sites of gamma-ray bursts (GRBs). Common for all these chapters is that they aim to improve our understanding of the physics of galaxy formation. Below is a short introduction to each of these topics with a focus on the connection between them.

1.1 Dark matter and collisionless dynamics

The majority of the matter in the Universe is in the form of dark matter (Planck Collaboration, 2013). While the actual physical nature of the dark matter remains an unsolved problem in cosmology there is generally consensus about the existence of dark matter in the Universe. Examples of observations that supports the existence of dark matter are galactic rotation curves (showing that the mass of galaxies is larger than that accounted for by stars and gas, Rubin et al. 1980), the Bullet cluster (where the baryonic matter is separated from the peak of the mass distribution; Clowe et al. 2006), and the velocity dispersion of galaxies inside galaxy clusters (Zwicky, 1933). In the Λ CDM theory, the paradigm in which this thesis is written, a key driver of structure formation is the gravitational attraction from the dark matter in the Universe (for an introduction to structure formation, see Dodelson, 2003).

Dark matter is often modelled as a collisionless fluid that only interacts through gravity. The 6-dimensional phase-space density of collisionless matter at a position \mathbf{x} and velocity \mathbf{v} is denoted by the distribution function, $f(\mathbf{x}, \mathbf{v})$ (see Binney & Tremaine 2008). This function is usually normalized, so the integral over the entire phase-space equals the mass of the system,

$$\int f(\mathbf{x}, \mathbf{v}) d^3\mathbf{x} d^3\mathbf{v} = M. \quad (1.1)$$

From the distribution function it is e.g. easy to obtain the mass density at a given point in space,

$$\rho(\mathbf{x}) = \int f(\mathbf{x}, \mathbf{v}) d^3\mathbf{v}. \quad (1.2)$$

The time-evolution of a collisionless fluid is governed by the *collisionless Boltzmann equation*,

$$\frac{df}{dt} = 0, \quad (1.3)$$

i.e. the density of phase-space is conserved when following the flow of a fluid element. Equation (1.3) can be derived by combining the continuum equation and Newtons equations of motion.

Section 2 and 3 of this thesis present studies of idealised simulations of e.g. collisionless mergers and the collapse of collisionless structures. These simulations were designed to imitate the mergers occurring between dark matter halos and the collapse of structures in the Universe. In these simulations the 6-dimensional phase-space is discretized by a number of Lagrangian interpolation points, which moves with the flow of the fluid. These interpolation points are usually just called *dark matter particles*, and their motion can be calculated by integrating Newtons 2nd law in the potential arising from all the particles in the simulation (Stadel, 2001; Springel, 2005).

My initial motivation for doing collisionless simulations was to study an *attractor* proposed by Hansen et al. (2010). In this study different halos were exposed to perturbations, and it was seen that all halos ended up obeying the same relation between the *velocity anisotropy parameter* (β), the slope of the density profile ($\gamma \equiv d \log \rho / d \log r$), and the slope of the radial velocity dispersion profile ($\kappa \equiv d \log \sigma_{\text{rad}}^2 / d \log r$). The velocity anisotropy parameter quantifies how much the velocity dispersion differs in the radial and the tangential direction at a given radius of a halo,

$$\beta(r) = 1 - \frac{\sigma_{\text{tan}}^2}{2\sigma_{\text{rad}}^2}, \quad (1.4)$$

with σ_{rad} being the radial velocity dispersion and σ_{tan} being the total tangential dispersion. In Hansen et al. (2010) this attractor was discovered by perturbing different halos by artificially interchanging energy between particles. In Chapter 2 of this thesis it is studied whether mergers produce halos that are on the attractor, and in Chapter 3 the same thing is studied for a wide range of physical setups; e.g. collapse-simulations and halos undergoing radial orbit instabilities. In addition to study whether halos end up on the attractor, it is also examined how the velocity anisotropy parameter and halo shape behave in the various simulations.

1.2 Galaxy formation and hydrodynamical simulations

As outlined above one of the key drivers of halo formation is the growth of dark matter halos. In order to explain the formation of galaxies, it is, however, necessary to account for additional baryonic physics. In the theory of galaxy formation galaxies form when gas falls into halos, accretion shocks form, and the gas starts to cool and forms stars (White & Frenk, 1991). An important question for galaxy formation models is to understand the physics of star formation and related feedback processes. It is established that stars form in dense giant molecular clouds (GMCs), but the detailed physics of such clouds are far from understood (Stahler & Palla, 2005). Processes that are likely important for the formation of stars in molecular clouds are the formation of H_2 (H_2 -cooling is important for creating star-forming cores), gravitational attraction (which compresses GMCs),

magnetic fields and turbulence (they suppress the collapse of clouds). In addition to the limited understanding we have of the formation of stars inside GMCs, it is also unknown how the actual process of star formation affects the gas in the GMC. A popular idea about star formation in GMCs is self-regulation, where the two processes of expulsion of gas around recently formed stars and the formation of dense regions in GMCs balance each other, and lead to a quasi-equilibrium state of star formation in galaxies (Mo et al., 2010).

This thesis contains a study of star formation in a hydrodynamical simulation of galaxy formation. The analysed simulation is the *Illustris simulation*, which is a large-scale cosmological simulation, which simulates the formation and evolution of more than 30000 galaxies in a cosmological box of size 106.25 Mpc. In addition to including the collisionless dynamics describing the distributions of dark matter, the simulation also includes stars, gas, stellar feedback, feedback from black holes, chemical evolution and several other astrophysical processes. With such a simulation it is possible to compute a wide range of galaxy properties, for example stellar masses, halo masses, the morphology of galaxies, and colours of galaxies. Chapter 4 studies star formation properties of galaxies with a focus on the relation between star formation rates and stellar masses, the formation of stars in dark matter halos with different masses, and star formation histories of individual galaxies.

1.3 Introduction to gamma-ray bursts and their host galaxies

Gamma-ray bursts are spectacular explosions that are so energetic that a single burst can dominate the entire gamma-ray radiation on the sky. GRBs are split into two populations with different durations (Kouveliotou et al., 1993): bursts with durations shorter than two seconds are classified as *short bursts* and bursts with longer durations are *long bursts*.

The long GRBs are associated with short-lived massive stars, and they therefore probe galaxies and GMCs with active star formation. Ground-based observations of GRB afterglows have led to the discovery of some of the most distant galaxies ever observed, e.g. GRB 090423 at a spectroscopic redshift of $z = 8.2$ (Tanvir et al., 2009) and GRB 090429B with a photometric redshift of $z \simeq 9.4$ (Cucchiara et al., 2011). Observations of such distant systems make GRBs an ideal probe of star formation at high redshift; Tanvir et al. (2012) for example shows that GRBs at high redshifts probe low-luminosity galaxies that are not detectable in normal flux-limited galaxy surveys.

1.3.1 The progenitors of gamma-ray bursts

In this thesis various aspects of GRBs are examined. In Chapter 5 the detection of a gamma-ray burst (GRB 101219B) with an associated core-collapse supernova (SN) is reported. Such an observation is important since it directly proves the relation between GRBs and the collapse of massive stars. At the time of observation several other gamma-ray bursts with an associated supernova had been observed, but 101219B was special because it has an unusual high redshift of $z = 0.55$. Within a few years several other supernovae were detected in the optical spectra of gamma-ray bursts; for example GRB 091127 ($z = 0.49$; Berger et al., 2011). Very recently, it has been shown that the supernovae associated with GRBs potentially can be used as cosmological standard candles (Cano & Jakobsson, 2014; Li et al., 2014). Establishing that GRB-supernovae can be observed at cosmological distances (at $z = 0.55$) is of high importance, since it shows that GRBs can

potentially be used to measure the cosmic expansion at such redshifts with the observational instruments currently available. Also note, that new observational facilities, such as the *James Webb Space Telescope*, potentially can probe cosmic expansion at even higher redshifts with GRBs (see discussion in Li et al. 2014).

1.3.2 X-ray observations of gamma-ray burst afterglows

The intense gamma-ray emission in GRBs is usually followed by a multi-wavelength afterglow, which is believed to arise from cooling processes in the ultra-relativistic shock, that appears when the ejecta from a GRB progenitor interacts with the interstellar medium in the host galaxy of the GRB. The afterglows have spectral energy distributions following a function with multiple broken power laws from the X-ray to radio energies (Sari et al., 1998). Chapter 6 studies the early X-ray afterglow of a large sample of gamma-ray bursts. One motivation for this study is to search for signs of black-body emission (in addition to the normal GRB afterglow) from supernovae at very early times (e.g. within a few minutes) after the GRB explosion. From such a detection it would likely be possible to learn something new about supernovae, since they are normally first detected weeks after the explosion. In this study 7 bursts with excess X-ray emission at early times were found. Under the assumption that this emission comes from a black body component, radii and temperatures of the emitting regions are derived. The derived radii are a few orders of magnitudes larger than the typical sizes of Wolf-Rayet stars, which are believed to host gamma-ray bursts, so it is possible that the emission originates from a medium surrounding the progenitor star (as suggested by Friis & Watson 2013).

1.3.3 Probing star formation at high redshift

As already mentioned the long GRBs are probes of star-forming environments. With spectroscopy of afterglows, it is possible to obtain column densities of HI and metals along GRB sight-lines (Fynbo et al., 2009), and the intrinsic broken power law nature of GRB afterglows makes them suitable for extracting dust extinction curves for the host galaxies (Krühler et al., 2011; Zafar et al., 2011). Chapter 7 studies the environment of a $z = 5$ gamma-ray burst. This study focuses on the metallicity and dust properties of the sight line through the galaxy hosting the gamma-ray burst. Observing such quantities for GRB host galaxies in the early Universe is interesting for many reasons: the measurements of the dust-to-metals ratio of high- z systems can help constraining dust-production mechanisms (see Chapter 7 for details), and the metallicity patterns at $z \simeq 10 - 20$ can help constraining properties of population III stars (Bromm & Loeb, 2006). At the time of publication the galaxy studied in Chapter 7 was the highest redshift GRB host galaxy with a well-measured metallicity. This was therefore an important step towards measuring the metallicity content of galaxies at even higher redshift.

Bibliography

- Berger E., et al., 2011, *ApJ*, 743, 204
- Binney J., Tremaine S., 2008, *Galactic Dynamics: Second Edition*. Princeton University Press
- Bromm V., Loeb A., 2006, *ApJ*, 642, 382
- Cano Z., Jakobsson P., 2014, *ArXiv*: 1409.3570
- Clowe D., et al., 2006, *ApJ*, 648, L109
- Cucchiara A., et al., 2011, *ApJ*, 736, 7
- Dodelson S., 2003, *Modern cosmology*. Academic Press. ISBN 0-12-219141-2
- Friis M., Watson D., 2013, *ApJ*, 771, 15
- Fynbo J. P. U., et al., 2009, *ApJS*, 185, 526
- Hansen S. H., Juncher D., Sparre M., 2010, *ApJ*, 718, L68
- Kouveliotou C., et al., 1993, *ApJ*, 413, L101
- Krühler T., et al., 2011, *A&A*, 534, A108
- Li X., Hjorth J., Wojtak R., 2014, *ArXiv*: 1409.3567
- Mo H., van den Bosch F. C., White S., 2010, *Galaxy Formation and Evolution*. Cambridge, UK: Cambridge University Press, 2010
- Planck Collaboration 2013, *ArXiv*: 1303.5076
- Rubin V. C., Ford W. K. J., Thonnard N., 1980, *ApJ*, 238, 471
- Sari R., Piran T., Narayan R., 1998, *ApJ*, 497, L17
- Springel V., 2005, *MNRAS*, 364, 1105
- Stadel J. G., 2001, PhD thesis, UNIVERSITY OF WASHINGTON
- Stahler S. W., Palla F., 2005, *The Formation of Stars*. Wiley-VCH, ISBN 3-527-40559-3.
- Tanvir N. R., et al., 2009, *Nature*, 461, 1254
- Tanvir N. R., et al., 2012, *ApJ*, 754, 46

White S. D. M., Frenk C. S., 1991, *ApJ*, 379, 52

Zafar T., et al., 2011, *A&A*, 532, A143

Zwicky F., 1933, *Helvetica Physica Acta*, 6, 110

Chapter 2

Collisionless dynamics I: mergers between dark matter halos

This chapter contains the following article:

Asymmetric velocity anisotropies in remnants of collisionless mergers

Published in Sparre & Hansen, 2012, JCAP,07,042

Authors: Martin Sparre & Steen H. Hansen

Abstract

Dark matter haloes in cosmological N-body simulations are affected by processes such as mergers, accretion and the gravitational interaction with baryonic matter. Typically the analysis of dark matter haloes is performed in spherical or elliptical bins and the velocity distributions are often assumed to be constant within those bins. However, the velocity anisotropy, which describes differences between the radial and tangential velocity dispersion, has recently been shown to have a strong dependence on direction in the triaxial halos formed in cosmological simulations. In this study we derive properties of particles in cones parallel or perpendicular to the collision axis of merger remnants. We find that the velocity anisotropy has a strong dependence on direction. The finding that the direction-dependence of the velocity anisotropy of a halo depends on the merger history, explains the existence of such trends in cosmological simulations. It also explains why a large diversity is seen in the velocity anisotropy profiles in the outer parts of high-resolution simulations of cosmological haloes.

2.1 Introduction

In the Λ CDM-paradigm the first bound dark matter haloes are formed through the collapse of overdense regions, which have decoupled from the Hubble expansion. These haloes grow when they accrete matter from their surroundings and when they merge.

Understanding merger remnants is therefore essential in order to understand the dark matter distribution in the universe.

The dark matter (DM), making up most of the matter in the universe Riess et al. (1998); Perlmutter et al. (1999); Komatsu et al. (2011), consists of particles interacting so weakly, that haloes can be well modelled with collisionless mechanics. An example of evidence for this collisionless nature of DM comes from observations and simulations of the Bullet Cluster Clowe et al. (2006); Bradač et al. (2006); Springel & Farrar (2007); Mastropietro & Burkert (2008), which consists of two merging galaxy clusters with the collisional baryonic matter separated from the collisionless dark matter.

A difference between collisional and collisionless particles is that collisionless particles tend to have anisotropic velocity distributions, typically parametrised by the velocity anisotropy parameter Binney & Tremaine (2008),

$$\beta(r) \equiv 1 - \frac{\sigma_{\text{tan}}^2(r)}{2\sigma_{\text{rad}}^2(r)}, \quad (2.1)$$

where σ_{tan} is the total tangential velocity dispersion at a given radius (r), and σ_{rad} is the radial velocity dispersion. The velocity distributions are radially dominated for $\beta > 0$, tangentially dominated for $\beta < 0$, and isotropic for $\beta = 0$. In cosmological simulations the β -profiles increase from $\beta \simeq 0$ in the central regions to $\beta \simeq 0.25$ at r_{-2} (Diemand et al., 2004; Ludlow et al., 2011), which is the radius with a density slope of $\gamma = -2$, where

$$\gamma \equiv \frac{d \log \rho}{d \log r}. \quad (2.2)$$

At larger radii the β -profiles vary from halo to halo.

Dark matter haloes from cosmological simulations have universal pseudo-phase-space density profiles following power laws (Taylor & Navarro, 2001),

$$\rho/\sigma_{\text{rad}}^3(r) \propto r^{-\alpha}, \quad (2.3)$$

with $\alpha \simeq 1.91$ (Ludlow et al., 2011). The density profiles are also universal (Navarro et al., 1996, 1997), with $\gamma \simeq -1$ in the inner parts and $\gamma \simeq -3$ in the outer parts. Typically haloes are parametrised with the NFW-profile, or the Einasto profile (Gao et al., 2008; Navarro et al., 2010). The universality of the density- and the pseudo-phase-space-density-profile in cosmological haloes determines $\sigma_{\text{rad}}^2(r)$. The velocity anisotropy, however, remains undetermined.

In an attempt to understand the physics of the velocity anisotropy, several studies have examined β -profiles in non-cosmological simulations. A linear relation Hansen & Moore (2006); Hansen & Stadel (2006) between β and γ is consistent with the inner parts of cosmological haloes. More recently a 1-dimensional relation (an *attractor*) between β , γ and the slope of the radial velocity dispersion profile has been found in controlled non-cosmological simulations Hansen et al. (2010); Barber et al. (2012). A tight relation between β and γ , which is predicted by this attractor, is, however, not consistent with the large scatter seen in the outer parts of cosmological haloes. In the two proposed relations, which determines $\beta(r)$ from a given density profile, $\gamma(r)$, it is implicitly assumed that β is constant in spherical or elliptical bins.

In a detailed study of a cosmological halo (Zemp et al., 2009), it has, however, been found that β behaves differently along different axes. The aim of this paper is to show that such direction-dependent β -profiles can arise because of mergers. We will address

this issue by studying the velocity anisotropy in different directions of merger remnants, to see whether β -profiles are direction dependent. In our analysis we will cut out cones of particles in different directions, and then calculate β and other variables for the particles inside each cone. In Section 2.2 we will present merger simulations, and in Section 2.3 we will map the velocity anisotropy parallel and perpendicular to the collision axis and determine whether they are different. We also show how structures are affected by smooth accretion (Section 2.4), and *skymaps* of the β -profiles are presented (Section 2.5). Section 2.6 discusses relations between β and γ , and Section 2.7 examines pseudo-phase-space density profiles. We also discuss the shape of the merger remnants (Section 2.8).

Throughout this paper we will use units with $G = 1$ and let $\log x$ denote the logarithm with base 10.

2.2 The merger simulations

2.2.1 Initial conditions

We are interested in doing a simulation of the merging of two identical dark matter haloes. To do so Eddington's formula Eddington (1916) (with $\beta = 0$) is used to generate a halo with a Hernquist density profile Hernquist (1990),

$$\rho(r) = \frac{\rho_0}{r/r_s} \frac{1}{(1 + r/r_s)^3}. \quad (2.4)$$

We choose $\rho_0 = 1/2\pi$ and $r_s = 1$, which gives a structure with a total mass of 1. The density profile is truncated at a radius of $10r_s$. This density profile is chosen because of its simple analytical properties, and because it resembles Springel et al. (2005) the NFW-profile, which describes haloes in cosmological simulations.

As initial conditions two such structures are generated, and placed $20r_s$ away from each other along the x -axis. 10^6 collisionless particles are used to represent each halo. The haloes approached each other with an initial velocity of 80% the escape velocity at this distance for an isolated Hernquist halo. Simulations were run with no impact parameter, and with an impact parameter of $10r_s$ (in the y -direction) and with the same initial velocity and initial offset along the x -axis.

Simulations were also made with an Osipkov-Merritt model Osipkov (1979); Merritt (1985) (still following the Hernquist profile described above) with the velocity anisotropy given by

$$\beta(r) = \frac{r^2}{r^2 + r_a^2}, \quad (2.5)$$

where r_a is the *anisotropy radius*, which we fix to $1.2r_s$. An anisotropy radius slightly larger than r_s is chosen to avoid instabilities Meza & Zamorano (1997).

Simulations with 1:10 mergers were also performed (only for the model with $\beta = 0$). A structure, identical to the $\beta = 0$ model defined above, was collided with a Hernquist structure with a 10 times lower total mass and a r_s -value and cutoff radius 3 times smaller.

2.2.2 Simulation details

The public version of the N-body simulation code Gadget-2 Springel (2005) was used to run the simulations. All particles were collisionless and a spline softening of 0.015 was used in all simulations. All simulations were run for 300 time units.

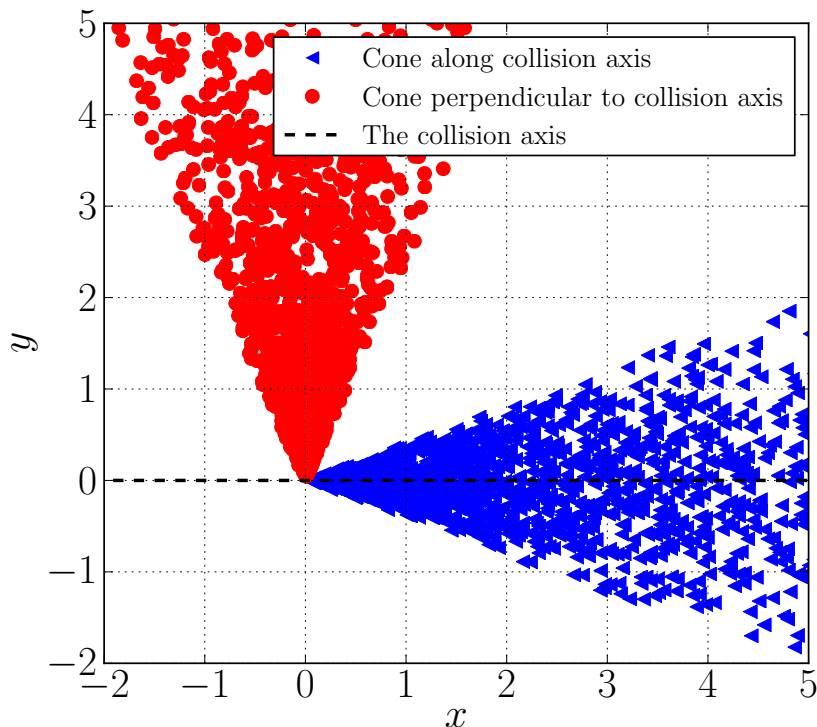


Figure 2.1: Properties of particles inside a cone parallel and a cone perpendicular to the collision axis are studied. Particles outside the cones are not shown.

2.3 Analysing particles in cones

To map the velocity anisotropy in the remnants, we defined cones pointing along the x -, y - and z -axis. The angle between the position vector (\mathbf{r}) of a particle and a unit vector ($\hat{\mathbf{n}}$) pointing in the direction of a cone is $\theta = \arccos(\hat{\mathbf{n}} \cdot \mathbf{r}/|\mathbf{r}|)$. We chose the cones to have an apex angle of 45° , so a particle is inside a cone if $\theta \leq 22.5^\circ$. The cones are centered in the center of the merger remnants, i.e. at the position of the particle with the lowest potential. Figure 2.1 shows the particles in two cones for one of the merger remnants.

2.3.1 Major mergers

First the remnant of the major merger simulation for the $\beta_{\text{initial}} = 0$ -haloes without an impact parameter is studied. Figure 2.2 (*left panel*) shows the velocity anisotropy in cones along each axis. Also shown is the spherically averaged value of $\beta(r)$. In the cone pointing in the direction of the collision axis (x -axis) the β -profile is clearly different from β in the two perpendicular cones along the y - and z -axis. In the inner parts (with $r < 1$) β is almost constant ($\beta \simeq 0.2 - 0.4$) along the collision axis, whereas it is an increasing function of radius in the two other cones.

In the figure an arrow marks the radius of r_{-2} , which has been found by examining $\gamma(r)$. For a Hernquist profile, which was used as initial conditions in the simulation, $r_{-2} = r_s/2$. In cosmological simulations the virial radius is typically $10r_{-2}$ (Macciò et al., 2008), and in our simulations this is also roughly the radius, to which structures are equi-

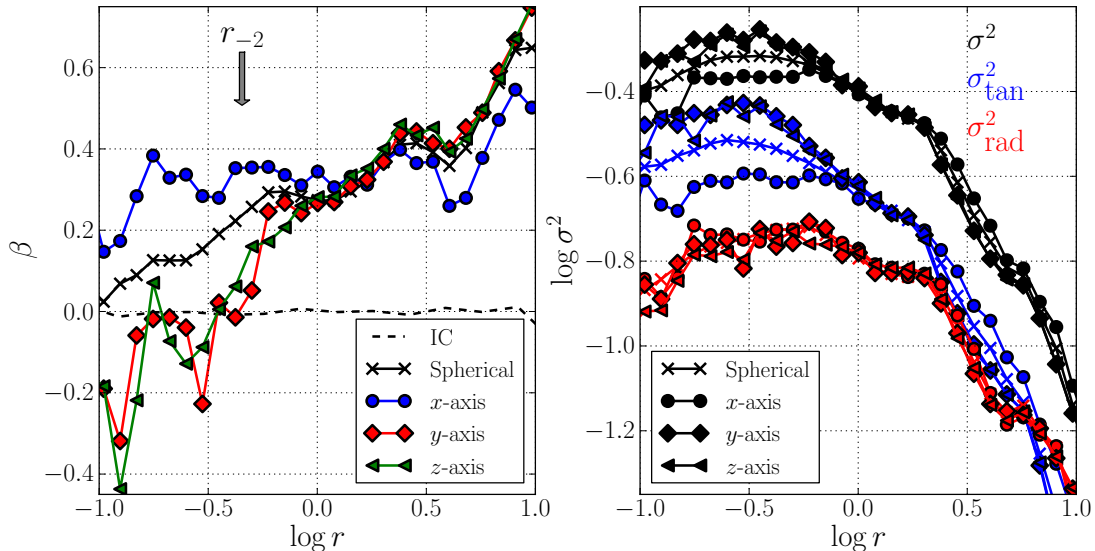


Figure 2.2: Properties of particles in cones along the x -, y - and z -axis are analysed together with the particles in spherical bins. The merger has no impact parameter, and the collision axis is the x -axis. $\beta_{\text{initial}} = 0$ for the haloes. The *left panel* shows the velocity anisotropy in each cone, and the *right panel* shows the total, the tangential and the radial velocity dispersion in each cone. The grey arrow shows the radius, where $\gamma = -2$.

librated.

The radial (σ_{rad}), tangential (σ_{tan}) and total (σ) velocity dispersions for each of the three cones are shown in the *right panel* of Figure 2.2. Most striking is the significantly lower value of the tangential dispersion along the collision axis. The radial dispersion profile is nearly the same in all the cones.

Figure 2.3 shows how the velocity anisotropy and the velocity dispersions (*upper panels*) depend on the local density in each cone. Using ρ as the abscissa corresponds to binning particles of equal density. $\beta(\rho)$ and $\sigma^2(\rho)$ are clearly different in the three cones, so the β -profiles and the velocity dispersions are not constant along contours of equal density.

Another observation (*lower panels*) is that the slopes, $\gamma(r)$, of the density profiles are similar along the different axes, but the actual value of ρ , is significantly larger in direction of the collision axis.

Comparison with the Via Lactea II halo

In the Via Lactea II simulation (Diemand et al., 2008) local properties of a Milky-Way-like halo have been examined (Zemp et al., 2009). A direction-dependent β -profile is found in the inner parts (at 8 kpc) of the halo: along the major axis β is larger ($0.2 \lesssim \beta \lesssim 0.45$), than along the intermediate axis ($-0.1 \lesssim \beta \lesssim 0.25$) and the minor axis ($-0.65 \lesssim \beta \lesssim -0.1$).

Section 2.8 will analyse and discuss the shape of the haloes from all our simulations. It will be found, that the merger remnant, which we have just studied, is elliptical with a major axis pointing along the x -direction. We can therefore confirm the finding (from (Zemp et al., 2009)) that β is largest along the major axis. Another similarity between our halo and the Via Lactea II halo is that the β -profiles are spherically symmetric at larger

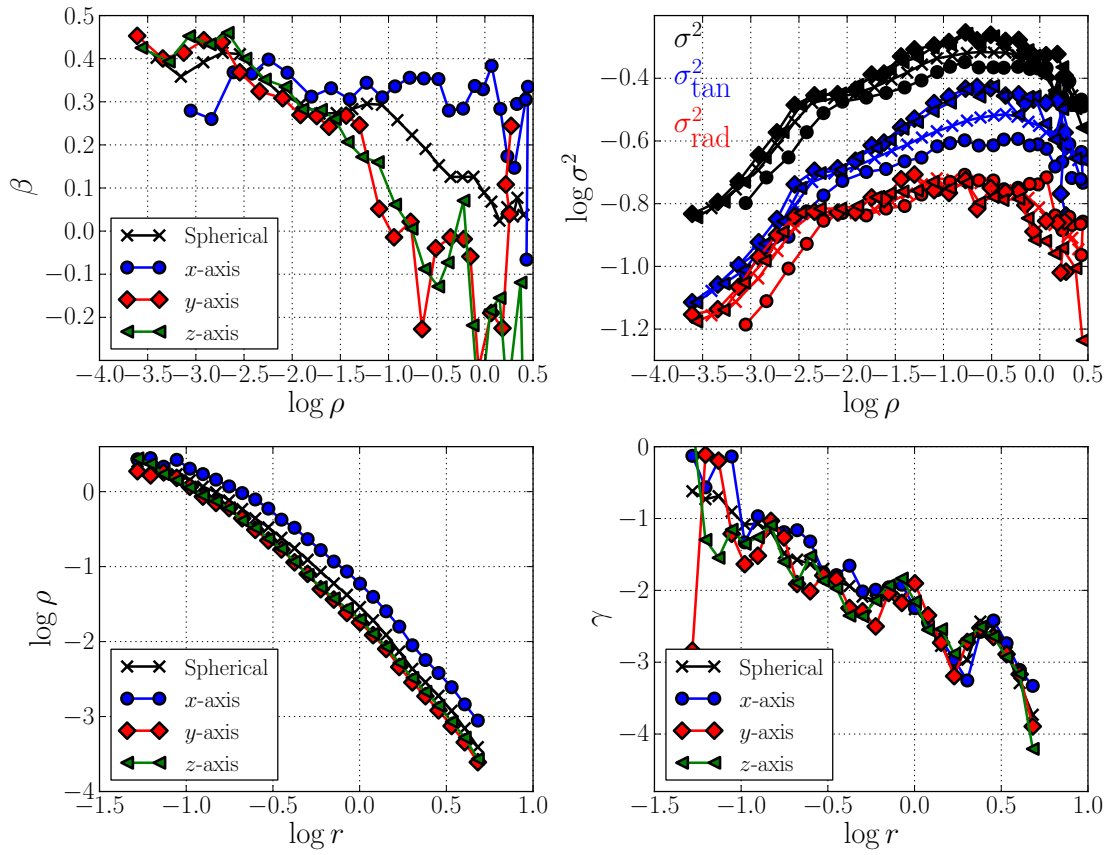


Figure 2.3: $\beta(\rho)$, $\sigma^2(\rho)$, $\rho(r)$ and $\gamma(r)$ in the different cones for a major merger without an impact parameter.

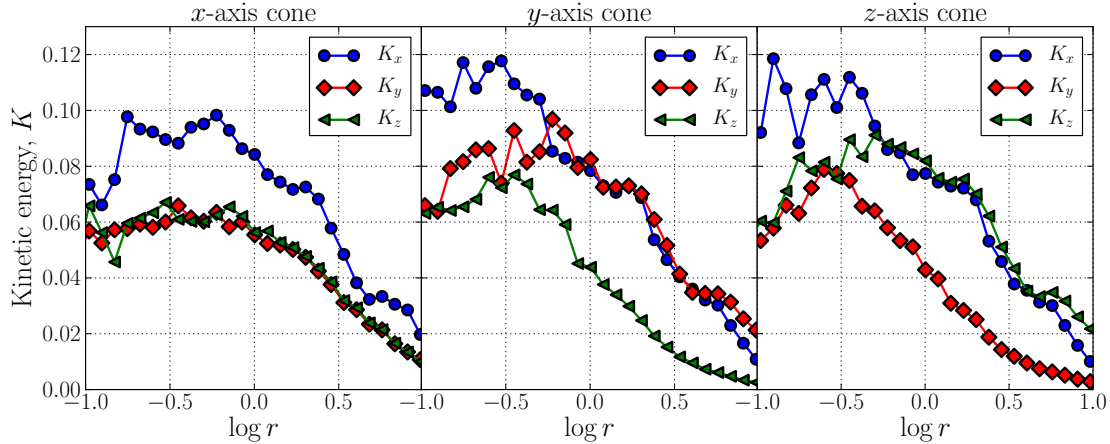


Figure 2.4: The mean kinetic energies in the x -, y - and z -direction along the three axes. K_x in the cone along the y -axis is larger than K_y in the cone along the x -axis. This shows that there is more kinetic energy along the collision axis of the merger remnant than along the other axes.

radii (e.g. $10r_{-2}$).

The redistribution of kinetic energy

Imagine two merging haloes, \mathcal{A} and \mathcal{B} , approaching each other with a velocity similar to the escape velocity at the cluster's separation distance. Seen from the center of mass of halo \mathcal{A} , the particles from halo \mathcal{B} have much larger kinetic energies along the collision axis than along the perpendicular axes due to the relative motion of the haloes. The reason why merger remnants have different β -profiles in different cones is likely that merging processes are inefficient at transferring the kinetic energy along the collision axis, into kinetic energy along the other axes. Many particles in a merger remnant are likely left on non-spherical orbits, where they oscillate back and forth along the collision axis. Such a scenario is perfectly consistent with what we see in Figure 2.2.

To test this explanation further the kinetic energies (K_x , K_y and K_z) along each axis are calculated in each cone, see Figure 2.4. Along the collision axis (x), we find that $K_y \simeq K_z$ at all radii. Along the y -axis, K_x is larger than K_z at all radii. This supports our claim, that the kinetic energy is not totally redistributed from the direction of the collision axis to the perpendicular directions in a merger.

An observation is that $K_x \simeq K_y$ in the outer parts of the cone along the y -axis. This means that in a cone perpendicular to the collision axis, we have that $\sigma(\text{collision axis}) \simeq \sigma_{\text{rad}}$ in the outer parts.

2.3.2 The effect of an impact parameter

The presence of impact parameters breaks the rotation symmetry around the collision axis (which was present in the simulation without impact parameters), since the merging haloes are spiralling around each other in the x - y plane.

Figure 2.5 shows the anisotropy and the velocity dispersions, when an impact parameter of $10r_s$ is present. The rotation velocity at a given radius was subtracted before the velocity dispersion in a given bin was calculated. The velocity anisotropy is constant and positive in the inner regions in both the x - and in the y -direction, and negative in

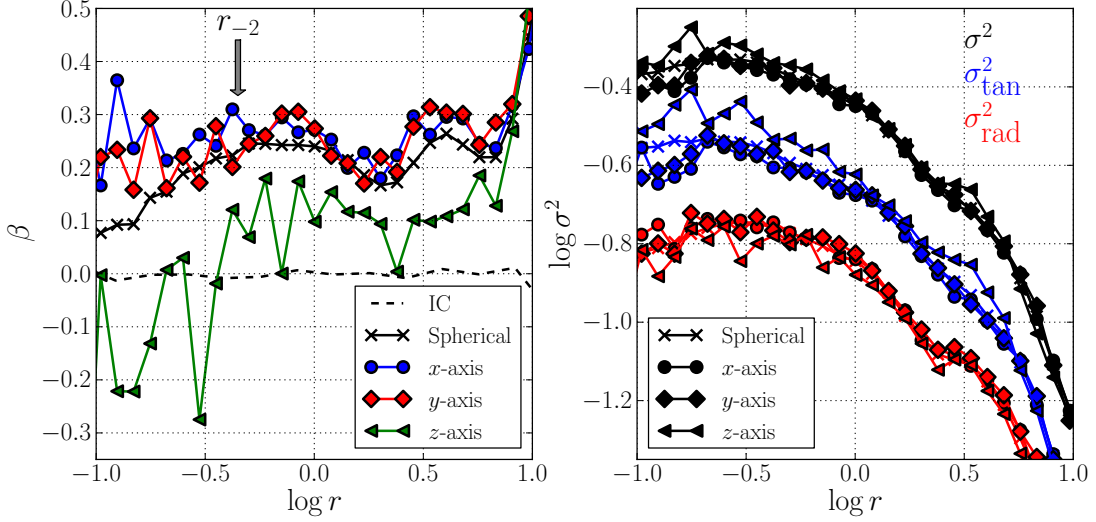


Figure 2.5: The velocity anisotropy and the velocity dispersion for the major merger simulation with an impact parameter. The merging process is taking place in the x - y plane.

the z -direction. It is different from the simulations without impact parameters, where β was negative in both the y - and the z -direction. The spherically averaged β -profile has a non-monotonic shape, similar to what is found in other studies of major merger remnants (e.g. McMillan et al. (2007)).

The velocity dispersions are similar in all the three cones, except for the inner parts, where the cone in the z -direction has a larger tangential and a lower radial dispersion.

2.3.3 Major mergers with Osipkov-Merritt haloes

Figure 2.6 shows the remnant of two Osipkov-Merritt haloes collided without an impact parameter. In this case the merger remnant again had different velocity anisotropies and velocity dispersions in the different cones.

Before the progenitor cores touched each other, the two haloes were clearly more elongated, when visually inspected, than for the $\beta_{\text{initial}} = 0$ mergers. Instabilities, such as the radial orbit instability, are therefore likely play an important role, and such instabilities might be the reason why the velocity anisotropies are not the same in the y - and the z -direction, which would be expected from the symmetries of the initial conditions.

2.3.4 Minor mergers

Figure 2.7 shows the velocity anisotropies in a 1:10 merger remnant for a simulations without an impact parameter. Three sets of particles are analysed: i) all the particles in the simulation (*left panel*), ii) the particles that started in the small halo (*central panel*) and iii) the particles originating from the main halo (*right panel*). The particles from the main halo remain at $\beta = 0$, and are almost unaffected by the merging process. The particles from the small halo are in orbits with $\beta = 0.3 - 1.0$. When all particles are analysed β is positive ($\beta \simeq 0.4$) along the collision axis, but a nearly isotropic velocity distribution ($\beta \simeq 0.1$) are present in the perpendicular directions.

With an impact parameter present the velocity anisotropies are as shown in Figure 2.8. The main halo particles remain at $\beta = 0$, but the spherically averaged β -profiles are again

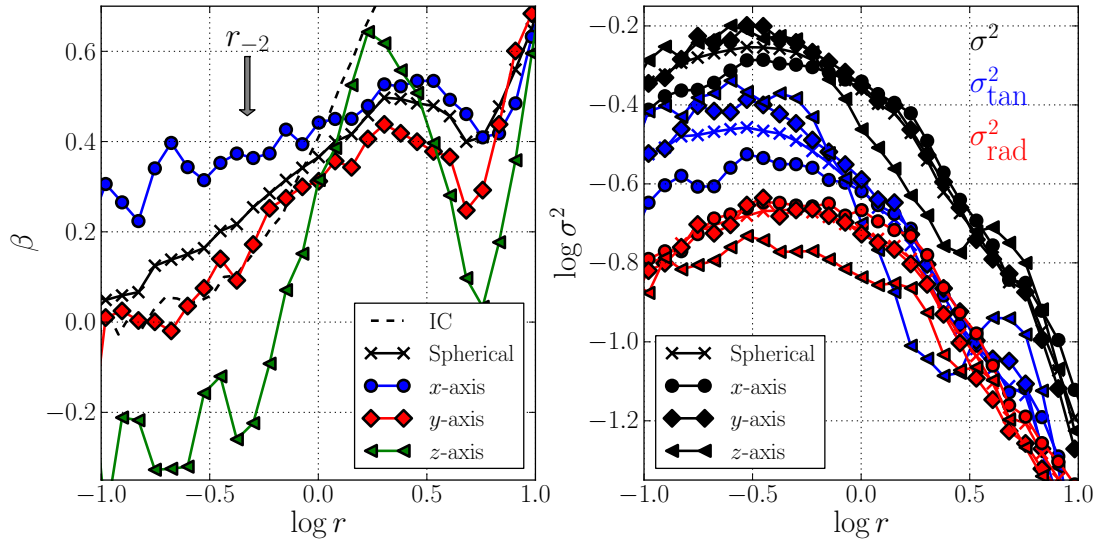


Figure 2.6: Same as Figure 2.2, but with initial haloes following Osipkov-Merritt models.

positive due to the contribution from the particles from the small halo. Also note that the velocity anisotropy in the y -direction is larger than in the simulation without an impact parameter.

The complicated direction-dependence of the velocity distributions in the minor merger remnants, is likely similar to the direction-dependent velocity structure in the substructure of cosmological simulations (Lisanti & Spergel, 2011).

2.4 The effect of an accretion process

Like mergers, smooth accretion of matter is a very important process for the build up of structure in the universe. We now want to study how the asymmetric β -profiles in merger remnants are affected by a spherically symmetric perturbation that mimics smooth accretion.

In the remnant of the major merger simulation without an impact parameter (from Section 2.3.1), we inserted particles in a spherical shell in the region, $4.8 < r/r_{-2} < 15$, with a density profile following, $\rho(r) \propto r^{-2}$. Each particle has a radial infall velocity identical to the escape velocity at its position. The number of particles in the shell and the mass of each particle are the same as in the major merger simulations (2×10^6 particles with a total mass of 2). The simulations were run for 300 time units, which corresponds to 250 dynamical times, $\sqrt{r^3/GM(r)}$, at r_{-2} of the final structure, and 20 dynamical times at $10r_{-2}$.

Figure 2.9 shows the evolution of the density profiles for the particles that started in the merger remnant, and for the infall particles that started in the shell. The infall particles only gives a minor contribution to the central densities of the final structure ($\lesssim 5\%$).

Figure 2.10 shows the anisotropy for the final structure for all the particles, the accreted particles and the particles that started in the merger remnant. For all sets of particles, β is largest in the x -direction, and smaller in the directions perpendicular to the merger axis. An interesting observation is that the β -profiles of the accreted particles are very similar to the β -profiles of the particles from the merger remnant.

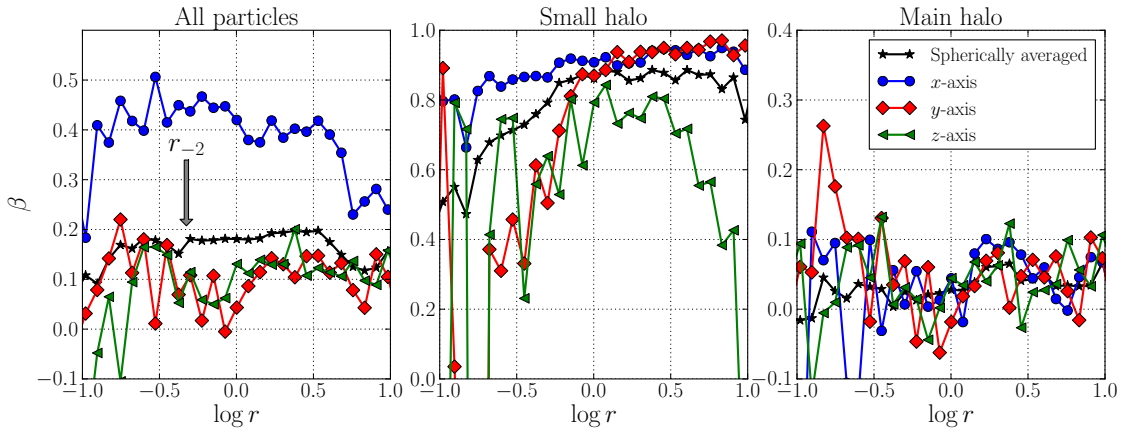


Figure 2.7: Particles in a remnant of a 1:10 merger without an impact parameter are analysed in cones. The *left panel* shows all the particles in the simulation, the *central panel* shows particles that started in the small halo, and the *right panel* shows particles from the main halo.

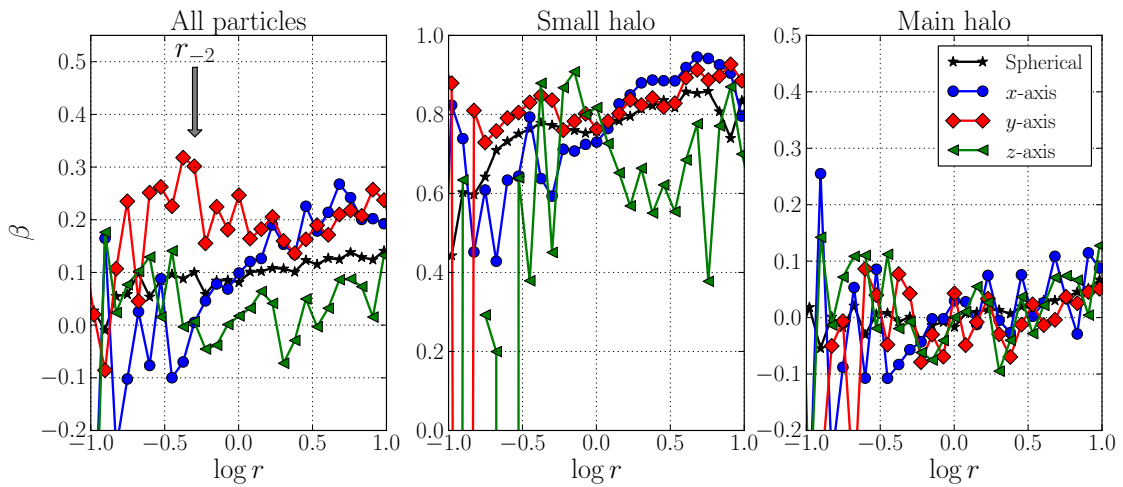


Figure 2.8: Same as Figure 2.7, but with an impact parameter along the y -axis.

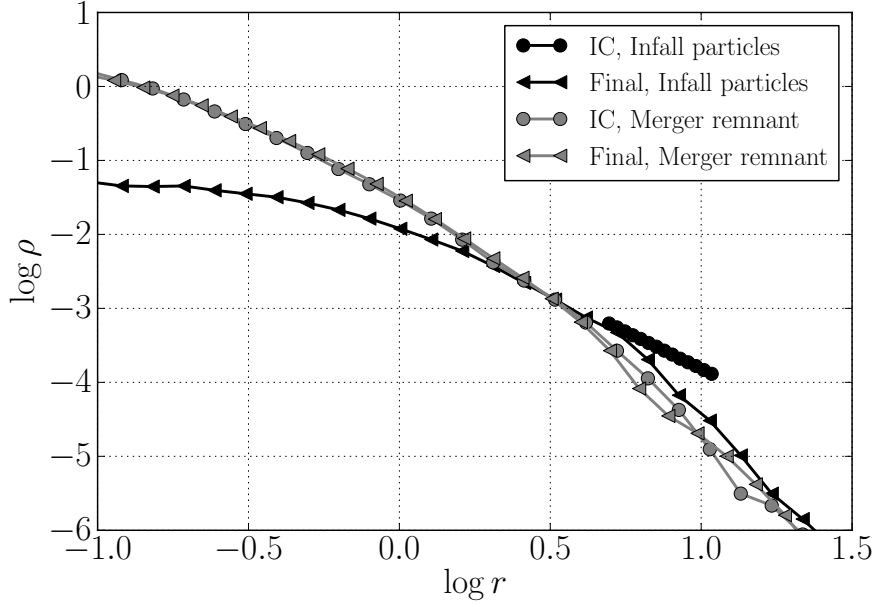


Figure 2.9: The initial conditions and the results of the simulations, where a merger remnant (grey points) is perturbed by a process that mimics smooth accretion. A group of particles accretes onto the structure from a shell at radii $4.8 < r/r_{-2} < 15$ (black circles).

We conclude that the asymmetric velocity anisotropies remain asymmetric, when perturbed by this accretion process.

2.5 Skymaps of the anisotropies

So far we have focused on analysing particles in cones in the x -, y - and z -direction. We will now take a more detailed look on the angular dependence of the β -profiles. To do so we distributed 192 points on a sphere using the HEALPIX framework (Górski et al., 2005), and defined a cone pointing in the direction of each point. The apex angle was still 45° , so the cone angle is larger than the size of one pixel.

Figure 2.11 shows a Mollweide projection (which is heavily used in CMB analysis) of β at a radius of 0.35 for the major mergers with $\beta_{\text{initial}} = 0$. Figure 2.12 shows the same plot for the major merger with an impact parameter along the y -axis, and Figure 2.13 shows the minor merger without an impact parameter.

In the Mollweide projection the positive x -direction is in the center of the plot, and negative x -direction are the points most to the right and left. The positive z -direction is the top point, and the negative z -direction is the bottom point. The y -axes are in the two points between the positive and negative x -axis (the positive y -axis is to the right, the negative to the left).

A visible effect is that the presence of an impact parameter breaks the symmetry along the y - z plane in Figure 2.12. It is also clear that the minor merger, mostly affects β along the infall direction (Figure 2.13).

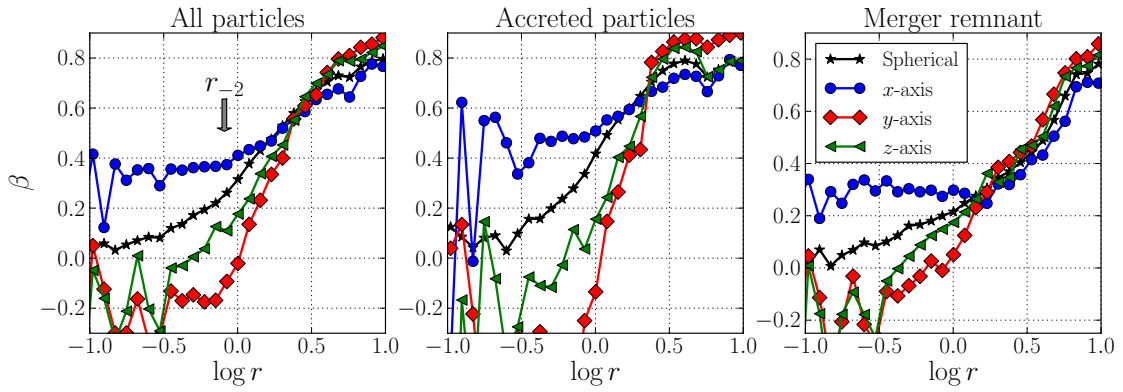


Figure 2.10: The velocity anisotropy of the particles in the accretion simulation. The *left panel* shows $\beta(r)$ for all the particles in the simulation, the *central panel* shows the particles from the accretion shell, and the *right panel* shows the particles that started in the merger remnant.

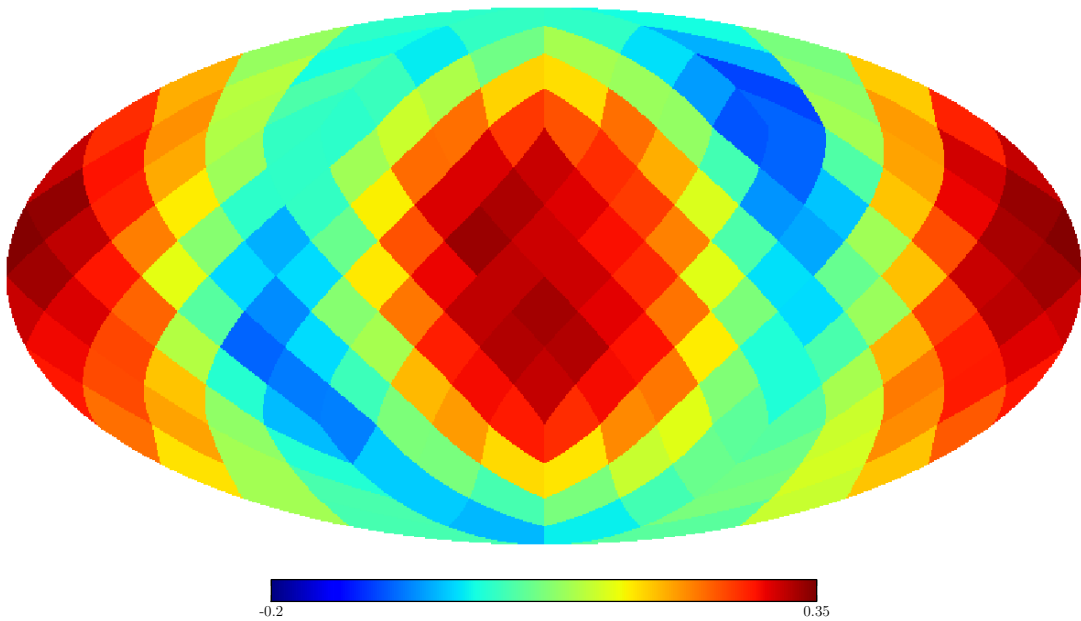


Figure 2.11: Sky map of β of the major merger with $\beta_{\text{initial}} = 0$.

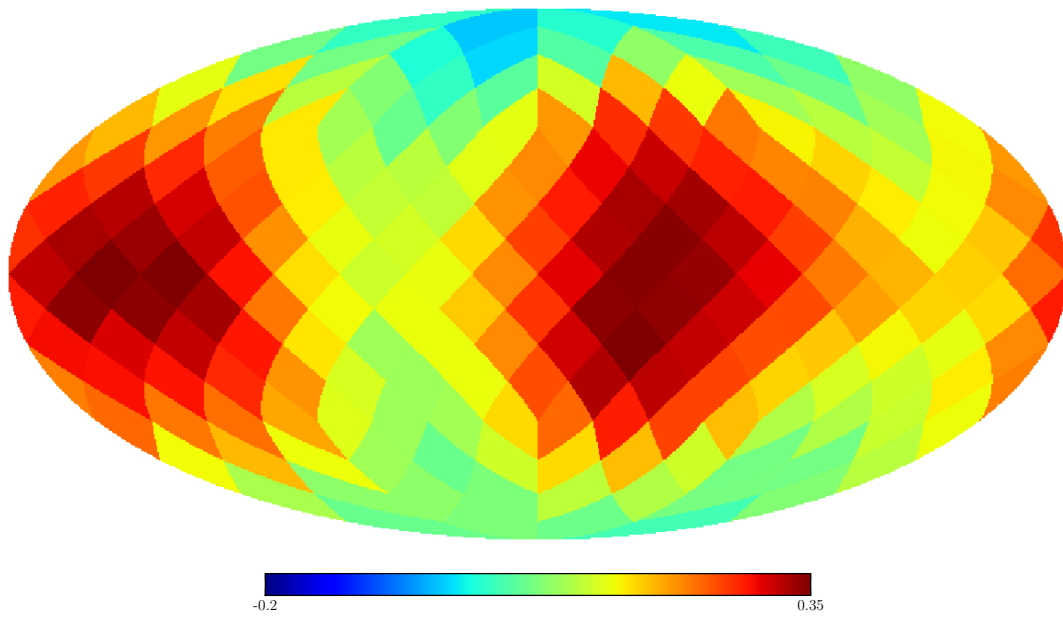


Figure 2.12: Skymap of β of the major merger with $\beta_{\text{initial}} = 0$ and an impact parameter along the y -axis.

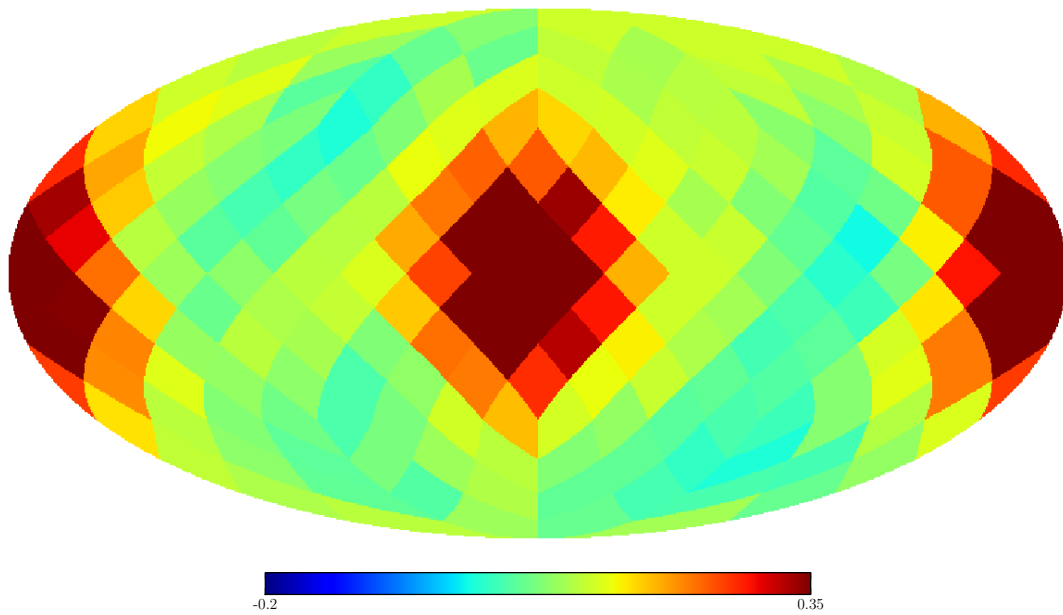


Figure 2.13: Skymap of β of the minor merger with $\beta_{\text{initial}} = 0$ and no impact parameter.

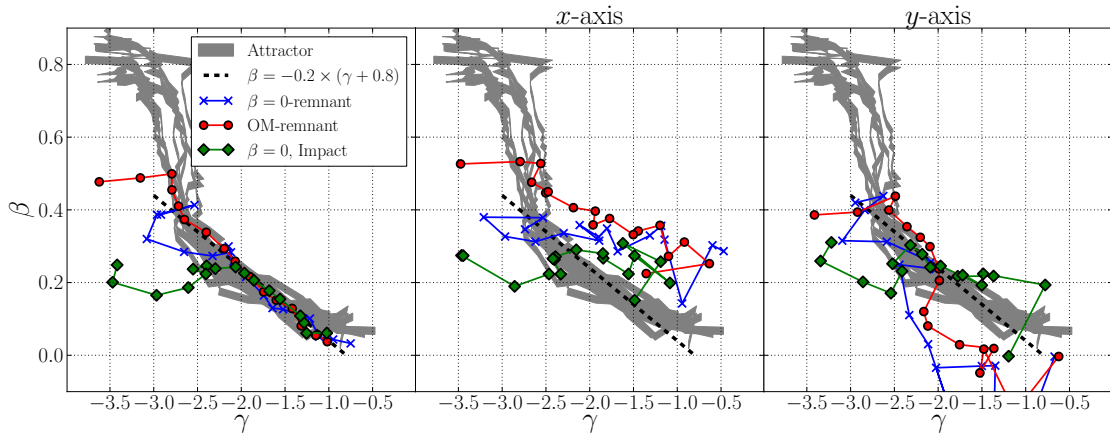


Figure 2.14: $\beta(\gamma)$ profiles for the remnant of the major merger between the $\beta_{\text{initial}} = 0$ haloes (with and without an impact parameter), and the major merger with two Osipkov-Merritt haloes. The remnants are compared between two proposed $\beta(\gamma)$ -relations: $\beta = -0.2 \times (\gamma + 0.8)$ (Hansen & Stadel, 2006) and the *attractor* (the grey lines are taken from (Hansen et al., 2010)). The *left panel* shows spherically averaged profiles, the *central panel* shows a cone along the collision axis, and *right panel* shows a cone perpendicular to the collision axis.

2.6 β - γ relations

We will now compare the merger remnants with the β - γ relation (Hansen & Stadel, 2006), $\beta = -0.2 \times (\gamma + 0.8)$, and the attractor (Hansen et al., 2010; Barber et al., 2012). Figure 2.14 (*left panel*) shows the spherically averaged $\beta(\gamma)$ profiles for the major merger remnants. The *central panel* and the *right panel* show the same for the cones along the x - and y -axis, respectively.

The β - γ relations are clearly not obeyed in the two plotted cones, but the spherically averaged β -profiles are in good agreement with the two predictions in the inner parts with $\gamma > -2.2$. The outer parts with $\gamma < -2.2$ deviate from the relations. It is seen that the spherically averaged β - and γ -profiles obey the β - γ -relations at the radii, where the β -profile is direction-dependent.

We see that the spherically averaged $\beta(\gamma)$ profile in the outer parts is strongly dependent on a remnants merging history. This finding can explain the large scatter of $\beta(\gamma)$ between haloes in cosmological simulations (Ludlow et al., 2011). In Figure 2.2, 2.3 and 2.6, we also find that $\beta(r)$ depends on the detailed merging history, so we conclude that the differences in $\beta(r)$ from halo to halo in cosmological simulations can be caused by their different merging histories.

2.7 Pseudo-phase-space density profiles

The pseudo-phase-space density profiles (PPSD's), $\rho/\sigma_{\text{rad}}^3$ and ρ/σ^3 , of the major merger remnants with $\beta_{\text{initial}} = 0$ are shown in Figure 2.15. The profiles are scaled with a factor of $r^{1.91}$, which roughly would give a constant in cosmological simulations (Ludlow et al., 2011). In both remnants the normalizations of the PPSD-profiles depend on the cone-direction. The best-fitting value for α only has a small variation from cone to cone.

In several studies dynamical constraints of dark matter haloes have been derived by assuming a radial power law behaviour of $\rho/\sigma_{\text{rad}}^3$ or ρ/σ^3 (Hansen, 2004; Austin et al.,

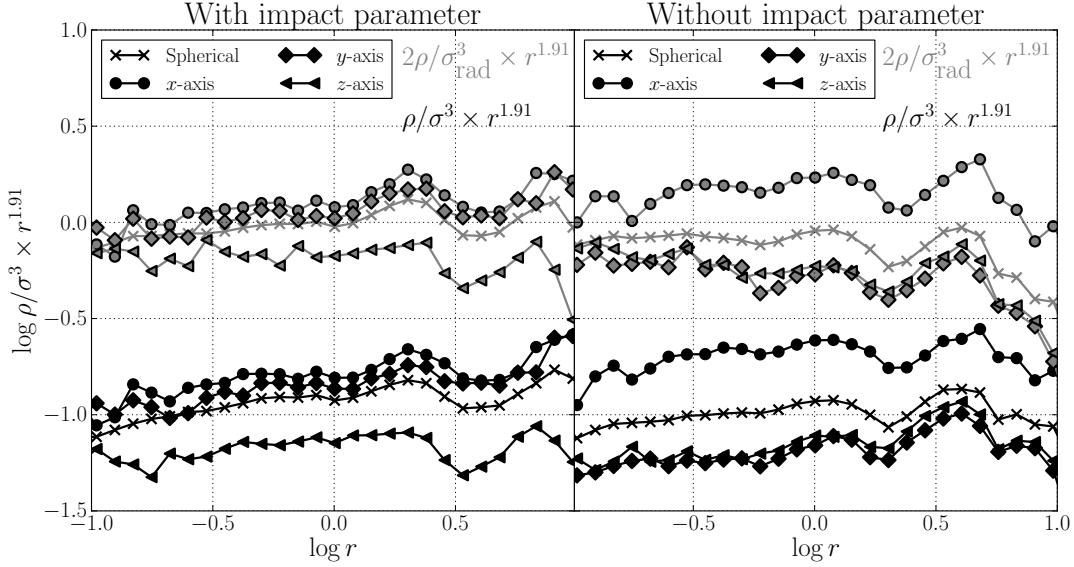


Figure 2.15: The pseudo-phase-space density profiles, $\rho/\sigma_{\text{rad}}^3$ and ρ/σ^3 , for the major merger remnant with an impact parameter (*left panel*) and without and impact parameter (*right panel*). $\rho/\sigma_{\text{rad}}^3$ is multiplied with a factor of 2 for presentation reasons.

2005; Dehnen & McLaughlin, 2005). In the merger remnants this assumption is however not correct, due to the different normalizations from cone to cone, so such an approximation does not describe the full dynamics of the remnants.

2.8 The shape of the haloes

It is established that a merger with two spherical haloes without angular momentum results in a prolate halo with a major axis along the collision axis (Moore et al., 2004). With angular momentum an oblate remnant is found and its short axis is aligned with the angular momentum vector (Moore et al., 2004). It has also been shown that the potential and velocity contours of a halo are more spherical than the density contours (Allgood et al., 2006; Kuhlen et al., 2007).

In our merger remnants we measure the minor to major axis ratio, c/a , by comparing density profiles in cones through points distributed uniformly of a sphere (with the same method as in Section 2.5). To be explicit we will find the maximum and minimum values of the radius for a given density, and then calculate the ratio between these two radii. The shape will only be determined at $r = 1$.

For all the mergers without an impact parameter the halo shapes were aligned with the collision axes. For the major mergers with $\beta_{\text{initial}} = 0$ the axis ratio was 0.59, for the minor merger we found a ratio of 0.84, and for the Osipkov-Merritt model we found 0.53. For the major merger with an impact parameter we found a ratio of 0.7, and for the minor merger with an impact parameter we found 0.86 with a major axis in the xy -plane and a minor axis along the z -axis.

By visually inspecting the major remnants we found, that the zero impact parameter collisions produced prolate haloes. The major merger with an impact parameter produced an oblate halo with a major axis in the xy -plane, and a minor axis along the z -axis.

Our simulations are therefore consistent with the discovery in (Zemp et al., 2009), in which it was discovered that β is aligned with the shape of cosmological haloes, with positive β -values along the major axis, and negative β -values along the minor axis.

The cosmological halo from the Via Lactea II simulation is prolate with $c/a = 0.52$ and $b/a = 0.62$, where b/a is the ratio between the intermediate axis and the major axis. In this sense the Via Lactea II halo is similar to the haloes without an impact parameter, which are also prolate. In cosmologically realistic haloes the exact shape and asymmetric nature of the velocity anisotropy will, however, likely be determined by several minor or major mergers, and therefore be more complicated, than the haloes studied in this article.

2.9 Conclusion

We have analysed the velocity distributions in different cones centered on merger remnants. The velocity anisotropy profiles and the velocity dispersions in the different cones behaved differently. This was both the case for major mergers with and without impact parameters, and for minor mergers. We also demonstrated that these asymmetries are not washed out by a process that mimics smooth accretion. Since mergers are frequent in the real universe, it is therefore not surprising that similar asymmetries are present in cosmological haloes (Zemp et al., 2009).

In the various merger simulations, the behaviour of $\beta(r)$ in the outer parts had a huge dependency on the initial conditions. We therefore conclude, that the different behaviour of $\beta(r)$ from halo to halo in cosmological simulations can be caused by their different merger histories.

Several studies (Lynden-Bell, 1967; Nakamura, 2000; Hansen, 2009; Hjorth & Williams, 2010; Williams & Hjorth, 2010; Williams et al., 2010; Kang & He, 2011; Hansen & Sparre, 2012) have attempted to derive or characterise distribution functions of completely relaxed haloes from first principles. We have demonstrated that merger remnants have the merger history encoded in their velocity anisotropy profiles, and they are therefore not expected to follow simple distribution functions, where β is constant within spherical bins or along the isodensity contours. Furthermore it is also clear that the β - γ relation or the *attractor* are not obeyed in all cones in merger remnants. We do, however, find that the spherically averaged properties of haloes obey these relations in the inner parts.

Finally, we note that the merger history likely is important for observational aspects of the dark matter haloes. This is exemplified through a correlation between the asymmetric nature of the velocity anisotropy of haloes and the surrounding large-scale structure (Wojtak et al., 2012), along which matter accretion typically occurs (Libeskind et al., 2011), and the differences in the line-of-sight velocity dispersions of galaxies along the major and minor axes of galaxy clusters (Skjelboe et al., 2012).

Bibliography

- Allgood, B., Flores, R. A., Primack, J. R., Kravtsov, A. V., Wechsler, R. H., Faltenbacher, A., & Bullock, J. S. 2006, *MNRAS*, 367, 1781
- Austin, C. G., Williams, L. L. R., Barnes, E. I., Babul, A., & Dalcanton, J. J. 2005, *ApJ*, 634, 756
- Barber, J. A., Zhao, H., Wu, X., & Hansen, S. H. 2012, *ArXiv e-prints*
- Binney, J., & Tremaine, S. 2008, *Galactic Dynamics: Second Edition* (Princeton University Press)
- Bradač, M., et al. 2006, *ApJ*, 652, 937
- Clowe, D., Bradač, M., Gonzalez, A. H., Markevitch, M., Randall, S. W., Jones, C., & Zaritsky, D. 2006, *ApJ*, 648, L109
- Dehnen, W., & McLaughlin, D. E. 2005, *MNRAS*, 363, 1057
- Diemand, J., Kuhlen, M., Madau, P., Zemp, M., Moore, B., Potter, D., & Stadel, J. 2008, *Nature*, 454, 735
- Diemand, J., Moore, B., & Stadel, J. 2004, *MNRAS*, 352, 535
- Eddington, A. S. 1916, *MNRAS*, 76, 572
- Gao, L., Navarro, J. F., Cole, S., Frenk, C. S., White, S. D. M., Springel, V., Jenkins, A., & Neto, A. F. 2008, *MNRAS*, 387, 536
- Górski, K. M., Hivon, E., Banday, A. J., Wandelt, B. D., Hansen, F. K., Reinecke, M., & Bartelmann, M. 2005, *ApJ*, 622, 759
- Hansen, S. H. 2004, *MNRAS*, 352, L41
- . 2009, *ApJ*, 694, 1250
- Hansen, S. H., Juncher, D., & Sparre, M. 2010, *ApJ*, 718, L68
- Hansen, S. H., & Moore, B. 2006, *New Astronomy*, 11, 333
- Hansen, S. H., & Sparre, M. 2012, *ArXiv e-prints*
- Hansen, S. H., & Stadel, J. 2006, *JCAP*, 5, 14
- Hernquist, L. 1990, *ApJ*, 356, 359

Hjorth, J., & Williams, L. L. R. 2010, *ApJ*, 722, 851

Kang, D.-B., & He, P. 2011, *A&A*, 526, A147

Komatsu, E., et al. 2011, *ApJS*, 192, 18

Kuhlen, M., Diemand, J., & Madau, P. 2007, *ApJ*, 671, 1135

Libeskind, N. I., Knebe, A., Hoffman, Y., Gottlöber, S., Yepes, G., & Steinmetz, M. 2011, *MNRAS*, 411, 1525

Lisanti, M., & Spergel, D. N. 2011, *ArXiv e-prints*

Ludlow, A. D., Navarro, J. F., White, S. D. M., Boylan-Kolchin, M., Springel, V., Jenkins, A., & Frenk, C. S. 2011, *MNRAS*, 937

Lynden-Bell, D. 1967, *MNRAS*, 136, 101

Macciò, A. V., Dutton, A. A., & van den Bosch, F. C. 2008, *MNRAS*, 391, 1940

Mastropietro, C., & Burkert, A. 2008, *MNRAS*, 389, 967

McMillan, P. J., Athanassoula, E., & Dehnen, W. 2007, *MNRAS*, 376, 1261

Merritt, D. 1985, *AJ*, 90, 1027

Meza, A., & Zamorano, N. 1997, *ApJ*, 490, 136

Moore, B., Kazantzidis, S., Diemand, J., & Stadel, J. 2004, *MNRAS*, 354, 522

Nakamura, T. K. 2000, *ApJ*, 531, 739

Navarro, J. F., Frenk, C. S., & White, S. D. M. 1996, *ApJ*, 462, 563

—. 1997, *ApJ*, 490, 493

Navarro, J. F., et al. 2010, *MNRAS*, 402, 21

Osipkov, L. P. 1979, *Soviet Astronomy Letters*, 5, 42

Perlmutter, S., et al. 1999, *ApJ*, 517, 565

Riess, A. G., et al. 1998, *AJ*, 116, 1009

Skielboe, A., et al. 2012, in prep

Springel, V. 2005, *MNRAS*, 364, 1105

Springel, V., Di Matteo, T., & Hernquist, L. 2005, *MNRAS*, 361, 776

Springel, V., & Farrar, G. R. 2007, *MNRAS*, 380, 911

Taylor, J. E., & Navarro, J. F. 2001, *ApJ*, 563, 483

Williams, L. L. R., & Hjorth, J. 2010, *ApJ*, 722, 856

Williams, L. L. R., Hjorth, J., & Wojtak, R. 2010, *ApJ*, 725, 282

Wojtak, R., et al. 2012, in prep

Zemp, M., Diemand, J., Kuhlen, M., Madau, P., Moore, B., Potter, D., Stadel, J., & Widrow, L. 2009, *MNRAS*, 394, 641

Chapter 3

Collisionless dynamics II: more idealized simulations of dark matter halos

This chapter contains the following article:

The behaviour of shape and velocity anisotropy in dark matter haloes

Published in Sparre & Hansen, 2012, JCAP,10,049

Authors: Martin Sparre & Steen H. Hansen

Abstract

Dark matter haloes from cosmological N-body simulations typically have triaxial shapes and anisotropic velocity distributions. Recently it has been shown that the velocity anisotropy, β , of cosmological haloes and major merger remnants depends on direction in such a way that β is largest along the major axis and smallest along the minor axis. In this work we use a wide range of non-cosmological N-body simulations to examine halo shapes and direction-dependence of velocity anisotropy profiles. For each of our simulated haloes we define 48 cones pointing in different directions, and from the particles inside each cone we compute velocity anisotropy profiles. We find that elongated haloes can have very distinct velocity anisotropies. We group the behaviour of haloes into three different categories, that range from spherically symmetric profiles to a much more complex behaviour, where significant differences are found for β along the major and minor axes. We encourage future studies of velocity anisotropies in haloes from cosmological simulations to calculate β -profiles in cones, since it reveals information, which is hidden from a spherically averaged profile. Finally, we show that spherically averaged profiles often obey a linear relation between β and the logarithmic density slope in the inner parts of haloes, but this relation is not necessarily obeyed, when properties are calculated in cones.

3.1 Introduction

The gravitational potential of galaxies and galaxy clusters are dominated by dark matter haloes. Such haloes have only been observed through their gravitational impact on other objects: e.g. in the Bullet Cluster (Clowe et al., 2006; Bradač et al., 2006), the motion of galaxies in clusters (Zwicky, 1933) and in the cosmic microwave background (Komatsu et al., 2011). Therefore, the most fruitful way to study the detailed dynamics of dark matter structures is through numerical simulations.

The formation and evolution of the large-scale structure in the universe can be simulated with N-body codes, where the density field and velocity field of the dark matter are represented by collisionless particles. In such simulations it is found, that the dark matter haloes follow a universal density profile, usually parametrised as an Einasto-profile (Navarro et al., 2004) or a NFW-profile (Navarro et al., 1996). A different universality is the pseudo-phase-space density profile, $\rho/\sigma_{\text{rad}}^3$, which is a power law in radius (ρ is the density and σ_{rad} is the radial velocity dispersion) (Taylor & Navarro, 2001; Hansen, 2004; Austin et al., 2005; Dehnen & McLaughlin, 2005). It is worth noting that particles in subhaloes and streams do not follow this power law behaviour (Ludlow et al., 2011). Subhaloes are also responsible for large peaks in the true 6-dimensional phase-space density distributions in haloes from cosmological simulations (Arad et al., 2004; Ascasibar & Binney, 2005; Sharma & Steinmetz, 2006; Stadel et al., 2009; Ludlow et al., 2010).

The mass distributions of haloes from cosmological simulations are triaxial ellipsoids with a major axis (with length a), an intermediate axis (with length b) and a minor axis (with length c). If $a \simeq b > c$ a halo is oblate (*pancake* shaped), if $a > b \simeq c$ a halo is prolate (*cigar* shaped), and if $a \simeq b \simeq c$ a halo is spherical. High-redshift haloes are typically more elongated than those at low redshift, and it is also a trend that light haloes are closer to being spherical than massive haloes (Allgood et al., 2006). One possible mechanism that likely is important for creating elongated haloes is mergers, that can produce both prolate and oblate haloes (White, 1978; Moore et al., 2004).

Dark matter systems can have anisotropic velocity distributions. The anisotropy is characterised by the velocity anisotropy parameter,

$$\beta(r) \equiv 1 - \frac{\sigma_{\text{tan}}^2}{2\sigma_{\text{rad}}^2}, \quad (3.1)$$

where σ_{rad} is the velocity dispersion in the radial direction, and σ_{tan} is the total tangential velocity dispersion. β is positive in regions with radially dominated anisotropy, and negative in regions with tangentially dominated anisotropy. The inner parts of haloes in cosmological simulations have β -profiles (calculated in spherically averaged bins) increasing from 0 in the deep interior to about 0.3 at the core radius (Diemand et al., 2004; Cuesta et al., 2008; Ludlow et al., 2011; Lemze et al., 2012). The β -profiles in the outer parts exhibit different behaviour from halo to halo.

From the outcome of a wide range of simulations (Hansen & Moore, 2006), a relation has been suggested between the spherically averaged value of β at a given radius (r) and the slope of the density profile,

$$\gamma(r) \equiv \frac{d \log \rho}{d \log r}. \quad (3.2)$$

The relation, $\beta(\gamma) = -0.2 \times (\gamma + 0.8)$, is valid in the inner parts of haloes in cosmological simulations (Hansen & Stadel, 2006). A more recent relation, the *attractor*, was found

in several different structures, which were exposed to an artificial process that instantaneously interchanged energy between particles (Hansen et al., 2010) (HJS). The role of the attractor in cosmological simulations, however, remains undetermined.

There exists evidence that β -profiles are not spherically symmetric functions (or functions that are constant along density or potential contours, if the structure is non-spherical) in all dark matter haloes. In a detailed study of remnants of collisionless mergers, it has been shown that the velocity anisotropy profiles of merger remnants exhibit different behaviour depending on whether they are calculated along the major or the minor axis (Sparre & Hansen, 2012). The behaviour of β were clearly correlated with the shape and the orientation of the haloes, in such a way that the largest velocity anisotropy was found along the major axis. Similar asymmetric β -profiles are also found in cosmological simulations (Zemp et al., 2009).

The aim of this article is to study the behaviour of direction-dependent velocity anisotropy profiles and halo shapes in a set of non-cosmological simulations. In section 3.2 we describe our simulations, and in section 3.3 we describe our analysis methods. Next (section 3.4) we study the direction-dependence of β -profiles together with halo shapes, and we compare our results to cosmological haloes in section 3.5. In section 3.6 we report halo shapes and spherically averaged β - and γ -profiles. Finally we compare haloes with the attractor from HJS (section 3.7).

3.2 Simulations

The overall purpose of our simulations is to expose haloes to a range of perturbations, so we can study velocity anisotropy profiles and halo shapes in haloes formed in several different ways. Simulation I is an artificial simulation, that involves an instantaneous change in the gravitational potential, simulation II is the energy exchange perturbation from HJS, simulation III is a collapse experiment, simulation IV involves multiple major mergers, simulation V involves unstable haloes and simulation VI shows the effect of substructure in a halo. An overview of parameters is given in Table 3.1, and an overview of the initial structures is given in Table 3.2.

3.2.1 Simulation code

To run our simulations we used the N-body simulation code, Gadget-2 (Springel et al., 2001; Springel, 2005). The simulations were run in a non-cosmological Newtonian box, and we only used collisionless particles. For all the simulations the spline softening, η , implemented in Gadget-2 was used. The time-step of each particle was calculated as $\Delta t = (2\eta\epsilon/|\mathbf{a}|)^{1/2}$ (for a discussion of time-step criteria see (Zemp et al., 2007)), where $|\mathbf{a}|$ is the magnitude of the acceleration and ϵ is the accuracy parameter, which was set to 0.05 in our simulations. In all simulations the energy conservation was better than 1.0 %.

3.2.2 Simulation I – An instantaneous change in the potential

The first of our simulations will show how structures respond to a process, where the gravitational potential changes instantaneously. Such a change perturbs the accelerations in contrast to the perturbations of the velocities performed in HJS (see section 3.2.3 for details).

Table 3.1: The softening, the total mass and the gravitational constant in the simulations. $r_s \equiv 1$ in all the initial structures.

	Description	Softening	Mass	G
I	G -variations	0.0050	1	0.8 – 1.2
II	Energy exchange (HJS)	0.0050	1	1
III	Cold collapse	0.0025	1	1
IV	Multiple mergers	0.0050	128	1
V	Unstable models	0.0050	1	1
VI	Substructure	0.0015	1	1

Table 3.2: An overview of the structures in the simulations. The *Colour* and *Symbol* columns refer to how structures are presented in figure 3.7-3.13.

^a Same collision axis in the two last simulations.

Name	ρ	β	Sim.	Colour	Symbol
A	Hernquist	0	I and II	maroon	\diamond
B	$1/(1+r)^5$	0	I and II	red	\circ
C	Hernquist	$r^2/(1+r^2), r_{\text{an}} = 1.0$	I and II	orange	\triangleleft
D	$1/(1+r)^{3.5}$	$r^2/(1.5^2+r^2), r_{\text{an}} = 1.5$	I and II	blue	x
E	Hernquist	0, Gaussian	I and II	pink	*
F	Hernquist	1/2, Gaussian	I and II	green	+
G	Hernquist	$r^2/(1+r^2)$, Gaussian	I and II	black	\triangleright
H	Hernquist	$1-r^2/(1+r^2)$, Gaussian	I and II	yellow	\triangledown
I	Hernquist	-	III	black	\circ
J	$1/(1+r)^5$	-	III	black	x
K	Hernquist	0	IV	red	\diamond
L	$1/(1+r)^5$	0	IV	red	*
M	$1/(1+r)^3$	0	IV	red	\triangleleft
N	Hernquist	0	IV ^a	blue	\circ
O	$1/(1+r)^5$	0	IV ^a	blue	*
P	$1/(1+r)^3$	0	IV ^a	blue	\triangleleft
Q	Hernquist	$r^2/(0.2^2+r^2), r_{\text{an}} = 0.2$	V	green, IC: blue	\triangleleft
R	$1/(1+r)^5$	$r^2/(0.2^2+r^2), r_{\text{an}} = 0.2$	V	green, IC: blue	*
S	Hernquist	0	VI	red, IC: black	\diamond , IC: \circ

First eight structures with different velocity anisotropies and density profiles were created. The density profiles were of the form,

$$\rho(r) = \frac{\rho_0}{(r/r_s)^{-\xi}} \frac{1}{(1 + r/r_s)^{-\zeta}}, \quad (3.3)$$

where r_s is the scale radius and ρ_0 is a normalization constant determining the total mass. Six structures followed a Hernquist density profile ($\xi = 1$ and $\zeta = 3$) (Hernquist, 1990), one structure had $(\xi, \zeta) = (0, 3.5)$ and one structure had $(\xi, \zeta) = (0, 5)$.

Two of the structures were created using Eddington's formula for $\beta = 0$ (Binney & Tremaine, 2008), and two structures were Osipkov-Merritt models (Merritt, 1985; Osipkov, 1979) with velocity anisotropy profiles given by,

$$\beta(r) = \frac{r^2}{r_{\text{an}}^2 + r^2}, \quad (3.4)$$

where r_{an} is the anisotropy radius.

For four of the Hernquist structures the initial velocity distributions were Gaussian distributions with velocity dispersions, σ_{rad} and σ_{tan} , calculated from the Jeans equation (Hernquist, 1993). Structures with $\beta_{\text{initial}} = 0$, $\beta_{\text{initial}} = 1/2$, $\beta_{\text{initial}} = r^2/(1 + r^2)$ and $\beta_{\text{initial}} = 1 - r^2/(1 + r^2)$ were created. Structures generated with this method are not in perfect equilibrium, so simulations were run for 100 time units, where the structures had time to equilibrate. We also ran such test simulations for the structures generated with Eddington's method and for the Osipkov-Merritt models to assure equilibration.

All structures had $r_s = 1$, and ρ_0 was chosen such that the total mass inside $r = 13r_s$ was 1. When structures are created in this way the dynamical time, $1/\sqrt{G\rho}$, for particles inside $r = 13r_s$ is smaller than 100 time units, which is the duration of all our simulations. The initial conditions were generated with $G = 1$. The structures used in this simulation are identical to those used in HJS. The initial density profiles and velocity anisotropy profiles are summarised in table 3.2.

The next step in our setup was to run a simulation for 100 time units, where the gravitational constant was set to $G = 0.8$. In this time the structures expanded due to the lowering of the potential. Next the gravitational potential was increased by setting $G = 1.2$, which caused a contraction in the following 100 time units. We kept changing between $G = 1.2$ and $G = 0.8$ every 100 time units until 2000 time units had passed. In the last of these simulation we had $G = 1.2$. An additional simulation with $G = 1.2$ was run for 100 time units, so the structures had more time equilibrate.

3.2.3 Simulation II – Exchange of energy

Simulation II is the simulation from HJS, where an exchange of kinetic energy between particles in the same spherical bin was performed. The experiment was performed for the haloes described in section 3.2.2. In each perturbation the kinetic energy of each particle was multiplied by a uniformly chosen random number in the range $[0.25, 1.75]$. Conservation of the total energy was taken care of by scaling all the kinetic energies by a constant (the constant was typically between 0.98 and 1.02). After this perturbation the haloes were evolved in time with a N-body simulation code. 20 of such perturbations (followed by time evolution of the system) were performed. See more details in HJS.

3.2.4 Simulation III – A cold collapse experiment with substructure

In this simulation we want to assemble a structure through a violent relaxation process (similar to (van Albada, 1982)), that mimics the way structures are assembled when they collapse in the early universe. Our setup will be a main halo, which contains several compact substructures. Initially, all particles had a velocity of zero, so this simulation is therefore effectively a collapse simulation, where the substructures break the spherical symmetry.

We distributed 5×10^5 particles according to a Hernquist density profile with $r_s = 1$ and a cutoff at $200r_s$. Next 5×10^5 particles, with the same total mass as the main halo particles, were distributed in 24 identical subhaloes, that also followed Hernquist profiles, but with a scale radius of 0.5 and a cutoff radius of 5. The positions of the subhaloes were sampled in the same way as the particles in the main halo. The total mass in the simulation was 1. With this setup the time scale of the collapse is 2.45 times larger for the main halo than in the subhaloes.

We ran the simulation for 200 time units, which corresponds to 200 dynamical times at the scale radius for the initial structure. An additional simulation was run, where the initial density profiles of the main halo and the subhaloes were,

$$\rho(r) = \frac{\rho_0}{(1 + r/r_s)^5}. \quad (3.5)$$

We defined $r_s = 1$, and ρ_0 was found by defining the total mass of the halo to be 1.

Note that this simulation is a physically realistic experiment, in the sense that no artificial perturbations have entered the simulation, even though the initial condition for the collapse is different from that of cosmological simulations, e.g. because the initial conditions have a cuspy density profile.

3.2.5 Simulation IV – Major mergers

Now we will build up a structure through major mergers. We first generated two identical structures with Eddington's formula with $\beta = 0$. The two structures were collided, and the remnant of this collision was duplicated and collided again. This procedure was repeated until seven collisions were done. In the collisions the impact parameters were 0, and the collision axis changed from simulation to simulation¹. The initial distances between the collided structures were 10.0, 12.5, 15.0, 25.0, 35.0, 40.0 and 50.0, respectively, and the structures had initial relative velocities of 0.

There were 10^4 dark matter particles in the first simulation and $1.28 \cdot 10^6$ in the last simulation. We used units where the total mass and r_s of the initial structure were defined to be 1, and a cutoff was made at a radius of 10. We ran the last simulation for 200 time units, so the structures had time to first collide (it happened after ~ 75 time units) and then form a new equilibrated halo.

The simulations were done for initial structures following three different density profiles: a Hernquist profile, $\rho(r) \propto 1/(1 + r)^3$ and Eq. (3.5).

Additional simulations were run with the same three density profiles, but instead of rotating the collision axis in the last simulation we used the same collision axis in simulation 6 and 7².

¹The collision axes were the following in the seven simulations: x, y, z, x, y, z, x . The structures were not rotated between the simulations.

²So the collisions occurred along the following axes in the mergers: x, y, z, x, y, z, z .

3.2.6 Simulation V – Unstable Osipkov-Merritt models

It is established that Osipkov-Merritt models following Hernquist profiles are unstable for low values of r_{an} (Meza & Zamorano, 1997), due to the onset of a radial orbit instability (Barnes, 1985), which creates a bar structure in the center of the halo. In this simulation we will study how such an instability affects the velocity anisotropy of a system. The perturbations in this simulation are therefore non-spherical because of the formation of a bar, despite the fact that initial conditions are spherically symmetric.

We ran simulations with two density profiles; a Hernquist profile and Eq. (3.5). In both cases we defined $r_s = 1$ and $r_{\text{an}} = 0.2r_s$. The total mass was 1. The two simulations were run for 200 time units and 10^6 collisionless particles were used to represent each halo.

3.2.7 Simulation VI – A halo and its subhaloes

To see how cosmologically realistic haloes are affected by the dynamical friction from the subhaloes inside them, we generated a halo and subhaloes similar to what is found in the Via Lactea II simulation, which contains a main halo with a mass of $1.94 \times 10^{12} M_\odot$ and a tidal radius of 462 kpc (Diemand et al., 2008).

We used 10^6 dark matter particles to represent the halo and the subhaloes, but only subhaloes heavier than $1.94 \times 10^8 M_\odot$ (the mass of 100 particles) were included. In total 7% of the mass was contained in subhaloes. All haloes followed Hernquist density profiles with the same radius of maximum circular velocity, tidal radius, tidal mass, position and velocity as in the public catalog from the Via Lactea II simulation. The velocities of the main halo particles and the subhalo particles were sampled from velocity distributions calculated using Eddington’s formula with $\beta = 0$. We ran the simulation for 100 time units, which is the same as 100 dynamical times for a particle at the scale radius.

3.3 Analysis methods

3.3.1 Analysing particles in cones

In our analysis we will study particles in cones pointing in different directions. Each cone has an apex angles of 45° . For each particle and axis we calculate $\theta = \arccos(\hat{\mathbf{n}} \cdot \mathbf{r}/|\mathbf{r}|)$, where $\hat{\mathbf{n}}$ is a unit vector pointing in the direction of a cone, and \mathbf{r} is a particle’s position vector (seen from the center of the halo). Particles are selected to be contained in a cone, if $\theta \leq 22.5^\circ$. Analysing structures in this way was also done in (Sparre & Hansen, 2012).

We created 48 cones centered on the most bound particle of each halo. To define the pointing direction of each cone we generated 48 points on a sphere. The points were distributed in the same way as a sphere is divided into pixels in typical studies of the cosmic microwave background (Górski et al., 2005). Note, that some cones will be overlapping each other in space, because of our choice of apex angle and number of cones.

3.3.2 Determination of halo shapes

Halo shapes and orientations are determined from the eigenvectors and eigenvalues of the moment of inertia tensor. First the shape in the central part is fitted with an ellipsoid, and next the shape is determined as function of radius with the procedure described in detail in (Katz, 1991). In the remaining part of this article we will refer to the shape found

with this method as the *shape* of a halo. In the following section we will also discuss contours of constant ρ and β in haloes, and in these cases we will explicitly mention, what kind of contour we are working with, so the different types of contours can be clearly distinguished.

Note that we in this article let r denote the physical radius, and not the elliptical radius as it is done in some other studies.

3.4 The behaviour of velocity anisotropy and halo shape

To analyse the behaviour of shape and the direction-dependence of the velocity anisotropy for our haloes, we will present plots of $\beta(r)$ and $\rho(r)$ through cones for a representative selection of haloes from our simulations.

3.4.1 Category 1: Haloes with well-behaved β -profiles

Figure 3.1 shows halo H from simulation II, where structures were perturbed by varying G in time. Each of the lines represent a property (β or ρ) calculated through a cone for the structure. Also shown (in the right panel) are the axis ratios, c/a and b/a , calculated from the inertia tensor. The plotted radii are in units of $r_{-2} \equiv r(\gamma = -2)$.

The right panel shows the prolate shape of the halo. From the panel that shows ρ in different cones, it can also be seen that the halo is elongated since there is an offset between the densities in different cones. From the plot of β in different cones, it is seen that β is systematically larger along the major axis than along the minor axis at any given radius.

The contours of constant β are more elongated than the contours of constant ρ . The minor to major axis ratio of each contour can be approximated by the length of the cyan line segment in figure 3.1, and it is found that the β -contour has a minor to major axis ratio of 0.1, and that the ρ -contour has a minor to major axis ratio of 0.6.

Halo A from simulation II, where a sudden change of particle energies was made, is shown in figure 3.2. This halo is also close to being prolate, and we again see that the largest velocity anisotropy is in the direction of the major axis³. The minor to major axis ratio of the β -contour is 0.35 and the axis ratio from the density shape is 0.49, so we again see that the β -contour is more elongated than the ρ -contour.

3.4.2 Category 2: Haloes with complex β -profiles

For halo H from the collapse simulation (figure 3.3) a slightly more complicated behaviour of β is seen. In the inner parts β is smallest along the minor axis of the density ellipsoid, and in the outer parts it is largest along this axis. Such a *crossover* is absent in the plot of ρ through different cones. Because of the crossover, the β -contours of the halo do not have an ellipsoidal shape.

Figure 3.4 and 3.5 show more examples of haloes with β -profiles that are clearly not ellipsoidal. For the merger remnant β is roughly constant and positive along the major axis and monotonically increasing along the minor axis. This behaviour is consistent with our previous study of major mergers (Sparre & Hansen, 2012). The instability simulation

³When 48 cones with apex angles of 45° are distributed on a sphere, it can happen that the minor axis (or one of the other principal axes) is contained in several cones, since some of the cones are overlapping. This is why several cones are marked as being along the minor axis in Figure 3.2.

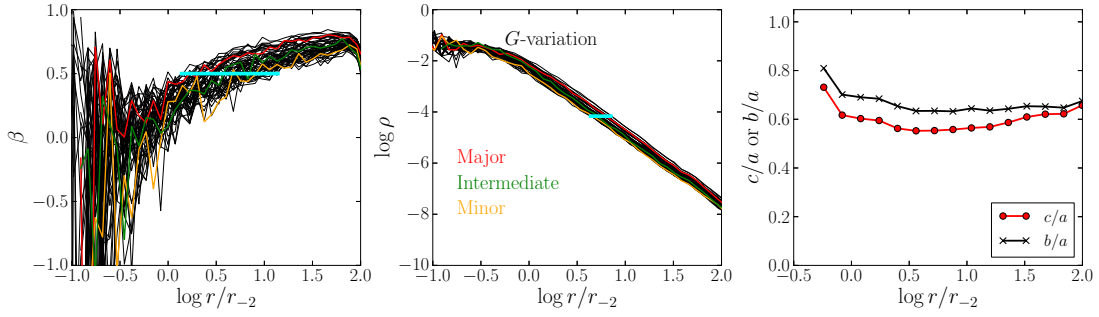


Figure 3.1: Velocity anisotropy profiles (*left panel*) and densities (*central panel*) calculated in 48 cones for halo H (a Hernquist profile with $\beta_{\text{initial}} = 1 - r^2/(1 + r^2)$) from the simulation, where G was changed instantaneously. Each line corresponds to a cone, and the coloured lines corresponds to cones which coincides with one of the principal axes. The *right panel* shows the axis ratios as function of radius. The cyan horizontal line segment in the *left (central) panel* shows the width of a contour with $\beta = 0.5$ ($\log \rho = -4.17$).

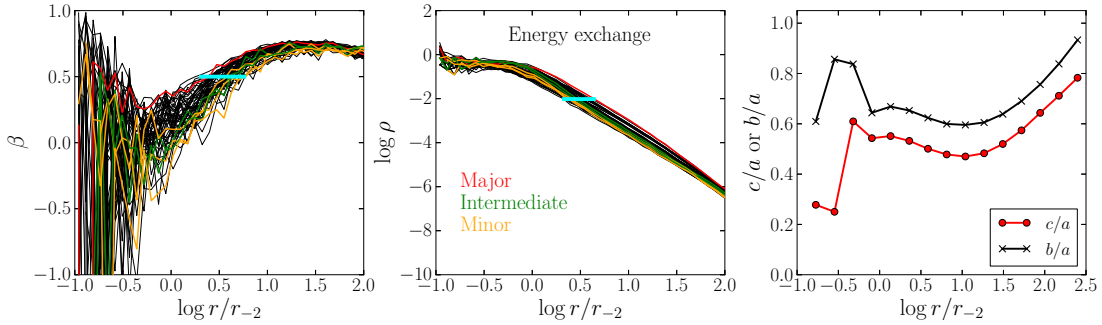


Figure 3.2: This plot shows properties of halo A (a Hernquist profile with $\beta_{\text{initial}} = 0$) from simulation II. As in figure 3.1, a larger β is found along the major axis compared to the minor axis at all radii.

gives a complicated behaviour of both β , ρ and the axis ratios. Is is e.g. seen that ρ has significant wiggles and bumps along the minor axis.

3.4.3 Category 3: The spherically symmetric haloes

Finally we will also note that perturbed haloes also can follow simple spherically symmetric distribution functions. Figure 3.6 shows halo A from simulation I, and it has a spherical shape, and β -profiles behaving similarly from cone to cone.

3.4.4 A summary of the categories

To summarise the behaviour of velocity anisotropy and shape in our haloes, we have grouped them into three categories:

1. One category is the triaxial haloes with β differing from cone to cone. The contours of constant β are typically more elongated than the constant- ρ contours. Examples of such haloes are shown in figure 3.1 and 3.2.
2. We also see examples of triaxial haloes, where the constant- β contours differ significantly from triaxial ellipsoids (see figure 3.3-3.5). We do for example see haloes,

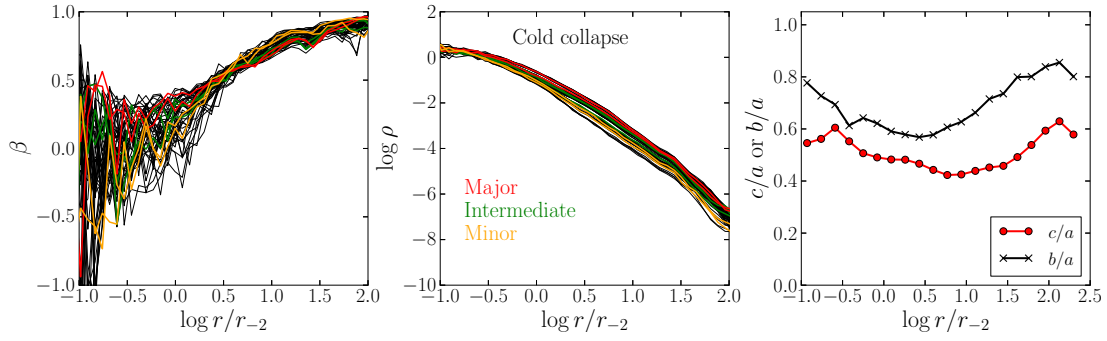


Figure 3.3: Halo I (a Hernquist profile) from the cold collapse simulation. In the inner parts β is largest along the major axis, whereas it is larger along the minor axis in the outer parts.

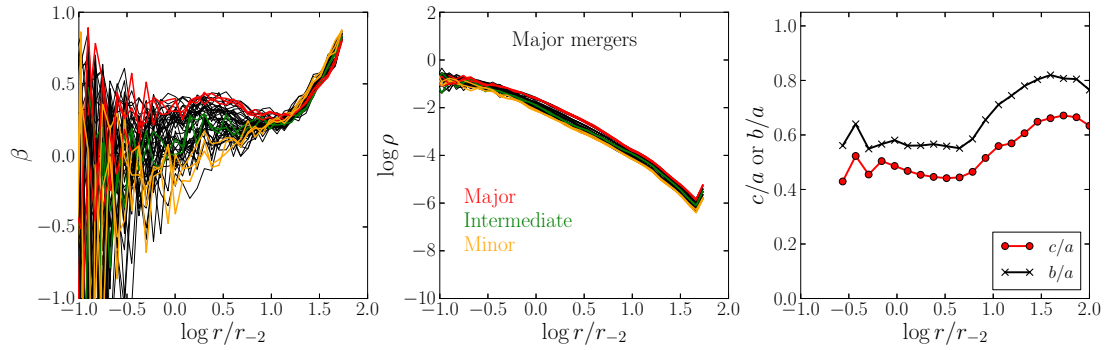


Figure 3.4: Halo K (a Hernquist profile with $\beta_{\text{initial}} = 0$) from the merger simulation. Along the major axis β is roughly constant in the inner parts, and along the minor axis it is monotonically increasing.

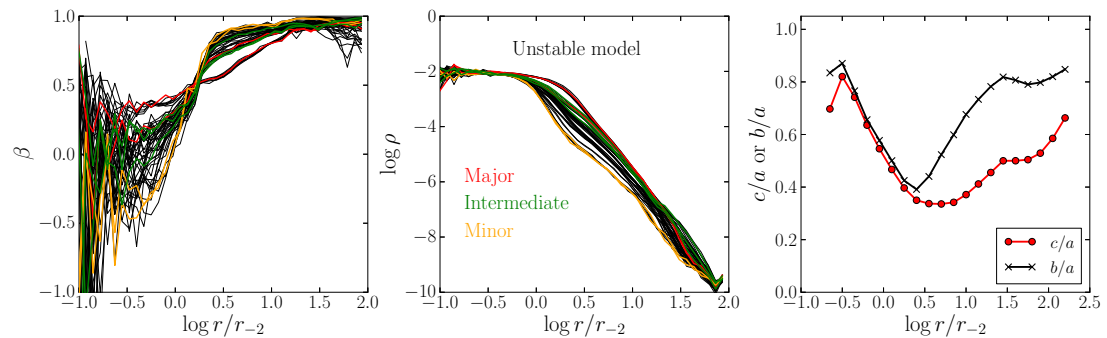


Figure 3.5: Halo R ($\rho \propto 1/(1+r)^5$) from the instability simulation. The density profile of this halo has several bumps and wiggles along the minor axis. β also exhibits different behaviour along different axes.

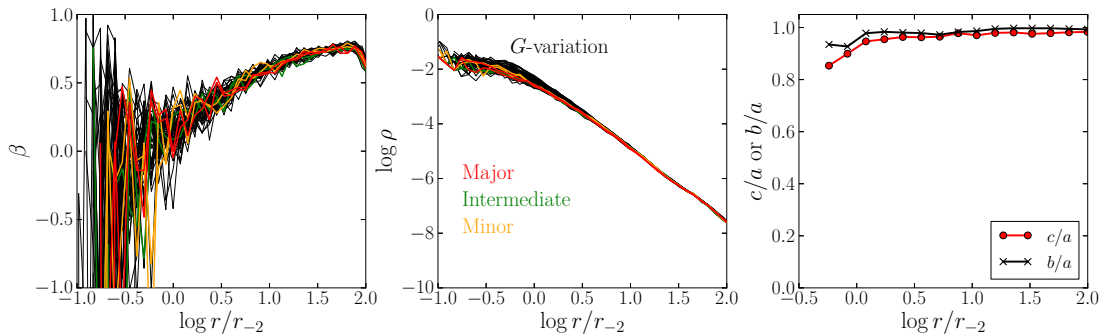


Figure 3.6: Halo A (a Hernquist profile with $\beta_{\text{initial}} = 0$) from the G -variation simulation. This halo has a spherical shape and a spherically symmetric velocity anisotropy.

where β is largest along one axis in the inner parts, and smallest along this same axis in the outer parts.

3. In our simulations we also see almost spherical structures, where β is behaving similarly along each axis (see figure 3.6).

Note, that the above list is not supposed to be a comprehensive list of all possible configurations of β - and ρ -profiles in dark matter haloes. The purpose of the list is to highlight features, which have not been extensively studied in the literature.

3.5 Relating the results to cosmological haloes

3.5.1 Comparison with a cosmological halo

A study which also examines halo shapes and the direction-dependence of β -profiles is the analysis of the Via Lactea II halo, where the probability distribution of the velocity anisotropy, $P(\beta)$, is calculated in four different radial bins, and along the major, intermediate and minor axes (see figure 7 from (Zemp et al., 2009)). The Via Lactea II halo has a behaviour, which in several ways is consistent with our merger simulation in figure 3.4. In both studies β is largest along the major axis ($\beta \simeq 0.3 - 0.4$) and smallest along the minor axis ($-0.6 \lesssim \beta \lesssim 0.0$) in the inner parts. The values of β along the intermediate axis are somewhere in between. The halo from the Via Lactea II simulation is close to being prolate ($c/a = 0.52$ and $b/a = 0.62$), which is also similar to the behaviour of our merger remnant. Due to the similarities with our merger remnants, we conclude that the Via Lactea II halo is in category 2 of the categories from section 3.4.4.

Merging is not the only process that can produce a halo, which is similar to the Via Lactea II halo. An example is the simulation of the unstable halo (figure 3.5), which has a β -profile that behaves similarly to the mergers in the inner parts. The unstable halo is, however, significantly more elongated than the Via Lactea II halo.

We encourage future studies of β -profiles of cosmological haloes to use cones, since it reveals information about halo dynamics, which is hidden when properties are calculated in spherically averaged bins.

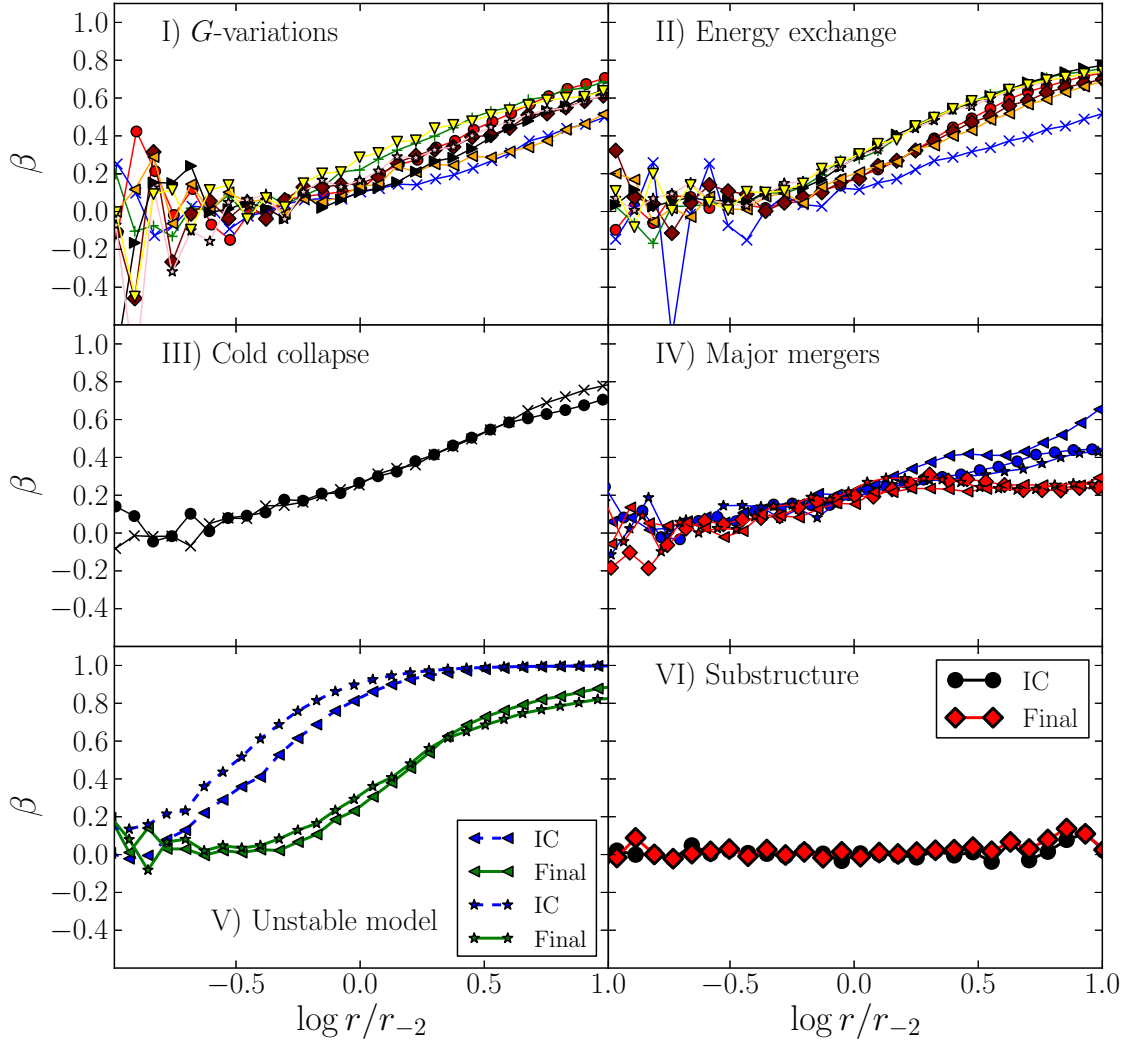


Figure 3.7: The spherically averaged velocity anisotropy profiles for the simulated haloes.

3.5.2 Spatial anisotropy of galaxy kinematics in galaxy clusters

In a recent study of galaxy clusters the line of sight velocity dispersion is calculated along the major and minor axis for a stacked sample of 1743 galaxies from the SDSS survey (Skielboe et al., 2012). It is found that a significantly larger velocity dispersion is found for galaxies with positions along the major axis. The difference of the velocity dispersions along the two axes is 38 ± 13 km/s. A possible explanation for this difference is the direction-dependence of the velocity anisotropy profile, which we have studied in this article. A different explanation could be that the cluster's non-spherical mass-distribution can produce different line-of-sight velocity dispersions along the minor and the major axis, even though β has the same behaviour along these axes.

3.6 Spherically averaged profiles

In this section we will report the spherically averaged profiles of β and γ together with the halo shapes.

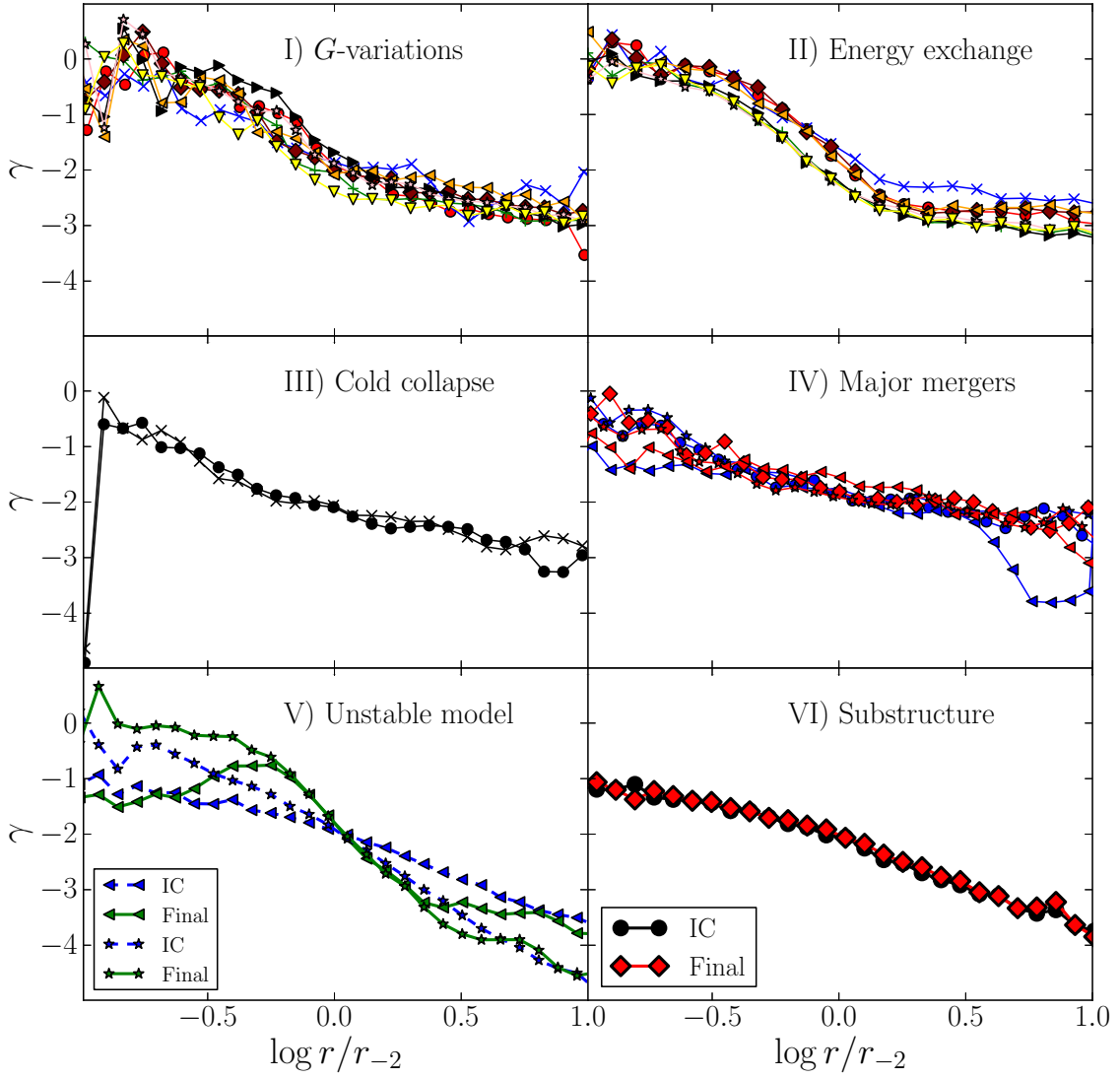


Figure 3.8: $\gamma(r)$ for all the haloes.

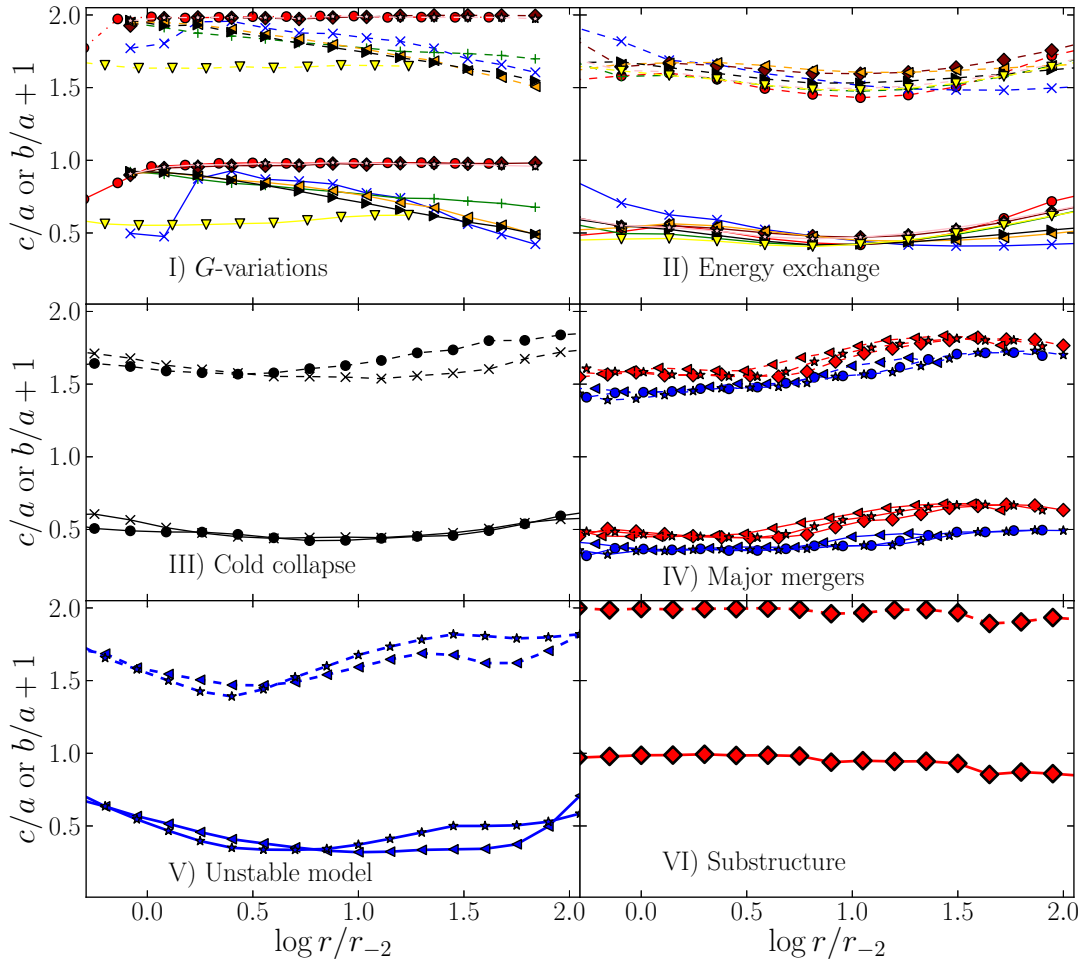


Figure 3.9: The axis ratios, c/a (solid lines) and b/a (dashed lines), for the haloes. $b/a + 1$ is plotted instead of b/a for presentation reasons.

3.6.1 Velocity anisotropy profiles

Different trends are seen in the spherically averaged velocity anisotropy profiles of our haloes, see figure 3.7. The setups in simulation I, II, III and V produce haloes with $\beta \simeq 0$ in the inner parts and $\beta \simeq 0.8$ in the outer parts. This is consistent with what is e.g. reported in cold collapse simulations (van Albada, 1982; MacMillan et al., 2006).

The spherically averaged velocity anisotropy profiles of the merger remnants (simulation IV) are typically increasing from $\beta = 0$ in the center of the halo out to the radius with $\beta = 0.3$, where a maximum appears. This behaviour is similar to many cosmological haloes (Ludlow et al., 2011), and in agreement with what is reported in other studies of merger remnants (Moore et al., 2004; McMillan et al., 2007; Sparre & Hansen, 2012).

In the substructure simulation (simulation VI) only a tiny evolution of $\beta(r)$ is seen, which means that the dynamical friction from subhaloes only have a minor effect on velocity anisotropy profiles. This is consistent with the finding that the density profiles of cosmological haloes are not perturbed by the substructure (Moore et al., 1999).

3.6.2 γ -profiles

The six different physical processes in our simulations produce different $\gamma(r)$ -profiles, see figure 3.8. In simulation I and II a core where $\gamma \simeq 0$ appears in the inner regions (with $\log r/r_{-2} \lesssim -0.5$). Such a core is absent in the remaining simulations. In the outer regions $\gamma(r)$ seems to be around $\gamma \simeq -3$ in simulation I, II and III.

3.6.3 Halo shapes

A huge diversity is seen in the halo shapes in figure 3.9. Several of the haloes from simulation I (with G -variations) are spherical and others are close to being prolate. In simulation II, III, IV and V the shapes of the haloes are close to being prolate. The halo in simulation VI (the simulation with subhaloes) remains spherical.

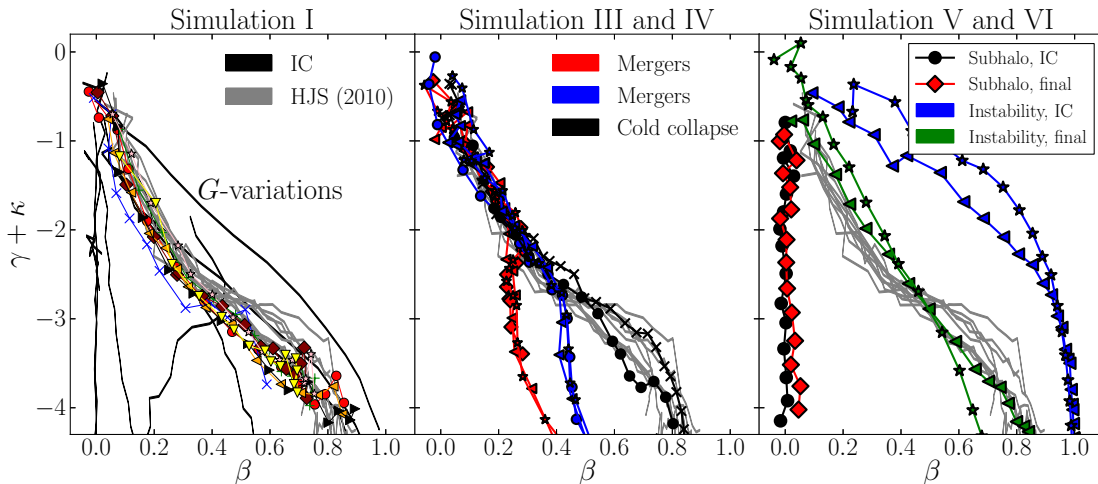


Figure 3.10: Comparison between the attractor from HJS (i.e. simulation II) in grey, and the other simulations. We have defined $\kappa \equiv d \log \sigma_{\text{rad}}^2 / d \log r$ and $\gamma \equiv d \log \rho / d \log r$. In Table 3.2 the different colours and symbols can be found. *Left panel:* The structures exposed to the perturbations, where G was changed instantaneously. *Central panel:* The difference between the red lines and the blue lines is the orientation of the merger axis in the last simulation (see section 3.2.5 for details). Two cold collapse simulations are also shown. *Right panel:* The two haloes from the instability simulation (V) and the subhalo simulation (VI).

3.7 Comparison with the attractor

An aim of the previous sections has been to examine the many different behaviours of halo shapes and β -profiles of dark matter haloes. In the current section we will instead look for similarities of the different haloes, and compare them with the attractor from HJS.

3.7.1 Motivation for the attractor

The three quantities, $\beta(r)$, $\gamma(r) \equiv d \log \rho / d \log r$ and $\kappa(r) \equiv d \log \sigma_{\text{rad}}^2 / d \log r$, are clearly of importance for spherical and static distributions of collisionless structures, since the Jeans equation (Binney & Tremaine, 2008) can be written as

$$-\frac{GM(r)}{r\sigma_{\text{rad}}^2(r)} = \gamma(r) + \kappa(r) + 2\beta(r). \quad (3.6)$$

This motivates an analysis of structures behaviour in the (β, γ, κ) -space. In the HJS-paper such an analysis was made for the structures from simulation II (the energy exchange simulation), and in this 3-dimensional space all haloes followed a 1-dimensional relation, i.e. an *attractor*. In this section we will compare this attractor prediction with our structures.

3.7.2 Comparing haloes with the attractor

First we will analyse structures in the $(\beta, \gamma + \kappa)$ -projection, see figure 3.10. The points show properties calculated in spherical bins distributed logarithmically in radius. For simulation I, where G was changed multiple times, the different haloes end up on a one-dimensional curve, like in HJS. The scatter at large β is smaller than in the original HJS-simulations, and there is an offset towards smaller $(\gamma + \kappa)$ -values in simulation I compared

to the HJS-simulations (simulation II). The same trend is seen in the study of the attractor by (Barber et al., 2012). The two haloes from the cold collapse simulations (simulation III), also end up on the attractor in this projection.

Simulation IV involves multiple major mergers. The result of the three simulations with different density profiles are shown as *red points* in figure 3.10. The *blue points* show the additional simulations with identical collision axes in the last two simulations. The spherically averaged profiles follow the attractor in the inner parts, even though β behaves different along each axis (see figure 3.4). When inspected the attractor is not obeyed when β , γ and κ are calculated in cones.

The unstable model in Simulation V ends up close to the attractor. The halo in simulation VI is not perturbed enough by the presence of the substructures to be dragged towards the attractor.

Different projections

In figure 3.11-3.13 the structures are plotted in the three principal projections, i.e. (γ, β) , (κ, β) and (γ, κ) . In all projections there is a very good agreement between simulation I and II, so from now we will define the attractor by the result of these two simulations.

In the (γ, β) -projection (figure 3.11) the cold collapse process produces haloes, which are consistent with the attractor prediction. The spherically averaged properties of the merger remnants follow the attractor in the inner parts. We also see that the haloes from simulation I-IV follow the linear γ - β relation from Hansen & Stadel (2006) in the inner parts, where $\gamma \gtrsim -2.2$. The unstable model is not on the attractor.

In the (κ, β) -projection (figure 3.12) the collapse simulations are again close to the attractor prediction, but some significant deviations are present in the inner parts with $\beta \lesssim 0.2$. The merger simulations behave differently and the unstable models only follow the attractor (in this projection) in the outer parts with $\beta \gtrsim 0.35$.

Comparison with cosmological pseudo-phase-space densities

Figure 3.13 shows the simulations projected onto the (γ, κ) -plane, together with the relation, $\kappa = \frac{2}{3}(\gamma + \alpha)$, which follows from the connection,

$$\rho/\sigma_{\text{rad}}^3(r) \propto r^{-\alpha}, \quad (3.7)$$

with $\alpha = 1.91$ (Ludlow et al., 2011), which comes from fitting cosmological haloes over their entire radial ranges.

We see that the attractor prediction is inconsistent with the relation from Eq. (2.3), which is obeyed by cosmological haloes. It can also be seen that the inner parts of the merger remnants and the haloes from the collapse simulations are closer to relation (2.3) than the attractor prediction.

Energy exchange in the relaxation processes

The purpose of this subsection is to study the change of particle energies in the relaxation processes. For our structures we identified the particles, that ended up in a thin spherical shell centered at $r_{-2} \equiv r(\gamma = -2)$ in the last snapshot, and monitored how their energies changed through the simulation. In figure 3.14 we have plotted the dimensionless quantity $t_{\text{dyn}}(r_{-2}) \times \langle |(dE_i/dt)/E_i| \rangle$ (E_i is the energy of the i 'th particle, and $\langle \dots \rangle$ denotes the mean of the particles that ended up in the shell at r_{-2}) as function of $t/t_{\text{dyn}}(r_{-2})$.

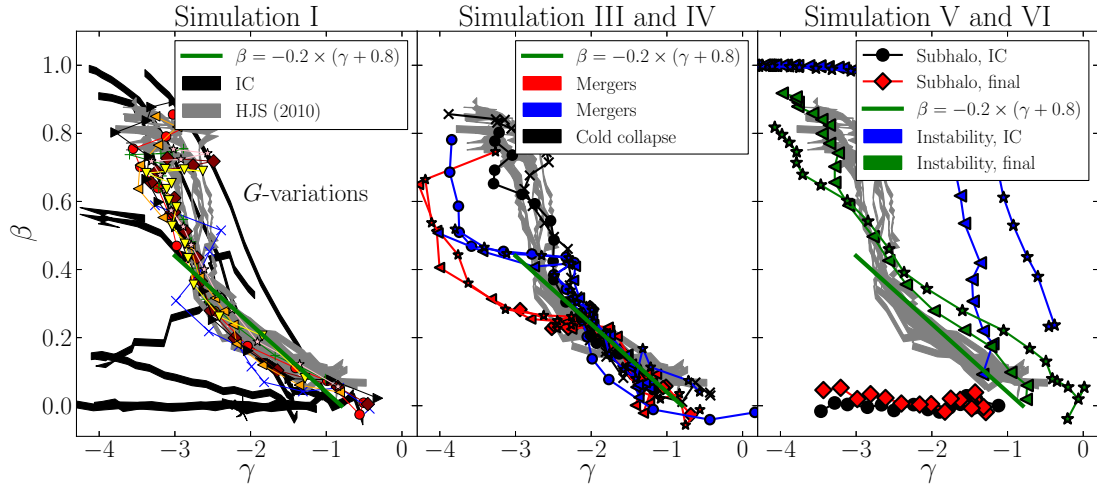


Figure 3.11: A projection in the (γ, β) -plane. Also plotted is the linear relation (*thick green line*) from Hansen & Stadel (2006).

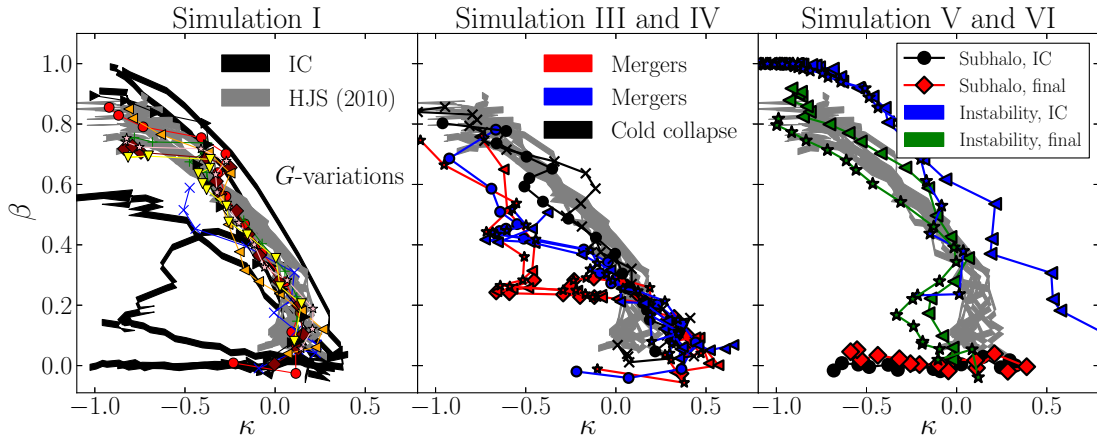


Figure 3.12: The (κ, β) -projection.

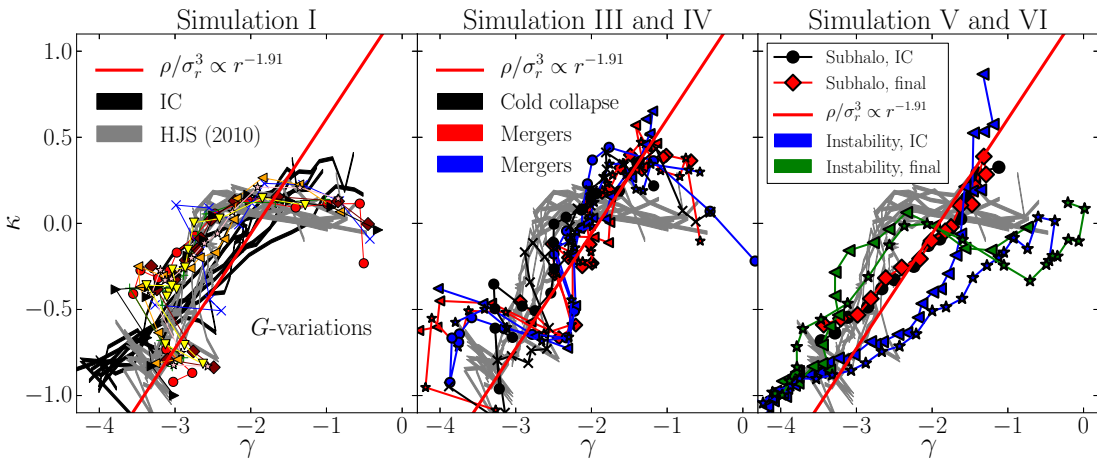


Figure 3.13: The (γ, κ) -projection.

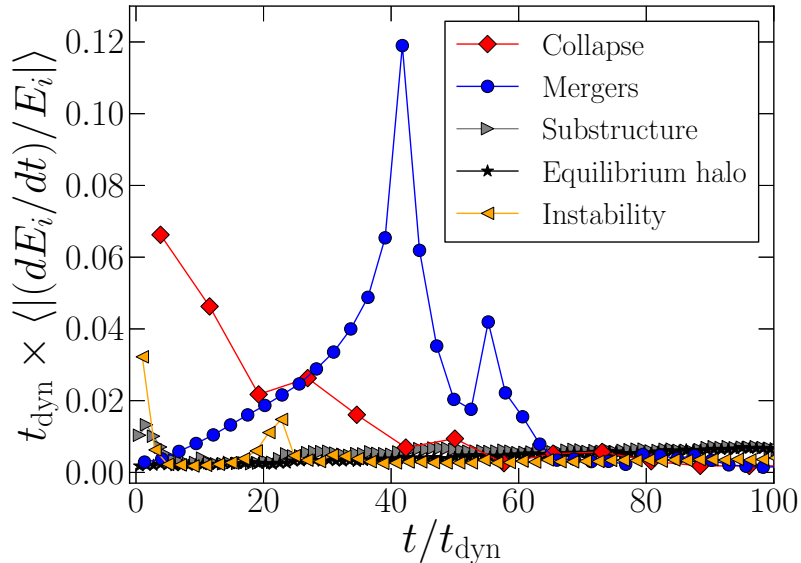


Figure 3.14: The fractional change in energy per dynamical time for particles that end up in a spherical shell around r_{-2} in the final snapshots. In the cold collapse simulation and the merger simulations large changes in the energy of the particles appear. Much lower variations in the energy are present in the simulation with the substructure. For reference an equilibrium structure with no substructure is also shown.

For the cold collapse experiment (the structure following a Hernquist profile is shown), the collapse begins immediately after the start of the simulation, and a redistribution of the energy occurs. For the merger experiment (the Hernquist profile is shown) the exchange of energy grows in the beginning, where the two haloes approach each other, and the largest peak occurs approximately when the two haloes collide for the first time ($t \simeq 40t_{\text{dyn}}$), and a smaller peak is present when they collide for the second time ($t \simeq 55t_{\text{dyn}}$). At later times the energy exchange is more than an order of magnitude lower than the peak values for both experiments.

The energy exchange in the simulation with an unstable model (the structure following Eq. (3.5) is shown) is weaker than in the collapse simulation and the mergers. The instability causes the energy-exchange around the peak at $t = 22t_{\text{dyn}}$. When inspecting the β -profile in each individual snapshot it is seen, that it changes shape from $t/t_{\text{dyn}} = 16$ until $t/t_{\text{dyn}} = 24$. In the later snapshots no significant evolution of this halo is seen.

In the subhalo simulation a small energy exchange is present throughout the simulation. To see the amount of energy exchange generated by the substructure, we ran a similar simulation with a halo in equilibrium; i.e. a halo where the subhaloes were removed, and ordinary particles were distributed throughout the halo to compensate for the removed mass. By comparing the two simulations we find that only the small bump at $t \lesssim 5t_{\text{dyn}}$, where some of the particles in the substructure are stripped, might be caused by the subhaloes.

3.7.3 An overview: which structures are on the attractor?

The overall pattern in our simulations is that the haloes that end exactly on an attractor are those from simulation I and II, which involved artificial processes that changed the

gravitational constant or the kinetic energy of the particles. The collapse simulations ended up close to the attractor, but not exactly on it, and the merger simulations had clear deviations in the outer parts.

We also found that haloes following the attractor deviate from the universality, $\rho/\sigma_{\text{rad}}^3 \propto r^{-\alpha}$, which is found in cosmological simulations. Our conclusion is that the dynamics and structure of cosmological haloes are different from the attractor. Further indications, that cosmological haloes are not on the attractor, comes from the finding that our cold collapse and merger simulations, which are both cosmologically realistic processes, produce haloes that are not exactly on the attractor. The strong direction-dependence of β found in the Via Lactea II halo (Zemp et al., 2009) also supports that cosmological haloes are not on the attractor.

For both the merger simulations and the collapse simulations we do, however, see that the β - and γ -profiles (spherically averaged) in the inner parts of the structures obey the attractor in the (γ, β) -projection. Since a very good agreement only is found in this projection, cosmological haloes are better described by the γ - β relation from (Hansen & Moore, 2006) than by the attractor.

It is important to note that this γ - β relation only applies to the spherically averaged values of β - and γ -profiles. The haloes still have freedom to have different β -profiles in different directions as long as the spherically averaged profiles obey this relation. An example of a halo in which the β - γ relation is not obeyed through cones in different directions, but only in spherically averaged bins, has been presented in the study of merger remnants in (Sparre & Hansen, 2012).

3.7.4 The relevance of the attractor

We have shown that typical cosmological haloes have departures from the attractor prediction. Even though this is the case, we still believe that there must be a physical origin of the similar behaviour of the haloes from simulation I and II, when they are analysed in the (β, γ, κ) -space. Understanding this behaviour could potentially lead to a better understanding of violent relaxation and mixing processes in collisionless systems.

3.8 Summary

In this article we have examined velocity anisotropy profiles and halo shapes in a range of pure dark matter simulations. We have found that haloes with elongated shapes can have several kinds of direction-dependent velocity anisotropies. In some cases the β -profile is aligned with the density profile, and the largest velocity anisotropy is found along the major axis. In other cases the β -profiles are more complicated, and it is not possible to define an axis along which the velocity anisotropy is largest at all radii. Such a behaviour is e.g. seen in the remnant of a major merger, which has a shape and a direction-dependence of β , that is very similar to the Via Lactea II halo. We suggest that future studies of cosmological haloes should calculate the velocity anisotropy profiles in cones, since it reveals properties of the true velocity distributions, which are hidden from the spherically averaged profile.

We have also compared our haloes with an attractor (Hansen et al., 2010), and we conclude that cosmological haloes have departures from the attractor prediction. We do, however, find that the spherically averaged β - and the γ -profile (γ is the logarithmic derivative of the density profile) obey an approximately linear relation (from (Hansen &

Moore, 2006)) in the inner parts, even though this relation is not necessarily obeyed for particles in individual cones pointing in different directions.

Bibliography

- Allgood, B., Flores, R. A., Primack, J. R., Kravtsov, A. V., Wechsler, R. H., Faltenbacher, A., & Bullock, J. S. 2006, *MNRAS*, 367, 1781
- Arad, I., Dekel, A., & Klypin, A. 2004, *MNRAS*, 353, 15
- Ascasibar, Y., & Binney, J. 2005, *MNRAS*, 356, 872
- Austin, C. G., Williams, L. L. R., Barnes, E. I., Babul, A., & Dalcanton, J. J. 2005, *ApJ*, 634, 756
- Barber, J. A., Zhao, H., Wu, X., & Hansen, S. H. 2012, *MNRAS*, 424, 1737
- Barnes, J. 1985, *MNRAS*, 215, 517
- Binney, J., & Tremaine, S. 2008, *Galactic Dynamics: Second Edition* (Princeton University Press)
- Bradač, M., et al. 2006, *ApJ*, 652, 937
- Clowe, D., Bradač, M., Gonzalez, A. H., Markevitch, M., Randall, S. W., Jones, C., & Zaritsky, D. 2006, *ApJ*, 648, L109
- Cuesta, A. J., Prada, F., Klypin, A., & Moles, M. 2008, *MNRAS*, 389, 385
- Dehnen, W., & McLaughlin, D. E. 2005, *MNRAS*, 363, 1057
- Diemand, J., Kuhlen, M., Madau, P., Zemp, M., Moore, B., Potter, D., & Stadel, J. 2008, *Nature*, 454, 735
- Diemand, J., Moore, B., & Stadel, J. 2004, *MNRAS*, 352, 535
- Górski, K. M., Hivon, E., Banday, A. J., Wandelt, B. D., Hansen, F. K., Reinecke, M., & Bartelmann, M. 2005, *ApJ*, 622, 759
- Hansen, S. H. 2004, *MNRAS*, 352, L41
- Hansen, S. H., Juncher, D., & Sparre, M. 2010, *ApJ*, 718, L68
- Hansen, S. H., & Moore, B. 2006, *New Astronomy*, 11, 333
- Hansen, S. H., & Stadel, J. 2006, *JCAP*, 5, 14
- Hernquist, L. 1990, *ApJ*, 356, 359
- . 1993, *ApJS*, 86, 389

Katz, N. 1991, *ApJ*, 368, 325

Komatsu, E., et al. 2011, *ApJS*, 192, 18

Lemze, D., et al. 2012, *ApJ*, 752, 141

Ludlow, A. D., Navarro, J. F., Springel, V., Vogelsberger, M., Wang, J., White, S. D. M., Jenkins, A., & Frenk, C. S. 2010, *MNRAS*, 406, 137

Ludlow, A. D., Navarro, J. F., White, S. D. M., Boylan-Kolchin, M., Springel, V., Jenkins, A., & Frenk, C. S. 2011, *MNRAS*, 937

MacMillan, J. D., Widrow, L. M., & Henriksen, R. N. 2006, *ApJ*, 653, 43

McMillan, P. J., Athanassoula, E., & Dehnen, W. 2007, *MNRAS*, 376, 1261

Merritt, D. 1985, *AJ*, 90, 1027

Meza, A., & Zamorano, N. 1997, *ApJ*, 490, 136

Moore, B., Kazantzidis, S., Diemand, J., & Stadel, J. 2004, *MNRAS*, 354, 522

Moore, B., Quinn, T., Governato, F., Stadel, J., & Lake, G. 1999, *MNRAS*, 310, 1147

Navarro, J. F., Frenk, C. S., & White, S. D. M. 1996, *ApJ*, 462, 563

Navarro, J. F., et al. 2004, *MNRAS*, 349, 1039

Osipkov, L. P. 1979, *Soviet Astronomy Letters*, 5, 42

Sharma, S., & Steinmetz, M. 2006, *MNRAS*, 373, 1293

Skjelboe, A., Wojtak, R., Pedersen, K., Rozo, E., & Rykoff, E. S. 2012, *ApJ*, 758, L16

Sparre, M., & Hansen, S. H. 2012, *JCAP*, 7, 42

Springel, V. 2005, *MNRAS*, 364, 1105

Springel, V., Yoshida, N., & White, S. D. M. 2001, *New Astronomy*, 6, 79

Stadel, J., Potter, D., Moore, B., Diemand, J., Madau, P., Zemp, M., Kuhlen, M., & Quilis, V. 2009, *MNRAS*, 398, L21

Taylor, J. E., & Navarro, J. F. 2001, *ApJ*, 563, 483

van Albada, T. S. 1982, *MNRAS*, 201, 939

White, S. D. M. 1978, *MNRAS*, 184, 185

Zemp, M., Diemand, J., Kuhlen, M., Madau, P., Moore, B., Potter, D., Stadel, J., & Widrow, L. 2009, *MNRAS*, 394, 641

Zemp, M., Stadel, J., Moore, B., & Carollo, C. M. 2007, *MNRAS*, 376, 273

Zwicky, F. 1933, *Helvetica Physica Acta*, 6, 110

Chapter 4

Star formation in a hydrodynamical galaxy formation simulation

This chapter contains the following article:

The star formation main sequence and stellar mass assembly of galaxies in the Illustris simulation

Submitted to MNRAS. Public available as arXiv preprint: 1409.0009.

Authors: Martin Sparre, Christopher C. Hayward, Volker Springel, Mark Vogelsberger, Shy Genel, Paul Torrey, Dylan Nelson, Debora Sijacki, Lars Hernquist

Abstract

Understanding the physical processes that drive star formation is a key challenge for galaxy formation models. In this article we study the tight correlation between the star formation rate (SFR) and stellar mass of galaxies at a given redshift, how halo growth influences star formation, and star formation histories of individual galaxies. We study these topics using Illustris, a state-of-the-art cosmological hydrodynamical simulation of galaxy formation. Illustris reproduces the observed relation (the star formation main sequence; SFMS) between SFR and stellar mass at redshifts $z = 0$ and $z = 4$, but at intermediate redshifts of $z \simeq 1 - 2$, the simulated SFMS has a significantly lower normalisation than reported by observations. The scatter in the relation is consistent with the observed scatter. However, the fraction of outliers above the SFR-stellar mass relation in Illustris is less than that observed. Galaxies with halo masses of $\sim 10^{12} M_{\odot}$ dominate the SFR density of the Universe, in agreement with the results of abundance matching. Furthermore, more-massive galaxies tend to form the bulk of their stars at high redshift, which indicates that ‘downsizing’ occurs in Illustris. We also studied the star formation histories of individual galaxies, including the use of a principal component analysis decomposition. We find that for fixed stellar mass, galaxies that form earlier have more-massive black holes at $z = 0$, indicating that star formation and black hole growth are tightly linked processes in Illustris. While many of the properties of normal star-forming galaxies are well-reproduced in the Illustris simulation, forming a realistic population of starbursts

will likely require higher resolution and probably a more sophisticated treatment of star formation and feedback from stars and black holes.

4.1 Introduction

In the Λ CDM paradigm, galaxies reside in dark matter halos that are built up hierarchically as gravity amplifies perturbations created in the early Universe (Zel'dovich, 1970). The structure and substructure of dark matter halos, and the cosmic web surrounding them, have been intensively studied using numerical simulations (e.g. Springel et al., 2005; Diemand et al., 2008; Klypin et al., 2011), in which the dark matter is modelled as collisionless particles that interact with each other only through gravity. In the last decade, such simulations have led to a general consensus about the distribution of dark matter on large scales. However, the formation and evolution of the baryons embedded in these halos are far from understood. In the canonical theory of galaxy formation (e.g. Silk, 1977; Rees & Ostriker, 1977; White & Rees, 1978), galaxies form stars when hot gas radiates away energy, cools and loses pressure support. The evolution of such galaxies is further influenced by their merger history, accretion of gas and dark matter, and regulation of star formation by feedback processes related to stellar winds, supernovae and active galactic nuclei. Much of our understanding of galaxies is based on observed relations and physical modelling of galaxy structure. Important observations include the relation between luminosity and velocity widths of galaxies (Faber & Jackson, 1976; Tully & Fisher, 1977), the global star formation rate as a function of redshift (Lilly et al., 1996; Madau et al., 1998), relations between mass and metallicity (Tremonti et al., 2004; Mannucci et al., 2010), global star formation laws (Schmidt, 1959; Kennicutt, 1998), and the morphologies of galaxies (Hubble, 1926; Dressler, 1980).

A recently established relation is the so-called ‘star formation main sequence’ (SFMS), which is an approximately linear relation between the star formation rate (SFR) and the stellar mass (M_*) of star-forming galaxies. The relation exists at both low ($z < 1$; Brinchmann et al., 2004; Salim et al., 2007) and high ($z \gtrsim 1$; Daddi et al., 2007) redshift and is recovered in optical, infrared (Elbaz et al., 2011) and radio observations (Karim et al., 2011). It is a tight relation in the sense that the scatter around the relation is small (e.g. Speagle et al. 2014 reports a scatter of $\sigma \simeq 0.2$ dex). The normalisation of the SFMS is observed to increase from $z = 0$ to $z = 2$, the redshift at which the global star formation rate density peaks. The tightness of the SFMS and the fact that most star-forming galaxies lie on it imply that the bulk of the star formation in the Universe occurs in a quasi-steady state (Noeske et al., 2007) and that the fraction of a given star-forming galaxy’s lifetime during which it lies significantly above the SFMS because of e.g. merger-induced starbursts is small.¹

In addition to characterising star-forming galaxies, the SFMS also provides a natural way to define starbursts as galaxies with SFRs well above the SFMS value for their stellar mass and redshift (Rodighiero et al., 2011; Sargent et al., 2012; Atek et al., 2014). Despite

¹It is sometimes claimed that galaxies on the SFMS must not be undergoing mergers. This is a misconception: for most of the duration of mergers, the SFR is not elevated significantly by the interaction (e.g. Cox et al., 2008; Hopkins et al., 2010). Consequently, merging galaxies often lie on the SFMS (see fig. 11 of Hayward et al. 2012). Thus, it is important to not equate galaxies that lie above the SFMS with mergers. Instead, galaxies above the SFMS should be referred to as ‘starbursts’ (by definition), which may or may not be merger-induced. Galaxies on the SFMS should be considered ‘quiescently star-forming’, and such galaxies may still be involved in an ongoing merger.

having large SFRs compared with normal galaxies, starbursts account for only a small fraction ($\sim 5 - 10$ per cent) of the global SFR density (Rodighiero et al., 2011) because they are rare and short-lived (because of their short gas-consumption timescales; Knapen & James 2009; Genzel et al. 2010; Daddi et al. 2010). This minor contribution of starbursts to the total SFR density is consistent with semi-empirical models for infrared galaxy number counts (Béthermin et al., 2012) and luminosity functions (Hopkins et al., 2010). ‘Red and dead’ or quiescent galaxies are galaxies that lie significantly below the SFMS. These galaxies are typically elliptical galaxies (Wuyts et al., 2011) with little gas available for star formation. They are likely the descendants of starbursts after their intense star formation has been quenched by feedback from active galactic nuclei (AGN; e.g. Sanders et al., 1988; Toft et al., 2014; Cemile Marsan et al., 2014) or other processes. Because we are interested in actively star-forming galaxies, we will largely ignore the quiescent galaxy population in this work.

Several attempts have been made to reproduce the SFMS in hydrodynamical simulations of galaxies (e.g. Davé et al., 2011; Torrey et al., 2014) and (semi-)analytical models (e.g. Dutton et al., 2010; Davé et al., 2012; Dekel et al., 2013). With both methods, a tight relationship between SFR and stellar mass can be recovered. However, reproducing the evolution of the normalisation is a challenge for theoretical models (e.g. Davé, 2008; Damen et al., 2009). The main problem is producing the correct normalisation at both $z = 0$ and $z = 2$. Potential solutions to this problem have been suggested, including a varying IMF (Davé, 2008) and modification of the timescale for reincorporation of gas ejected by feedback processes (Mitchell et al., 2014).

A different important characteristic of a population of galaxies is the connection between the growth of halos and the formation of stars inside them. Dark matter halos build up hierarchically through accretion and mergers. The formation of stars is a more complex phenomenon that is heavily influenced by feedback processes and gas cooling. By matching the abundance of halos in cosmological dark matter simulations to real observations of galaxies it has been shown that stars form most efficiently in $\simeq 10^{12} M_{\odot}$ halos (Moster et al., 2013; Behroozi et al., 2013a,b; Kravtsov et al., 2014), which is believed to occur because star formation is suppressed by stellar feedback and feedback from active galactic nuclei at lower and higher halo masses, respectively (Vogelsberger et al., 2013; Torrey et al., 2014; Schaye et al., 2014). An implication is that galaxies that reside in massive (e.g. $\sim 10^{14} M_{\odot}$ at $z = 0$) halos formed their stars earlier than galaxies that reside in $\sim 10^{12} M_{\odot}$ halos (at $z = 0$) because galaxies inside $10^{12} M_{\odot}$ halos at $z = 0$ are still forming stars with the highest possible efficiency. A consequence of this complicated relation between halo growth and star formation is the ‘downsizing’ scenario, in which the galaxies with the most-massive stellar components (e.g. $M_{*} \sim 10^{11} M_{\odot}$) at $z = 0$ formed their stars earlier than galaxies of more-moderate masses (e.g. $M_{*} \sim 10^{10} M_{\odot}$).

The aim of this article is to study properties of star-forming galaxies, especially the SFMS and the relation between halo growth and star formation, in the Illustris cosmological simulation. Section 4.2 describes Illustris, Section 4.3 analyses properties of the star formation main sequence, and Section 4.4 examines how the halo mass affects star formation in galaxies. In Section 4.5 we study star formation histories of galaxies, and we examine how the star formation history of a galaxy depends on its dark matter halo mass and black hole mass. We discuss our findings in Section 4.6 and summarize our conclusions in Section 4.7.

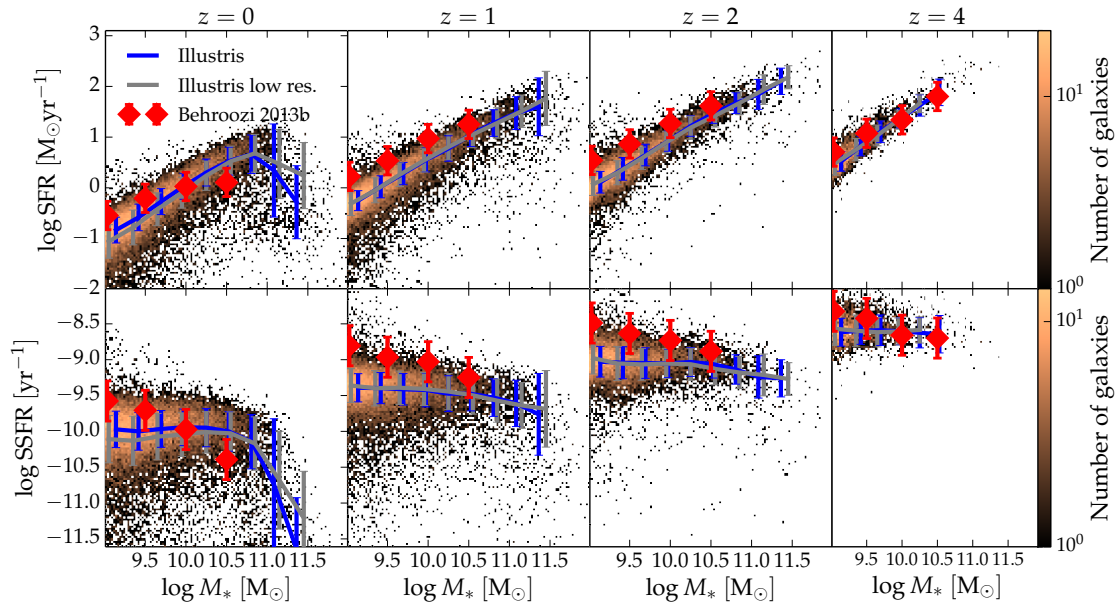


Figure 4.1: The star formation main sequence at $z = 0, 1, 2$ and 4 for the Illustris simulation (the two-dimensional histogram in the background). The upper panels show the median SFR, and the lower panels show the median SSFR. The simulation results are compared to the compilation of observations from Behroozi et al. (2013b), where the error bars indicate 68% confidence intervals for the inter-publication variance. The grey and blue error bars denote the 1σ errors estimated by fitting Gaussian functions to the SFR distributions of galaxies in narrow mass bins in the low-resolution and high-resolution versions of Illustris, respectively.

4.2 The Illustris simulation

Illustris is a cosmological hydrodynamical simulation of a comoving volume of $(106.5\text{Mpc})^3$. The cosmological model used in Illustris is the ΛCDM cosmology with parameters from the WMAP7 data release (Hinshaw et al., 2013). Besides gravity and hydrodynamics, it includes treatments of gas cooling, star formation, and feedback from stellar winds, supernovae and AGN (see Vogelsberger et al., 2013, 2014a,b; Torrey et al., 2014). The Illustris simulation has previously been used to study a range of different galaxy properties, such as the evolution of damped Ly- α absorbers (Bird et al., 2014), the formation of elliptical and spiral galaxies (Vogelsberger et al., 2014b), the evolution of galaxy properties from high to low redshift (Genel et al., 2014), and the relation between the dark matter and stellar components in the faint outskirts of galaxies (Pillepich et al., 2014).

The initial conditions at a redshift of $z = 127$ include 1820^3 dark matter particles, 1820^3 gas cells, and 1820^3 Monte Carlo tracer particles (Genel et al., 2013). The gravitational softening length for the dark matter particles is 1420 comoving pc. The gravitational softening lengths of the gas cells depend on the cell size; they have a minimum value of 710 physical pc. Star particles have a softening length of 1420 comoving pc at $z \geq 1$, and at lower redshifts, the softening length is fixed to 710 physical pc. The mass of the dark matter particles is $6.26 \times 10^6 M_\odot$, and the gas cell target mass is $1.26 \times 10^6 M_\odot$. In this paper we will also study a simulation with lower resolution (a total of 3×910^3 dark matter, gas and tracer particles, implying 8 times worse mass resolution and two times poorer spatial resolution), but with the same physical galaxy formation model. We will refer to this simulation as the *Illustris low resolution run*.

The hydrodynamical calculations in Illustris are done with the AREPO code (Springel, 2010), where the hydrodynamical forces are computed on a moving mesh built with a Voronoi tessellation. With a spatial resolution of $\simeq 1$ kpc there is no hope to resolve giant molecular clouds, where star formation takes place in the Universe. Instead a sub-resolution model is implemented (Springel & Hernquist, 2003; Vogelsberger et al., 2013, 2014a), where unresolved physical processes such as the formation of molecular clouds, thermal instabilities, and supernova feedback are coarsely described with an effective equation of state. When a gas cell exceeds a hydrogen number density of $\rho_{\text{th}} = 0.13 \text{ cm}^{-3}$ it produces star particles stochastically on a density-dependent timescale of

$$t_*(\rho) = t_0^* \left(\frac{\rho}{\rho_{\text{th}}} \right)^{-1/2}, \quad (4.1)$$

where $t_0^* = 2.2$ Gyr. With the chosen values of ρ_{th} and t_0^* , galaxies obey the empirical Kennicutt-Schmidt relation between the gas surface density and the star formation rate per surface area of a galaxy (Kennicutt, 1989). A star particle in this model represents an entire stellar population born with a Chabrier initial mass function (Chabrier, 2003). During each timestep of the simulation, the amount of H, He, C, N, O, Ne, Mg, Si and Fe released by each stellar population is calculated and returned to the gas.

The formation of stars is accompanied by the release of kinetic winds from supernovae, which contribute to expelling the surrounding gas and to the chemical enrichment of the interstellar gas. The wind velocity is 3.7 times the one-dimensional velocity dispersion of the dark matter near the star forming region.

In friends-of-friends groups more massive than $1.7 \times 10^{10} M_{\odot}$ black holes are seeded, and a model of AGN feedback is included (Springel et al., 2005; Sijacki et al., 2007), where a quasar can be in a radio-quiet or radio-loud mode. In the latter mode, thermal energy is injected into the gas surrounding the black hole. Also included is a treatment of AGN radiative feedback, which heats the gas surrounding the AGN and changes its ionization state (see full description in Vogelsberger et al., 2013).

Also implemented are processes such as radiative cooling, chemical evolution, and an ultraviolet background. For a full description of the physical model of Illustris, see Vogelsberger et al. (2013) and Torrey et al. (2014).

4.3 The star formation main sequence

A *star formation main sequence* (SFMS) that relates the star formation rate and the stellar mass of galaxies is recovered in Illustris; see Figure 4.1, which shows the relation at $z = 0, 1, 2$ and 4 . The SFMS is plotted in terms of both the SFR and specific SFR, $\text{SSFR} \equiv \text{SFR}/M_*$, versus M_* . The simulation is compared with the compilation of observations by Behroozi et al. (2013b, Table 8), who fit a relation to a large number of measurements from different authors and quantified the scatter in the observations of the SFMS from different publications. This scatter, which is denoted by the error bars in Figure 4.1, quantifies the inter-publication variance of the SFMS and therefore accounts for the systematic error arising when measuring the SFMS with different methods. The normalisation in Illustris agrees with the observational constraints from Behroozi et al. (2013b) at $z = 0$. The figure also shows that the normalisation of the SFMS in Illustris is well converged above $M_* = 10^9 M_{\odot}$.

At $z = 4$, Illustris is also in excellent agreement with the observed relation. However, despite being in good agreement at $z = 0$ and $z = 4$, the normalisation of the SFMS is

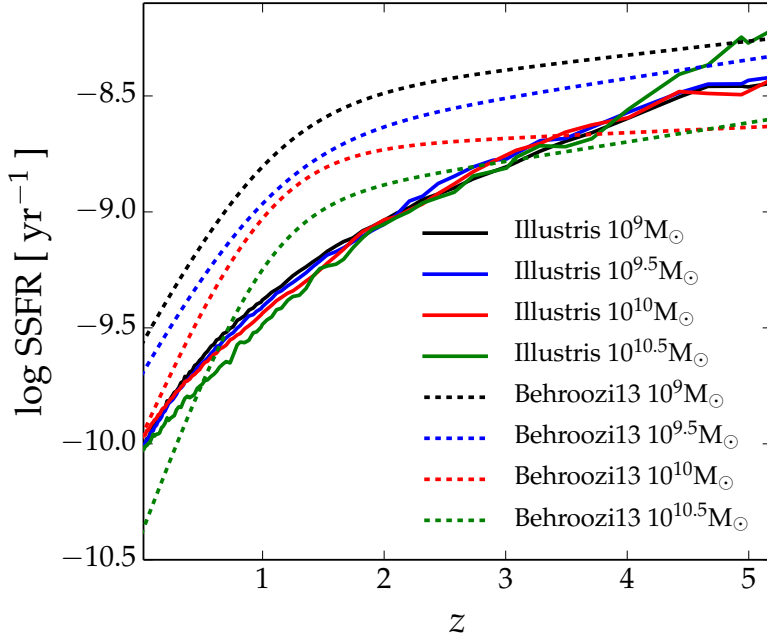


Figure 4.2: The median SSFR as function of redshift for galaxies with different stellar masses. At each redshift the SSFR of galaxies in the given stellar mass bin is computed. The dashed lines show the compilation of observations from Behroozi et al. (2013b). The different evolution of the SSFR from $z = 4$ to $z = 0$ is closely related to the too low normalisation of the star formation main sequence at $z = 1$ and $z = 2$ in Figure 4.1.

significantly lower than the observational constraints at intermediate redshifts of $z = 1$ and $z = 2$ (this has been previously noted and discussed for Illustris; see Genel et al. 2014). Several studies have previously pointed out discrepancies between the observed SFMS relation and galaxy formation models (e.g., Daddi et al., 2007; Davé, 2008; Damen et al., 2009), especially at $z \simeq 2$. In Illustris, this problem takes only the form of reproducing the correct evolution of the main sequence at intermediate times between $z = 4$ and $z = 0$, whereas the simulated relations at these boundary epochs are consistent with observations.

The SSFR in Illustris becomes approximately independent of mass for $M_* < 10^{10.5} M_\odot$ (Figure 4.1, *lower panels*), which is a small but remarkable difference from the observations of Behroozi et al. (2013b), which indicate a declining SSFR as function of mass. Figure 4.2 shows the redshift evolution of the SSFR for galaxies with different stellar masses. The SSFR is here determined by calculating the normalisation of the SFMS in different stellar mass bins. Since the SSFR is independent of mass at fixed redshift in Illustris, the SSFRs of galaxies from different mass bins have the same redshift evolution. The fitting relations from Behroozi et al. (2013b) show a somewhat different evolution, partially because the SSFR is mass-dependent at fixed redshift. We note that the problem with reproducing the evolution of the SSFR (in Figure 4.2) is closely related to the problem of reproducing the normalisation of the SFMS at $z = 1$ and $z = 2$ (in Figure 4.1). Genel et al. (2014) also studied the redshift evolution of the SSFR in Illustris and found that the SSFR of galaxies is closely tied to the galaxies' dark matter accretion rate.

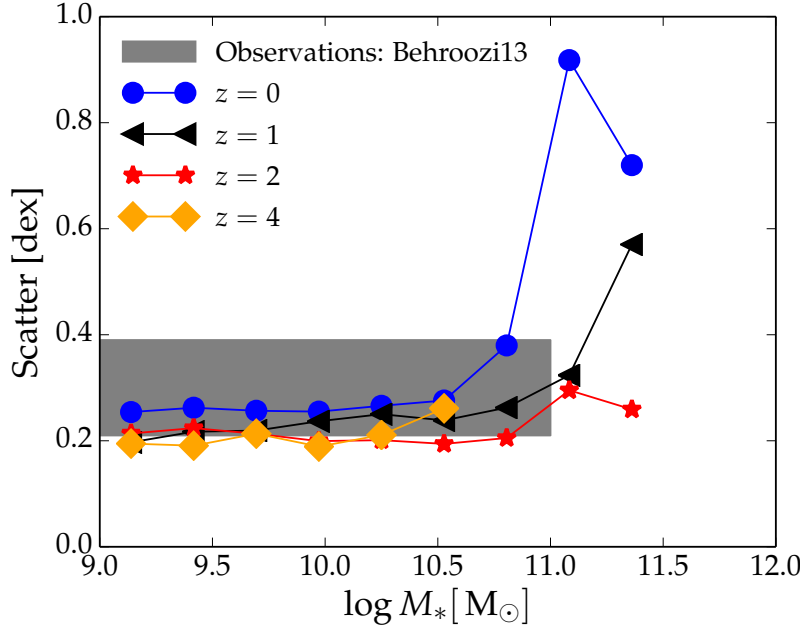


Figure 4.3: The scatter in the main sequence as function of mass for four different redshifts. The grey box shows the range of scatter in typical observations (from Behroozi et al. 2013b). Above $10^{11} M_\odot$ there are no reliable observational constraints for the scatter.

4.3.1 The scatter in the main sequence

The intrinsic scatter in the galaxy main sequence is predicted to be driven by the different gas accretion histories of different galaxies (see the analytical modelling of Dutton et al., 2010). Observations typically reveal a scatter of 0.21-0.39 dex (this reflects the range of values given in Table 9 in Behroozi et al. 2013b), but the measured scatter will of course depend on the exact selection criteria for the star-forming galaxies which form the main sequence (e.g. Whitaker et al., 2012) as well as on the uncertainties in SFR indicators.

To measure the scatter in the SFMS, we perform a Gaussian fit to the distributions of SFRs in different stellar mass bins. This method is similar to what is used in Rodighiero et al. (2011). In Figure 4.3, we show the scatter in the Illustris galaxies' SFR values as function of stellar mass for four different redshifts. Below $10^{10.5} M_\odot$, the scatter is constant at 0.2 – 0.3 dex at each redshift, which is in excellent agreement with observational constraints. At the high-mass end ($M_* > 10^{10.5} M_\odot$), the scatter deviates from the value at lower masses because the galaxy main sequence is ill-defined at these high masses in Illustris (this is also seen in Figure 4.1).

4.3.2 Star formation above the main sequence relation

After having examined the behaviour of the main sequence relation and its scatter in the Illustris simulation, we will now look at starburst galaxies that lie significantly above the main sequence relation. In Figure 4.4 the fraction of stars formed in galaxies on and above the main sequence is computed at different redshifts. We define a galaxy to be on the main sequence relation if the SFR is within 2.5σ of the SFMS relation, which is the same criterion used in Rodighiero et al. (2011). For $M_* > 10^{10} M_\odot$ the fraction of stellar mass formed in galaxies above the SFMS relation is lower than the observational result

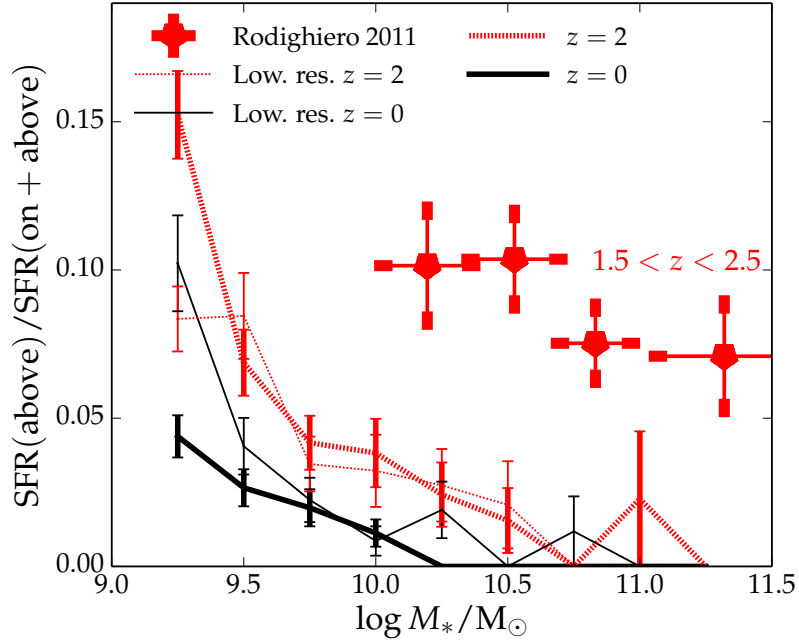


Figure 4.4: The fraction of stellar mass formed by galaxies 2.5σ or higher above the SFMS at $z = 0$ and $z = 2$. The thick and thin lines show the high- and low-resolution Illustris runs, respectively. The error bars indicate the contribution of Poisson noise. The simulated galaxy distribution is compared to the observational measurement at $1.5 < z < 2.5$ from Rodighiero et al. (2011).

reported by Rodighiero et al. (2011) at $1.5 < z < 2.5$. We also note that the fraction of star formation that occurs above the main sequence is consistent in the high- and low-resolution Illustris runs for $M_* > 10^{9.5} M_\odot$. In Section 4.6.2 we will further discuss the paucity of starbursts in Illustris.

4.3.3 The choice of SFR indicator

The SFR of a galaxy can be inferred using different diagnostics, such as the $H\alpha$ luminosity, the ultraviolet luminosity or the total infrared luminosity (Kennicutt & Evans, 2012). Different diagnostics are sensitive to the past SFR in a galaxy smoothed over different timescales, so if a galaxy has a very rapidly changing SFR, different indicators will yield different SFR values. The timescale for which different indicators are sensitive can vary from tens to hundreds of megayears. A situation in which one has to be particularly careful to rely on such averaging is in the post-starburst phase of merging galaxies, where simulations show that the SFR inferred from the total infrared luminosity overestimates the actual SFR of a galaxy by as much as two orders of magnitudes (Hayward et al., 2014).

In Figure 4.5 the scatter in the main sequence is shown for four different definitions of the SFR. First, the SFR is calculated from the instantaneous gas properties of galaxies, which we regard as the true SFR of the galaxies. We additionally calculate the mean SFR from the mass of stars formed in the last 50, 250 and 500 Myr in a galaxy. The scatter in the main sequence is essentially the same in the cases where the SFR is calculated from the gas or the stars formed during the last 50 Myr. For the case where the SFR is calculated from the mass of stars formed in the last 250 Myr, the scatter in the main sequence decreases by 0.03 dex at both $z = 0$ and $z = 2$, and when averaged over 500 Myr, the scatter decreases

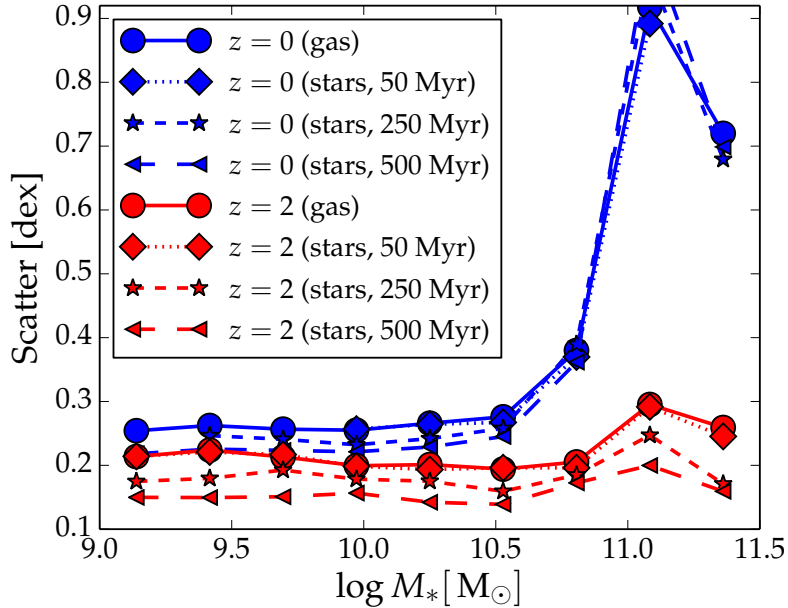


Figure 4.5: The main sequence scatter at $z = 0$ and $z = 2$ with the SFR measured in four different ways: from the instantaneous gas properties, and from the initial mass of the stars formed in the last 50, 250 and 500 Myr in the galaxies. When estimating the SFR from the stars formed in the last 500 Myr, the scatter is lower than in the other cases.

by 0.05 dex. It is not surprising that the scatter declines when increasing the time over which the SFR is averaged, since the SFHs of galaxies are more similar when variability on a timescale smaller than e.g. 500 Myr is smoothed out.

For actively star-forming galaxies, most of the widely used SFR indicators are sensitive to timescales smaller than 200 Myr (Kennicutt & Evans, 2012). Thus, we conclude that the timescale over which the SFR indicator is sensitive is very unlikely to change the derived scatter in the main sequence relation for the physics model used in Illustris, for which star formation is less bursty than in reality. The systematic offsets between different indicators are likely of much greater importance.

It is possible that the role of the characteristic timescale of an SFR indicator will have an impact on the derived SFR for feedback models other than the one used in Illustris. Hopkins et al. (2013) and Governato et al. (2014), for example, present feedback models with typical variability timescales of 10-100 Myr. In Section 4.5 we further discuss the characteristic variability timescales of feedback models.

4.4 Halo mass and star formation properties of galaxies

4.4.1 Halo and stellar masses of star-forming galaxies

Closely related to the main sequence of star forming galaxies is the cosmic comoving SFR density (SFRD). Assuming that all galaxies lie on the main sequence relation, the SFRD can be calculated as

$$\text{SFRD} = \int \text{SFR}_{\text{SFMS}}(M_*) \times \frac{dn}{dM_*} dM_*, \quad (4.2)$$

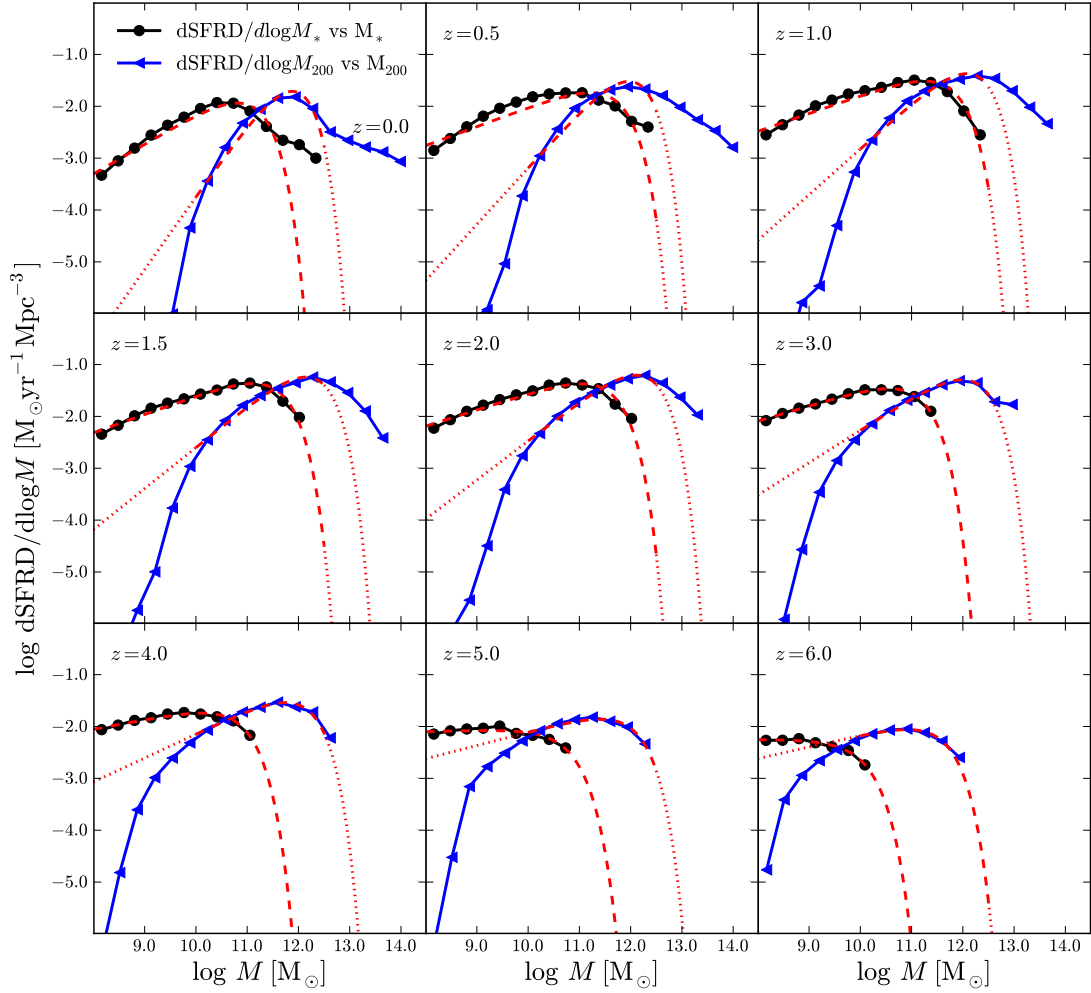


Figure 4.6: The contribution of halos with different stellar masses (black circles) and halo masses (blue triangles) to the total SFRD in the Universe at different redshifts. The red dashed lines are Schechter functions of the form of Eq. (4.3) fit to the simulation data (outside the fit range the extrapolated Schechter functions are dotted). The distributions evolve with redshift as halos and galaxies grow. This is also seen in Figure 4.7, where evolution of the peak mass is examined.

M_{200}/M_{\odot}	$\text{med}(M_{200})/M_{\odot}$	$\text{min}(M_{200})/\text{med}(M_{200})$	$\text{max}(M_{200})/\text{med}(M_{200})$
10^{11}	10^{11}	1.00	1.00
10^{12}	10^{12}	0.97	1.03
10^{13}	9.2×10^{12}	0.77	1.42

Table 4.1: Three samples with different halo masses, M_{200} . Each sample includes the 100 galaxies with masses closest to 10^{11} , 10^{12} and $10^{13} M_{\odot}$ at $z = 0$.

where n is the comoving number density of galaxies, M_* is the stellar mass, and $\text{SFR}_{\text{SFMS}}(M_*)$ is the main sequence relation. The SFRD is observed to peak at $z \simeq 2$ (Lilly et al., 1996; Madau et al., 1998; Hopkins, 2004; Hopkins & Beacom, 2006; Labbé et al., 2010; Cucciati et al., 2012), with the physical drivers of the evolution being the build-up of massive halos and the suppression of star formation by feedback from stellar winds and AGN (Schaye et al., 2010; Vogelsberger et al., 2013; Torrey et al., 2014).

Figure 4.6 shows how galaxies with different stellar masses and halo masses (M_{200}) contribute to the SFRD. This has been computed by summing the contribution to the SFRD from galaxies in equally spaced logarithmic mass-bins from $10^8 M_{\odot}$ to $10^{14.5} M_{\odot}$. Bins containing 7 or fewer galaxies are excluded from the plot in order to avoid bins with very high Poisson noise. The plot also shows how Schechter functions of the form,

$$\text{SFRD}(M) \propto \left(\frac{M}{M_{\text{sch}}}\right)^{\alpha} \times \exp\left(-\frac{M}{M_{\text{sch}}}\right), \quad (4.3)$$

fit to the measurements, where M is either M_{200} or the stellar mass in a halo and M_{sch} and α are free fit parameters. For the fits in terms of halo mass, we exclude halos outside the range $10^{10} M_{\odot} < M_{200} < 10^{12.5} M_{\odot}$, since a Schechter function does not yield a good fit over the entire range of M_{200} -values of the halos. For fits in terms of stellar mass, all galaxies with $10^8 M_{\odot} < M_* < 10^{12.5} M_{\odot}$ are included. The actual distributions measured from the Illustris simulation are overall quite well described by the Schechter fits. This is consistent with the observations from Karim et al. (2011), where the distributions of $\text{dSFR}/\text{dlog } M_*$ are also well fit by a Schechter function for (at least) $M_* > 10^8 M_{\odot}$.

The peak masses of the distributions for $\text{dSFR}/\text{dlog } M_{200}$ and $\text{dSFR}/\text{dlog } M_*$ are plotted at different redshifts in Figure 4.7. At $z \leq 4$ the peaks in the distributions occur at $10^{11.5} < M_{200}/M_{\odot} < 10^{12.5}$ and $10^{10.0} < M_*/M_{\odot} < 10^{11.0}$. Illustris is therefore in agreement with the observations from Karim et al. (2011), where $\text{dSFR}/\text{dlog } M_*$ peaks at $M_* \simeq 10^{10.5 \pm 0.2} M_{\odot}$ for $z \lesssim 2.5$. A large contribution of star formation from halos with $M_{200} = 10^{12} M_{\odot}$ is, e.g., also seen in the abundance matching analysis of Béthermin et al. (2013).

At $M_{200} \simeq 10^{12} M_{\odot}$, halos are most efficient in turning their baryons into stars. This is for example evident when examining M_*/M_{200} , which peaks around $M_{200} \simeq 10^{12} M_{\odot}$ (this relation is plotted for Illustris in Vogelsberger et al. 2014a and Genel et al. 2014). This is because AGN feedback suppresses the formation of stars in halos above this characteristic mass, and stellar winds are responsible for suppressing the formation of stars in lower mass halos. It is therefore not surprising that the peak in $\text{dSFR}/\text{dlog } M_*$ is present at $M_{200} \simeq 10^{12} M_{\odot}$ at $z \lesssim 4$. At $z \gtrsim 4$ there is a decline in the typical masses (both stellar and halo masses) at which stars are formed in Illustris, since halos and galaxies are less massive at high redshifts.

A feature that is also visible in Figure 4.7 is that the mass (both for halo and stellar mass) at which most of the star formation occurs declines from $z = 1$ to $z = 0$. This is

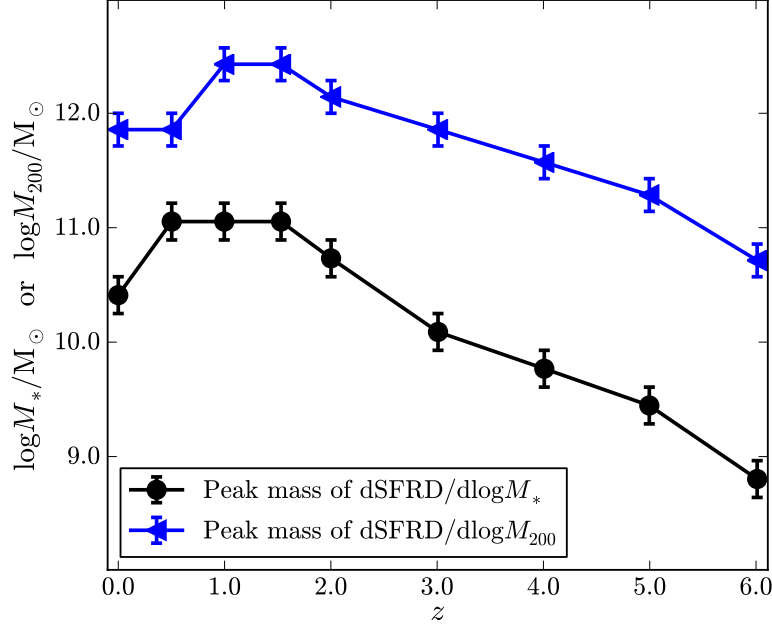


Figure 4.7: The redshift evolution of the peak stellar mass and halo mass for $dSFR/d\log M_{200}$ and $dSFR/d\log M_*$, respectively, for the distributions in Figure 4.6. The peak mass (for both stars and halos) increases from $z = 6$ to $z \simeq 1 - 2$, after which it turns over. The error bars are set by the bin width of the histograms shown in Figure 4.6.

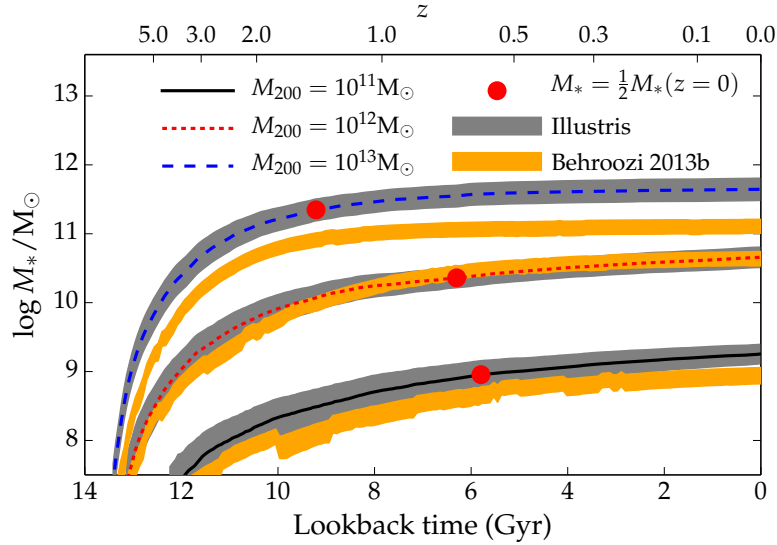


Figure 4.8: The fraction of the current stellar mass formed as function of lookback time for galaxies residing in halos with M_{200} -values of $10^{11} M_\odot$, $10^{12} M_\odot$ and $10^{13} M_\odot$ (see details about samples in Table 4.1). The grey shaded regions correspond to 1σ scatter in each mass range. The orange regions are the 1σ confidence intervals from the abundance matching of Behroozi et al. (2013b) for $M_{200}/M_\odot = 10^{11} M_\odot$, $10^{12} M_\odot$ and $10^{13} M_\odot$.

M_*/M_\odot	$\text{med}(M_*)/M_\odot$	$\text{min}(M_*)/\text{med}(M_*)$	$\text{max}(M_*)/\text{med}(M_*)$
10^9	1.0×10^9	0.99	1.02
10^{10}	1.0×10^{10}	0.95	1.05
10^{11}	9.4×10^{10}	0.83	1.30
$> 1.57 \times 10^{11}$, most massive	2.6×10^{11}	0.60	12.70

Table 4.2: Four different samples of galaxies in different stellar-mass-ranges. The first three samples include the 500 galaxies with stellar masses (M_*) closest to 10^9 , 10^{10} and $10^{11} M_\odot$ at $z = 0$. The fourth range includes the 500 galaxies with the largest stellar masses at $z = 0$. The median, minimum and maximum stellar mass for each sample is also listed.

consistent with the downsizing scenario, where the most-massive galaxies at $z = 0$ have older stellar populations than less-massive galaxies.

4.4.2 Build up of stellar components at different halo masses

To study how halo mass affects the average formation history of stars we create samples of halos with $M_{200} = 10^{11}$, 10^{12} and $10^{13} M_\odot$. Each sample contains the 100 galaxies with halo masses closest to the mass that defines the samples. Table 4.1 summarizes the median, minimum and maximum halo mass in each sample. For each galaxy in each sample we compute the stellar mass growth history by calculating the amount of a galaxy’s stellar mass at $z = 0$ that was formed at different lookback times. For this analysis we include all stars within a halo at $z = 0$, including the stars residing in subhalos.

Figure 4.8 shows the median stellar growth history for each of the three samples. The galaxies ending up in the most-massive halos considered ($\sim 10^{13} M_\odot$) form their stars much earlier than the galaxies ending up in the least massive halos. This is most easily seen by comparing the times at which half of the stellar mass present at $z = 0$ is formed (shown as red circles in the figure). It is perhaps not surprising that very massive halos form their stars earlier than less massive ones, since halos of $10^{12} M_\odot$ contribute most to the global SFR in the Universe, as shown above. However, this trend runs counter to the formation time of the dark matter halos themselves, where the most massive halos form latest as a result of hierarchical structure growth.

We compare Illustris to the results from Behroozi et al. (2013b), where the stellar growth history is derived from the stellar mass – halo mass relation ($M_*(M_h, z)$), which is determined by comparing dark matter merger trees with observations of the cosmic SFR, the specific SFR vs. M_* and stellar mass functions. For $10^{12} M_\odot$ halos, we find excellent agreement between Illustris and Behroozi et al. (2013b). At $10^{11} M_\odot$ and $10^{13} M_\odot$, Illustris predicts stellar components roughly 0.4 dex more massive than Behroozi et al. (2013b). This overproduction of stellar mass in halos of mass $\sim 10^{11} M_\odot$ and $\sim 10^{13} M_\odot$ is essentially independent of redshift. Genel et al. (2014) and Vogelsberger et al. (2014a) found similar deviations between the Illustris simulation and abundance matching results when analysing the high- and low-mass ends of the stellar mass function. Genel et al. (2014) regard these tensions as significant and suggest that more realistic feedback models could potentially help suppress the formation of too-massive stellar components in low- and high-mass galaxies.

4.5 Star formation histories of galaxies

4.5.1 Outliers from the average star formation histories

An alternative to studying statistical properties of galaxies with different stellar masses is to analyse their individual star formation histories in more detail. To compute the star formation history (SFH) we select the stars ending up in a galaxy at $z = 0$, and then create a histogram of the initial mass of stars formed in 100 equally spaced bins in terms of lookback time. We include all stars that end up in the main stellar component of a galaxy (i.e. we exclude satellites) when calculating the SFH in this way. We do not distinguish between stars formed in-situ or ex-situ. We study galaxies in four different stellar mass ranges at $z = 0$. Three ranges are centered around $M_* = 10^9 M_\odot$, $M_* = 10^{10} M_\odot$ and $M_* = 10^{11} M_\odot$, with the widths of the different ranges chosen such that they include 500 galaxies each. We additionally create a range of the 500 galaxies with the most-massive stellar components. Basic properties of the different samples are summarised in Table 4.2.

The mean and median star formation histories of the galaxies in the different mass-ranges are shown in Figure 4.9. For the $10^{11} M_\odot$ range and the 500 most-massive galaxies the SFH peaks at $z \simeq 2$, and decreases at later epochs. These trends are qualitatively in good agreement with other studies of star formation histories of galaxies (e.g. Behroozi et al., 2013b; Simha et al., 2014). For the $10^9 M_\odot$ and $10^{10} M_\odot$ mass ranges, the peak is significantly broader, and it occurs at $z \simeq 1$. In general, the mean SFR is 10-20% larger than the median value, since the mean is more sensitive to extreme outliers with high SFRs.

Different galaxies experience a variety of gas accretion and merger histories, and they are therefore expected to exhibit diverse SFHs. We illustrate this in Figure 4.10, where we show for each mass range the SFR of the galaxies that form 50% of their stellar mass earliest or latest, compared to the average history of the corresponding sample. In all mass ranges, it is possible to find SFHs with early or late star formation. The galaxies with decidedly early star formation histories exhibit a similarly bursty epoch at a lookback time of $\simeq 10 - 13$ Gyr, and the galaxies with late star formation histories display a prominent star forming mode contributing at $z \lesssim 0.5$ and hardly any high-redshift star formation.

4.5.2 Modes of star formation in a principal component analysis

The relative similarity seen in Fig. 4.10 of the galaxies in the tails of the star formation history distribution, forming their stars extremely late or early, suggests that a more systematic study of the star formation modes in the Illustris galaxies is worthwhile. As a tool for statistically characterizing the star formation histories we have adopted a *principal component analysis* (PCA; inspired by Cohn & van de Voort, 2014) where the SFH of a galaxy is seen as a vector in a N -dimensional space, where N is the number of bins used to characterize the SFH of a galaxy (we use $N = 100$). A key quantity in a PCA analysis is the average SFH of the galaxies in the sample,

$$\langle \text{SFR} \rangle(t_i) = \frac{1}{N_{\text{galaxies}}} \sum_{j=0}^{N_{\text{galaxies}}-1} \text{SFR}_j(t_i), \quad (4.4)$$

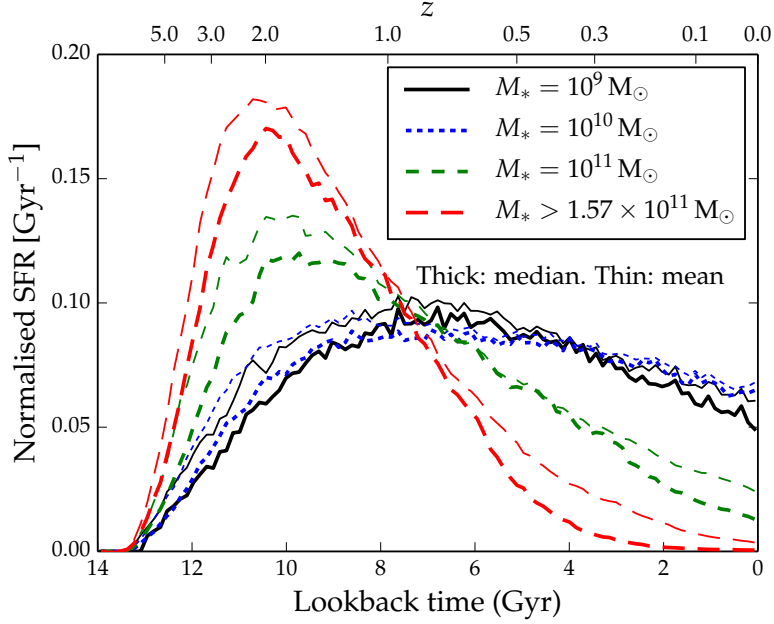


Figure 4.9: Mean and median (thin and thick lines, respectively) star formation histories of galaxies in the four different stellar mass ranges (see Table 4.2). The star formation rates are normalised so that $\int \text{SFR}(t)dt = 1$.

for $i = 0, \dots, N - 1$. We furthermore define the scatter matrix,

$$C_{mn} = \sum_{j=0}^{N_{\text{galaxies}}-1} [\text{SFR}_j(t_m) - \langle \text{SFR} \rangle(t_m)] [\text{SFR}_j(t_n) - \langle \text{SFR} \rangle(t_n)], \quad (4.5)$$

Of special interest are the eigenvectors of C_{mn} , which are called the *principal components* (PC_i , for $i = 0, \dots, N - 1$) and describe the deviations between the SFH of individual galaxies and the mean SFH of a sample. Principal components diagonalize the scatter matrix, implying that the scatter between different PC_i 's is uncorrelated. Conventionally the PCs are ordered in descending order by the contribution they make to the total variance. Often, the first components account for much of the variance, and the corresponding eigenvectors can be interpreted in physical terms. In our case they can serve the purpose of characterizing the most important 'modes' of the SFH.

In terms of the principal components, the SFH of a galaxy can be written as

$$\text{SFR} = \langle \text{SFR} \rangle + \sum_{i=0}^{N-1} q_i \times \text{PC}_i, \quad (4.6)$$

where q_i is the coefficient determining the strength of the contribution of PC_i for a specific galaxy. Since we have binned our SFHs in $N = 100$ bins we formally get 100 principal components, and for each of the 500 galaxies in each sample we obtain 100 coefficients q_i . The limited size of our galaxy set means that only the leading PC components are robust against the noise.

Figure 4.11 shows the mean SFH for the $M_* = 10^{10} M_{\odot}$ sample together with the three leading modes, PC_0 , PC_1 and PC_2 . The PC_0 -mode accounts for galaxies forming

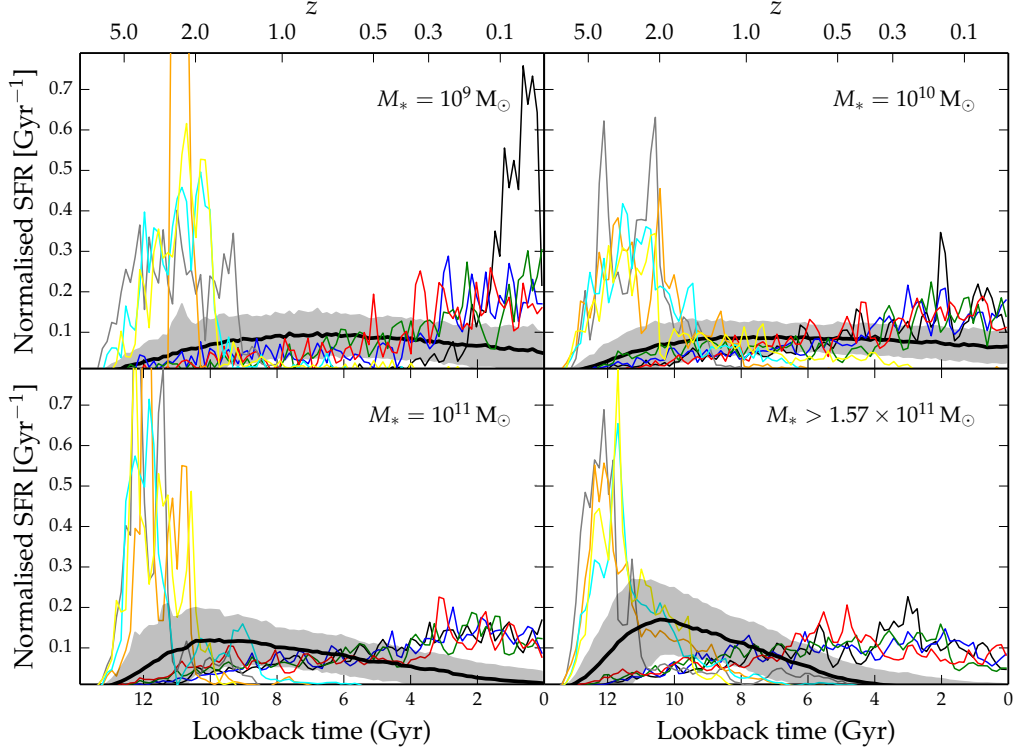


Figure 4.10: For each M_* -range, we have selected the four galaxies that form 50% of their stars earliest or latest (thin lines). The galaxies that form their stars early are shown in grey, orange, cyan and yellow, and the late galaxies are black, blue, green and red. The median profiles for each range are shown by the thick black lines, and the 68% confidence intervals are the grey shaded regions. The normalisation convention is $\int \text{SFR}(t) dt = 1$.

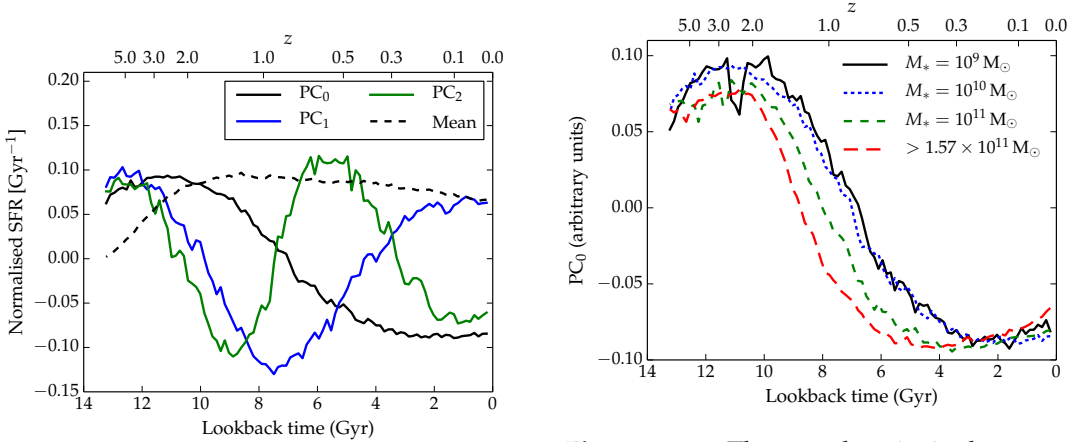


Figure 4.11: The mean SFR for the sample with $M_* = 10^{10} M_\odot$ (from Table 4.2) together with the first three principal components (PC_i for $i = 0, 1, 2$) describing the scatter around the mean. The normalisations of the principal components are arbitrary.

Figure 4.12: The zeroth principal component for the four different mass samples in Table 4.2. In all mass samples the PC_0 component is of similar shape and shows a positive contribution at a lookback time of 11 Gyr, and a negative contribution at lookback times smaller than $\simeq 7$ Gyr.

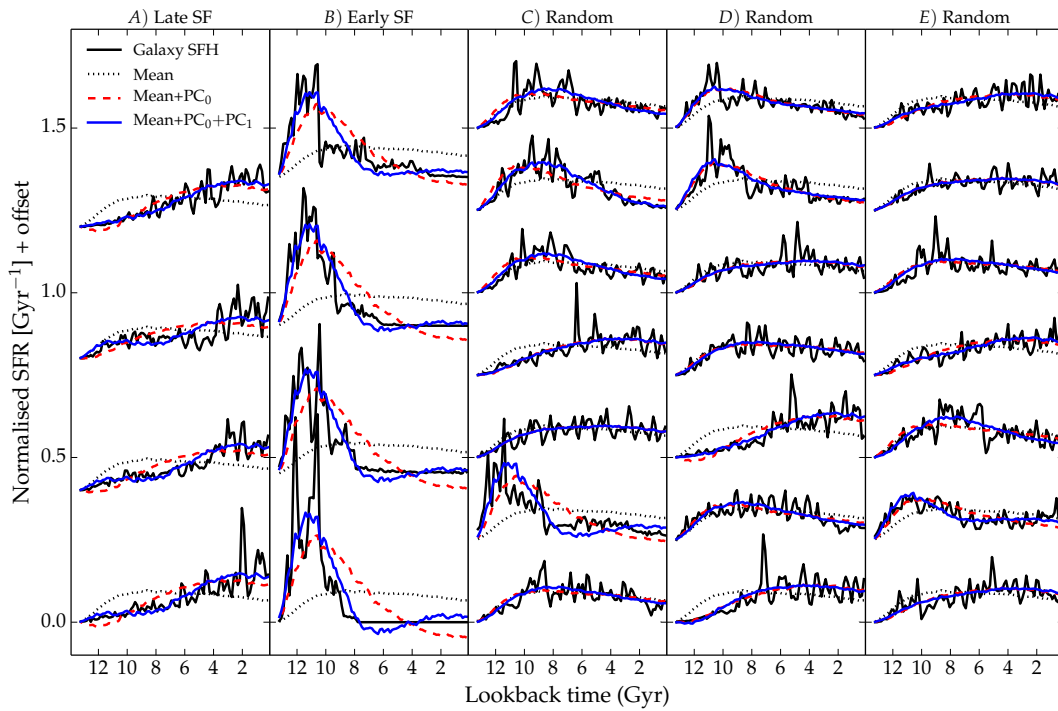


Figure 4.13: Star formation histories of individual galaxies (black lines) and the mean profile for the sample of galaxies with $M_* = 10^{10} M_\odot$ (grey dashed lines). Also shown are profiles including the contribution from the zeroth principal component (red dashed line) and components 0 and 1 (blue line). Panels *A* and *B* show 8 galaxies that form their stars late and early, respectively (the same profiles are shown in Figure 4.10). Panels *C*, *D* and *E* show 21 randomly selected galaxies from the sample with $M_* = 10^{10} M_\odot$.

stars early or late, depending on whether the coefficient q_0 is positive or negative. PC_1 and PC_2 cross the zero-point two and three times, respectively, and they are therefore determining the more detailed evolution of the SFH. In general, PC_i crosses the zero-point $i + 1$ times, and therefore is associated with a physical timescale of order $t_H/(i + 1)$, where $t_H = 13.7$ Gyr is the Hubble time.

For all the four mass samples from Table 4.2, the PC_0 is plotted in Figure 4.12. They all appear similar and have the feature that a positive q_0 -value describes a galaxy forming stars earlier than the mean of the sample. The only remarkable difference between the PC_0 eigenvectors from the different samples is that the lookback time where the change from positive to negative contributions occurs shifts to higher values for the more massive galaxies. The trend that massive galaxies have earlier bursty epochs than less massive galaxies is therefore both reflected by the mean star formation history and a 0th principal component that peaks at higher redshift.

Figure 4.13 compares the actual SFHs for a selection of galaxies to the mean SFH of the $M_* = 10^{10} M_\odot$ sample, and the SFHs reconstructed by including only PC_0 and by including both PC_0 and PC_1 . By including PC_0 it is possible to capture whether a galaxy forms its stars early or late. Including the PC_1 mode as well gives of course a better fit to the actual SFH of the galaxies. Components 0 and 1 account for 33% and 10% of the total scatter in the sample. These percentages indicate that while a given galaxy's SFH can already be described reasonably well by just PC_0 and PC_1 , variability on timescales much shorter than described by them needs to be considered for an accurate description.

We note that it could potentially be useful to construct a family of SFHs based on a combination of the mean SFH for the Illustris galaxies and one or more of the principal components from the PCA analysis. An attractive property of a model based on the mean SFH and the leading principal component would be that it could describe a realistic SFH of a galaxy with only one free parameter (the relative contribution of the mean SFH and the leading principal component). Such a model would be more physically motivated than e.g. single-burst models or τ -models, which are often used when fitting spectral energy distributions of galaxies. In future work we will construct such a model and show how it can be used for fitting spectral energy distributions. Such an approach could yield significant advantages because the accuracy and robustness of spectral energy distribution modelling can be very sensitive to the assumed SFH (e.g. Michałowski et al. 2012, 2014; C. Hayward & D. Smith, submitted; P. Torrey et al., submitted).

4.5.3 Assessing the SFH variability timescale

As each principal component has an associated timescale, the PCA analysis may also be used to characterize variability of the star formation histories, which in turn is influenced by the adopted physical model for feedback processes and the ISM. In Figure 4.14, we show the cumulative fraction of the variance accounted for as a function of the number of principal components included. The two most-massive samples behave similarly for the low and high resolution run. For the two low mass bins the difference between the low and high resolution run is larger. To quantitatively measure how well-converged the cumulative fractions in Figure 4.14 are, we use the difference in the fraction of the scatter accounted for by the 25 first components in the low and high resolution run. For the various bins the differences are 21%, 11%, 3% and 1% (from lowest to highest mass). The two most-massive ranges are therefore well-converged, unlike the two least-massive ranges, where some of the scatter comes from Poisson noise. This is also consistent with

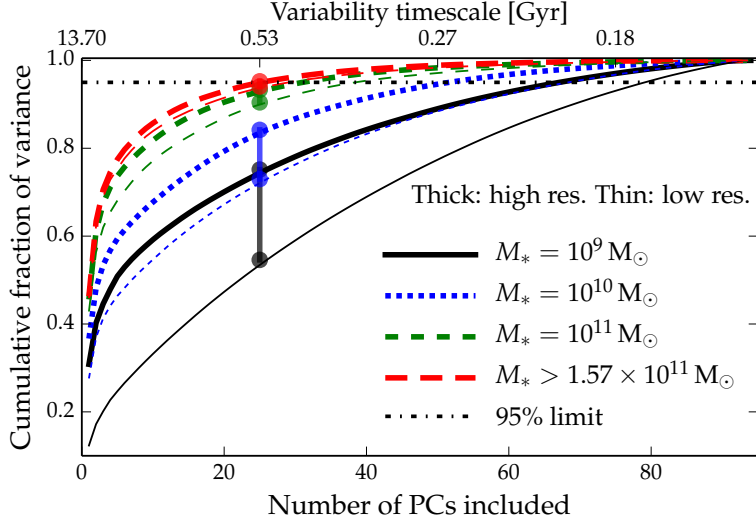


Figure 4.14: The cumulative fraction of the total variance in the star formation histories accounted for as a function of the number of principal components that are included. The thick lines show the full resolution run and the thin lines show the low resolution run. The vertical lines (connected by circles) measure how well-converged the variability timescale is for the different mass-ranges.

Figure 4.9, where the mean and median star formation history of the low-massive range seem to be more affected by noise than the most-massive range.

The timescale at which 95% of the scatter is accounted for is 500 Myr in the two most-massive bins, and for the other mass-ranges this timescale is smaller, which might be a consequence of the contribution of Poisson noise being more important in the low-massive galaxies, where there are fewer star particles per time bin. Based on the variability timescale of the most-massive range, the characteristic timescale for fluctuations in the galactic star formation for the ISM model adopted in Illustris has a characteristic timescale of 500 Myr. In Section 4.3.3 we saw that the scatter in the SFMS decreased significantly (by 0.05 dex), when the SFH was smoothed on this timescale, and that the decrease in the scatter was more moderate when smoothing over shorter timescales.

We note that there exist other simulation feedback models which show variability timescales an order of magnitude lower than Illustris. Hopkins et al. (2013), for example, include a treatment of radiative feedback from young stars and more localized supernova feedback in giant molecular clouds. Another model with a short variability timescale is Governato et al. (2014), where this is achieved through a high-star formation threshold and delayed radiative cooling. Interestingly, variability itself could be used as an important constraint of feedback models, although the fact that highly variable feedback models will induce differences between SFR indicators may make this complicated in practice.

4.5.4 Relations between the SFH main mode and galaxy properties

We have previously shown that the q_0 -value of the PCA-decomposed star formation history of a galaxy captures whether its stellar population forms early or late. We therefore expect correlations between q_0 and other quantities sensitive to the age of stellar populations. Figure 4.15 shows how q_0 for the different galaxy mass bins relates to the lookback time when half of the stellar mass is formed (T_{50}), the $g - r$ colour at $z = 0$, the black

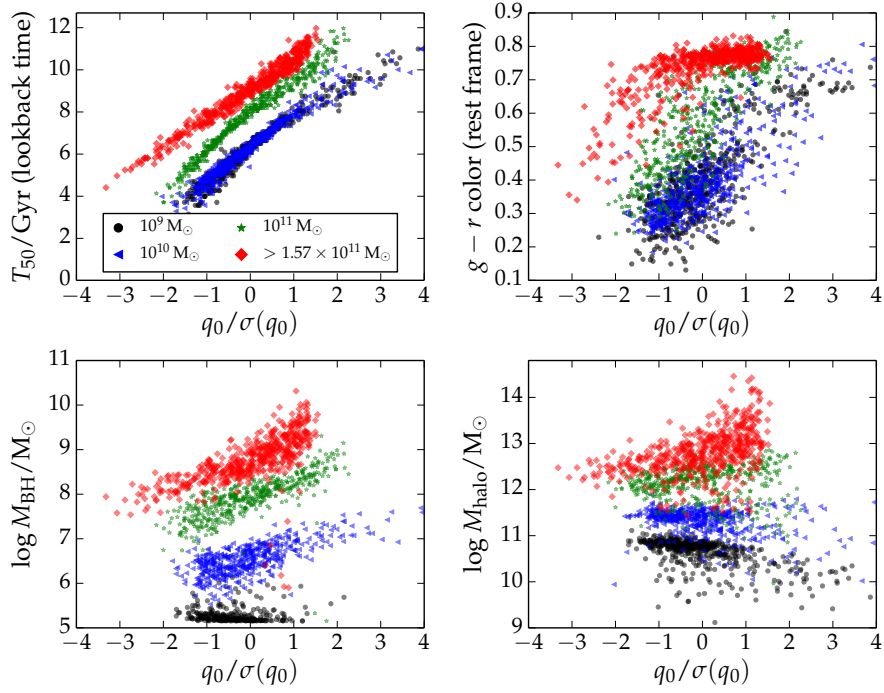


Figure 4.15: The dependence of various galaxy properties on the coefficient describing the contribution from the zeroth principal component (q_0) for each galaxy in the samples with stellar masses of $M_*/M_\odot = 10^9, 10^{10}, 10^{11}$, as well as for the 500 most-massive galaxies. The *upper left panel* shows that the lookback time at which 50% of the stars in a galaxy is formed (T_{50}) correlates strongly with q_0 . There also exists correlations with the $g - r$ colour (*upper right panel*), and the black hole mass at $z = 0$ (*lower left panel*). For the two most-massive stellar mass samples, q_0 correlates with the dark matter halo mass. For the two least-massive stellar mass samples, an anti-correlation is observed (*lower right panel*). q_0 is normalised by the standard deviation of this parameter for the 500 galaxies in each sample.

hole mass at $z = 0$, and the dark matter mass (friends-of-friends) at $z = 0$. q_0 correlates strongly with T_{50} , which is in agreement with the star formation histories in Figure 4.13. There is an offset between the normalisation of this correlation between the different samples. This is partially because the most-massive galaxies form their stars before the least massive galaxies (see also Figure 4.9).

The correlation between q_0 and $g - r$ is also expected, since old stellar populations are expected to be redder than younger stellar populations. In all the samples there is a bimodality in the $g - r$ colour, which splits the galaxies into red galaxies (with high values of $g - r$) with large q_0 -values and blue galaxies (low values of $g - r$) with lower q_0 -values. The division between the blue and red galaxy populations is seen most clearly for the $M_* = 10^{11} M_\odot$ galaxies, where the red galaxies have $g - r \gtrsim 0.65$. For the sample containing the most-massive galaxies there is a larger fraction of red galaxies than for the samples of less massive galaxies, where the blue population dominates.

The presence of a red and blue population of galaxies that form their stars late and early, respectively, is consistent with the *red and blue cloud*, which are connected through the *green valley*, established from observations of galaxies (e.g. Strateva et al., 2001; Faber et al., 2007; Bowler et al., 2014; Schawinski et al., 2014). Galaxies in the blue cloud are known to be actively star-forming, whereas the red cloud consists of passive galaxies that are most likely quenched by feedback processes. In Illustris, there is a correlation between the star formation history and the black hole mass at $z = 0$ for the three most-massive bins (*lower left panel*, Figure 4.15), which suggests that the galaxies that form their stars early are quenched by AGN feedback, although other interpretations of the correlation cannot be ruled out by the analysis presented here. For the $10^9 M_\odot$ galaxies, such a trend is not evident in the simulation, which is expected because the black hole feedback models in Illustris do not significantly affect galaxies in this mass range.

The panel that shows the dark matter halo mass, M_{halo} , at $z = 0$ versus q_0 reveals that these two variables are correlated for the samples with the two highest stellar masses. Furthermore, galaxies that form their stars late (low q_0) have halo masses that are close to $10^{12} M_\odot$, whereas galaxies that form stars early have higher halo masses. This is expected within the framework in which stars are most likely to form in halos of mass $10^{12} M_\odot$. For the samples with $M_* = 10^9 M_\odot$ and $10^{10} M_\odot$ a weak anti-correlation between q_0 and M_{halo} is present. The anti-correlation most likely arises because a halo mass of $10^{12} M_\odot$ is never reached for these galaxies, so they form stars most efficiently at low redshift, when the dark matter halo mass is as close as possible to $10^{12} M_\odot$.

4.6 Discussion

4.6.1 The normalisation of the star formation main sequence

In Section 4.3, we demonstrated that in Illustris, star-forming galaxies exhibit a tight, approximately linear correlation between the SFR and stellar mass, as is observed for real galaxies. Although the normalisation agrees well with observations at $z = 0$ and $z = 4$, the normalisation in Illustris is less than that observed for intermediate redshifts $z \sim 1 - 2$. A similar problem of underpredicting the normalisation of the main sequence relation at $z \simeq 2$ has previously been noted by several authors (e.g., Daddi et al., 2007; Davé, 2008; Damen et al., 2009), and it appears to be a generic problem for cosmological hydrodynamical simulations and semi-analytical models. Thus, it is worthwhile to consider potential solutions to this problem and discuss whether it is indeed a serious problem.

Potential theoretical solutions

In Illustris and other cosmological hydrodynamical simulations, the SFR-stellar mass relation is a result of the correlation of gas inflow and outflow rates with halo mass (e.g. Davé et al., 2011, 2012; Dekel et al., 2013). Thus, inaccurate gas net accretion rates would lead to an incorrect normalisation of the SFR-stellar mass relation. Damen et al. (2009) compared the growth rate of galaxies in observations with semi-analytical models (Guo & White, 2008) and argued that a time-varying IMF cannot resolve the issue of too low normalisations at $1 \lesssim z \lesssim 2$. Instead, Damen et al. suggest that the discrepancy may be due to the simplified schemes for gas accretion used in semi-analytical models. Mitchell et al. (2014) identified the same problem of a too low normalisation of the main sequence at $z = 2$ in semi-analytical models. They showed that a modification of the timescale over which gas ejected by feedback is reincorporated into galaxies can help to fix this problem for galaxies with $M_* \lesssim 10^{10} M_\odot$ (a modification of the reincorporation timescale was also studied by Henriques et al. 2013), but it cannot solve the problem for more-massive galaxies.

Concerns regarding gas inflow rates are less applicable to the Illustris simulation than to semi-analytical models because in Illustris gas accretion is explicitly treated using an accurate hydrodynamics algorithm (e.g. Sijacki et al., 2012; Vogelsberger et al., 2012; Kereš et al., 2012; Bauer & Springel, 2012). Still, it is possible that the gas cooling rates in Illustris are systematically offset. For example, if the phase structure or metal content of the hot halo gas is incorrect, gas inflow rates could end up being inaccurate (Nelson et al., 2013; Hayward et al., 2014).

Outflows are also important for setting the normalisation of the SFR-stellar mass relation, but they must still be treated with sub-resolution models even in state-of-the-art large-volume cosmological hydrodynamical simulations. One can easily imagine altering the normalisation of the SFR-stellar mass relation by e.g. modifying the mass-loading factor of stellar winds. However, the parameters of the sub-resolution feedback models used in Illustris were determined by requiring the simulation to match observations such as the $z = 0$ stellar mass function. Thus far, attempts to tune the parameters to reconcile the discrepancy with which we are concerned here without breaking these constraints were unsuccessful (Torrey et al., 2014). Nevertheless, this does not preclude the possibility of solving the discrepancy through the use of more sophisticated feedback models.

4.6.2 The paucity of starbursts in Illustris

The small number of strong starbursts (i.e. galaxies that lie significantly above the star formation main sequence) identified in Illustris is another discrepancy in addition to the disagreement in the normalisation of the SFR-stellar mass relation discussed above. As shown in Fig. 4.4, at all redshifts considered, 2.5σ outliers from the SFR-stellar mass relation contribute at most a few per cent of the total SFR density in massive galaxies ($M_* \gtrsim 10^{10} M_\odot$), and this contribution is a factor of at least a few less than what is inferred from observations. Furthermore, by combining scalings derived from idealised merger simulations with a semi-empirical model, Hopkins et al. (2010) estimated that at all redshifts, merger-induced starbursts account for $\sim 5 - 10$ per cent of the SFR density of the Universe, which is also at odds with the Illustris results.

One possible reason for the relative shortage of starbursts in Illustris is its kiloparsec-scale spatial resolution. Although the comparison of the low- and high-resolution runs presented in Figure 4.4 suggests that the fraction of starbursts is converged, it is possible

that this conclusion will change if the resolution is increased significantly, as is often done using zoom-in simulations of galaxies (e.g.; Guedes et al., 2011; Marinacci et al., 2014). It is for example possible that the spatial resolution in both the high- and low-resolution Illustris runs is insufficient to resolve the tidal torques that drive starbursts in mergers. Indeed, the compact sizes (of order 100 pc) of the starbursting regions in local ULIRGs (e.g. Sakamoto et al., 2008; Engel et al., 2011) support this interpretation. Furthermore, examination of the individual star formation histories presented in Fig. 4.10 indicates that the galaxies’ star formation was burstier at high redshift ($z \gtrsim 2$). Because a fixed comoving softening yields finer resolution at higher redshifts, this observation may also indicate that resolution is the reason for the lack of starbursts in Illustris.

The relatively stiff equation of state of the Springel & Hernquist (2003) sub-resolution ISM model may also serve to suppress starbursts in Illustris. However, in higher-resolution idealised merger simulations that employed the same ISM model, SFR elevations of an order of magnitude or more have been found (e.g. Cox et al., 2008; Hayward et al., 2011, 2014; Torrey et al., 2012). Furthermore, the resulting SFR elevations are sufficient to match the observed interaction induced SFRs of close-pair galaxies in SDSS (Scudder et al., 2012; Patton et al., 2013). We note however that galaxy merger simulations with much softer equations of state show still stronger (albeit shorter) SFR increases (e.g. Mihos & Hernquist, 1996). Also, the elevation depends sensitively on the mass ratio and orbital parameters of the merger (e.g. Di Matteo et al., 2007, 2008; Cox et al., 2008). Thus, the sub-resolution ISM model may contribute to the suppression of merger-driven starbursts in Illustris but is unlikely to be the sole reason. But mergers are not the only mechanism that can drive starbursts: it has been suggested that violent disk instability is also an important channel for driving starbursts (e.g. Dekel et al., 2009; Ceverino et al., 2010; Cacciato et al., 2012; Porter et al., 2014). Such events may be suppressed in Illustris because of the sub-resolution ISM model.

Finally, it is possible that the IR luminosity-inferred star formation rates of extreme outliers from the main sequence are overestimates of the true SFR. For highly obscured galaxies, at the peak of the starburst, simulations suggest that older stellar populations (Hayward et al., 2014) and obscured AGN (L. Rosenthal et al., in preparation) may contribute to the IR luminosity and thus cause the SFR to be overestimated by a factor of a few. These effects are almost certainly not significant for the bulk of the star-forming galaxy population and thus should not affect the normalization of the SFR-stellar mass relation, but, if they are relevant for any real galaxies, it will likely be those galaxies that are well above the galaxy main sequence. Consequently, these effects may explain the tension between observations and Illustris demonstrated in Section 4.3.2.

4.7 Conclusions

In this work, we have examined the star formation main sequence and individual star formation histories of galaxies in the Illustris simulation. Our main findings can be summarized as follows:

- The normalisation of the star formation main sequence is consistent with the observations at $z = 0$ and $z = 4$. At intermediate redshifts, $z \sim 2$, the normalisation is significantly lower than reported in observations. There is also a slight tension between the slope of the star formation main sequence for low-mass galaxies, for which Illustris predicts an approximately mass-independent specific SFR,

whereas observations indicate that the specific SFR is a decreasing function of stellar mass. We speculate that more-sophisticated feedback models are required in order to properly recover the observed slope and normalisation of the SFMS.

- The highest star formation efficiency is found in halos with masses of $10^{12} M_{\odot}$, and the largest contribution to the star formation rate density comes from galaxies in halos with masses of $10^{11.5} - 10^{12.5} M_{\odot}$ at $z \lesssim 4$. At higher redshift, the dominant contribution originates in less-massive halos because of the declining abundance of halos with high masses. The stellar masses of the galaxies contributing most strongly to the global star formation rate density lie in the range $10^{10} - 10^{11} M_{\odot}$, which is in agreement with observational constraints on this peak mass. Another result is that galaxies with stellar masses above $\simeq 10^{11} M_{\odot}$ that reside in $\sim 10^{12} M_{\odot}$ halos form their stars later than galaxies in more-massive halos. This is a consequence of star formation being most efficient in $\sim 10^{12} M_{\odot}$ halos.
- We have studied the dominant modes and the time variability of individual star formation histories with a principal component analysis, finding that the characteristic timescale of star formation fluctuations in the simulation is 500 Myr. Another result of this principal component analysis is that many features of a galaxy's star formation history can be described by the leading principal component. This leads us to suggest that star formation histories based on one or several principal components can be useful when fitting the spectral energy distribution of observed galaxies.
- Compared to observations, there is a paucity of strong starbursts in Illustris, as evidenced by the small number of galaxies that lie significantly above the star formation main sequence. This is likely caused in part by a lack of spatial resolution in the cosmological simulation, but it may also reflect the relatively stiff equation of state model used in Illustris' subgrid model for the regulation of star formation in the ISM.

In future cosmological simulations of galaxy formation, the relative frequency of starbursts may well turn out to be an important constraint that informs about adequate models for the ISM. In Illustris, starbursts are presumably damped in intensity and stretched in time by the stiff ISM model, without much affecting the stellar mass and the structural properties of merger remnants. If a significant number of starbursts are triggered by disk instabilities, which are suppressed by the ISM model used in Illustris, the resulting discrepancies could potentially be more significant. Refined simulation models will be necessary to clarify this question.

Acknowledgments

We thank Sune Toft, Peter Behroozi, Nicholas Lee and David Sanders for useful discussions. The Dark Cosmology Centre is funded by the Danish National Research Foundation. CCH is grateful to the Klaus Tschira Foundation and the Gordon and Betty Moore Foundation for financial support. VS acknowledges support by the European Research Council under ERC-StG EXAGAL-308037.

Bibliography

- Atek H., et al., 2014, arXiv:1406.4132
- Bauer A., Springel V., 2012, MNRAS, 423, 2558
- Behroozi P. S., Wechsler R. H., Conroy C., 2013a, ApJ, 762, L31
- Behroozi P. S., Wechsler R. H., Conroy C., 2013b, ApJ, 770, 57
- Béthermin M., Daddi E., Magdis G., Sargent M. T., Hezaveh Y., Elbaz D., Le Borgne D., Mullaney J., Pannella M., Buat V., Charmandaris V., Lagache G., Scott D., 2012, ApJ, 757, L23
- Béthermin M., Wang L., Doré O., Lagache G., Sargent M., Daddi E., Cousin M., Aussel H., 2013, A&A, 557, A66
- Bird S., Vogelsberger M., Haehnelt M., Sijacki D., Genel S., Torrey P., Springel V., Hernquist L., 2014, arXiv:1405.3994
- Bowler R. A. A., et al., 2014, MNRAS, 440, 2810
- Brinchmann J., Charlot S., White S. D. M., Tremonti C., Kauffmann G., Heckman T., Brinkmann J., 2004, MNRAS, 351, 1151
- Cacciato M., Dekel A., Genel S., 2012, MNRAS, 421, 818
- Cemile Marsan Z., et al., 2014, arXiv:1406.0002
- Ceverino D., Dekel A., Bournaud F., 2010, MNRAS, 404, 2151
- Chabrier G., 2003, PASP, 115, 763
- Cohn J. D., van de Voort F., 2014, arXiv:1406.2967
- Cox T. J., Jonsson P., Somerville R. S., Primack J. R., Dekel A., 2008, MNRAS, 384, 386
- Cucciati O., et al., 2012, A&A, 539, A31
- Daddi E., et al., 2007, ApJ, 670, 156
- Daddi E., et al., 2010, ApJ, 714, L118
- Damen M., Förster Schreiber N. M., Franx M., Labbé I., Toft S., van Dokkum P. G., Wuyts S., 2009, ApJ, 705, 617
- Davé R., 2008, MNRAS, 385, 147

Davé R., Finlator K., Oppenheimer B. D., 2012, MNRAS, 421, 98

Davé R., Oppenheimer B. D., Finlator K., 2011, MNRAS, 415, 11

Dekel A., Sari R., Ceverino D., 2009, ApJ, 703, 785

Dekel A., Zolotov A., Tweed D., Cacciato M., Ceverino D., Primack J. R., 2013, MNRAS, 435, 999

Di Matteo P., Bournaud F., Martig M., Combes F., Melchior A.-L., Semelin B., 2008, A&A, 492, 31

Di Matteo P., Combes F., Melchior A.-L., Semelin B., 2007, A&A, 468, 61

Diemand J., Kuhlen M., Madau P., Zemp M., Moore B., Potter D., Stadel J., 2008, Nature, 454, 735

Dressler A., 1980, ApJ, 236, 351

Dutton A. A., van den Bosch F. C., Dekel A., 2010, MNRAS, 405, 1690

Elbaz D., et al., 2011, A&A, 533, A119

Engel H., Davies R. I., Genzel R., Tacconi L. J., Sturm E., Downes D., 2011, ApJ, 729, 58

Faber S. M., et al., 2007, ApJ, 665, 265

Faber S. M., Jackson R. E., 1976, ApJ, 204, 668

Genel S., et al., 2014, arXiv:1405.3749

Genel S., Vogelsberger M., Nelson D., Sijacki D., Springel V., Hernquist L., 2013, MNRAS, 435, 1426

Genzel R., et al., 2010, MNRAS, 407, 2091

Governato F., et al., 2014, arXiv:1407.0022

Guedes J., Callegari S., Madau P., Mayer L., 2011, ApJ, 742, 76

Guo Q., White S. D. M., 2008, MNRAS, 384, 2

Hayward C. C., et al., 2014, arXiv:1402.0006

Hayward C. C., Jonsson P., Kereš D., Magnelli B., Hernquist L., Cox T. J., 2012, MNRAS, 424, 951

Hayward C. C., Kereš D., Jonsson P., Narayanan D., Cox T. J., Hernquist L., 2011, ApJ, 743, 159

Hayward C. C., Torrey P., Springel V., Hernquist L., Vogelsberger M., 2014, MNRAS, 442, 1992

Henriques B. M. B., White S. D. M., Thomas P. A., Angulo R. E., Guo Q., Lemson G., Springel V., 2013, MNRAS, 431, 3373

Hinshaw G., et al., 2013, ApJS, 208, 19

Hopkins A. M., 2004, *ApJ*, 615, 209

Hopkins A. M., Beacom J. F., 2006, *ApJ*, 651, 142

Hopkins P. F., Keres D., Onorbe J., Faucher-Giguere C.-A., Quataert E., Murray N., Bullock J. S., 2013, arXiv:1311.2073

Hopkins P. F., Younger J. D., Hayward C. C., Narayanan D., Hernquist L., 2010, *MNRAS*, 402, 1693

Hubble E. P., 1926, *ApJ*, 64, 321

Karim A., et al., 2011, *ApJ*, 730, 61

Kennicutt R. C., Evans N. J., 2012, *ARA&A*, 50, 531

Kennicutt Jr. R. C., 1989, *ApJ*, 344, 685

Kennicutt Jr. R. C., 1998, *ApJ*, 498, 541

Kereš D., Vogelsberger M., Sijacki D., Springel V., Hernquist L., 2012, *MNRAS*, 425, 2027

Klypin A. A., Trujillo-Gomez S., Primack J., 2011, *ApJ*, 740, 102

Knapen J. H., James P. A., 2009, *ApJ*, 698, 1437

Kravtsov A., Vikhlinin A., Meshscheryakov A., 2014, ArXiv: 1401.7329

Labbé I., et al., 2010, *ApJ*, 716, L103

Lilly S. J., Le Fevre O., Hammer F., Crampton D., 1996, *ApJ*, 460, L1

Madau P., Pozzetti L., Dickinson M., 1998, *ApJ*, 498, 106

Mannucci F., Cresci G., Maiolino R., Marconi A., Gnerucci A., 2010, *MNRAS*, 408, 2115

Marinacci F., Pakmor R., Springel V., 2014, *MNRAS*, 437, 1750

Michałowski M. J., Dunlop J. S., Cirasuolo M., Hjorth J., Hayward C. C., Watson D., 2012, *A&A*, 541, A85

Michałowski M. J., Hayward C. C., Dunlop J. S., Bruce V. A., Cirasuolo M., Cullen F., Hernquist L., 2014, arXiv:1405.2335

Mihos J. C., Hernquist L., 1996, *ApJ*, 464, 641

Mitchell P. D., Lacey C. G., Cole S., Baugh C. M., 2014, arXiv:1403.1585

Moster B. P., Naab T., White S. D. M., 2013, *MNRAS*, 428, 3121

Nelson D., Vogelsberger M., Genel S., Sijacki D., Kereš D., Springel V., Hernquist L., 2013, *MNRAS*, 429, 3353

Noeske K. G., Faber S. M., Weiner B. J., Koo D. C., Primack J. R., Dekel A., Papovich C., Conselice C. J., Floc'h E. L., Rieke G. H., Coil A. L., Lotz J. M., Somerville R. S., Bundy K., 2007, *ApJ*, 660, L47

Patton D. R., Torrey P., Ellison S. L., Mendel J. T., Scudder J. M., 2013, MNRAS, 433, L59

Pillepich A., et al., 2014, arXiv:1406.1174

Porter L. A., Somerville R. S., Primack J. R., Johansson P. H., 2014, arXiv:1407.0594

Rees M. J., Ostriker J. P., 1977, MNRAS, 179, 541

Rodighiero G., et al., 2011, ApJ, 739, L40

Sakamoto K., Wang J., Wiedner M. C., Wang Z., Peck A. B., Zhang Q., Petitpas G. R., Ho P. T. P., Wilner D. J., 2008, ApJ, 684, 957

Salim S., et al., 2007, ApJS, 173, 267

Sanders D. B., Soifer B. T., Elias J. H., Madore B. F., Matthews K., Neugebauer G., Scoville N. Z., 1988, ApJ, 325, 74

Sargent M. T., Béthermin M., Daddi E., Elbaz D., 2012, ApJ, 747, L31

Schawinski K., et al., 2014, MNRAS, 440, 889

Schaye J., et al., 2010, MNRAS, 402, 1536

Schaye J., et al., 2014, ArXiv:1407.7040

Schmidt M., 1959, ApJ, 129, 243

Scudder J. M., Ellison S. L., Torrey P., Patton D. R., Mendel J. T., 2012, MNRAS, 426, 549

Sijacki D., Springel V., Di Matteo T., Hernquist L., 2007, MNRAS, 380, 877

Sijacki D., Vogelsberger M., Kereš D., Springel V., Hernquist L., 2012, MNRAS, 424, 2999

Silk J., 1977, ApJ, 211, 638

Simha V., Weinberg D. H., Conroy C., Dave R., Fardal M., Katz N., Oppenheimer B. D., 2014, arXiv:1404.0402

Speagle J. S., Steinhardt C. L., Capak P. L., Silverman J. D., 2014, arXiv:1405.2041, accepted to ApJS

Springel V., 2010, MNRAS, 401, 791

Springel V., Di Matteo T., Hernquist L., 2005, MNRAS, 361, 776

Springel V., et al., 2005, Nature, 435, 629

Springel V., Hernquist L., 2003, MNRAS, 339, 289

Strateva I., et al., 2001, AJ, 122, 1861

Toft S., et al., 2014, ApJ, 782, 68

Torrey P., Cox T. J., Kewley L., Hernquist L., 2012, ApJ, 746, 108

Torrey P., Vogelsberger M., Genel S., Sijacki D., Springel V., Hernquist L., 2014, MNRAS, 438, 1985

Tremonti C. A., et al., 2004, *ApJ*, 613, 898
Tully R. B., Fisher J. R., 1977, *A&A*, 54, 661
Vogelsberger M., et al., 2014a, arXiv:1405.2921
Vogelsberger M., et al., 2014b, *Nature*, 509, 177
Vogelsberger M., Genel S., Sijacki D., Torrey P., Springel V., Hernquist L., 2013, *MNRAS*, 436, 3031
Vogelsberger M., Sijacki D., Kereš D., Springel V., Hernquist L., 2012, *MNRAS*, 425, 3024
Whitaker K. E., van Dokkum P. G., Brammer G., Franx M., 2012, *ApJ*, 754, L29
White S. D. M., Rees M. J., 1978, *MNRAS*, 183, 341
Wuyts S., et al., 2011, *ApJ*, 742, 96
Zel'dovich Y. B., 1970, *A&A*, 5, 84

Chapter 5

The origin of gamma-ray bursts: the explosion of a massive star at $z \simeq 0.55$

This chapter contains the following article:

Spectroscopic evidence for SN 2010ma associated with GRB 101219B

Published in Sparre et al. 2011, ApJ, 735L, 24.

Authors: M. Sparre, J. Sollerman, J. P. U. Fynbo, D. Malesani, P. Goldoni, A. de Ugarte Postigo, S. Covino, V. D’Elia, H. Flores, F. Hammer, J. Hjorth, P. Jakobsson, L. Kaper, G. Leloudas, A. J. Levan, B. Milvang-Jensen, S. Schulze, G. Tagliaferri, N. R. Tanvir, D. J. Watson, K. Wiersema, R. A. M. J. Wijers

Abstract

We report on the spectroscopic detection of supernova SN 2010ma associated with the long gamma-ray burst GRB 101219B. We observed the optical counterpart of the GRB on three nights with the X-shooter spectrograph at the VLT. From weak absorption lines, we measure a redshift of $z = 0.55$. The first epoch UV–near-infrared afterglow spectrum, taken 11.6 hr after the burst, is well fit by a power law consistent with the slope of the X-ray spectrum. The second and third epoch spectra (obtained 16.4 and 36.7 days after the burst), however, display clear bumps closely resembling those of the broad-lined type-Ic SN 1998bw if placed at $z = 0.55$. Apart from demonstrating that spectroscopic SN signatures can be observed for GRBs at these large distances, our discovery makes a step forward in establishing a general connection between GRBs and SNe. In fact, unlike most previous unambiguous GRB-associated SNe, GRB 101219B has a large gamma-ray energy ($E_{\text{iso}} = 4.2 \times 10^{51}$ erg), a bright afterglow, and obeys the “Amati” relation, thus being fully consistent with the cosmological population of GRBs.

5.1 Introduction

Within the last 13 years a connection between two of the most energetic phenomena in our universe, long-duration gamma-ray bursts (GRBs, $T_{90} > 2$ s; Kouveliotou et al. 1993)

and core-collapse supernovae (SNe), has been established (e.g., Woosley & Bloom, 2006).

The first SN associated with a GRB was reported by Galama et al. (1998), who found the extremely luminous SN 1998bw to be associated with GRB 980425. Subsequently, several other GRB–SNe were found, and a few of these have also been spectroscopically confirmed, most prominently GRB 030329 (Hjorth et al., 2003; Stanek et al., 2003), GRB 031203 (Malesani et al., 2004), GRB 060218 (Pian et al., 2006; Sollerman et al., 2006), and GRB 100316D (Starling et al., 2011; Bufano et al., 2011; Chornock et al., 2010; Cano et al., 2011). All these SNe are broad-lined type Ic; they lack lines from hydrogen and helium in their spectra and have broader lines than typical core-collapse SNe.

Most of these spectroscopic SN-associated GRBs are low-luminosity GRBs for which the emitted energies in the γ -ray band are in the range 10^{48} – 10^{50} erg (e.g., Amati et al., 2007; Nysewander et al., 2009), which is 2–4 orders of magnitude smaller than for typical GRBs detected at larger distances. They also had comparably fainter or undetected optical and X-ray afterglows, and did not always obey the $E_{\text{peak}}-E_{\text{iso}}$ correlation (Amati et al., 2007). The only well-known exception is GRB 030329 at $z = 0.167$. It is therefore crucial to test whether the SN-GRB connection holds in general for high-redshift, high-luminosity GRBs. To date, evidence in this direction is provided by the photometric detection of SN-like bumps in the late-time light curves of several GRBs (e.g., Zeh et al., 2004; Fynbo et al., 2004; Tanvir et al., 2010; Cano et al., 2011). Spectroscopy was also obtained in a few cases (e.g., Garnavich et al., 2003; Della Valle et al., 2003, 2006, 2008), although the contamination from the host galaxy and the faintness of the targets makes it difficult to reach firm conclusions in some of these cases.

GRB 101219B was detected by the *Swift* Burst Alert Telescope (BAT) on 2010 December 19 at 16:27:53 UT. Its afterglow was promptly detected by *Swift* both in the X-ray and UV/optical bands (Gelbord et al., 2010a). The GRB was observed to have a duration of $T_{90} = 34 \pm 4$ s in the 15–150 keV band (Cummings et al., 2010). It was also observed by *Fermi*/GBM, where a duration of $T_{90} = 51 \pm 2$ s was determined in the 10–1000 keV band (van der Horst et al., 2010). The spectrum of the prompt emission as measured by GBM is well fitted by the Band model with a peak energy at 70 ± 8 keV. The fluence measured by GBM is $(5.5 \pm 0.4) \times 10^{-6}$ erg cm $^{-2}$ (10–1000 keV). Given a redshift of 0.55 (see § 5.3.1), this corresponds to an isotropic equivalent energy $E_{\text{iso}} = 4.2 \times 10^{51}$ erg.

In this *Letter* we report on the spectroscopic detection of a SN associated with GRB 101219B. In § 2 we describe our observations, in § 3 we present the redshift measurement and the detection of the SN. Finally, in § 4 we offer a discussion of how this GRB-SN fits in our current understanding of the GRB-SN connection.

For the cosmological calculations we assume a Λ CDM-universe with $h_0 = 0.71$, $\Omega_m = 0.27$, and $\Omega_\Lambda = 0.73$.

5.2 Observations and data reduction

We observed the afterglow of GRB 101219B using the X-shooter spectrograph (D’Odorico et al., 2006; Vernet et al., 2010) mounted at UT2 of the ESO-VLT on Cerro Paranal. X-shooter is an echelle spectrograph with three arms covering the full spectral range from the atmospheric cut-off around 3000 Å to the *K* band (24,800 Å).

An overview of the observations is given in Table 5.1. For the UVB, VIS and NIR arms, slit-widths of 1''0, 0''9, and 0''9, respectively, were used. The binning was 1×2 in all UVB and VIS exposures, and NIR-exposures were unbinned. The slit was always aligned

Table 5.1: Overview of the X-shooter observations. The R -band magnitudes were derived from the acquisition images.

	Epoch 1	Epoch 2	Epoch 3
Mean time (UT)	2010 Dec 20.17	2011 Jan 5.09	2011 Jan 25.55
Time since GRB	11.6 hr	16.4 days	36.9 days
Exposure time (s)	4800	7200	7200
Seeing (arcsec)	0.93–1.11	0.78–0.85	0.89–0.97
Airmass	1.56–2.60	1.19–1.99	1.43–2.11
R magnitude	19.8 ± 0.2	22.7 ± 0.2	> 22.7

along the parallactic angle, and the instrument has an atmospheric dispersion corrector for the UVB and VIS arms.

We processed the spectra using the X-shooter data reduction pipeline (Goldoni et al., 2006; Modigliani et al., 2010) version 1.2.2. The pipeline performs all the standard reductions required to obtain flux calibrated echelle spectra.

All three spectra were corrected for Galactic extinction using $R_V = 3.1$ and the prescription from Cardelli et al. (1989) with $E(B - V) = 0.02$ mag (Schlegel et al., 1998). The spectra were reduced in staring mode and flux-calibrated using observations of the spectrophotometric standard star LTT 3218 (Hamuy et al., 1993). We performed photometry of the transient on the R -band acquisition images of X-shooter (Table 5.1). Although our photometry could be calibrated only relative to two faint USNO stars, our results are fully consistent with nearly simultaneous measurements obtained by GROND (Olivares et al., 2010). We therefore decided to scale our spectra in order to match the GROND photometry. A relatively large correction (a factor of 2.0) was needed for the first-epoch spectrum, probably due to the high airmass of the observation. The second spectrum was also scaled to the GROND photometry (Olivares et al., 2011), but only a small correction (5%) was necessary.

For the third epoch, we compared our spectrum with late-time $ugri$ imaging secured by us with the Gemini South telescope equipped with GMOS on Jan 29 (u) and on Jan 30 (gri), about 40 days after the BAT trigger. The flux in the spectrum matches well our photometric measurements.

5.3 Results

5.3.1 Redshift measurement

The first epoch spectrum is characterized by a power-law spectral shape typical for GRB afterglows. Only weak absorption lines are present, which makes it difficult to firmly determine the spectroscopic redshift. We tentatively reported a redshift of $z = 0.5519$ (de Ugarte Postigo et al., 2011) mainly based on the MgII 2796, 2803 Å doublet. We do not detect significant absorption at the positions of the FeII lines at 2382.76, 2586.65 and 2600.17 Å, but these are located in noisier parts of the spectrum. There is also a feature consistent with MgI 2853 Å at this redshift.

We have remeasured the redshift from the fully calibrated spectrum and find $z = 0.55185 \pm 0.00005$. To quantify the robustness of this detection we created a mean absorption profile by stacking the positions of the three Mg lines assuming a redshift of $z = 0.55185$. The resulting mean profile is shown in velocity space in Fig. 5.1. There is

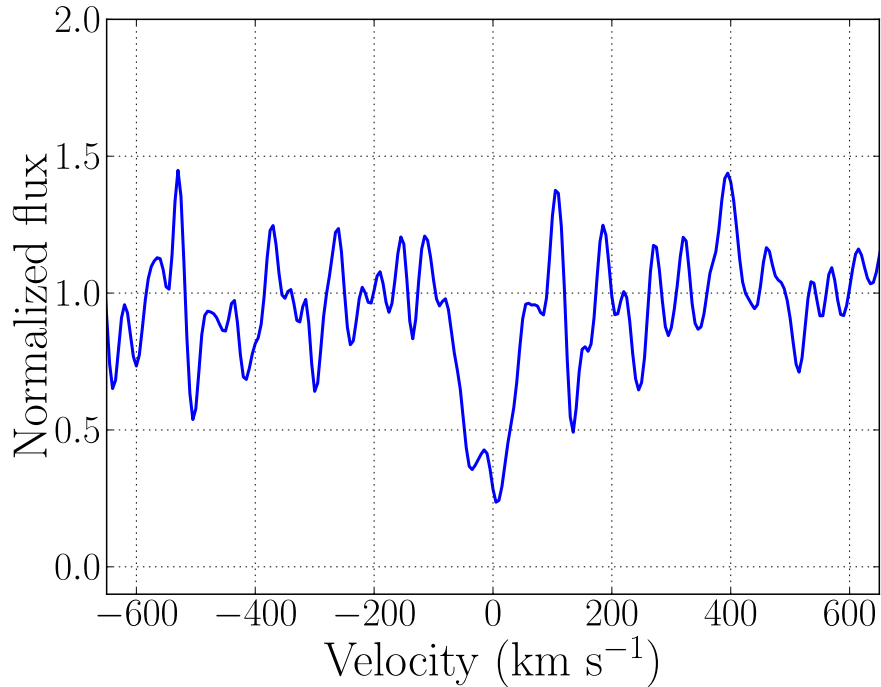


Figure 5.1: The mean velocity profile for the first epoch spectrum, for three Mg absorption lines detected at 4339.6, 4350.7, and 4427.5 Å assuming a redshift of $z = 0.55185$. Each line was converted to rest frame vacuum wavelength zero velocity before stacking.

indeed a fairly clear signal in the mean profile assuming this redshift. The formal significance of the stacked line is $\sim 7\sigma$. The two later epochs contain insufficient flux to significantly improve on this estimate. We note that the redshift is consistent with the limit of $z < 1.5$ reported from *Swift*-UVOT detections in the UVW2 filter (Kuin et al., 2011).

5.3.2 The first epoch afterglow

Our first epoch afterglow spectrum is well fitted using a simple power-law ($F_\nu \propto \nu^{-\beta}$, i.e. $F_\lambda \propto \lambda^{\beta-2}$). Using the UV – optical range, we find $\beta_{\text{opt}} = 0.92$ (Fig. 5.2), with systematic errors from the wavelength-dependence of the slit-loss around 10% indicated by the shaded area in the figure. The observed slope is consistent with the X-ray power-law slope measured by the *Swift* X-Ray Telescope (XRT), $\beta_X = 0.88 \pm 0.09$ (Evans et al., 2009).

Also shown in Fig. 5.2 are the nearly simultaneous measurements from GROND and those from *Swift*-UVOT, (Kuin et al. 2010; Kuin, private communication). A temporal decay $F_\lambda \propto t^{-1}$ is adopted to correct for the (small) time difference.

From the X-ray and optical fluxes, we calculate the broad-band spectral index (β_{OX}) (see Jakobsson et al., 2004). We find $\beta_{\text{OX}} = 1.02 \pm 0.10$, where the error arises from the uncertainty in the spectral index reported in the XRT spectrum and from the choice of the two wavelength points.

The fact that β_X , β_{opt} and β_{OX} are identical within their uncertainties shows that not only the slopes, but also the normalizations of the optical and X-ray spectra are consistent, hence both components belong to the same power-law segment. This also indicates that

little dust can be present along the line of sight (see § 5.3.4).

5.3.3 Detection of a supernova

In Fig. 5.3, spectra from all the three epochs are shown together with the first epoch power-law fit. GRB afterglows have power-law spectra, which is seen in the first epoch (as highlighted in Fig. 5.2). This is clearly not what we observe at later times; in the second epoch spectrum there is a prominent bump at 7800 \AA and an increase in flux from 5000 to 5500 \AA . The third-epoch spectrum also reveals a bump at $\sim 8400 \text{ \AA}$.

We have overplotted on the second epoch spectrum a combination of the fading power-law afterglow (~ 20 times dimmer than in the first epoch) and the spectrum from SN 1998bw (8 day past explosion and corrected for Galactic extinction; Patat et al., 2001) redshifted to $z = 0.55185$. We scaled the flux of SN 1998bw by a factor of 1.4 to match our observations from 5000 to 8000 \AA . This reproduces fairly well both the bump and the flux increase. Epoch 2 corresponds to 10.6 days in the rest frame of the burst, for which the SN 1998bw spectrum at 8 days is the closest available match with sufficient wavelength coverage. We note that SN 1998bw brightened by about 0.3 mag between 8 and 10.6 days (Galama et al., 1998), hence the flux level is consistent between the two events.

For the third epoch we overplotted a spectrum of SN 1998bw at an epoch of 23 days after the burst in the rest frame. This spectrum of SN 1998bw was chosen to best match the rest-frame epoch for our spectral observations of GRB 101219B and moved to $z = 0.55185$ with no additional flux scaling. The data are again consistent with the presence of a SN similar to SN 1998bw, although the possible contribution from residual afterglow and from the host galaxy (see § 5.3.4) limit the scope of this comparison.

We emphasize that in making these comparisons we have made very few assumptions and used few free parameters. The redshift was fixed to that measured from the absorption lines and the afterglow spectral slope is consistent with the X-ray slope. The SN 1998bw spectra were chosen for epochs dictated by our observations. We attribute the bluest part of the second epoch spectrum to the optical afterglow, since the SN is unlikely to contribute substantially in this regime (due to UV line blanketing, see e.g.; Mazzali et al., 2003). The afterglow is thus 21 ± 1 times fainter than in the first epoch. The only free parameter in the comparison with the epoch 2 spectrum is that we scaled the spectrum of SN 1998bw up by 40% (consistent with the time evolution of SN 1998bw).

The only plausible explanation for the nice match is that an energetic SN was indeed associated with GRB 101219B. We note that Olivares et al. (2011), using GROND, reported photometric evidence for a SN component in their light curves of GRB 101219B with an estimated redshift of $z \approx 0.4\text{--}0.7$. Following our discovery, the IAU dubbed this event SN 2010ma (Sparre et al., 2011).

5.3.4 Dust extinction and host galaxy continuum

The fact that our power-law fit agrees with the first epoch spectrum all the way out to the bluest end, and even extrapolates into the UVOT and XRT regimes (Fig. 5.2), demonstrates that this GRB suffered from negligible extinction. Adding an SMC-like dust extinction when fitting the afterglow did not improve the fit. To put an upper limit to the V-band absorption A_V , we fitted the normalization and the spectral slope to a model, where A_V was fixed to 0.1 mag. In the UVB part of our spectrum this model gave a worse fit than the dust-free fit, and it also did not match the UVOT points, so we conclude

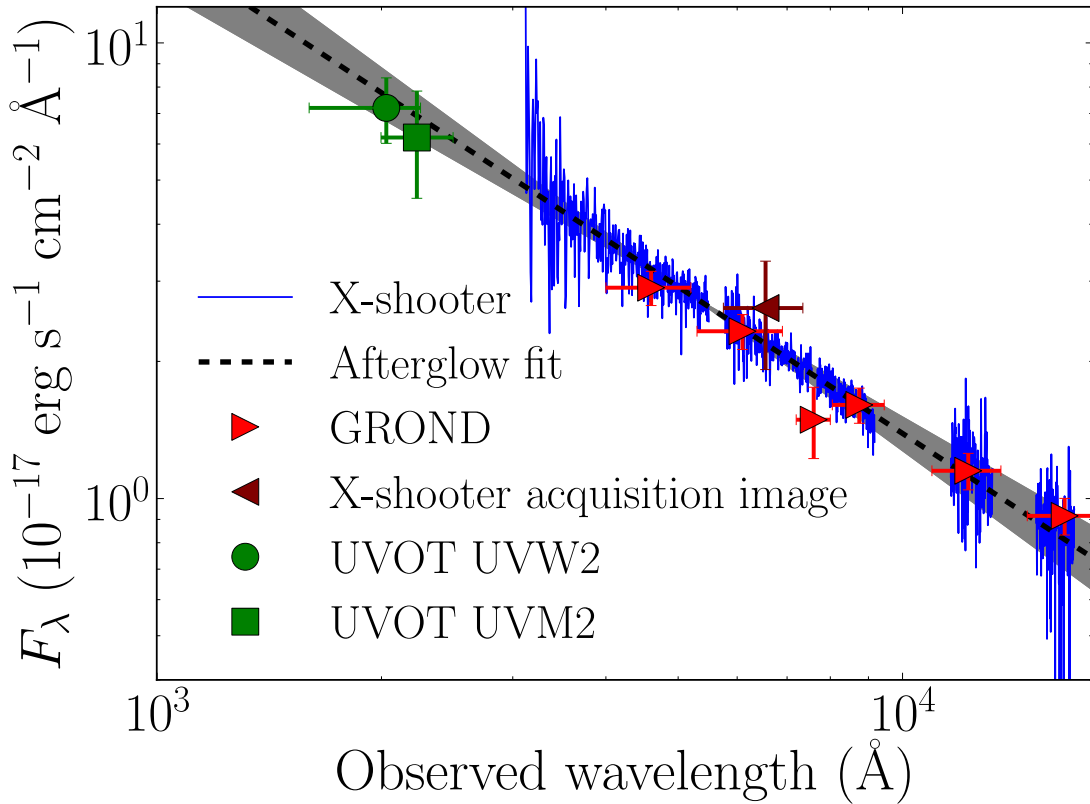


Figure 5.2: The first epoch spectrum, which was taken 11.6 hr after the burst, fitted with a power-law. Also shown are fluxes from imaging with GROND, *Swift*-UVOT, and our own acquisition image. The GROND-fluxes were used to fix the normalization of our spectrum. Regions dominated by atmospheric features and instrumental artifacts are excluded from the plot and from the fit. In the fit we excluded the NIR ($\lambda > 11,000 \text{ \AA}$), due to a possible systematic error in the offset between the flux-calibrated spectra in the VIS and in the NIR.

Table 5.2: Equivalent widths for the absorption features in the first epoch spectrum, both in the observer and rest frames. Limits are at 3σ .

Feature	$EW_{\text{obs}} (\text{\AA})$	$EW_{\text{rest}} (\text{\AA})$
FeII $\lambda 2586$	<0.96	<0.62
FeII $\lambda 2600$	<0.90	<0.58
MgII $\lambda 2796$	1.34 ± 0.25	0.86 ± 0.16
MgII $\lambda 2803$	0.98 ± 0.20	0.63 ± 0.13
MgI $\lambda 2852$	0.89 ± 0.18	0.57 ± 0.12

that $A_V < 0.1$ mag. The lack of excess X-ray absorption (Gelbord et al., 2010b) and the weakness of the absorption features (§ 5.3.5) are consistent with a tenuous host galaxy medium.

From the Gemini images obtained on Jan 29 and Jan 30 we infer the following limits and measurements of the source: $u > 24.5$, $g = 24.1 \pm 0.2$, $r = 23.7 \pm 0.2$, and $i = 23.8 \pm 0.2$. This corresponds to a monochromatic flux of about $9 \times 10^{-19} \text{ erg cm}^{-2} \text{ s}^{-1} \text{ \AA}^{-1}$ in the r band, consistent with the third epoch spectrum. It is not clear if this corresponds to the host galaxy alone or whether there is some contribution from the afterglow or the SN. To test how much such a contribution could affect the luminosity of the SN in the second epoch, we assumed as an upper limit that the host galaxy has a wavelength-independent flux corresponding to what is measured in the third epoch spectrum. To this value we added a faded afterglow and a contribution from SN 1998bw. In this way, the SN would be 30% fainter than assuming no host contamination. The host galaxy is thus unlikely to affect the conclusion that a luminous SN component is dominating our epoch 2 spectrum.

We have also searched the spectra for the strongest host galaxy emission lines. Unfortunately, at $z = 0.55185$ [OII] $\lambda 3727$ and $H\alpha$ fall in the transition regions between the UVB/VIS and VIS/NIR arms, respectively. However, [OIII] $\lambda 5007$ is located in a clear part of the spectrum. To derive an upper limit on the line flux we added artificial emission lines of increasing strength to the data, until the line was easily detectable. For [OIII] $\lambda 5007$ we find that an emission line of $3 \times 10^{-17} \text{ erg s}^{-1} \text{ cm}^{-2}$ would have been detected. At the redshift of the burst this corresponds to a luminosity of $L_{[\text{Oiii}]} = 4 \times 10^{40} \text{ erg s}^{-1}$. While this limit is not unprecedented (for example, the host galaxy of GRB 030329 has $L_{[\text{Oiii}]} = 3 \times 10^{40} \text{ erg s}^{-1}$; Hjorth et al. 2003), this value lies at the lower end of the distribution (Savaglio et al., 2009), consistent with a faint host galaxy.

5.3.5 Mg absorption in the host galaxy

Table 5.2 displays the equivalent widths of the absorption features in the first epoch spectrum. MgII $\lambda 2796$ is stronger than MgII $\lambda 2803$ and their ratio (1.37 ± 0.37) is consistent with the average value (1.16 ± 0.03) of the composite spectrum presented by Christensen et al. (2011). These lines are weaker than the ones of the typical GRB spectrum, but similar or even weaker cases have been seen before (e.g., GRB 050922C: Piranomonte et al. 2008; GRB 070125: Fynbo et al. 2009). The detection limits of iron lines are consistent with the weak magnesium features.

5.4 Discussion

In this paper we report on our detection of the spectral signature of a SN, SN 2010ma, in the fading afterglow spectrum of GRB 101219B.

The redshift was measured to be $z = 0.55185$ based on our detections of weak MgII absorption lines in the first epoch spectrum. At this redshift, a SN similar to SN 1998bw can well match our second epoch spectrum. The broad spectral features indicate high velocities in the expanding ejecta, whereas a normal SN Ib/c clearly does not match the observations. A SN interpretation is consistent with the drop at $\sim 5000 \text{ \AA}$ being due to UV blanketing in the SN spectra, where the UV part is instead dominated by the blue afterglow component. The host galaxy appears to be relatively faint, which likely contributed to obtain a clean signal from the supernova. There is little room for host galaxy extinction.

The GRB itself is clearly of long duration and has, at the measured redshift, an isotropic equivalent energy of $4.2 \times 10^{51} \text{ erg}$. It has a bright afterglow with a standard light curve, and obeys the $E_p - E_{\text{iso}}$ (“Amati”) relation (Amati et al., 2007). It is thus fully representative of the high-luminosity, routinely observed high-redshift population of GRBs, for which we now can provide a robust, spectroscopic association with a SN.

Since 4 out of the 5 previously unambiguously spectroscopically confirmed SN–GRBs were in fact rather low luminosity bursts with unusual afterglows and spectral properties, there have been suggestions in the literature (e.g., Kaneko et al., 2007) that the GRB–SN association is only proven for the local universe. Our new association favours a GRB–SN connection also for the main population of cosmological GRBs. This confirms previous observations of photometric bumps and tentative spectroscopic SN detections for distant bursts. In the recent compilation by Hjorth & Bloom (2011), the evidence for the SN association of GRB 101219B was graded just after the five ‘ironclad’ cases mentioned in § 1. The fact that we were able to see the SN component emerge over three epochs with the same instrumentation leaves little room for confusion by afterglow or host galaxy emission — also thanks to the faintness of the host. The X-shooter spectrograph will with no doubt continue to contribute to this area of research.

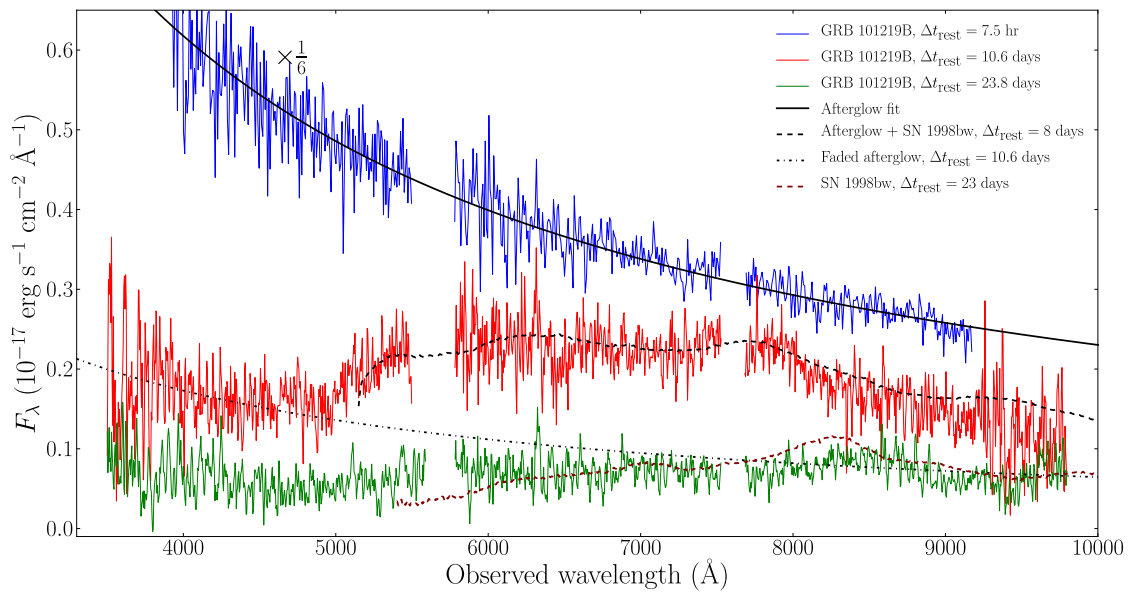


Figure 5.3: Three epochs of spectral observations. The second epoch is compared with a faded afterglow component and the flux from SN 1998bw (8 days after the explosion), multiplied by 1.4. In the third epoch the contributions from the faded afterglow and possible host galaxies are ignored, and the observations are compared to SN 1998bw alone. The flux of the first epoch has been divided by 6 for presentation purposes. The NIR spectra are not shown, because of their low signal-to-noise ratio in the second and the third epoch. Regions dominated by atmospheric and instrumental features are removed from the plot. The spectra are rebinned to a resolution of 0.8 \AA .

Bibliography

- Amati, L., Della Valle, M., Frontera, F., Malesani, D., Guidorzi, C., Montanari, E., & Pian, E. 2007, *A&A*, 463, 913
- Bufano, F., Benetti, S., Sollerman, J., Pian, E., & Cupani, G. 2011, *Astronomische Nachrichten*, 332, 262
- Cano, Z., et al. 2011, ArXiv: 1104.5141C
- Cano, Z., et al. 2011, *MNRAS*, 413, 669
- Cardelli, J. A., Clayton, G. C., & Mathis, J. S. 1989, *ApJ*, 345, 245
- Chornock, R., et al. 2010, ArXiv:1004.2262
- Christensen, L., Fynbo, J. P. U., Prochaska, J. X., Thöne, C. C., de Ugarte Postigo, A., & Jakobsson, P. 2011, *ApJ*, 727, 73
- Cummings, J. R., et al. 2010, GRB Coordinates Network, 11475
- de Ugarte Postigo, A., et al. 2011, GRB Coordinates Network, 11579
- Della Valle, M., et al. 2008, *Central Bureau Electronic Telegrams*, 1602, 1
- . 2003, *A&A*, 406, L33
- . 2006, *ApJ*, 642, L103
- D’Odorico, S., et al. 2006, in Presented at the Society of Photo-Optical Instrumentation Engineers (SPIE) Conference, Vol. 6269, Society of Photo-Optical Instrumentation Engineers (SPIE) Conference Series
- Evans, P. A., et al. 2009, *MNRAS*, 397, 1177
- Fynbo, J. P. U., et al. 2009, *ApJS*, 185, 526
- . 2004, *ApJ*, 609, 962
- Galama, T. J., et al. 1998, *Nature*, 395, 670
- Garnavich, P. M., et al. 2003, *ApJ*, 582, 924
- Gelbord, J., et al. 2010a, GRB Coordinates Network, 11473
- . 2010b, GRB Coordinates Network, 11481

- Goldoni, P., Royer, F., François, P., Horrobin, M., Blanc, G., Vernet, J., Modigliani, A., & Larsen, J. 2006, in Presented at the Society of Photo-Optical Instrumentation Engineers (SPIE) Conference, Vol. 6269, Society of Photo-Optical Instrumentation Engineers (SPIE) Conference Series
- Hamuy, M., et al. 1993, *AJ*, 106, 2392
- Hjorth, J., & Bloom, J. S. 2011, ArXiv e-prints [astro-ph/1104.2274](https://arxiv.org/abs/1104.2274)
- Hjorth, J., et al. 2003, *Nature*, 423, 847
- Jakobsson, P., Hjorth, J., Fynbo, J. P. U., Watson, D., Pedersen, K., Björnsson, G., & Gorosabel, J. 2004, *ApJ*, 617, L21
- Kaneko, Y., et al. 2007, *ApJ*, 654, 385
- Kouveliotou, C., Meegan, C. A., Fishman, G. J., Bhat, N. P., Briggs, M. S., Koshut, T. M., Paciesas, W. S., & Pendleton, G. N. 1993, *ApJ*, 413, L101
- Kuin, N., et al. 2010, GRB Coordinates Network, 11482
- Kuin, N., et al. 2011, GRB Coordinates Network, 11516
- Malesani, D., et al. 2004, *ApJ*, 609, L5
- Mazzali, P. A., et al. 2003, *ApJ*, 599, L95
- Modigliani, A., et al. 2010, in Society of Photo-Optical Instrumentation Engineers (SPIE) Conference Series, Vol. 7737, Society of Photo-Optical Instrumentation Engineers (SPIE) Conference Series
- Nysewander, M., Fruchter, A. S., & Pe'er, A. 2009, *ApJ*, 701, 824
- Olivares, F., et al. 2010, GRB Coordinates Network, 11478
- . 2011, GRB Coordinates Network, 11578
- Patat, F., et al. 2001, *ApJ*, 555, 900
- Pian, E., et al. 2006, *Nature*, 442, 1011
- Piranomonte, S., et al. 2008, *A&A*, 492, 775
- Savaglio, S., Glazebrook, K., & Le Borgne, D. 2009, *ApJ*, 691, 182
- Schlegel, D. J., Finkbeiner, D. P., & Davis, M. 1998, *ApJ*, 500, 525
- Sollerman, J., et al. 2006, *A&A*, 454, 503
- Sparre, M., Fynbo, J., de Ugarte Postigo, A., Malesani, D., & Sollerman, J. 2011, Central Bureau Electronic Telegrams, 2706, 1
- Stanek, K. Z., et al. 2003, *ApJ*, 591, L17
- Starling, R. L. C., et al. 2011, *MNRAS*, 411, 2792
- Tanvir, N. R., et al. 2010, *ApJ*, 725, 625

van der Horst, A., et al. 2010, GRB Coordinates Network, 11477

Vernet, J., et al. 2010, in Society of Photo-Optical Instrumentation Engineers (SPIE) Conference Series, Vol. 7735, Society of Photo-Optical Instrumentation Engineers (SPIE) Conference Series

Wosley, S. E., & Bloom, J. S. 2006, ARA&A, 44, 507

Zeh, A., Klose, S., & Hartmann, D. H. 2004, ApJ, 609, 952

Chapter 6

The X-ray afterglow of gamma-ray bursts

This chapter contains the following article:

A search for thermal X-ray signatures in Gamma-Ray Bursts II: The *Swift* sample

Published in Sparre & Starling 2012, MNRAS, 427, 2965

Authors: Martin Sparre & Rhaana L. C. Starling

Abstract

In several gamma-ray bursts (GRBs) excess emission, in addition to the standard synchrotron afterglow spectrum, has been discovered in the early time X-ray observations. It has been proposed that this excess comes from black body emission, which may be related to the shock break-out of a supernova in the GRBs progenitor star. This hypothesis is supported by the discovery of excess emission in several GRBs with an associated supernova. Using mock spectra we show that it is only likely to detect such a component, similar to the one proposed in GRB 101219B, at low redshift and in low absorption environments. We also perform a systematic search for black body components in all the GRBs observed with the *Swift* satellite and find six bursts (GRB 061021, 061110A, 081109, 090814A, 100621A and 110715A) with possible black body components. Under the assumption that their excess emission is due to a black body component we present radii, temperatures and luminosities of the emitting components. We also show that detection of black body components only is possible in a fraction of the *Swift* bursts.

6.1 Introduction

Gamma-ray bursts (GRBs) emit extreme amounts of γ -rays on a short time scale; typically $10^{50} - 10^{54}$ erg are released in 0.1 – 100 seconds. Only violent processes, such as a compact object merger or the collapse of a massive star, can explain these large energy releases,

which have made GRBs observable out to high redshifts of $z \approx 8 - 9$ (Tanvir et al., 2009; Salvaterra et al., 2009; Cucchiara et al., 2011).

There exists strong evidence, that the collapse of massive stars can produce long GRBs ($T_{90} > 2$ s; Kouveliotou et al., 1993), since spectroscopic features from supernovae (SNe) have been detected in optical follow-up observations of GRBs (e.g. Galama et al. (1998); Hjorth et al. (2003); Starling et al. (2011)). Also see review by Hjorth & Bloom (2011)). All these SNe are of type Ic with broad lines and no signs of Hydrogen or Helium. Besides these spectroscopic detections, evidence for SN Ic features is also found in light curves of some GRBs (Patat et al., 2001; Lipkin et al., 2004; Cobb et al., 2010; Cano et al., 2011).

One burst of particular interest was GRB 060218 (Soderberg et al., 2006; Mazzali et al., 2006). It had an associated supernova (Pian et al., 2006), and its X-ray afterglow could best be described by a combination of synchrotron emission, which is usual for afterglows, and black body emission (Campana et al., 2006). Waxman et al. (2007) showed that this black body emission could origin in a shock generated by the breakout of a supernova through the surface of the GRBs progenitor star. Subsequently, thermal X-ray emission which may be described by a black body has been suggested in GRB 090618, GRB 100316D and GRB 101219B, which all have associated SNe (Page et al. (2011), Starling et al. (2011), Starling et al. (2012), respectively. See also Starling et al. (2012)). This supports the connection of the black body component with emission from a supernova. Deviations from a single power law in the early X-ray spectra in GRBs, was also found by Butler (2007), who identified a soft emission component in 5 – 10 % of the bursts in the studied sample.

In this series of papers, we search for more bursts with X-ray black body components, and derive the conditions under which such components may be reliably recovered. In Paper I (Starling et al., 2012) black body components were identified in bursts with spectroscopic or photometric signatures in the optical. The aim of this paper is to perform a systematic search for more bursts with X-ray black body components in the *Swift* sample, and to derive the conditions under which such components may be reliably recovered. In Section 2 the sample and model fitting are described, and in Section 3 we create simulated spectra to set constraints on the detectability of black body components. In Section 4 bursts are selected as candidates for having black body emission, and Section 5 presents and discusses the final list of candidates. Section 6 extracts physical parameters, assuming that the excess emission is black body emission, and the fraction of GRBs with probable excess emission is examined.

For the cosmological calculations we assume a Λ CDM-universe with $h_0 = 0.71$, $\Omega_m = 0.27$, and $\Omega_\Lambda = 0.73$. All stated errors and error bars are 90% confident. In the plots n_H is in units of 10^{22} cm^{-2} unless stated otherwise. We will use the words *thermal components* and *black body components* interchangeably.

6.2 Fitting models with black body components to a sample of GRBs

6.2.1 A sample of *Swift* bursts

The sample, in which we will search for X-ray black body components, consists of the GRBs observed with the Swift XRT (Burrows et al., 2005), where redshifts are determined with optical spectroscopy, or simultaneous multi-band photometry, as obtained from the GROND-instrument (Krühler et al., 2011a). Furthermore we only select bursts, where

Table 6.1: The parameters in the four fitting models (M1-M4). It is shown whether a parameter is free (if marked as *free*), fixed (*fixed*), not included (-) or fitted to the late time spectrum (*late fit*).

	Description	M1	M2	M3	M4
z	Redshift of the GRB	fixed	fixed	fixed	fixed
$n_{\text{H,gal}}$	Galactic column density	fixed	fixed	fixed	fixed
$n_{\text{H,int}}$ or n_{H}	Intrinsic column density in the GRB host galaxy	free	free	late fit	late fit
Γ	Photon index, defined as $F_E \propto E^{-\Gamma}$ (F_E is flux)	free	free	free	free
F_{PL}	Flux of the power law component of the afterglow in a 0.3 – 10 keV band	free	free	free	free
kT	Black body temperature (in the rest frame of the burst)	-	free	-	free
F_{BB}	Flux of the black body emission in a 0.3 – 10 keV band	-	free	-	free

Windowed Timing mode (WT mode) observations exist, since this assures that data were taken shortly after the trigger. The sample consists of 190 bursts with the most recent burst from August 8th 2011.

We used the publicly available¹ WT mode data, see Evans et al. (2009). Note, that the sample also includes bursts not triggered by *Swift*. We make use of the time-averaged WT mode spectra, which have all been created in the same manner according to Evans et al. (2009) and using the *Swift* software version 3.8 and the latest calibration data.

6.2.2 Spectral modelling

In order to identify black body emission for a burst, it is necessary to understand the interplay between all contributing components in the observed spectrum: the afterglow continuum, the black body emission and the absorption of the source emission by gas in the line-of-sight within the host galaxy and the Galaxy. These properties can be parametrised by the seven parameters in Table 6.1. Note, that not all parameters are free: in our sample the redshift of each burst is known, and the Galactic column density can, in most cases, be determined to within $\pm 5\%$ (Kalberla et al., 2005).

For each burst we fitted four different models to the WT spectrum. These models are also shown in Table 6.1. Model 1 (M1) is an absorbed power law, whereas Model 2 (M2) also includes black body emission at the redshift of the bursts. Model 3 and 4 (M3 and M4) are similar to Model 1 and 2, with the only difference, that $n_{\text{H,int}}$ is fitted to the late-time Photon Counting mode spectrum, which we expect to be free from additional components and therefore a reliable measure of any absorbing column, instead of from the early-time (WT) spectrum itself. The atomic data used are Solar abundances from Wilms et al. (2000) and cross-sections from Verner et al. (1996).

For all the WT spectra we group the spectra in 20 counts per bin and perform a χ^2 -fit. For the late time observations, used to determine $n_{\text{H,int}}$ in Model 3 and 4, ungrouped spectra are fitted with Cash statistics Cash (1979).

¹Website for XRT data: <http://www.swift.ac.uk/>

6.2.3 Selecting candidates with the F-test

The F-test (e.g.; Lampton et al., 1976) is a statistical test, which gives the probability that an improvement in the reduced χ^2 , with the inclusion of extra parameters, is due to an improvement in the fitting model. To test whether a black body component is present in a spectrum, we therefore use the F-test to compare Model 1 and 2 and Model 3 and 4. Protassov et al. (2002) showed, that the F-test is not a stringent test, but in the following section we will explicitly show, that the F-test in many cases is sufficient to recover black body components, when they are present. In Section 6.4 we will select the candidates.

6.3 Recovering a black body component in mock spectra of GRB 101219B

In Section 6.4 it will be found, that one of the candidates for having a black body component is GRB 101219B with a temperature of 0.22 keV in the Model 2 fit (see Section 6.4 and Table 6.2). This value is consistent with the value found in Paper I. With a redshift of $z = 0.55$ (de Ugarte Postigo et al., 2011) GRB 101219B is one of the most distant GRBs with a spectroscopically detected supernova (Sparre et al., 2011). Now mock spectra will be used to derive the range of column densities, redshifts and afterglow parameters for which a detection of the black body component is possible, and we will use this information to refine our candidate list.

6.3.1 The role of column densities

To reveal the role of the column densities, the F-test significances of the black body detections are calculated for several 101219B-like mock spectra with n_H -values varying from 0.0 to $0.8 \times 10^{22} \text{ cm}^{-2}$. The other parameters used to create the mock spectra are identical to the recovered value in the fit of Model 2 from the real data.

The *left panel* in Figure 6.1 shows how the F-test significance (calculated from Model 1 and 2) depends on the n_H -value used to generate the mock spectra. If the F-test significance is lower than 10^{-4} we will say that Model 2 is favoured over Model 1 (i.e. the presence of a black body component is favoured). The *central* and the *right panel* show the n_H and kT recovered by the fits of the same mock spectra. When the n_H used to generate the mock data is larger than $0.4 \times 10^{22} \text{ cm}^{-2}$, the n_H recovered by the fit is often too small, and in most cases a temperature with a large error is recovered. For $n_H < 0.4 \times 10^{22} \text{ cm}^{-2}$ the F-test favours the existence of a black body component, and correct kT and n_H -values are recovered within their errors.

Similar mock spectra without black body components were also made, and no significant detections of black body components were favoured by the F-test.

Fixing n_H to the late time spectrum

For the fits of the real data the n_H -values in Model 3 and 4 are fixed to the fitted value from the late time spectrum. Now it will explicitly be shown, that this method might lead to significant black body detections for spectra with no real black body components, when n_H is fixed to a too large value.

First spectra with photon indices and power law normalizations identical to GRB 101219B are generated, but with n_H varying from 0 to $0.8 \times 10^{22} \text{ cm}^{-2}$. All the spectra are gener-

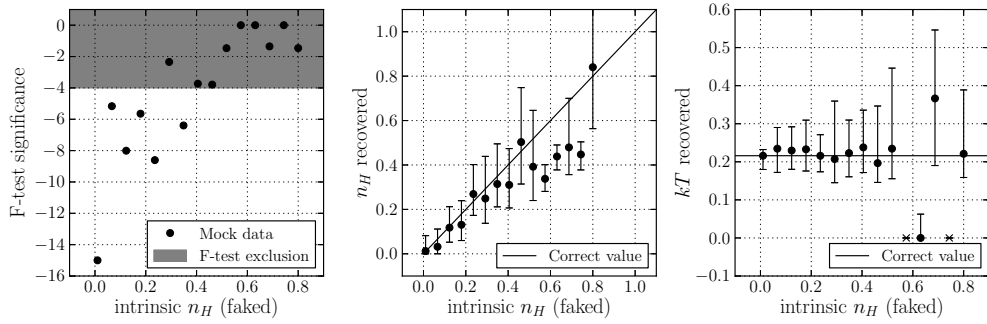


Figure 6.1: *Left:* The F-test significance of the recovery of a 101219B-like black body component as function of n_H (in units of 10^{22} cm^{-2}). *Central:* The n_H -value recovered (in the Model 2 fit) as function of the correct n_H . *Right:* The recovered temperature (in keV).

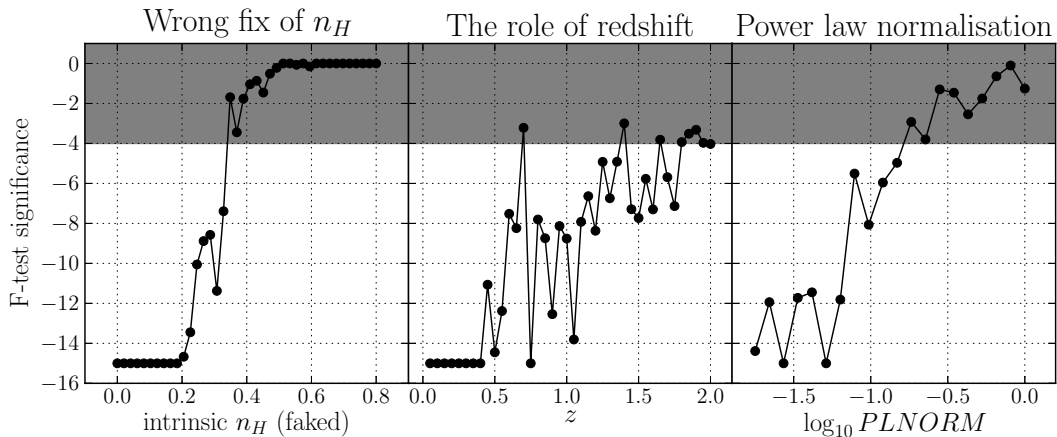


Figure 6.2: *Left:* In the fits the n_H -value is fixed to $0.5 \times 10^{22} \text{ cm}^{-2}$, which is different from the n_H used to generate the spectra, shown as abscissa. Spurious detections appear, when n_H is fixed to a too large value. *Central:* The F-test significance as function of z for a GRB 101219B-like burst. *Right:* The role of the power law normalization (in arbitrary units).

ated without black body components. In the fitting function n_H is fixed to $0.5 \times 10^{22} \text{ cm}^{-2}$ for all the spectra, just like if this value had come from the fit of a late time spectrum. In Figure 6.2 (*left panel*) it is shown that the F-test favours a black body component when $n_H \lesssim 0.35 \times 10^{22} \text{ cm}^{-2}$. All the recovered black body components had temperatures between 0.08 keV and 0.2 keV. We conclude that, if n_H is fixed to a value $\sim 0.15 \times 10^{22} \text{ cm}^{-2}$ larger than the real value, a spurious black body component will compensate for the flux lost due to the high column density absorption parameter.

A side result of this analysis is that typical Galactic column densities can not lead to spurious detections of black body components. $n_{H,gal}$ is typically of order $\sim 0.05 \times 10^{22} \text{ cm}^{-2}$ with a 10 per cent error (Kalberla et al., 2005), which is well below the critical value of $0.15 \times 10^{22} \text{ cm}^{-2}$ found above.

6.3.2 Redshift and afterglow parameters

To find the redshifts for which it is possible to observe a GRB 101219B-like black body component, simulations like those in Section 6.3.1 are performed, with the only difference that z is varied instead of n_H . Figure 6.2 (*central panel*) shows, that black body components

are recovered with F-test significances $\lesssim 10^{-8}$ when $z < 1$. For $1 < z < 2$ the significance of the detections are lowered by several orders of magnitudes.

The role of the parameters describing the synchrotron emission from the afterglow will now be quantified. First we fix the photon index to the GRB 101219B-value and simulate spectra with power law normalizations covering the values observed in our sample. The resulting F-test significances of our fits are shown in Figure 6.2 (*right panel*). A low normalization constant is essential in order not to dilute the signal from the black body component with noise from the afterglow emission. We also fitted simulated spectra with a fixed normalisation and a varying photon index, see Figure 6.3. A trend in the complicated pattern is that GRB 101219B-like black bodies are most likely to be detected with low photon indices.

6.4 Selecting Candidates

Now we will start searching for candidates with black body components in our sample. The bursts with F-test probabilities lower than 0.005 in the Model 1-2 comparison or the Model 3-4 comparison were selected. For now, we are only interested in making an initial list of candidates, which will be refined later. We are therefore using a looser F-test significance threshold here than in Section 6.3 (a limit of 0.005 is now used instead of 10^{-4}). The selected candidates are listed in Table 6.2.

6.4.1 Ruling out candidates with uncertain n_H

It is important to understand the contribution of n_H in order to make a reliable detection of a black body component. We therefore removed all bursts with a 90% error on n_H larger than $0.4 \times 10^{22} \text{ cm}^{-2}$ for Model 2 or larger than $0.8 \times 10^{22} \text{ cm}^{-2}$ for Model 4. A lower threshold was chosen for Model 2, so candidates with a degenerate n_H -value were excluded. In Table 6.2 a burst is marked with *uncertain n_H* , if it is excluded due to this criterion. The analysis was done for larger values of the thresholds, but it did not lead to the detection of more candidates in the refined analysis, which will be presented in Section 6.4.3 and 6.4.4.

Table 6.2: The initial candidates for having a black body component. Candidates with $z > 3$ are omitted. The F-test significances are marked as **bold** if the burst is a candidate in the given model. If the recovered n_H is too uncertain the burst is marked with "unc. n_H " (see Section 6.4.1 for details).

GRB	z	F-stat (M1-2)	F-stat (M3-4)	kT (M2)	kT (M4)	n_H (M2)	n_H (M4, fixed)	Note
050724	0.257	2.1×10^{-7}	overflow	0.9 ± 0.1	underflow	0.33 ± 0.06	0.2 ± 0.1	
050820A	2.6147	1.0×10^{-7}	overflow	$0.4^{+3.6}_{-0.4}$	underflow	0^{+20}_{-0}	$0.00^{+0.09}_{-0.00}$	unc. n_H High- z
060124	2.3	0.041	3.4×10^{-8}	0.6 ± 0.1	0.46 ± 0.07	0.6 ± 0.1	0.8 ± 0.2	High- z
060202	0.783	4.2×10^{-6}	4.3×10^{-14}	$0.38^{+0.06}_{-0.05}$	0.34 ± 0.03	1.6 ± 0.1	1.7 ± 0.2	
060218	0.0331	1.0×10^{-174}	9.6×10^{-110}	0.123 ± 0.002	0.186 ± 0.002	0.76 ± 0.02	0.40 ± 0.04	
060418	1.49	3.0×10^{-6}	overflow	0.61 ± 0.05	$0.00^{+0.03}_{-0.00}$	0.5 ± 0.1	$0.2^{+0.3}_{-0.2}$	
060502A	1.5026	5.6×10^{-5}	4.7×10^{-5}	0.35 ± 0.04	0.31 ± 0.02	0.4 ± 0.2	0.5 ± 0.2	unc. n_H (M2 only)
060604	2.68	0.16	2.1×10^{-9}	$0.15^{+0.09}_{-0.02}$	$1.6^{+0.3}_{-0.2}$	$2.2^{+0.7}_{-0.4}$	1.1 ± 0.3	High- z
060714	2.7108	0.27	2.0×10^{-9}	$0.24^{+0.06}_{-0.11}$	1.9 ± 0.3	3.0 ± 1.1	$1.1^{+0.6}_{-0.5}$	unc. n_H High- z
060904B	0.7029	0.0014	1.0	$0.29^{+0.06}_{-0.05}$	$0.00^{+0.05}_{-0.00}$	$0.53^{+0.07}_{-0.06}$	0.4 ± 0.1	
061021	0.3463	2.9×10^{-7}	3.2×10^{-15}	$0.12^{+0.03}_{-0.02}$	0.12 ± 0.01	$0.08^{+0.13}_{-0.08}$	0.08 ± 0.02	
061110A	0.7578	6.5×10^{-11}	0.00019	0.32 ± 0.02	overflow	0.14 ± 0.04	$0.3^{+0.4}_{-0.3}$	
061121	1.3145	1.5×10^{-8}	1.1×10^{-9}	0.50 ± 0.06	0.45 ± 0.03	0.5 ± 0.1	0.61 ± 0.08	
070318	0.8397	0.0075	9.9×10^{-11}	0.3 ± 0.1	0.24 ± 0.04	$0.6^{+0.2}_{-0.1}$	0.8 ± 0.1	
070419A	0.9705	0.17	1.2×10^{-7}	0.4 ± 0.1	0.18 ± 0.04	0.5 ± 0.1	$0.8^{+1.7}_{-0.8}$	unc. n_H
070508	0.82	1.0×10^{-5}	0.074	$0.066^{+0.002}_{-0.004}$	$0.030^{+0.002}_{-0.001}$	$1.12^{+0.09}_{-0.07}$	0.6 ± 0.2	
070724A	0.457	0.15	0.0014	$0.15^{+0.10}_{-0.04}$	$0.8^{+0.2}_{-0.1}$	1.0 ± 0.5	$0.1^{+0.3}_{-0.1}$	
071031	2.6918	6.1×10^{-9}	8.4×10^{-67}	$2.1^{+0.4}_{-0.3}$	1.44 ± 0.06	0.9 ± 0.1	$0.0^{+0.7}_{-0.0}$	High- z
071112C	0.8227	0.00011	0.00013	$0.40^{+0.06}_{-0.07}$	$0.37^{+0.03}_{-0.04}$	$0.08^{+0.08}_{-0.07}$	$0.1^{+0.2}_{-0.1}$	
080210	2.6419	0.10	0.0020	$1.0^{+0.3}_{-0.2}$	$1.0^{+0.3}_{-0.2}$	$1.0^{+1.2}_{-1.0}$	$1.5^{+0.8}_{-0.7}$	unc. n_H High- z
080310	2.4274	0.052	1.7×10^{-22}	$2.0^{+1.1}_{-0.7}$	1.3 ± 0.1	$0.63^{+0.07}_{-0.09}$	$0.4^{+0.3}_{-0.2}$	High- z
080319B	0.9382	1.4×10^{-25}	1.0	$1.02^{+0.08}_{-0.07}$	underflow	0.12 ± 0.01	$0.08^{+0.04}_{-0.03}$	
080413A	2.433	0.27	2.0×10^{-7}	$0.14^{+0.04}_{-0.03}$	1.0 \pm 0.1	$2.8^{+0.9}_{-1.0}$	$0.5^{+1.0}_{-0.5}$	unc. n_H High- z
080430	0.767	0.00020	3.3×10^{-5}	0.24 ± 0.06	0.21 ± 0.03	$0.3^{+0.3}_{-0.1}$	0.36 ± 0.06	
080603B	2.6892	0.042	2.8×10^{-13}	$1.7^{+0.6}_{-0.3}$	$1.6^{+0.2}_{-0.1}$	0.8 ± 0.3	$0.2^{+0.6}_{-0.2}$	unc. n_H High- z
080604	1.4171	0.0010	3.0×10^{-6}	$0.34^{+0.06}_{-0.10}$	0.28 ± 0.04	$0.04^{+0.21}_{-0.04}$	$0.2^{+0.5}_{-0.2}$	

(continues on next page)

(continued from previous page)

GRB	z	F-stat (M1-2)	F-stat (M3-4)	kT (M2)	kT (M4)	n_H (M2)	n_H (M4, fixed)	Note
080605	1.6403	0.00011	0.84	$0.087^{+0.020}_{-0.006}$	$0.04^{+0.09}_{-0.04}$	$1.2^{+0.2}_{-0.1}$	0.6 ± 0.3	
080721	2.5914	2.6×10^{-10}	5.3×10^{-51}	$0.21^{+0.01}_{-0.02}$	2.0 ± 0.1	2.2 ± 0.3	0.5 ± 0.2	unc. n_H High- z
080805	1.5042	0.38	1.1×10^{-7}	$0.06^{+0.05}_{-0.02}$	0.27 ± 0.05	$0.65^{+0.16}_{-0.07}$	1.2 ± 0.5	unc. n_H
080928	1.6919	2.9×10^{-5}	overflow	$1.7^{+0.4}_{-0.3}$	underflow	0.5 ± 0.1	0.3 ± 0.1	
081007	0.5295	0.0016	0.00032	$0.20^{+0.07}_{-0.05}$	0.30 ± 0.03	$0.8^{+0.3}_{-0.2}$	0.5 ± 0.1	unc. n_H (M2 only)
081008	1.967	0.057	6.7×10^{-33}	2.1 ± 0.8	$1.19^{+0.08}_{-0.07}$	0.9 ± 0.1	0.3 ± 0.3	
081109	0.9787	0.047	1.0×10^{-5}	$1.0^{+0.3}_{-0.2}$	0.13 ± 0.04	0.5 ± 0.1	1.0 ± 0.2	
081203A	2.05	0.00073	0.053	0.5 ± 0.08	overflow	1.4 ± 0.5	2^{+2}_{-1}	unc. n_H High- z
081222	2.77	0.086	2.9×10^{-5}	$0.16^{+0.05}_{-0.07}$	$1.3^{+0.3}_{-0.2}$	$1.0^{+0.4}_{-0.3}$	0.4 ± 0.2	High- z
081230	2.03	0.12	0.00023	$2.8^{+0.7}_{-1.0}$	1.5 ± 0.4	$0.8^{+0.4}_{-0.3}$	0.2 ± 0.2	High- z
090418A	1.608	0.062	8.3×10^{-5}	0.5 ± 0.2	0.27 ± 0.09	$0.5^{+0.6}_{-0.3}$	1.1 ± 0.2	
090424	0.544	0.0041	0.0042	$1.5^{+0.2}_{-0.3}$	1.3 ± 0.2	$0.44^{+0.03}_{-0.02}$	0.42 ± 0.06	
090618	0.54	0.00026	4.1×10^{-6}	1.9 ± 0.2	$0.38^{+0.04}_{-0.03}$	0.26 ± 0.02	0.19 ± 0.02	
090809	2.737	0.020	4.3×10^{-7}	0.21 ± 0.03	2.1 ± 0.3	6 ± 1	0.6 ± 0.3	High- z
090812	2.452	1.5×10^{-5}	1.9×10^{-8}	$1.5^{+0.5}_{-0.2}$	0.10 ± 0.02	$0.8^{+0.2}_{-0.1}$	$1.2^{+0.7}_{-0.6}$	High- z
090814A	0.696	1.6×10^{-10}	1.3×10^{-10}	0.28 ± 0.03	0.26 ± 0.01	0.14 ± 0.06	$0.2^{+0.3}_{-0.2}$	
090926B	1.24	2.9×10^{-9}	1.8×10^{-9}	0.53 ± 0.07	0.52 ± 0.04	$1.5^{+0.3}_{-0.2}$	$1.5^{+1.2}_{-0.8}$	unc. n_H
091029	2.752	2.0×10^{-5}	0.0054	$0.38^{+0.08}_{-0.07}$	overflow	$1.0^{+0.7}_{-0.5}$	0.5 ± 0.2	unc. n_H High- z
100117A	0.92	0.0055	1.7×10^{-10}	$1.2^{+0.4}_{-0.2}$	0.09 ± 0.2	0.2 ± 0.2	$2.2^{+1.6}_{-1.2}$	unc. n_H
100418A	0.6235	0.00074	2.3×10^{-11}	$0.21^{+0.03}_{-0.04}$	0.24 ± 0.01	0.2 ± 0.1	$0.1^{+0.4}_{-0.1}$	
100621A	0.542	0.00011	2.7×10^{-5}	$0.48^{+0.05}_{-0.06}$	$0.29^{+0.03}_{-0.04}$	1.4 ± 0.2	2.0 ± 0.2	
101219B	0.55	2.2×10^{-13}	3.9×10^{-27}	0.22 ± 0.03	0.20 ± 0.1	$0.06^{+0.06}_{-0.05}$	0.1 ± 0.1	
110205A	2.22	0.021	4.7×10^{-10}	3 ± 1	$1.6^{+0.3}_{-0.2}$	$0.54^{+0.08}_{-0.10}$	0.4 ± 0.1	High- z
110715A	0.82	0.40	6.6×10^{-6}	$0.15^{+0.06}_{-0.08}$	$0.15^{+0.04}_{-0.03}$	1.0 ± 0.4	1.3 ± 0.3	
110731A	2.83	0.22	0.0049	$0.12^{+0.07}_{-0.04}$	$1.7^{+0.6}_{-0.5}$	1.8 ± 0.3	$1.1^{+0.7}_{-0.6}$	unc. n_H High- z
110808A	1.348	0.0017	0.00068	0.29 ± 0.07	$0.22^{+0.02}_{-0.03}$	$0.2^{+0.3}_{-0.2}$	$0.6^{+0.4}_{-0.3}$	unc. n_H

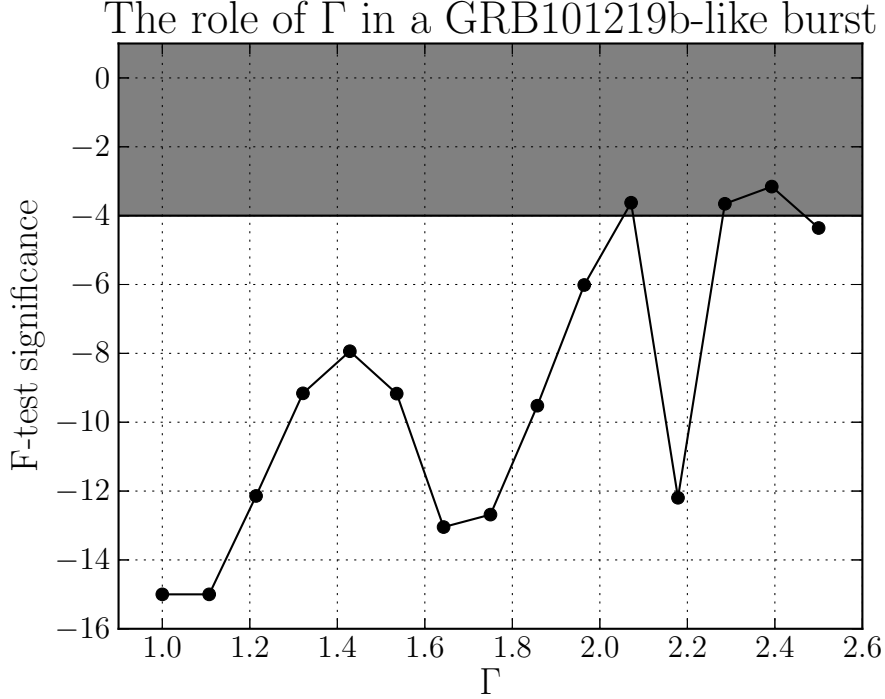


Figure 6.3: The F-test significance as function of the photon index.

6.4.2 Candidates at high and low redshift

The high-redshift candidates ($z > 2$)

For $z > 2$ GRB 101219B-like black body components are difficult to detect (see Section 6.3.2 and Figure 6.2). A number of candidates with $z > 2$ have, however, emerged in our analysis. They typically exhibit high temperatures ($kT \gtrsim 1$ keV), which is much higher than most previously claimed examples (e.g.; Campana et al., 2006; Starling et al., 2011). They also have an uncertain n_H , which increases the risk of a spurious detection.

At low redshift (e.g. $z < 1$), only a few candidates have temperatures larger than 1 keV, even though a detection of such a black body component is expected to be easier at lower redshift. The high-redshift candidates are therefore unlikely to represent real black bodies, and they will not be examined further in this work.

The low-redshift candidates ($z < 2$)

Three of the candidates, GRB 060218, GRB 090618 and GRB 101219B, already have identified black body components in other studies, and they also have a spectroscopically confirmed SN in the optical. Among our candidates is also GRB 100418A, which also has a SN in the optical (de Ugarte Postigo et al. in prep.). Paper I studied the early X-ray spectrum of GRB 100418, and also find that a model with a powerlaw and a black body model can give a good fit. However, they cannot rule out an absorbed power law model given the large uncertainty on the intrinsic absorbing column of this GRB host, which may be higher than the limit for detectability we find in Section 6.3.1 of $0.4 \times 10^{22} \text{ cm}^{-2}$. Paper I also studied GRB 081007, and found an indication of a black body component, but no conclusive evidence.

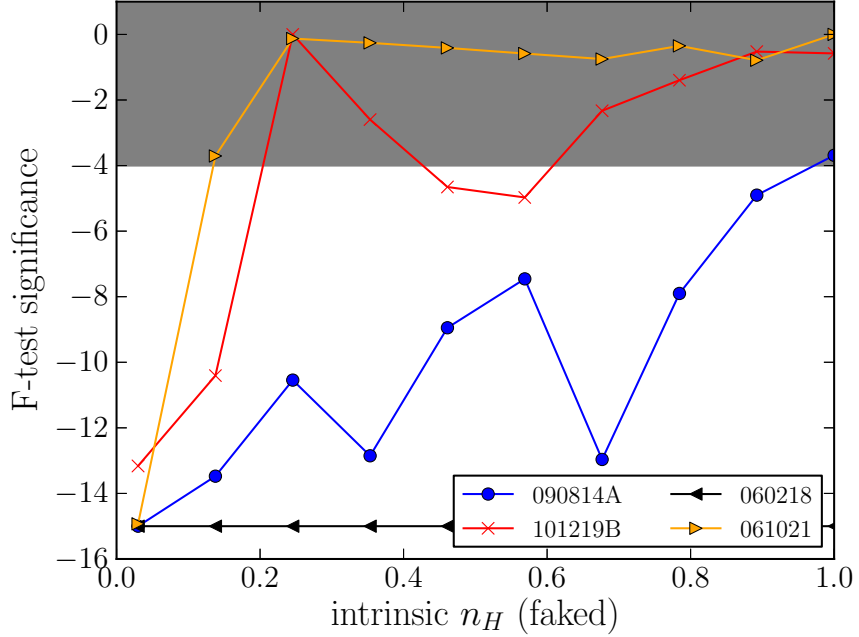


Figure 6.4: Same as Figure 6.1 (left), but with three additional bursts.

At first sight it is worrying, that GRB 100316D, which Starling et al. (2011) showed had an excess black body emission, is not among our candidates. An examination of this burst shows, that it is not selected due to a F-test value of 0.007 (for the Model 1-2 comparison), which is slightly above our threshold of 0.005 defined in Section 6.2.3. It is therefore clear that our candidate selection algorithm will not find all bursts with black body components (discussed further in Section 6.6.1).

Figure 6.4 and 6.5 show how the F-test significances of the black body component detections in a selection of our low redshift candidates depend on column density and redshift. In general the same trends found for GRB 101219B above applies for both GRB 090814A and GRB 061021. A black body component, similar to the one present in GRB 060218, is expected to be detectable at high redshifts (e.g. $z \gtrsim 2$).

6.4.3 Approach I: Fitting with 5 free parameters

The final step in our selection procedure is to do a time sliced analysis of the remaining candidates, i.e. those without remarks in Table 6.2. In this section we will focus on the candidates selected in the comparison between Model 1 and 2. In Section 6.4.4 we will fit and analyse the candidates selected with Model 3 and 4.

For each of the candidates, where Model 2 is favoured by the F-test, we manually inspected the light curves, and selected time intervals, where the light curves exhibit a single power law decay. We especially tried to avoid time intervals with flares and plateaus.

To each time sliced spectrum all the models were fit, see a summary of the fits in Table 6.3. Several candidates with no flare-free epochs are excluded from the table. The candidates with excess emission are GRB 061021, GRB 061110A and GRB 090814A. They have low column densities ($n_H < 0.3 \times 10^{22} \text{ cm}^{-2}$) for both Model 2, where the n_H is a

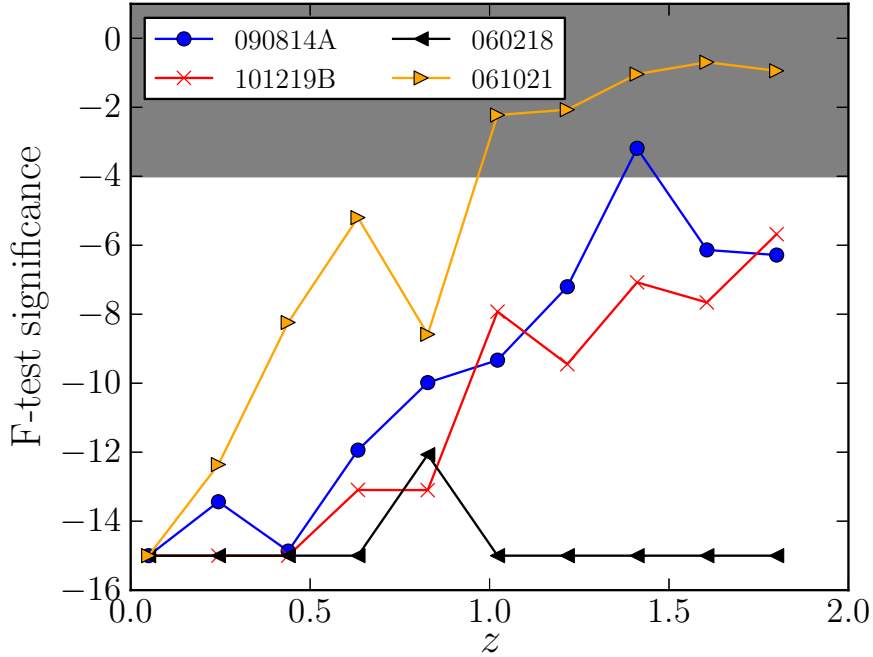


Figure 6.5: Same as Figure 6.2 (central), but with three additional bursts.

free parameter, and Model 4, where n_H is fitted with the late time spectrum. In all the fits the presence of a black body component is favoured by the F-test with significances from 0.0005 to 2.4×10^{-13} . The temperatures are between 0.1 and 0.3 keV, which is consistent with claimed black body components in other studies.

In Table 6.3, some bursts are also listed as candidates with some caveats. These are GRB 100621A (because it has a F-test significance of 0.00144, and a large n_H), GRB 061121 (it has large kT and z , and the F-test does not favour a black body component in Model 3 and 4) and GRB 050724 (it has an unexpectedly high kT). We note that GRB 050724 has been classified as a short burst with extended emission (Barthelmy et al., 2005), so its origins may not lie in the collapse of a massive star as is the case for the rest of our sample which are all long GRBs.

6.4.4 Approach II: Breaking N_H -degeneracies with the late time spectrum

The three bursts, which were candidates for having black body components in the previous subsection, all have low column densities $n_H < 0.3 \times 10^{22} \text{ cm}^{-2}$. This is expected from Figure 6.4 which showed, that it is hard to recover a black body component at large n_H , when it is fitted as a free parameter (as in Model 1 and 2).

We will now do a new search for black body components, where we use the the late time spectrum to fit n_H , i.e. use Model 3 and 4. This method can break the degeneracies between n_H and the other parameters, but it also has the disadvantage that a spurious black body component can be found if a too high value of n_H is recovered in the late time spectrum (see Section 6.3.1).

We fitted Model 3 and 4 to the candidates. Table 6.4 summarizes the fits. Several of the candidates are not shown in the table, since they have complex and bumpy light curves,

or too little data to extract a good spectrum.

Several bursts have favourable F-test significances. To explicitly check whether the fixing of n_H might have caused spurious black body detections, we made additional fits, where n_H was fixed to a range of different values within the 90% confidence intervals recovered in the late time fits. Figure 6.6 shows how the significances of the detections depend on the value to which n_H is fixed. The detection is not robust for GRB 060202 and GRB 061121 because of degeneracies between kT and n_H from the late time spectrum. The list of candidates from the Model 3 to 4 comparison consists of GRB 061021, 061110A, 081109, 090814A, 100621A and 110715A.

Table 6.3: The time sliced fits from Section 6.4.3, where bursts are selected with Model 1 and 2. Three reliably detected black body components are found.

Candidates with probable excess emission:								
GRB	z	Time	F-test M1-2	F-test M3-4	kT (M2)	kT (M4)	n_H (M2)	n_H (M4, fixed)
061021	0.3663	87 – 170	3.1×10^{-7}	2.4×10^{-13}	$0.13^{+0.03}_{-0.02}$	0.13 ± 0.01	$0.08^{+0.13}_{-0.08}$	0.08 ± 0.02
061110A	0.7578	180 – 240	2.5×10^{-6}	0.00050	0.25 ± 0.01	0.19 ± 0.01	$0.00^{+0.07}_{-0.00}$	$0.3^{+0.3}_{-0.2}$
090814A	0.696	166 – 265	4.0×10^{-7}	2.2×10^{-9}	0.32 ± 0.03	0.30 ± 0.01	0.12 ± 0.06	$0.2^{+0.3}_{-0.2}$
090814A	0.696	265 – 390	1.1×10^{-6}	2.1×10^{-8}	$0.19^{+0.05}_{-0.04}$	0.20 ± 0.02	$0.2^{+0.2}_{-0.1}$	$0.2^{+0.3}_{-0.2}$
Candidates with some caveats:								
GRB	z	Time	F-test M1-2	F-test M3-4	kT (M2)	kT (M4)	n_H (M2)	n_H (M4, fixed)
050724	0.257	100 – 190	1.3×10^{-6}	–	0.9 ± 0.1	–	0.36 ± 0.09	0.2 ± 0.1
061121	1.3145	125 – 215	1.1×10^{-5}	1	$0.44^{+0.05}_{-0.06}$	$0.0^{+0.1}_{-0.0}$	0.6 ± 0.1	0.61 ± 0.07
100621A	0.542	80 – 120	0.022	0.86	$0.69^{+0.06}_{-0.07}$	0.05 ± 0.05	$1.4^{+0.6}_{-0.3}$	2.0 ± 0.2
100621A	0.542	190 – 230	0.0014	6.0×10^{-7}	0.33 ± 0.06	0.25 ± 0.03	$1.3^{+0.4}_{-0.3}$	2.0 ± 0.2
Candidates where a black body component is not favoured:								
GRB	z	Time	F-test M1-2	F-test M3-4	kT (M2)	kT (M4)	n_H (M2)	n_H (M4, fixed)
060202	0.783	148 – 303	0.0023	0.12	$0.42^{+0.07}_{-0.06}$	$0.045^{+0.003}_{-0.002}$	1.6 ± 0.1	1.7 ± 0.2
060202	0.783	745 – 1000	0.28	0.0058	overflow	$0.25^{+0.08}_{-0.06}$	1.6 ± 0.2	1.7 ± 0.2
060418	1.49	240 – 450	0.29	0.20	0.6 ± 0.2	$0.6^{+0.2}_{-0.1}$	0.2 ± 0.2	$0.2^{+0.3}_{-0.2}$
070508	0.82	200 – 500	0.19	0.17	$0.06^{+0.09}_{-0.02}$	0.031 ± 0.002	$1.0^{+0.3}_{-0.1}$	0.6 ± 0.2
070508	0.82	500 – 1000	0.055	0.33	$1.0^{+0.8}_{-0.2}$	$0.030^{+0.014}_{-0.004}$	0.8 ± 0.2	0.6 ± 0.2
071112C	0.8227	89 – 179	0.022	undef	$0.40^{+0.08}_{-0.09}$	$0.00^{+0.04}_{-0.00}$	0.2 ± 0.1	$0.1^{+0.2}_{-0.1}$
080319B	0.9382	200 – 500	0.0077	1.0	$1.0^{+0.4}_{-0.2}$	$0.00^{+0.03}_{-0.00}$	0.13 ± 0.03	0.08 ± 0.03
080430	–	–	–	–	–	–	–	–
080604	1.4171	125 – 200	0.14	0.059	$0.21^{+0.15}_{-0.06}$	$0.27^{+0.06}_{-0.07}$	$0.3^{+0.4}_{-0.3}$	$0.2^{+0.5}_{-0.2}$
080605	1.6403	300 – 700	0.054	1.0	$0.084^{+0.004}_{-0.008}$	$0.003^{+0.094}_{-0.003}$	$1.3^{+0.2}_{-0.1}$	0.6 ± 0.2
080928	1.6919	280 – 320	0.0014	undef	$2.3^{+0.9}_{-0.6}$	$0.0^{+0.1}_{-0.0}$	0.7 ± 0.3	0.3 ± 0.1
090424	0.544	700 – 1000	0.62	0.017	$1.1^{+0.8}_{-0.4}$	0.8 ± 0.2	0.52 ± 0.07	0.42 ± 0.05

6.5 The final candidates and potential caveats

We will refer to the bursts in Table 6.4 as our final list of candidates for having a black body component. In this section we will discuss potential caveats for each candidate.

6.5.1 The Redshifts

It is essential that the redshift, which is a fixed parameter in all our models, is reliably determined. Table 6.5 summarizes how the redshift has been found for the bursts with excess emission. GRB 061021, GRB 090814A and GRB 110715 have redshifts found with only two absorption lines. It is however possible that these absorption lines come from other galaxies than the host galaxy of the bursts. The remaining bursts have more reliably determined redshifts with several absorption and/or emission lines.

6.5.2 Light curves and spectral evolution

Figure 6.7 shows the parts of the light curves which were used in the time sliced analysis of the final candidates. We tried to avoid achromatic and X-ray flares and effects from flattening of the light curves, when the time intervals were selected, but we note that evolution of the spectral parameters, the power law index and/or the black body temperature and normalisation, may be occurring during any of our spectra. When analysing time sliced spectra this risk is lowered, and we examined the hardness ratios in the XRT Repository in order to flag incidences of strong spectral evolution. GRBs 061021, 061110A, 090814A and 110715A have approximately constant hardness ratios in the intervals where time sliced spectra were analysed. GRB 081109 shows a slowly hardening spectrum, while GRB 100621A becomes significantly softer during the first time slice but shows no spectral evolution during our second time slice. Therefore the parameters we derive in Table 6.6 for these latter two GRBs should be considered more uncertain than the error bars allow. Evolution of the black body component has been demonstrated for GRBs 060218 (e.g. Campana et al., 2006), 090618 (Page et al., 2011), 100316D (Starling et al., 2011; Olivares E. et al., 2012) and 101219B (Paper I), where the black body cools and expands with time, but typically this evolution is slow compared with the exposure times covered by our X-ray spectra.

6.5.3 Contribution from the prompt emission

It is important that the prompt emission, which has a spectrum peaking at the energy, E_{peak} , is not entering our X-ray spectrum for the *Swift* XRT (0.3 – 10 keV), since this potentially could give features resembling black body components. Here is a summary of the measurement of E_{peak} for each burst:

061021 E_{peak} was measured to lie above 540 keV up to 8 seconds after the trigger (Golenetskii et al., 2006). This is well above XRT-energies.

061110A No spectral break or cutoff was seen with *Swift*/BAT, so no E_{peak} information is present. The role of the prompt emission remains unknown for this burst.

Table 6.4: The time sliced fits from Section 6.4.4, where bursts are selected with Model 3 and 4. Three reliably detected black body components are found.

Candidates with probable excess emission:

GRB	z	Time	F-test M3–4	kT (M4)	n_H (M4, fixed)
061021	0.3463	87 – 170	2.4×10^{-13}	0.13 ± 0.01	0.08 ± 0.02
061110A	0.7578	180 – 240	0.00050	0.19 ± 0.01	$0.3^{+0.3}_{-0.2}$
081109	0.9787	90 – 200	6.3×10^{-7}	0.16 ± 0.03	$1.0^{+0.2}_{-0.1}$
090814A	0.696	166 – 265	2.2×10^{-9}	0.30 ± 0.01	0.3 ± 0.2
090814A	0.696	265 – 390	2.1×10^{-8}	0.20 ± 0.02	0.2 ± 0.2
100621A	0.542	80 – 120	0.86	0.05 ± 0.05	2.0 ± 0.2
100621A	0.542	190 – 230	6.0×10^{-7}	0.25 ± 0.03	2.0 ± 0.2
110715A	0.82	97 – 501	6.6×10^{-6}	0.15 ± 0.03	1.3 ± 0.2

Candidates with some caveats:

GRB	z	Time	F-test M3–4	kT (M4)	n_H (M4, fixed)
060202	0.783	148 – 303	0.12	$0.045^{+0.004}_{-0.002}$	1.7 ± 0.2
060202	0.783	745 – 1000	0.0058	$0.25^{+0.07}_{-0.06}$	1.7 ± 0.2
061121	1.3145	125 – 215	7.5×10^{-6}	0.43 ± 0.03	$0.61^{+0.07}_{-0.06}$

Candidates where a black body component is not favoured:

GRB	z	Time	F-test M3–4	kT (M4)	n_H (M4, fixed)
071112C	0.8227	89 – 179	undef	$0.00^{+0.04}_{-0.00}$	$0.1^{+0.2}_{-0.1}$
080604	1.4171	125 – 200	0.059	0.3 ± 0.1	$0.2^{+0.5}_{-0.2}$
090424	0.544	700 – 1000	0.017	0.8 ± 0.2	0.42 ± 0.05

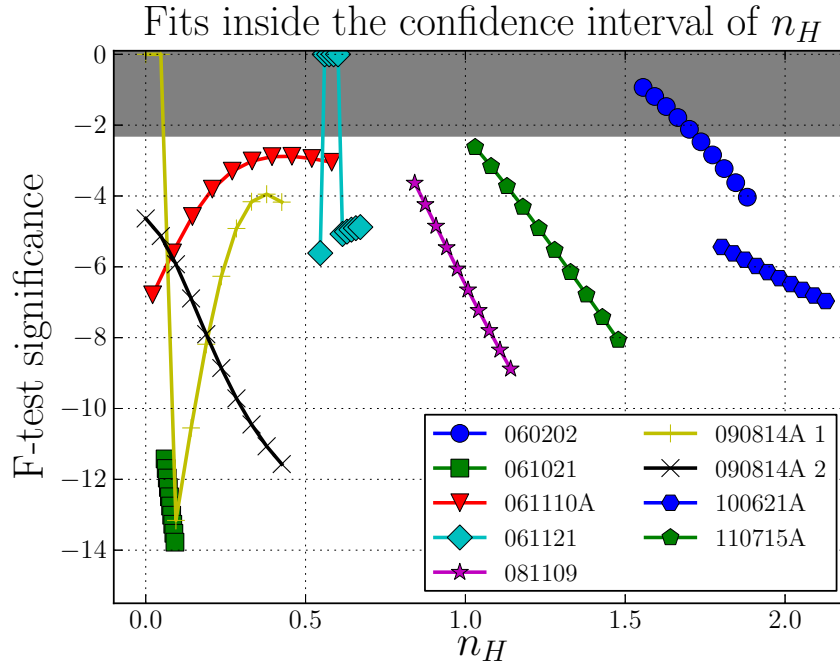


Figure 6.6: In Model 3 and 4 n_H is fixed to a value determined from late time observations. This figure examines how the F-test significances of the candidates from Table 6.4 depend on n_H -values with the 90% confidence intervals found in the fits of the late time spectra.

Table 6.5: A schematic summary of how the redshift has been determined for each of the final candidates for having black body components.

GRB	Redshift	Absorption lines	Emission lines	References
061021	0.3463	MgII2796, MgII2803	-	Fynbo et al. (2009).
081109	0.9787	-	GROND photometry	Krühler et al. (2011b).
090814A	0.696	MgII and CaII	-	Jakobsson et al. (2009).
110715A	0.82	CaII, CaI	-	Piranomonte et al. (2011).

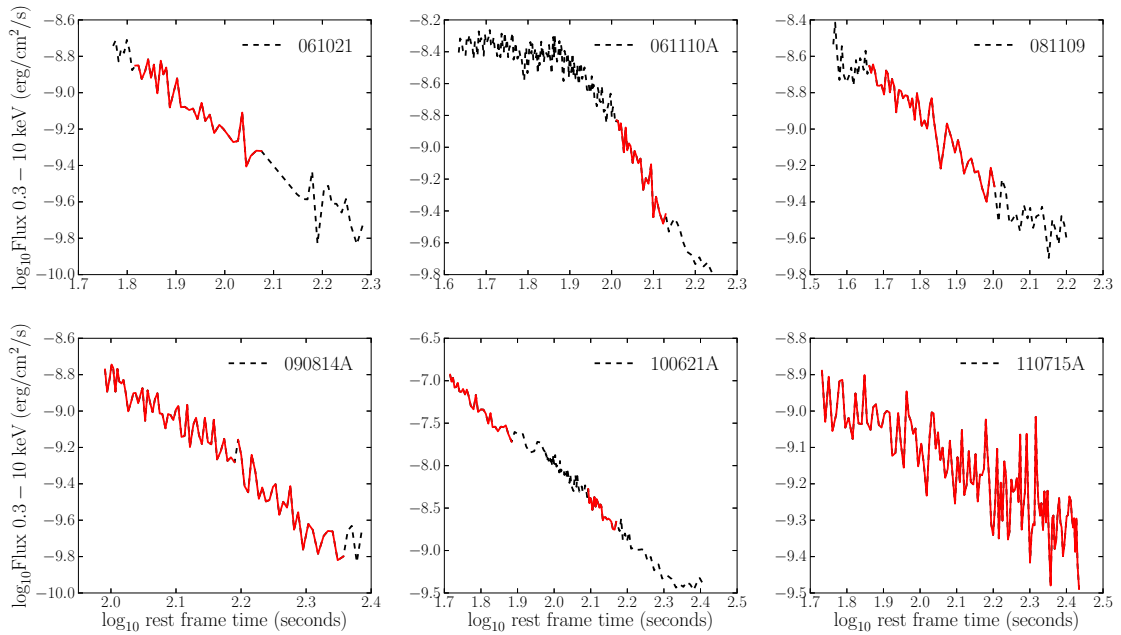


Figure 6.7: The light curves for each of the bursts with probable excess emission. The curve is red (and solid) in the intervals selected for a time sliced analysis.

090814A No spectral break or cutoff was seen by *Swift*/BAT. The role of the prompt emission remains unknown for this burst.

081109 Fermi/GBM measured $E_{\text{peak}} = 240 \pm 60$ keV (von Kienlin, 2008) after 26 seconds. Our spectrum is well below that energy.

100621A Konus-Wind fits their spectrum covering 0 – 74 seconds with $E_{\text{peak}} = 95^{+18}_{-13}$ keV (Golenetskii et al., 2010). Our spectrum starts at 80 s, so probably the peak energy was still well above the XRT band.

110715A 18 seconds after trigger Konus-wind measured $E_{\text{peak}} = 120^{+12}_{-11}$ keV (Golenetskii et al., 2011), and BAT found 120 ± 21 keV (Ukwatta et al., 2011). It is unlikely, that this affects our XRT spectrum, which starts at 98 seconds.

Table 6.6: Radii, temperatures and luminosities of the black body components of the final candidates. Candidates from this work and other works are shown. If a value is **bold**, it has been calculated using Stefan-Boltzmann's law (see Eq. (6.1)), from the two non-**bold** values for a given candidate. If a E_{iso} -value is underlined, it has been calculated from the fluence in the 15-150 keV band and it should only be seen as a lower limit.

GRB	Radius (m)	kT (keV)	L (10^{47} erg s^{-1})	ref	z	Time (s)	T_{90} (s)	E_{iso} (erg)
061021	6.6×10^{10}	0.13	1.4	this work	0.3663	87 – 170	46	4.6×10^{51}
061110A	1.4×10^{11}	0.19	25.6	this work	0.7578	180 – 240	41	<u>2.9×10^{51}</u>
081109	2.0×10^{11}	0.16	27.1	this work	0.9787	90 – 200	190	<u>1.8×10^{52}</u>
090814A	3.1×10^{10}	0.30	8.4	this work	0.696	166 – 265	80	<u>2.8×10^{51}</u>
090814A	4.7×10^{10}	0.20	3.7	this work	0.696	165 – 390	80	<u>2.8×10^{51}</u>
100621A	8.7×10^{10}	0.25	32.4	this work	0.542	190 – 230	64	<u>2.8×10^{52}</u>
110715A	2.7×10^{11}	0.15	43.0	this work	0.82	97 – 501	13	<u>4.1×10^{52}</u>
060218	1.0×10^{10}	0.20	0.2	Campana et al. (2006)	0.033	200	2100	6.2×10^{49}
090618	3.0×10^{10}	1.00	1000.0	Page et al. (2011)	0.54	150	113	2.5×10^{53}
090618	1.0×10^{11}	0.20	100.0	Page et al. (2011)	0.54	250	113	2.5×10^{53}
100316D	3×10^{10}	0.14	0.3	Starling et al. (2011)	0.0591	250	> 1300	3.9×10^{49}
101219B	2.4×10^{10}	0.20	1.0	Paper I	0.5519	250	34	4.2×10^{51}

6.5.4 Is it a black body component?

The six bursts in our final candidate list (GRB 061021, GRB 061110A, GRB 081109, GRB 090814A, GRB 100621A and GRB 110715A) are clearly special, since models with a black body component included give better fits than absorbed power laws. We do, however, not have conclusive evidence that the actual emission mechanism is a black body component. Other possible explanations could be a model with multiple absorption components at different redshifts, the prompt emission peak could be moving through the band, there could be strong spectral evolution, or the determined redshift could be wrong. We have a total of 190 bursts in our sample, so some of them will likely be affected by such features. Due to these caveats we will not report *discovery of black body emission*, but instead we will report the finding of bursts with *possible black body emission*.

6.6 Properties of the black body components

In this section, we will assume, that the actual mechanism behind the excess emission in the spectra of the six bursts is a single temperature black body component. Table 6.6 shows radius (assuming spherical symmetry) and temperature for these bursts together with values reported in other studies. For our final candidates the radii are calculated from the fitted temperature and luminosity. In the calculation we assume a spherically symmetric black body, in thermal equilibrium, which can be described by the Stefan-Boltzmann law,

$$L(\text{erg s}^{-1}) = 1.105 \times 10^{29} \times r^2(\text{m}) \times T^4(\text{keV}) \quad (6.1)$$

Also note that the luminosities and radii in the table are lower limits, since only the photons in a 0.3 – 10 keV are included in the luminosity calculation. Due to these caveats, the values in the table should be seen as rough estimates only.

The bursts have temperatures in the range, 0.1 – 0.3 keV, which is consistent with the previously proposed black body components in the time-averaged WT spectra of GRB 060218, 090618, 100316D and 101219B. They also have luminosities consistent with these previously studied bursts, whereas the radii are slightly larger for GRB 061110A, 081109 and 110715A than the previously claimed examples.

In the case of GRB 060218 several studies (Ghisellini et al., 2007a,b; Chevalier & Fransson, 2008; Li, 2007) disfavour the scenario that the excess emission is due to a black body component, since they can not explain the large black body luminosities. All our bursts with possible black body emission have a luminosity larger than GRB 060218 (Table 6.6), so they might suffer from a similar problem.

All the bursts have durations (T_{90}) between 13 and 190 seconds, which is typical for long bursts. The redshifts are in the range, $z = 0.37 - 0.98$, so they are slightly more distant than the cases reported in other studies ($z = 0.03 - 0.55$).

6.6.1 The fraction of bursts with black body components

In the Model 1 to 2 comparison we found three new candidates (GRB 061021, 061110A, 090814A) and we re-discovered GRB 060218, 090618, 101219B. So we found a black body component in 6 out of the 116 bursts (i.e. 5%) with successful fits.

We will now shed light on the fraction of *Swift* bursts for which it is possible to recover a black body component like the one in GRB 101219B. In Section 6.3 it was found that such

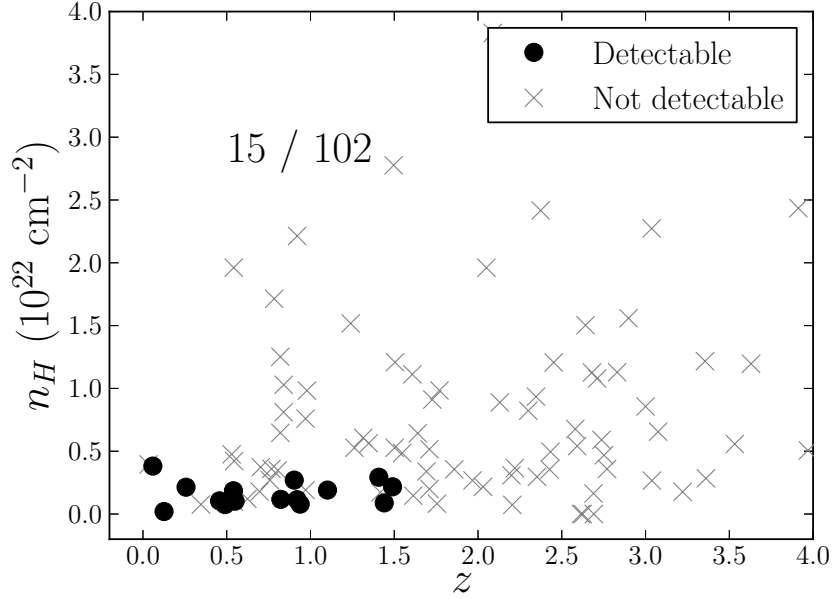


Figure 6.8: n_H versus z for all the successfully fitted bursts. If a black body component, like the one present in GRB 101219B, is detectable in a GRB it is marked with a *black circle*. In 15 out of 102 bursts it is possible to recover such a black body component.

a black body component can be detected (with the F-test comparison of Model 1 and 2) if $z < 1.5$, $n_H < 0.4 \times 10^{22} \text{ cm}^{-2}$ and the logarithm of the powerlaw normalisation is below -0.5 (see Figure See Figure 6.1, 6.2 and 6.3). Figure 6.8 shows n_H versus z for all the bursts in our sample with successful fits. It is marked whether a bursts passes these detection criteria. We see that in 15 %, 15 out of 102 bursts, a detection will be possible. This calculation is, of course, only a rough estimate. The X-ray black body components need not all be like the one in GRB 101219B, and the limits we have used on z , n_H , Γ and power law normalisation are expected to be degenerate with each other. This calculation is, however, sufficient to establish that black body components only are detectable in a fraction of the bursts, even if such a black body component is present in all GRBs.

None of the new candidates found in this work have a optically confirmed SN. Note, however, that we excluded bursts which already are discussed in other works, including Paper I where several bursts with associated SNe are analysed.

6.7 Conclusion

We have first examined under which conditions a black body component, like the one proposed to be in GRB 101219B, can be recovered. At high redshift and in environments with intermediate or high column densities a detection of such a component will not be possible. We also find that it will be hard to recover a black body component, when a bright afterglow emission is present. We show that detection of a black body component only will be possible in a small fraction of all GRBs in our sample.

We have searched for black body components in all the *Swift* bursts with known redshift and created a list of bursts with possible black body components (GRB 061021,

061110A, 081109, 090814A, 100621A and 110715A). They have temperatures, radii and luminosities similar to those found in previous studies of black body components in GRBs.

Bibliography

- Barthelmy S. D., et al., 2005, *Nature*, 438, 994
- Burrows D. N., et al., 2005, *SSRv*, 120, 165
- Butler N. R., 2007, *ApJ*, 656, 1001
- Campana S., et al., 2006, *Nature*, 442, 1008
- Cano Z., et al., 2011, *MNRAS*, 413, 669
- Cash W., 1979, *ApJ*, 228, 939
- Chevalier R. A., Fransson C., 2008, *ApJ*, 683, L135
- Cobb B. E., Bloom J. S., Perley D. A., Morgan A. N., Cenko S. B., Filippenko A. V., 2010, *ApJ*, 718, L150
- Cucchiara A., et al., 2011, *ApJ*, 736, 7
- de Ugarte Postigo A., et al., 2011, *GRB Coordinates Network*, 11579, 1
- Evans P. A., et al., 2009, *MNRAS*, 397, 1177
- Fynbo J. P. U., et al., 2009, *ApJS*, 185, 526
- Galama T. J., et al., 1998, *Nature*, 395, 670
- Ghisellini G., Ghirlanda G., Tavecchio F., 2007a, *MNRAS*, 382, L77
- Ghisellini G., Ghirlanda G., Tavecchio F., 2007b, *MNRAS*, 375, L36
- Golenetskii S., Aptekar R., Mazets E., Pal'Shin V., Frederiks D., Cline T., 2006, *GRB Coordinates Network*, 5748, 1
- Golenetskii S., et al., 2010, *GRB Coordinates Network*, 10882, 1
- Golenetskii S., et al., 2011, *GRB Coordinates Network*, 12166, 1
- Hjorth J., Bloom J. S., 2011, *ArXiv e-prints astro-ph/1104.2274*
- Hjorth J., et al., 2003, *Nature*, 423, 847
- Jakobsson P., et al., 2009, *GRB Coordinates Network*, 9797, 1
- Kalberla P. M. W., Burton W. B., Hartmann D., Arnal E. M., Bajaja E., Morras R., Pöppel W. G. L., 2005, *A&A*, 440, 775

Kouveliotou C., Meegan C. A., Fishman G. J., Bhat N. P., Briggs M. S., Koshut T. M., Paciesas W. S., Pendleton G. N., 1993, *ApJ*, 413, L101

Krühler T., et al., 2011a, *A&A*, 526, A153

Krühler T., et al., 2011b, *A&A*, 534, A108

Lampton M., Margon B., Bowyer S., 1976, *ApJ*, 208, 177

Li L.-X., 2007, *MNRAS*, 375, 240

Lipkin Y. M., et al., 2004, *ApJ*, 606, 381

Mazzali P. A., Deng J., Nomoto K., Sauer D. N., Pian E., Tominaga N., Tanaka M., Maeda K., Filippenko A. V., 2006, *Nature*, 442, 1018

Milvang-Jensen B., et al., 2010, *GRB Coordinates Network*, 10876, 1

Olivares E. F., et al., 2012, *A&A*, 539, A76

Page K. L., Starling R. L. C., Fitzpatrick G., Pandey S. B., Osborne J. P., et al., 2011, *MNRAS*, 416, 2078

Patat F., et al., 2001, *ApJ*, 555, 900

Pian E., et al., 2006, *Nature*, 442, 1011

Piranomonte S., Vergani S. D., Malesani D., Fynbo J. P. U., Wiersema K., Kaper L., 2011, *GRB Coordinates Network*, 12164, 1

Protassov R., van Dyk D. A., Connors A., Kashyap V. L., Siemiginowska A., 2002, *ApJ*, 571, 545

Salvaterra R., et al., 2009, *Nature*, 461, 1258

Soderberg A. M., et al., 2006, *Nature*, 442, 1014

Sparre M., et al., 2011, *ApJ*, 735, L24

Starling R. L. C., et al., 2011, *MNRAS*, 411, 2792

Starling R. L. C., et al., 2012, *ArXiv e-prints*, astro-ph/1207.1444

Starling R. L. C., Page K. L., M. Sparre 2012, Accepted to the proceedings of IAU 279 'Death of massive stars: supernovae and gamma-ray bursts'

Tanvir N. R., et al., 2009, *Nature*, 461, 1254

Ukwatta T. N., et al., 2011, *GRB Coordinates Network*, 12160, 1

Verner D. A., Ferland G. J., Korista K. T., Yakovlev D. G., 1996, *ApJ*, 465, 487

von Kienlin A., 2008, *GRB Coordinates Network*, 8505, 1

Waxman E., Mészáros P., Campana S., 2007, *ApJ*, 667, 351

Wilms J., Allen A., McCray R., 2000, *ApJ*, 542, 914

Chapter 7

Probing high-redshift galaxies with gamma-ray bursts

This chapter contains the following article:

The metallicity and dust content of a redshift 5 gamma-ray burst host galaxy

Published in Sparre et al. 2014,ApJ,785,150

Authors: M. Sparre, O. E. Hartoog, T. Krühler, J. P. U. Fynbo, D. J. Watson, K. Wiersema, V. D'Elia, T. Zafar, P. M. J. Afonso, S. Covino, A. de Ugarte Postigo, H. Flores, P. Goldoni, J. Greiner, J. Hjorth, P. Jakobsson, L. Kaper, S. Klose, A. J. Levan, D. Malesani, B. Milvang-Jensen, M. Nardini, S. Piranomonte, J. Sollerman, R. Sánchez-Ramírez, S. Schulze, N. R. Tanvir, S. D. Vergani, R. A. M. J. Wijers

Abstract

Observations of the afterglows of long gamma-ray bursts (GRBs) allow the study of star-forming galaxies across most of cosmic history. Here we present observations of GRB 111008A from which we can measure metallicity, chemical abundance patterns, dust-to-metals ratio and extinction of the GRB host galaxy at $z = 5.0$. The host absorption system is a damped Lyman- α absorber (DLA) with a very large neutral hydrogen column density of $\log N(\text{HI})/\text{cm}^{-2} = 22.30 \pm 0.06$, and a metallicity of $[\text{S}/\text{H}] = -1.70 \pm 0.10$. It is the highest redshift GRB with such a precise metallicity measurement. The presence of fine-structure lines confirms the $z = 5.0$ system as the GRB host galaxy, and makes this the highest redshift where FeII fine-structure lines have been detected. The afterglow is mildly reddened with $A_V = 0.11 \pm 0.04$ mag, and the host galaxy has a dust-to-metals ratio which is consistent with being equal to or lower than typical values in the Local Group.

7.1 Introduction

The study of gamma-ray bursts (GRBs) has an impact on a wide range of topics in astrophysics. It is now well established that long-duration GRBs originate from the collapse of massive stars (e.g., Galama et al., 1998; Hjorth et al., 2003; Stanek et al., 2003; Modjaz et al., 2006; Campana et al., 2006; Sparre et al., 2011; Berger et al., 2011; Hjorth & Bloom, 2012; Xu et al., 2013), although we have yet to elucidate the detailed nature of the progenitor systems.

Spectroscopy of GRB afterglows requires the most advanced and largest ground-based optical to near-infrared (NIR) telescopes, especially when these events occur at high redshift, since the source is weaker and the rest-frame UV absorption lines we detect are shifted to longer wavelengths. GRB afterglows can probe star forming regions out to redshifts of $z = 8-9$ (Tanvir et al., 2009; Salvaterra et al., 2009; Cucchiara et al., 2011), and allow us to study galaxies in the early Universe that would normally have been too faint to be detected (Tanvir et al., 2012; Basa et al., 2012). In some cases it is possible to determine column densities of both HI and metals in their host galaxies and hence calculate abundances for a wide range of chemical elements (e.g., Fynbo et al., 2006; Savaglio, 2006; Prochaska et al., 2007b; Ledoux et al., 2009; D’Elia et al., 2010; Thöne et al., 2013).

Observational selection effects restrict the samples of GRBs for which chemical enrichment can be probed by this means. For many GRBs, even when spectroscopy is obtained, it proves insufficient to probe the rest-frame UV due to unfortunate redshifts that leave the relevant transitions (in particular HI) out of the observable range. In other cases, dust extinction within the host galaxies (the likely explanation for many ‘dark’ bursts, see Jakobsson et al. 2004; Perley et al. 2009; Krühler et al. 2011) makes the afterglows too faint for useful spectroscopy. Therefore the sample of bursts with afterglow spectroscopy is not representative for all GRBs (e.g., Fynbo et al., 2009; Krühler et al., 2013).

With observations of GRB afterglows one can hope to obtain the imprints in the ISM of chemical enrichment from core-collapse supernovae (SNe), which are believed to dominate the metal production for very young systems (e.g., Matteucci & Greggio, 1986). The signature of such a chemical enrichment profile is an over-abundance of α -elements as seen in metal-poor stars in the Local Group and in $z > 4$ DLAs¹. (e.g., Tolstoy, 2011; Rafelski et al., 2012).

The aim of this article is to study the metal and dust properties of the host galaxy of GRB 111008A at $z = 5.0$, which provides a rare opportunity of measuring such characteristics for a high-redshift star-forming galaxy. The paper is structured as follows. In Section 7.2 we present our observations, in Section 7.3 we determine the metallicity of the host galaxy, and we also discuss the presence and strength of fine-structure lines. In Section 7.4 we describe the spectral energy distribution (SED) of the NIR-to-X-ray data. In Section 7.5 we investigate an intervening DLA at $z = 4.6$, in Section 7.6 we present an attempt to identify the intervening absorber and the GRB host galaxy in emission and in Section 7.7 we study the amount of dust and metals in the host galaxy.

For the cosmological calculations we assume a Λ CDM-universe with $\Omega_\Lambda = 0.73$, $\Omega_m = 0.27$, and $h_0 = 0.71$. We use 1σ error bars and 2σ upper and lower limits.

¹DLA: damped Lyman- α absorber: a sight line absorber with $\log N(\text{HI})/\text{cm}^{-2} > 20.30$ (Wolfe et al., 2005)

7.2 Observations

GRB 111008A was discovered by *Swift*/BAT (Saxton et al., 2011) with a duration of $T_{90} = 63.46 \pm 2.19$ s (Baumgartner et al., 2011). An X-ray counterpart was subsequently discovered with *Swift*/XRT (Beardmore et al., 2011), and the optical counterpart was later observed using several instruments (Levan et al., 2011a; Xu et al., 2011; Nardini et al., 2011) before a spectroscopic redshift of $z = 5.0$ was identified with Gemini/GMOS (Levan et al., 2011b). This was later confirmed with VLT/X-shooter, and an intervening absorber at $z = 4.6$ was also identified (Wiersema et al., 2011). The details of our observations are given below.

7.2.1 X-shooter spectroscopy

We obtained optical/NIR spectroscopy of the afterglow of GRB 111008A with X-shooter (Vernet et al., 2011) mounted at UT2 of the European Southern Observatory’s (ESO) Very Large Telescope. Our spectrum covers the wavelength range of 3000 – 24800 Å, and was taken simultaneously in three arms (UVB, VIS and NIR) using slit widths of 1.0, 0.9 and 0.9'' for UVB, VIS and NIR respectively. The nominal values of the spectral resolution for these configurations are $R = \lambda/\Delta\lambda(\text{FWHM}) = 5100, 8800$ and 5100, respectively.

X-shooter spectroscopy started on 2011-10-09 05:55:49 UT, 8.52 hr after the trigger (Wiersema et al., 2011), and was performed at a median seeing of 1.1'' and an average airmass of 1.04. We obtained five exposures with a total integration time of 8775 s in the UVB and VIS arm, and 14 exposures (total exposure of 8400 s) in the NIR arm. A second X-shooter epoch was obtained the following night (starting 20.10 hr after the trigger, on 2011-10-10 04:24:25 UT) with a total integration time 7897 s in UVB and VIS, and 7200 s in NIR. All frames were reduced separately using the ESO X-shooter pipeline v2.0.0 (Modigliani et al., 2010), and the resulting frames were stacked per night with a weighting based on the signal-to-noise ratio (SNR) of the afterglow detection. Flux calibration was performed against the spectro-photometric standard GD71 observed starting on 2011-10-08 08:58:03 UT. The one-dimensional spectra were extracted using optimal, variance weighting (Horne, 1986). The optimal extraction and the stacking of science frames were done by a custom-made script developed for this purpose. Unless stated explicitly (as in Section 7.3.2), we base our results on the combined spectrum of the first night of X-shooter observations, because of the superior SNR.

The complete VIS and NIR part of the X-shooter spectrum, and the measured absorption lines, are shown in Appendix 7.11.

7.2.2 GMOS spectroscopy

We observed the afterglow of GRB 111008A using the Gemini Multi-Object Spectrograph (GMOS) on the Gemini-South telescope². After identification of the optical afterglow (Levan et al., 2011b), a series of four exposures with a total integration time of 2400 s were taken, using the R400 grism and a 1.0'' slit width, starting at 2011-11-09 03:29:29.7 UT.

The four exposures were taken using dithers in both the dispersion direction (50 Å) and the spatial direction (along the slit) to sample over the chip gaps and regions affected by amplifier location. We reduced the data using the Gemini GMOS reduction package

²For an overview of Gemini afterglow spectra see: <http://grbspecdb.ucolick.org/>

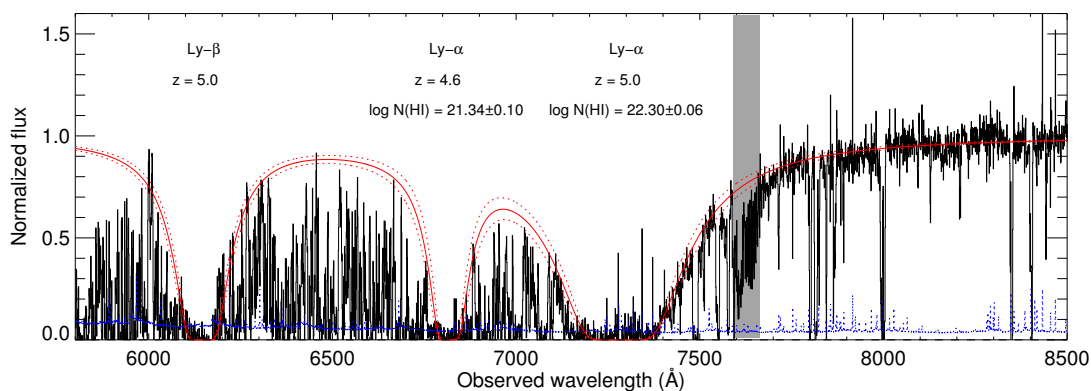


Figure 7.1: Excerpt of the VIS spectrum showing absorption from Ly- β and Ly- α of the host galaxy of GRB 111008A ($z = 5.0$) and Ly- α of the strong intervening system at $z = 4.6$. The red line displays a Voigt-profile fit to the DLAs Ly- α and Ly- β lines. The dashed line shows the 1σ error on the fit result, and the dotted line shows the error spectrum. The shaded gray indicates a region with strong telluric contamination.

(version 1.11) within IRAF, combining the four exposures after extraction, resulting in a wavelength range of $\sim 3900 - 8170 \text{ \AA}$. The resolution of the exposures is $R \sim 870$.

7.2.3 GROND photometry

The Gamma-Ray burst Optical/Near-infrared Detector (GROND; Greiner et al., 2008) at the 2.2m MPI/ESO telescope on the La Silla observatory started photometric observations of the field of GRB 111008A on 2011-11-09, 04:38:45 UT, which is 6.43 hr after the BAT trigger. Simultaneous photometry in seven optical/NIR filters (similar to the SDSS $g'r'i'z'$ and the 2MASS JHK_s bands) was obtained continuously until 09:02:10 UT. GROND data were reduced in a standard fashion (Krühler et al., 2008), using a custom pipeline written in IRAF/pyraf. The photometric solution was obtained by using magnitudes of stars in an SDSS field (Aihara et al., 2011) observed directly after the GRB field under photometric conditions in the case of the $g'r'i'z'$ filters, and via the magnitudes of 2MASS stars in JHK_s (Skrutskie et al., 2006). Based on the scatter of individual calibration stars, we estimate the absolute accuracy of our photometry to be 4% in $g'r'i'z'$, 5% in J/H and 8% in K_s .

7.3 The GRB host absorber

In Fig. 7.1 we provide an excerpt of the VIS spectrum (from X-shooter), which has been rebinned by a factor of 4 for graphical reasons. The VIS spectrum exhibits a very strong DLA, which is identified as absorption within the host galaxy, providing the redshift of the GRB. The corresponding Ly β line is also detected. Shown in red is a Voigt-profile fit to the DLA and Ly β lines corresponding to an HI column density of $\log N/\text{cm}^{-2} = 22.30 \pm 0.06$. Also seen in the VIS spectrum is an intervening DLA at redshift $z = 4.6$ which will be discussed in Section 7.5. When determining the HI column density of the two absorbers, we fix the redshift to the value measured from the metal line fit (see Section 7.3.1), and next we determine $\log N(\text{HI})$ subjectively by looking at the red wing of the Lyman- α and Lyman- β profiles. The error reflects what we consider the acceptable

range of possible column densities.

7.3.1 The chemical composition

To determine abundances of the atomic ground state levels we proceed with Voigt-profile fitting of the X-shooter spectrum³. We find that a model with two absorption components per transition is sufficient to fit the low-ionization absorption lines. The spectral resolution is set to the nominal values from the X-shooter manual (a velocity resolution of 34 km s⁻¹ for VIS and 57 km s⁻¹ for NIR, both full-width-at-half-maximum). The choice of spectral resolution and the placement of the continuum are unlikely to change the logarithm of the column densities by more than 0.15 dex.

The two Voigt-profiles have Doppler parameters of $b = 20.9 \pm 2.3$ km s⁻¹ and $b = 27.7 \pm 2.3$ km s⁻¹, and redshifts of 4.99005 ± 0.00007 and 4.99142 ± 0.00006 , respectively (these are the precise measured redshifts for the two absorption components in the GRB host absorption system. For brevity we will refer to the GRB host redshift as 5.0 in the remaining parts of the article). We linked the Doppler parameters for the different atoms assuming turbulent broadening, which is a standard procedure for low-ionization absorption lines (Wolfe et al., 2005). We also linked the redshifts for each of the absorption components. Fig. 7.2 shows the fit of the line transitions for SiII, SII, CrII, MnII, FeII, NiII and ZnII.

The derived metal column densities for the sum of the two components are provided in Table 7.1. Note that this table also includes the column densities in excited levels (from Section 7.3.2). The best determined column densities are Ni and Fe, since they are constrained by relatively weak transitions (NiII λ 1370 and FeII λ 1611) located in regions with a good SNR. For FeII λ 1611 the measured spectrum exhibits excess absorption (at $\simeq -15$ km s⁻¹) compared to the fit model. It is unclear whether this feature is due to an additional absorption component or a systematic error. If it is due to an additional absorption component our column density of FeII is slightly underestimated by $\lesssim 15\%$.

For the SII λ 1253 transition the SNR is also high, and the measurement is reliable even though this line is mildly saturated (see a detailed explanation in Appendix 7.10). For CrII we were able to estimate the column density with CrII λ 2056 and CrII λ 2066.

Systematic errors in the fitting of Si, Mn and Zn for the GRB host

The estimate of the column density of Si is unreliable because it is estimated using two lines, where one of them is saturated (SiII λ 1526) and the other is affected by a sky-line (SiII λ 1808). We therefore only report a lower limit on the column density based on SiII λ 1808. The estimated column density of Zn is also uncertain, since the blue component of the ZnII λ 2062 transition is blended with CrII λ 2062⁴. Visually, the model fit of MnII λ 2606 does not convincingly fit the data (and $\chi^2/\text{d.o.f.} = 4.55$ for this transition, which also indicates a bad fit), so our measurement of the Mn column density is unreliable.

In the last column of Table 7.1 these caveats are summarized. Since the derived column densities of Si, Mn and Zn are unreliable, we will not draw any conclusions based on them.

³The absorption lines are fitted with VPFIT version 10.0: <http://www.ast.cam.ac.uk/~rfc/vpfit.html>

⁴In our estimate we assumed that $\log N/\text{cm}^{-2}$ for the blue component of Zn is 0.1 dex lower than for the red component, since this is what we see for NiII λ 1370.

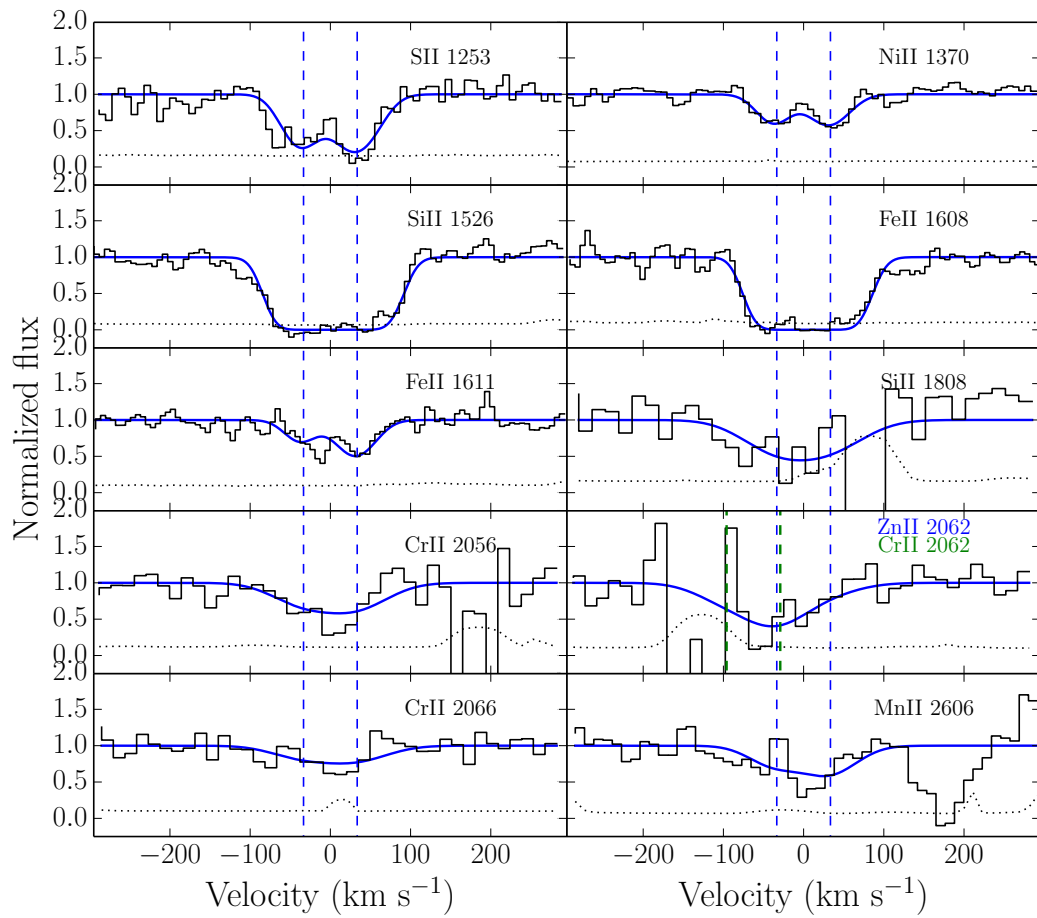


Figure 7.2: The fitted absorption lines from the host galaxy at $z = 5.0$. The black line is the spectrum, the blue line is the fitting model and the dotted line is the error spectrum. The centers of the absorption line components are marked with dashed vertical lines.

Table 7.1: The abundance pattern of the transitions (including excited levels) in the GRB 111008A host galaxy and for the intervening absorber. Lower limits are at a 2σ level. Abundances from the solar photosphere from Asplund et al. (2009) were used as reference.

Element	$\log N(X)/\text{cm}^{-2}$	$[X/H]$	Lines used in fit	Note
GRB host				
H	22.30 ± 0.06	-	Ly α , Ly β	
Si	$> 15.86 (2\sigma)$	$> -1.96 (2\sigma)$	SiII $\lambda 1808$, SiII $\lambda 1526$	Lines are saturated
S	15.71 ± 0.09	-1.70 ± 0.10	SII $\lambda 1253$	
Cr	14.17 ± 0.09	-1.76 ± 0.11	CrII $\lambda 2056$, CrII $\lambda 2062$, CrII $\lambda 2066$	
Mn	13.72 ± 0.08	-2.01 ± 0.10	MnII $\lambda 2606$	Fit is not convincing
Fe	16.05 ± 0.05	-1.74 ± 0.08	FeII $\lambda 1608$, FeII $\lambda 1611$	
Ni	14.89 ± 0.18	-1.64 ± 0.19	NiII $\lambda 1370$	
Zn	13.28 ± 0.21	-1.58 ± 0.21	ZnII $\lambda 2062$	Blended with CrII $\lambda 2062$
$z = 4.6$ system				
H	21.34 ± 0.10	-	Ly α	
Si	$> 14.91 (2\sigma)$	$> -2.15 (2\sigma)$	SiII $\lambda 1526$	Lines are saturated
Fe	15.23 ± 0.15	-1.61 ± 0.17	FeII $\lambda 1608$, FeII $\lambda 1611$	
Ni	14.23 ± 0.08	-1.33 ± 0.12	NiII $\lambda 1370$, NiII $\lambda 1741$	

7.3.2 Fine-structure lines

At $z = 5.0$ we detect lines that arise from the following fine-structure and metastable levels: C II $^2P_{3/2}^{\circ}$ (**), O I $^3P_0^{\circ}$ (**), Si II $^2P_{3/2}^{\circ}$ (*), Fe II ($^6D_{7/2}$, $^6D_{5/2}$, $^6D_{1/2}$, $^4F_{9/2}$, $^4F_{5/2}$, $^4D_{7/2}$, $^4D_{5/2}$, $^4D_{3/2}$) and Ni II $^4F_{9/2}$. To date, this is the highest redshift at which lines of these excited states of FeII and NiII have been detected. Lines from these excited levels are expected in GRB host galaxies and often detected at lower redshifts, but due to their relative weakness the SNR required to detect them is often not reached at high redshift. Lines from Fe II $^6D_{3/2}$ and $^4F_{7/2}$ are not clearly detected due to their unfortunate placing either outside atmospheric windows or because they are severely affected by telluric lines. The Gemini/GMOS and X-shooter data together cover a time span from 5 to 40 hours after the burst (observers frame), making the data set suited to look for variability in lines from excited levels. Line variability is expected, because the fine-structure and metastable levels are populated through indirect UV-pumping by the GRB afterglow (Prochaska et al., 2006; Vreeswijk et al., 2007). The lines from excited states and their corresponding ground states that fall in the spectral region covered both by GMOS and X-shooter are all likely saturated, therefore we compare their rest-frame equivalent width (EW_{rest}), see Table 7.2. The values of EW_{rest} for the lines and line blends (including both resonance and excited states) at the top of Table 7.2 are constant in time within 2σ , except Si II* $\lambda 1309$. However, the temporal variation of this line does not match that of the stronger Si II* $\lambda 1264$ lines, which it should follow. One possible explanation for this is that the uncertainty on Si II* $\lambda 1309$ are probably underestimated, especially in the last epoch.

The lines from the excited states of Fe II and Ni II, which are not covered by GMOS, are weaker (and not saturated) and can be fitted with Voigt profiles in the X-shooter spectra. We couple z and b and fit one component to the lines of these levels in the first X-shooter epoch. The redshift is consistent with the red component of the resonance lines. With the obtained z and b kept fixed, this fit is repeated on the second X-shooter epoch, though none of the lines are clearly detected. Therefore, we report 2σ upper limits on the population of these excited states (see Table 7.2). Here again we see no evidence for time variation for an individual excited state. We note, that the upper limits on the derived column densities are larger in the second X-shooter epoch compared to the first X-shooter epoch, since the signal-to-noise is lower in the second epoch.

From the measurements on the first X-shooter spectrum we conclude that the column density of the metastable level Fe II $^4F_{9/2}$ is, despite its higher energy, as high as that of the first excited state Fe II $^6D_{7/2}$ and that of all other, lower energy Fe II fine-structure states. Furthermore, Ni II $^4F_{9/2}$ is more populated than the Ni II ground state. This situation is typically the result of population by indirect radiative pumping. The Ni II $^4F_{9/2}$ population is expected to peak much later than the Fe II fine-structure states (after $\sim 2 - 10$ hr post burst in the rest frame, depending on light curve shape, see also Hartoog et al. 2013), which is consistent with our time of observations. Although a detailed model of the excitation has not been carried out in this paper, and despite the fact that we do not have evidence for variability in individual lines, our observations are consistent with the UV-pumping scenario, which confirms the $z = 5.0$ DLA as the host galaxy.

Table 7.2: Measurements of lines from fine-structure and metastable states at the host-galaxy redshift ($z = 5.0$) in three different epochs. The limits are at a 2σ confidence level.

Time of mid exposure ^a (hr)		6.27	10.15	34.82
		GMOS	X-shooter 2011-11-09	X-shooter 2011-11-10
Ion	Line (blend)	EW _{rest} (Å) of saturated lines and blends		
C II + C II*	$\lambda 1334 + \lambda 1335$	2.05 ± 0.33	1.94 ± 0.04	1.77 ± 0.12
O I	$\lambda 1302$	1.02 ± 0.02	1.05 ± 0.03	0.93 ± 0.05
O I**	$\lambda 1306$	0.62 ± 0.17	0.36 ± 0.03	0.42 ± 0.07
S II + Si II	$\lambda 1259 + \lambda 1260$	1.58 ± 0.03	1.64 ± 0.03	1.79 ± 0.14
Si II*	$\lambda 1264 + \lambda 1265$	1.15 ± 0.03	1.05 ± 0.03	1.12 ± 0.10
Si II*	$\lambda 1309$	0.37 ± 0.03	0.40 ± 0.02	0.14 ± 0.05
Ion	Level	Column densities $\log N(X)/\text{cm}^{-2}$ from line fits		
Fe II	${}^6D_{9/2}$ (ground)	<i>b</i>	15.72 ± 0.08^c	< 16.14
	${}^6D_{7/2}$	<i>b</i>	14.63 ± 0.06	< 14.74
	${}^6D_{5/2}$	<i>b</i>	14.53 ± 0.07	< 14.80
	${}^6D_{1/2}$	<i>b</i>	13.71 ± 0.11	-
	${}^4F_{9/2}$	<i>b</i>	14.66 ± 0.12	-
	${}^4F_{5/2}$	<i>b</i>	14.09 ± 0.24	-
	${}^4D_{7/2}$	<i>b</i>	13.66 ± 0.05	< 13.68
	${}^4D_{5/2}$	<i>b</i>	13.34 ± 0.08	< 13.91
	${}^4D_{3/2}$	<i>b</i>	12.95 ± 0.12	< 14.01
Ni II	${}^2D_{5/2}$ (ground)	14.62 ± 0.77	14.34 ± 0.05	14.33 ± 0.20
	${}^4F_{9/2}$	<i>b</i>	14.73 ± 0.26	-

^aTime since burst.

^bNot taking into account that we use an average spectrum weighted by the SNR of a fading source.

^cAll lines are outside the spectral range of GMOS.

^cThis is only the red component, which coincides with the position of the fine-structure lines.

7.4 Determining the dust extinction

We retrieved the X-ray spectrum of the afterglow of GRB 111008A from the *Swift*/XRT repository (Evans et al., 2007, 2009) and fit it together with the GROND broad-band photometry in a standard manner (see e.g., Krühler et al., 2013, for details). The fit is shown in Fig. 7.3. We use synchrotron emission models, reddened by extinction laws from the Local Group (Pei, 1992), and fit them to the available data. The absorption of soft X-rays is modeled with two absorbers at solar metallicity, one in the Galaxy (Kalberla et al. 2005, see also Willingale et al. 2013), the other at the GRB redshift. The fit is performed with data at a mean photon arrival time of 35 ks after the trigger. AB magnitudes of the afterglow at this epoch in the different filters are $g' > 25.5$ mag, $r' = 23.11 \pm 0.07$ mag, $i' = 21.33 \pm 0.05$ mag, $z' = 20.37 \pm 0.05$ mag, $J = 19.91 \pm 0.06$ mag, $H = 19.72 \pm 0.06$ mag, $K_s = 19.62 \pm 0.10$ mag. We note, that the $g'r'i'$ -band data are not part of the fit, because they are located bluewards of the Ly α transition. For the z' -filter, the strong absorption lines from the GRB-DLA and strong intervening system reduce the observed flux significantly. We use the X-shooter spectrum to estimate their effect on the z' -band measurement, and find that the continuum emission is approximately $7 \pm 1\%$ above what is measured with GROND. This correction factor is applied in the following. The effect on the JHK_s magnitudes is $\lesssim 4\%$.

The data are well fitted ($\chi^2 = 1.6$ in the optical/NIR, and Cash-statistic = 385 in the X-ray energy range, for a total of 362 degrees of freedom) with a broken power-law with a low-energy spectral index $\beta_1 = 0.46 \pm 0.06$ and a small amount of reddening in an SMC-like (Small Magellanic Cloud) extinction law ($E_{B-V} = 0.037 \pm 0.012$ mag, corresponding to a visual extinction of $A_V = 0.11 \pm 0.04$ mag). The high-energy spectral index β_2 is tied to β_1 through $\beta_2 = \beta_1 + 0.5$ as expected for synchrotron emission (predicted by Sari et al. 1998, and observed by Greiner et al. 2011; Zafar et al. 2011 and Covino et al. 2013), and the best fit soft X-ray absorption at $z = 5.0$ corresponds to $N(\text{H})_{\text{X}} = (1.8 \pm 0.4) \times 10^{22} \text{ cm}^{-2}$. Because of the small amount of reddening, an LMC (Large Magellanic Cloud) dust model provides a reasonable description of the optical/NIR data as well ($\chi^2 = 3.8$), and yields similar values for all parameters within the errors. A fit with a MW-dust model is significantly worse ($\chi^2 = 9.4$) because of the lack of a 2175 Å dust feature in our data.

7.5 The intervening system at $z = 4.6$

In the line of sight towards the afterglow of GRB 111008A an additional DLA system is detected at $z = 4.6$, with a neutral hydrogen column density of $\log N(\text{HI})/\text{cm}^{-2} = 21.34 \pm 0.10$ (Fig. 7.1). A number of strong metal absorption lines are detected from this system, including C IV, Mg I, Mg II, Si II, Si IV, Fe II and Ni II. We note that the EW_{rest} of Si II $\lambda 1526$ is the second highest ever detected for a DLA at $z > 4$ ($\text{EW}_{\text{rest}} = 2.30 \pm 0.02$ Å), indicating a relatively high metallicity for this redshift (Prochaska et al., 2008; Rafelski et al., 2012).

The low as well as the high ionization lines show multiple components. Due to their saturation, we do not include the Si IV and C IV lines in our analysis. The absorption lines from singly ionized species are fitted with Voigt profiles, in which we assume that the different ions have the same velocity structure; i.e. equal z and b -parameters per velocity component. In Fig. 7.4 we show the best fit for the most constraining absorption lines, which needs five components for the strongest lines. In the Voigt profile fitting we have included more lines than shown in the figure, most of which are visually absent, but

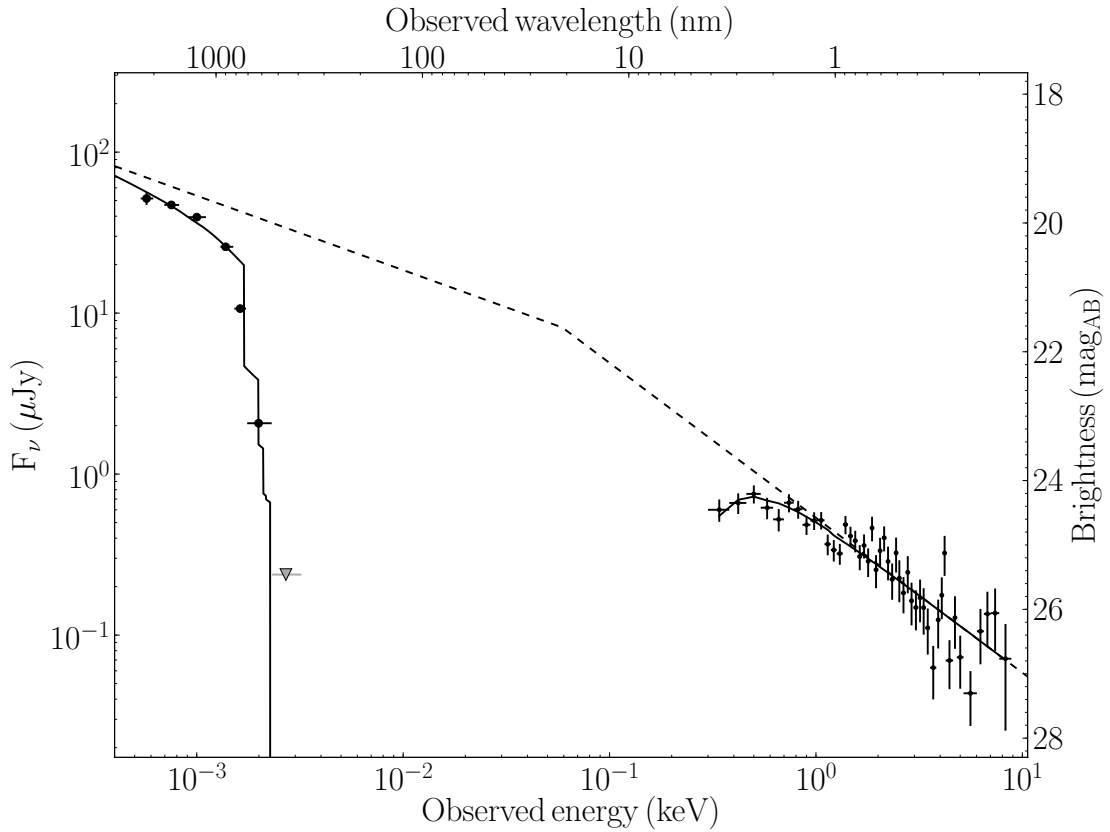


Figure 7.3: NIR-to-X-ray spectral energy distribution and model for the afterglow of GRB 111008A at an observed time of 35 ks after the GRB trigger. GROND photometry and the g' band upper limit are shown in larger black circles and a grey downward triangle, respectively. *Swift*/XRT X-ray data are plotted in smaller black dots. The best-fit model including gas and dust absorption is shown with solid lines, while the dashed line illustrates the underlying synchrotron emission. X-ray data have been binned to yield a S/N of at least 8 to enhance clarity. The $g'r'i'$ -band photometry is not fitted, because these filters are located or extend bluewards of the $\text{Ly}\alpha$ transition.

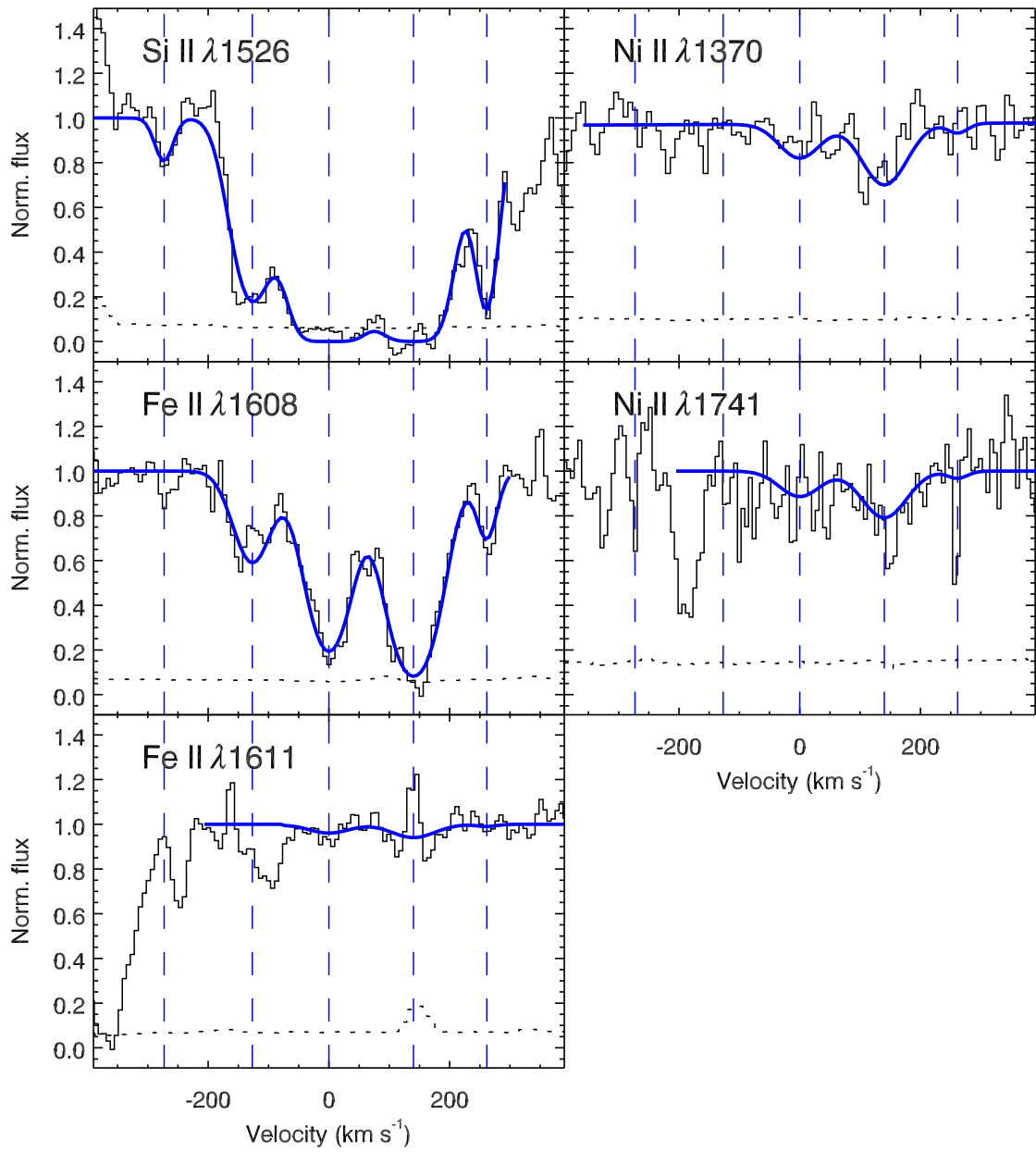


Figure 7.4: The most constraining metal lines from the intervening absorber at $z = 4.6$. The solid profiles are resulting Voigt profile fits with five absorption components (the dashed vertical lines show the velocity of the absorption components). The dotted line shows the error spectrum.

we have avoided regions with strong telluric contamination. Including both strong and weak lines, predominantly of Fe II, helps to constrain the b parameters. For the different absorption components the Voigt profile fitting results in the following b -parameters (z -values): $5.0 \pm 27.7 \text{ km s}^{-1}$ (4.60337 ± 0.00009), $36.4 \pm 2.8 \text{ km s}^{-1}$ (4.60611 ± 0.00004), $41.8 \pm 2.9 \text{ km s}^{-1}$ (4.60848 ± 0.00003), $45.2 \pm 2.3 \text{ km s}^{-1}$ (4.61110 ± 0.00003) and $10.7 \pm 2.0 \text{ km s}^{-1}$ (4.61337 ± 0.00002). Outside this section we will refer to the redshift of the intervening absorber as $z = 4.6$.

The total column densities of Si II, Fe II and Ni II can be constrained, and are summarized in Table 7.1. The column densities of Fe II and Ni II are robust because they are determined from optically thin lines. The fit for Si II is mainly determined by the saturated Si II $\lambda 1526$ transition, as Si II $\lambda 1808$ is in a low SNR region, so we conservatively report a 2σ lower limit of $\log N(\text{Si II})/\text{cm}^{-2} > 14.91$ based on the equivalent width of this line.

The conservative lower limit on the metallicity based on the equivalent width of Si II $\lambda 1526$ is 1% solar. The value of $[\text{Ni}/\text{H}]$ indicates a metallicity of 3–6% solar, and $[\text{Fe}/\text{H}]$ corresponds to 2–4% solar. For QSO and GRB DLAs at these metallicities (e.g., Dessauges-Zavadsky et al., 2006; Prochaska et al., 2007b; Savaglio et al., 2003) these elements (especially Ni and Fe) are often depleted onto dust grains, which implies that the true metallicity might be (much) higher. Generally, the ratio $[\text{Zn}/\text{Fe}]$, if available, is used to correct for dust depletion, since Zn is expected to be mainly in the gas phase even if a lot of dust is present. Unfortunately, for this intervening absorber we could not reliably constrain the column density of Zn, since Zn II $\lambda 2026$ is coincident with a skyline, and Zn II $\lambda 2062$ is blended with Cr II $\lambda 2062$.

7.6 Searching for emission from the host and from the intervening absorber

In the night of August 1st to August 2nd 2013, we obtained deep imaging of the field of GRB 111008A using the ESO/Very Large Telescope and FORS2 (Appenzeller et al., 1998) to search for the counterparts of the host and for the intervening DLA in emission (as it has been done for e.g. GRB 070721B, see Schulze et al. 2012). Our FORS2 observations consisted of 31 dithered exposures of 3 minutes integration time each in the z_{Gunn} -band filter which is centered around 9100 \AA . The data were processed and calibrated in a similar way to the GROND imaging data (see Section 7.2.3). The stacked FORS2 image has a full-width at half maximum of the stellar PSF of $0.9''$ and reaches a 2σ depth of a z -band magnitude of $26 \text{ mag}_{\text{AB}}$.

We do not detect emission centered at the position of the optical transient, and we set an upper limit of $z > 25.6 \text{ mag}_{\text{AB}}$ for the brightness of the GRB host galaxy by measuring the flux at the GRB position in an aperture of size of one FWHM. Especially at the highest redshifts, GRB hosts are faint (Hjorth et al., 2012; Tanvir et al., 2012) and the lack of a clear counterpart to the GRB-DLA in our imaging is thus not particularly surprising.

We detect significant emission centered at a projected distance of $0.65 \pm 0.15''$ to the optical counterpart with an AB magnitude of $z = 25.4 \pm 0.3$. We consider this a more likely candidate for the counterpart of the intervening DLA at $z = 4.6$ than for the $z = 5.0$ host system. Also, finding an unrelated galaxy at these flux levels is not unlikely. The probability (estimated following Bloom et al. 2002) of finding a random field galaxy with $z < 25.4 \text{ mag}$ at this distance to the GRB is approximately 3 percent. An association

between the detected source and the DLA could be supported or rejected from further imaging, for example. At $z = 4.6$, a galaxy is expected to show a strong Lyman- α break between the r and the i -band and no flux transmitted below 5100 \AA .

If associated with the DLA at $z = 4.6$ the FORS2 z -band measurement yields an absolute magnitude of $M_{UV} = -20.9 \pm 0.3 \text{ mag}$ at a rest-frame wavelength of $\sim 1600 \text{ \AA}$, typical of the brightest Lyman break galaxies at this redshift. Compared to the galaxy luminosity function, this magnitude corresponds to $\approx L_*$ (Bouwens et al., 2007). The measured spatial offset between GRB line of sight and galaxy center would be $4 \pm 1 \text{ kpc}$ at $z = 4.6$.

Since the absorber has a high metallicity and a high velocity width the chances are that this absorber is part of a massive galaxy (Wolfe et al., 2008). This would agree with the detection this bright Lyman break galaxy.

7.7 Dust-to-metals ratio

The study of the dust-to-metals ratio (DTM) as a function of metallicity holds the potential to probe the dust formation mechanism. If dust is primarily produced by SNe, the DTM is expected to be independent of metallicity (Morgan & Edmunds, 2003). If dust grains grow in the ISM, a decline of the DTM is expected at low metallicities (Draine, 2009; Mattsson et al., 2012; Herrera-Camus et al., 2012). The host galaxy of GRB 111008A is characterized by a variety of metal absorption lines and the afterglow SED is well-calibrated. Thus, in this line of sight we have the opportunity to examine the question of the DTM of the GRB host galaxy through dust extinction along the line of sight.

For a system with a given extinction and metallicity we can calculate the dust-to-metals ratio relative to the Local Group value as

$$DTM = \frac{1}{DTM_{LG}} \times \frac{A_V}{N_{HI} \times 10^{[M/H]}}, \quad (7.1)$$

where $DTM_{LG} \equiv 10^{-21.3} \text{ mag cm}^2$ is the dust-to-metals ratio in the Local Group (Watson, 2011). Recently, Zafar & Watson (2013), using different classes of objects, found that DTM is independent of galaxy type or age, redshift, or metallicity, and is very close to the value in the Local Group.

The measured extinction along the sight line of GRB 111008A is affected by the host galaxy as well as the intervening absorber. Assuming that all the extinction is from the host galaxy and that the host galaxy has a metallicity of $[M/H] = [S/H]$, we find that the host galaxy has

$$DTM = 0.57 \pm 0.26. \quad (7.2)$$

We calculated the mean and the error of the DTM in a Monte Carlo fashion, where 50000 values for both A_V , $\log N_{HI}$ and $[M/H]$ are drawn from normal distributions with $A_V = 0.11 \pm 0.04 \text{ mag}$, $\log N_{HI}/\text{cm}^{-2} = 22.30 \pm 0.06$ and $[M/H] = -1.70 \pm 0.10$. For each triplet of sampled values a DTM is calculated, and finally the mean and the standard deviation of the 50000 DTM -values are computed.

In Fig. 7.5 we plot the DTM versus the metallicity for the GRB 111008A host with GRB-DLAs, QSO-DLAs, nearby lensed galaxies, and with the value found in the Local Group (see Zafar & Watson 2013 and Chen et al. 2013 for details). Given the uncertainty in A_V , the host has a DTM , which – within a 1σ error bar – is consistent with the DTM observed in the Local Group. Our data is also consistent with the scenario where the host

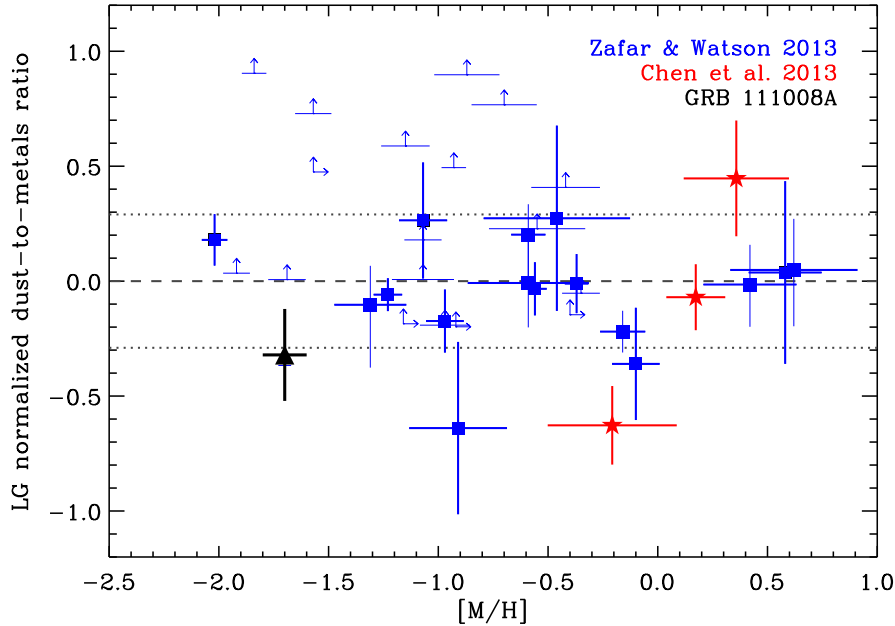


Figure 7.5: The dust-to-metals ratio versus metallicity. The dashed line shows the Local Group value, and the dotted lines indicate the scatter in the Local Group. The host of GRB 111008A, which is shown as a black triangle, has a dust-to-metals ratio which is consistent with being equal to or lower than the value in the Local Group. The other data points are from Zafar & Watson (2013) and Chen et al. (2013).

has a much lower *DTM* than the Local Group, especially if part of the extinction along the line of sight is due to the intervening absorber at $z = 4.6$.

7.8 Discussion

7.8.1 The GRB host galaxy

The abundance analysis shows that the GRB host absorber is a relatively low-metallicity system (about 2% solar metallicity) compared to the other GRB-DLAs at $z > 4.5$ (GRB 100219A and GRB 050904), see Fig. 7.6. The relative abundances are close to solar, as shown in Table 7.1, but we are unable to address whether the metals are depleted onto dust grains, since we have no reliable measurement of $[\text{Zn}/\text{Fe}]$ (typically decreasing with metallicity in both QSO- and GRB-DLAs: Wolfe et al., 2005; Savaglio et al., 2003; Dessauges-Zavadsky et al., 2006; Prochaska et al., 2007b; Noterdaeme et al., 2008; Rafelski et al., 2012), which is normally used to determine the amount of dust depletion.

In Fig. 7.7 the two high- z GRBs 100219A and 111008A (i.e. the only two GRBs with $z > 4.7$ and measured metallicities with errors smaller than 0.5 dex) are compared to the recently measured QSO-DLA metallicities (from Rafelski et al. 2014) at similar redshifts. The GRB metallicities fall within the range spanned by QSO-DLAs, but typically in the upper end of the distribution. This trend is also present at lower redshift (Fynbo et al., 2008). This phenomenon can be explained by the fact that GRB afterglows generally probe the star-forming ‘hearts’ of galaxies, while QSO-DLAs have a higher chance to probe the (less metal rich) outskirts of galaxies (see e.g. Prochaska et al. 2007b and

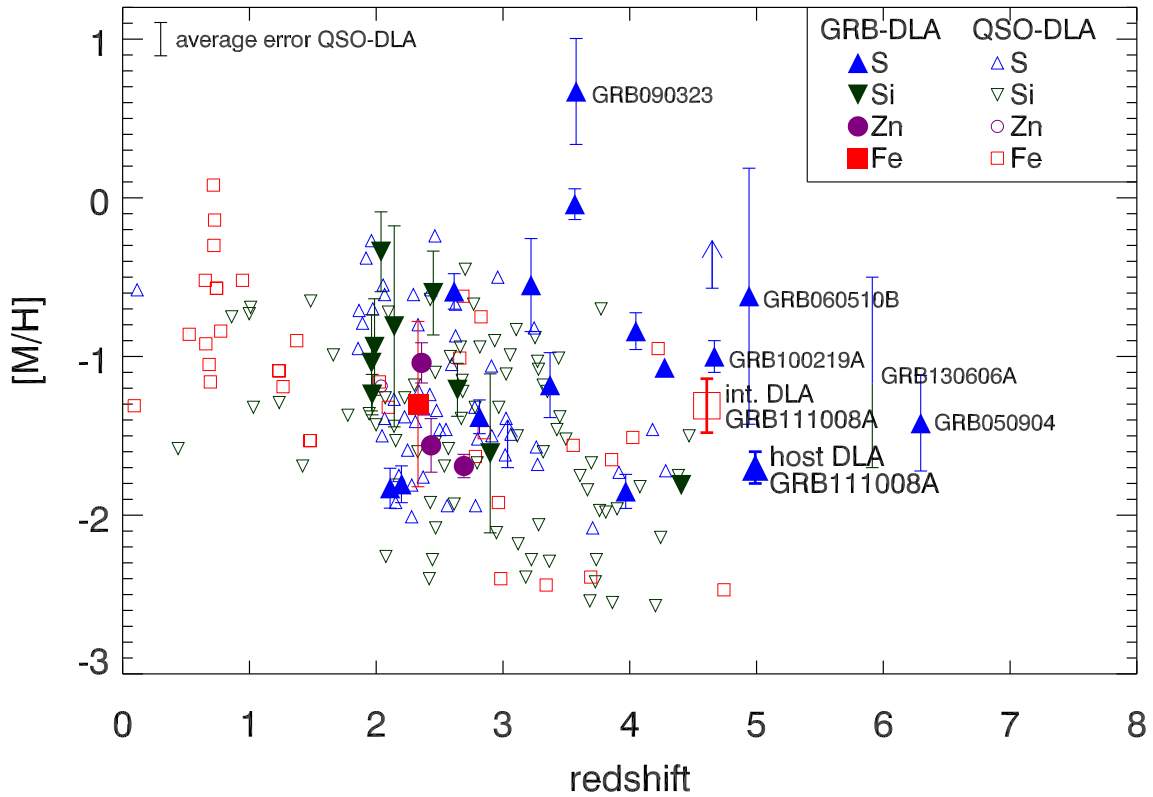


Figure 7.6: Absorption-line based metallicities $[M/H]$ as a function of redshift for GRB-DLAs (filled symbols) and QSO-DLAs (open symbols). The figure is adapted from Rafelski et al. (2012), with added GRB-DLAs from the following references: Savaglio et al. (2003); Vreeswijk et al. (2004); Fiore et al. (2005); Kawai et al. (2006); Watson et al. (2006); Berger et al. (2006); Prochaska et al. (2007a); Price et al. (2007); Chary et al. (2007); Thöne et al. (2008); Prochaska et al. (2009); D’Avanzo et al. (2010); D’Elia et al. (2010); Schady et al. (2011); De Cia et al. (2011); D’Elia et al. (2012); Thöne et al. (2013); Krühler et al. (2013); Chornock et al. (2013); D’Elia et al. (2014) (For the measurement of the metallicity of GRB 130606A from Chornock et al. (2013) the lower limit is based on Si and the upper limit is based on S. We have indicated this by the colors of the error bar belonging to this data point). Following Rafelski et al. (2012), we apply $[M/H] = [Fe/H] + 0.3$ in cases where the metal is iron, and no less-refractory element abundance is measured (this correction is also applied to the intervening absorber in the GRB 111008A sight line).

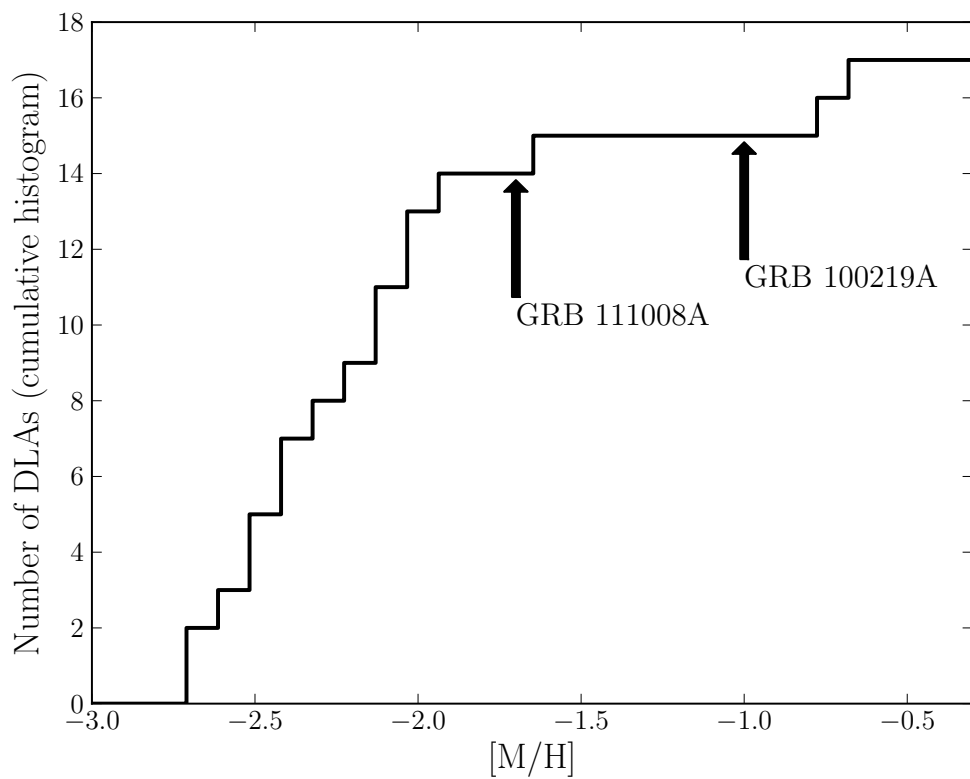


Figure 7.7: This figure compares the metallicity of the two high-redshift GRBs 100219A and 111008A with the 17 QSO-DLAs at $3.64 < z < 5.08$ from Rafelski et al. (2014). The two GRB-DLAs are clearly in the upper part of the metallicity distribution of QSO-DLAs, a trend which is also present at lower redshift.

Lemasle et al. 2013). It is remarkable, however, that the metallicity of GRB-DLAs does not seem to be as redshift dependent as the metallicity of QSO-DLAs. At lower redshifts the HI column density of GRB absorbers is much larger than that of QSO-DLAs.

Concerning α -element overabundance, Rafelski et al. (2012) argue that the α -to-iron-group abundance ratios in QSO-DLAs are consistent with those of halo-stars in the Milky Way. Unfortunately, with the lack of a reliably determined column density of zinc we cannot distinguish the scenario, where dust-depletion and α -element overabundance both are present, from the scenario where α -element overabundance and dust-depletion both are absent.

address the issue of α -elements overabundance.

The afterglow spectrum of the high-redshift GRB 100219A ($z = 4.7$) studied by Thöne et al. (2013) reveals a substantially higher metallicity of $[M/H] = -1.0 \pm 0.1$ and evidence for either depletion on dust grains or a strong α -element overabundance ($[S/Fe] = 0.8$). The GRB 100219A absorber is also substantially more complex with five velocity components spread over 160 km s^{-1} whereas we only require two components separated by 70 km s^{-1} to fit the metal lines from the GRB 111008A absorber. Higher velocity widths for GRB 100219A compared to GRB 111008A are also expected due to the relation between velocity width and metallicity (Ledoux et al., 2006; Neeleman et al., 2013).

The study by Rafelski et al. (2014) measures metallicities of 17 QSO-DLAs with $z = 3.64 - 5.08$. They show that the metallicity of QSO-DLAs decreases rapidly at $z > 4.7$, likely because the state of the gas in the outer part of DLA-galaxies changes at this redshift. It is unknown whether GRB-DLAs exhibit the same trend. So far the only GRB-DLAs with a well-determined metallicity at $z > 4.7$ are GRB 111008A and GRB 100219A. Since GRB-DLA sight lines have a different origin than QSO-DLAs it is not evident whether or not a similar decline in the metallicity of GRB-DLAs is present.

7.8.2 The intervening DLA

The $z = 4.6$ intervening DLA absorber has a high neutral hydrogen column density, which is consistent with being among the highest column densities of the 18 QSO-DLAs observed at similar high redshifts by Rafelski et al. (2014). A high metallicity is also indicated by the large equivalent width of SiII $\lambda 1526$. This suggests that this is not a typical intervening system likely associated with the outer regions of the absorber (Prochaska et al., 2007b). It is possible that the line of sight towards the GRB crossed inner parts of the foreground absorber, thus showing higher column densities and metallicity. Further observations can potentially reveal the nature of the intervening absorber.

7.9 Summary

With spectroscopy of the GRB 111008A afterglow we have a rare chance of studying the properties of a sight line originating in a star forming region of a $z = 5.0$ galaxy. By analyzing absorption lines from the interstellar medium of the GRB's host galaxy a metallicity of $[S/H] = -1.70 \pm 0.10$ is measured, and from fitting the spectral energy distribution the dust extinction is determined to be $A_V = 0.11 \pm 0.04 \text{ mag}$. The dust-to-metals ratio is equal to or lower than what is observed in the Local Group. Determination of the dust-to-metals ratio of such high-redshift environments is important, since it can potentially constrain dust production mechanisms.

GRB111008A offers two noteworthy features: it is the highest redshift GRB host galaxy with such a precise metallicity measurement, and it is also the first time fine structure lines from FeII have been observed at such a high redshift. This is special because the signal-to-noise required to detect the relatively weak fine-structure lines is often not reached at high redshift. Their presence unambiguously confirms the absorption system as the GRB's host galaxy.

In the sight line towards the GRB is also a DLA at $z = 4.6$. The metallicity of this system is constrained by $[\text{Si}/\text{H}] > -2.15$ at a 2σ limit, $[\text{Fe}/\text{H}] = -1.61 \pm 0.17$ and $[\text{Ni}/\text{H}] = -1.33 \pm 0.12$. The role of dust depletion is unclear. With photometric observations of the field surrounding the GRB's position performed roughly two years after explosion we detect emission from a source, which could be the intervening system. The offset between the detected source and the GRB sight line would be 4 ± 1 kpc at the redshift of the intervening DLA. Deeper observations could potentially reveal whether or not this source is related to the intervening DLA at $z = 4.6$.

Bibliography

- Aihara, H., et al. 2011, *ApJS*, 193, 29
- Appenzeller, I., et al. 1998, *The Messenger*, 94, 1
- Asplund, M., Grevesse, N., Sauval, A. J., & Scott, P. 2009, *ARA&A*, 47, 481
- Basa, S., Cuby, J. G., Savaglio, S., Boissier, S., Clément, B., Flores, H., Le Borgne, D., & Mazure, A. 2012, *A&A*, 542, A103
- Baumgartner, W. H., et al. 2011, *GRB Coordinates Network*, 12424, 1
- Beardmore, A. P., Evans, P. A., Goad, M. R., & Osborne, J. P. 2011, *GRB Coordinates Network*, 12425, 1
- Berger, E., et al. 2011, *ApJ*, 743, 204
- Berger, E., Penprase, B. E., Cenko, S. B., Kulkarni, S. R., Fox, D. B., Steidel, C. C., & Reddy, N. A. 2006, *ApJ*, 642, 979
- Bloom, J. S., Kulkarni, S. R., & Djorgovski, S. G. 2002, *AJ*, 123, 1111
- Bouwens, R. J., Illingworth, G. D., Franx, M., & Ford, H. 2007, *ApJ*, 670, 928
- Campana, S., et al. 2006, *Nature*, 442, 1008
- Chary, R., Berger, E., & Cowie, L. 2007, *ApJ*, 671, 272
- Chen, B., Dai, X., Kochanek, C. S., & Chartas, G. 2013, *astroph/1306.0008*
- Chornock, R., Berger, E., Fox, D. B., Lunnan, R., Drout, M. R., Fong, W.-f., Laskar, T., & Roth, K. C. 2013, *ApJ*, 774, 26
- Covino, S., et al. 2013, *MNRAS*, 432, 1231
- Cucchiara, A., et al. 2011, *ApJ*, 736, 7
- D'Avanzo, P., et al. 2010, *A&A*, 522, A20
- De Cia, A., et al. 2011, *MNRAS*, 412, 2229
- D'Elia, V., Campana, S., Covino, S., D'Avanzo, P., Piranomonte, S., & Tagliaferri, G. 2012, *Memorie della Societa Astronomica Italiana Supplementi*, 21, 206
- D'Elia, V., et al. 2010, *A&A*, 523, A36
- . 2014, *ArXiv astroph/1402.4026*

- Dessauges-Zavadsky, M., Prochaska, J. X., D'Odorico, S., Calura, F., & Matteucci, F. 2006, *A&A*, 445, 93
- Draine, B. T. 2009, in *Astronomical Society of the Pacific Conference Series*, Vol. 414, *Cosmic Dust - Near and Far*, ed. T. Henning, E. Grün, & J. Steinacker, 453
- Evans, P. A., et al. 2009, *MNRAS*, 397, 1177
- . 2007, *A&A*, 469, 379
- Fiore, F., et al. 2005, *ApJ*, 624, 853
- Foreman-Mackey, D., Hogg, D. W., Lang, D., & Goodman, J. 2013, *PASP*, 125, 306
- Fynbo, J. P. U., et al. 2009, *ApJS*, 185, 526
- Fynbo, J. P. U., Prochaska, J. X., Sommer-Larsen, J., Dessauges-Zavadsky, M., & Møller, P. 2008, *ApJ*, 683, 321
- Fynbo, J. P. U., et al. 2006, *A&A*, 451, L47
- Galama, T. J., et al. 1998, *Nature*, 395, 670
- Greiner, J., et al. 2008, *PASP*, 120, 405
- . 2011, *A&A*, 526, A30
- Hartoog, O. E., et al. 2013, *MNRAS*, 430, 2739
- Herrera-Camus, R., et al. 2012, *ApJ*, 752, 112
- Hjorth, J., & Bloom, J. S. 2012, *The Gamma-Ray Burst - Supernova Connection* (Cambridge University Press, Cambridge), 169–190
- Hjorth, J., et al. 2012, *ApJ*, 756, 187
- . 2003, *Nature*, 423, 847
- Horne, K. 1986, *PASP*, 98, 609
- Jakobsson, P., Hjorth, J., Fynbo, J. P. U., Watson, D., Pedersen, K., Björnsson, G., & Gorosabel, J. 2004, *ApJ*, 617, L21
- Kalberla, P. M. W., Burton, W. B., Hartmann, D., Arnal, E. M., Bajaja, E., Morras, R., & Pöppel, W. G. L. 2005, *A&A*, 440, 775
- Kawai, N., et al. 2006, *Nature*, 440, 184
- Krühler, T., et al. 2011, *A&A*, 534, A108
- . 2008, *ApJ*, 685, 376
- . 2013, *A&A*, 557, A18
- Ledoux, C., Petitjean, P., Fynbo, J. P. U., Møller, P., & Srianand, R. 2006, *A&A*, 457, 71

- Ledoux, C., Vreeswijk, P. M., Smette, A., Fox, A. J., Petitjean, P., Ellison, S. L., Fynbo, J. P. U., & Savaglio, S. 2009, *A&A*, 506, 661
- Lemasle, B., et al. 2013, *A&A*, 558, A31
- Levan, A. J., Wiersema, K., & Tanvir, N. R. 2011a, GRB Coordinates Network, 12426, 1
- . 2011b, GRB Coordinates Network, 12429, 1
- Matteucci, F., & Greggio, L. 1986, *A&A*, 154, 279
- Mattsson, L., Andersen, A. C., & Munkhammar, J. D. 2012, *MNRAS*, 423, 26
- Modigliani, A., et al. 2010, in *Society of Photo-Optical Instrumentation Engineers (SPIE) Conference Series*, Vol. 7737, Society of Photo-Optical Instrumentation Engineers (SPIE) Conference Series
- Modjaz, M., et al. 2006, *ApJ*, 645, L21
- Morgan, H. L., & Edmunds, M. G. 2003, *MNRAS*, 343, 427
- Nardini, M., Klose, S., Greiner, J., & Afonso, P. 2011, GRB Coordinates Network, 12428, 1
- Neeleman, M., Wolfe, A. M., Prochaska, J. X., & Rafelski, M. 2013, *ApJ*, 769, 54
- Noterdaeme, P., Ledoux, C., Petitjean, P., & Srianand, R. 2008, *A&A*, 481, 327
- Pei, Y. C. 1992, *ApJ*, 395, 130
- Perley, D. A., et al. 2009, *AJ*, 138, 1690
- Price, P. A., et al. 2007, *ApJ*, 663, L57
- Prochaska, J. X., Chen, H.-W., & Bloom, J. S. 2006, *ApJ*, 648, 95
- Prochaska, J. X., et al. 2007a, *ApJS*, 168, 231
- Prochaska, J. X., Chen, H.-W., Dessauges-Zavadsky, M., & Bloom, J. S. 2007b, *ApJ*, 666, 267
- Prochaska, J. X., Chen, H.-W., Wolfe, A. M., Dessauges-Zavadsky, M., & Bloom, J. S. 2008, *ApJ*, 672, 59
- Prochaska, J. X., et al. 2009, *ApJ*, 691, L27
- Rafelski, M., Neeleman, M., Fumagalli, M., Wolfe, A. M., & Prochaska, J. X. 2014, *ApJ*, 782, L29
- Rafelski, M., Wolfe, A. M., Prochaska, J. X., Neeleman, M., & Mendez, A. J. 2012, *ApJ*, 755, 89
- Salvaterra, R., et al. 2009, *Nature*, 461, 1258
- Sari, R., Piran, T., & Narayan, R. 1998, *ApJ*, 497, L17
- Savaglio, S. 2006, *New Journal of Physics*, 8, 195

Savaglio, S., Fall, S. M., & Fiore, F. 2003, *ApJ*, 585, 638

Saxton, C. J., et al. 2011, *GRB Coordinates Network*, 12423, 1

Schady, P., Savaglio, S., Krühler, T., Greiner, J., & Rau, A. 2011, *A&A*, 525, A113

Schulze, S., et al. 2012, *A&A*, 546, A20

Skrutskie, M. F., et al. 2006, *AJ*, 131, 1163

Sparre, M., et al. 2011, *ApJ*, 735, L24

Stanek, K. Z., et al. 2003, *ApJ*, 591, L17

Tanvir, N. R., et al. 2009, *Nature*, 461, 1254

—. 2012, *ApJ*, 754, 46

Thöne, C. C., et al. 2013, *MNRAS*, 428, 3590

—. 2008, *A&A*, 489, 37

Tolstoy, E. 2011, *Science*, 333, 176

Vernet, J., et al. 2011, *A&A*, 536, A105

Vreeswijk, P. M., et al. 2004, *A&A*, 419, 927

—. 2007, *A&A*, 468, 83

Watson, D. 2011, *A&A*, 533, A16

Watson, D., et al. 2006, *ApJ*, 652, 1011

Wiersema, K., et al. 2011, *GRB Coordinates Network*, 12431, 1

Willingale, R., Starling, R. L. C., Beardmore, A. P., Tanvir, N. R., & O'Brien, P. T. 2013, *MNRAS*, 431, 394

Wolfe, A. M., Gawiser, E., & Prochaska, J. X. 2005, *ARA&A*, 43, 861

Wolfe, A. M., Prochaska, J. X., Jorgenson, R. A., & Rafelski, M. 2008, *ApJ*, 681, 881

Xu, D., et al. 2013, *ApJ*, 776, 98

Xu, D., Malesani, D., Buchhave, L. A., Schulze, S., & Jakobsson, P. 2011, *GRB Coordinates Network*, 12427, 1

Zafar, T., & Watson, D. 2013, *A&A*, 560, A26

Zafar, T., Watson, D., Fynbo, J. P. U., Malesani, D., Jakobsson, P., & de Ugarte Postigo, A. 2011, *A&A*, 532, A143

7.10 APPENDIX: The issue of saturation for the S II 1253-transition

In Section 7.3.1 it is mentioned that the SII $\lambda 1253$ transition is mildly saturated. To clearly address the issue of saturation for this transition we developed a multi-component line fitting code, where the Monte Carlo Markov Chain (MCMC) package, *Emcee* (Foreman-Mackey et al., 2013), is used as fitting method. Such MCMC-algorithms are ideal for cases with degenerate models. A fit is performed for NiII $\lambda 1370$ and SII $\lambda 1253$. In the MCMC run we use a flat prior with $8 < b(\text{km s}^{-1}) < 40$ and $12 < \log N/\text{cm}^{-2} < 19$ for both S and Ni. Again, we use two absorption components for each transition, and the b - and z -values are linked between NiII $\lambda 1370$ and SII $\lambda 1253$. We sample 96000 points from the likelihood function after a burn-in of 32000 points (to ensure convergence of the chain).

In Fig. 7.8 the 1σ , 2σ and 3σ contours are shown for the b - and N -values, as well as contours of constant equivalent width. For NiII $\lambda 1370$ the column density is well-constrained for both components⁵. For SII $\lambda 1253$ the blue component has a well-constrained column density, whereas the red component is saturated (the column density can vary by four orders of magnitude within the 2σ confidence interval).

For NiII $\lambda 1370$ the difference in $\log N$ for the two components is relatively small (for the blue component $\log N/\text{cm}^{-2}$ is only 0.1 dex lower than for the red component). Assuming the same difference in $\log N/\text{cm}^{-2}$ for the two components of SII $\lambda 1253$, we derive $\log N/\text{cm}^{-2} = 15.79 \pm 0.08$, which is clearly consistent with the value reported in Table 7.1. Thus, the column density of SII can be reliably determined even though one of the components is saturated.

Finally, we note that the blue component has a larger b -value than the red component in the model in the present section. This is contradicting the results from Section 7.3.1, where the red component has a larger b -value than the blue component. The explanation is that more absorption lines are included in the model in Section 7.3.1. If we remove all other absorption components than SII and NiII from the model in Section 7.3.1 we get $b = 22.8 \pm 4.0 \text{ km s}^{-1}$ for the blue component and $b = 15.6 \pm 4.3 \text{ km s}^{-1}$ for the red component, which is consistent with the b -values from the present section. In all cases (i.e. in the MCMC model, and in the two VPFIT models) we obtain column densities which are consistent with each other, so this is not an important caveat.

7.10.1 The effect a third absorption component

An assumption in the above derivation of the sulfur column density is that there are only two absorption components. We will now discuss how a third hidden component would affect the derived column density of sulfur. The red component of SII $\lambda 1253$ is mildly saturated, and it would therefore be possible to add a narrow line with the same redshift as the red component without affecting the way the spectrum looks. We could for example add an extra component with $b = 10 \text{ km s}^{-1}$ and $\log N/\text{cm}^{-2} = 16.3$ without affecting the spectrum, if the component has a redshift coinciding with the red component.

The blue component is not saturated, so here it is not possible to add such a component without heavily modifying the spectrum. The situation is therefore the same as in Fig. 7.8; the blue component is reliably determined, and the red component is uncertain because it is saturated, so we can only derive the total column density under the assumption that the ratio between the column density of the blue and the red component is the

⁵Note that here the contribution from fine structure lines is not included in the column density of nickel (unlike in Table 7.1, where it is included).

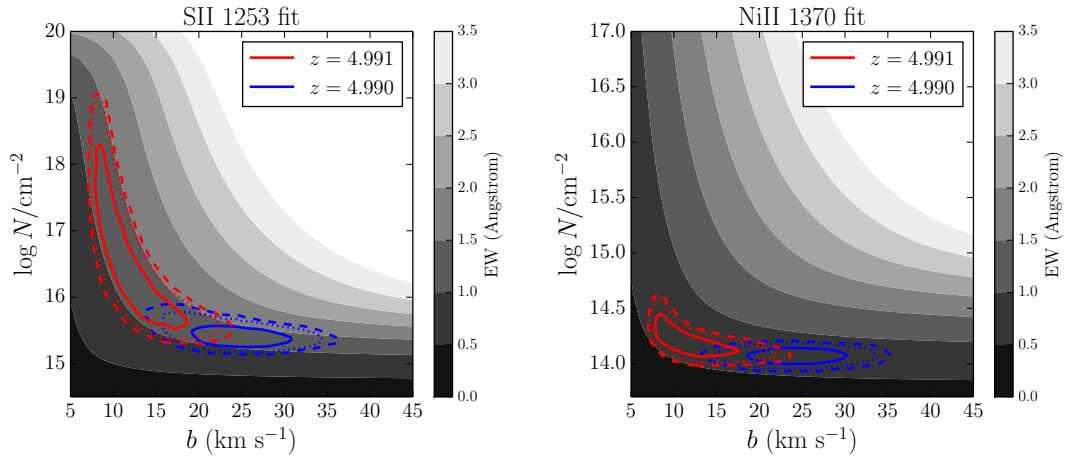


Figure 7.8: 1σ , 2σ and 3σ confidence levels (solid, dotted and dashed contours, respectively) for the Doppler-parameters and the column densities for SII and NiII. The grey contours show regions of constant equivalent width.

same as for nickel. Our conclusion is that the probability that large column densities are present in a hidden saturated component is low.

7.11 APPENDIX: The X-shooter spectrum

Fig. 7.9 and 7.10 show absorption lines in the normalized X-shooter spectrum for the VIS and NIR arms.

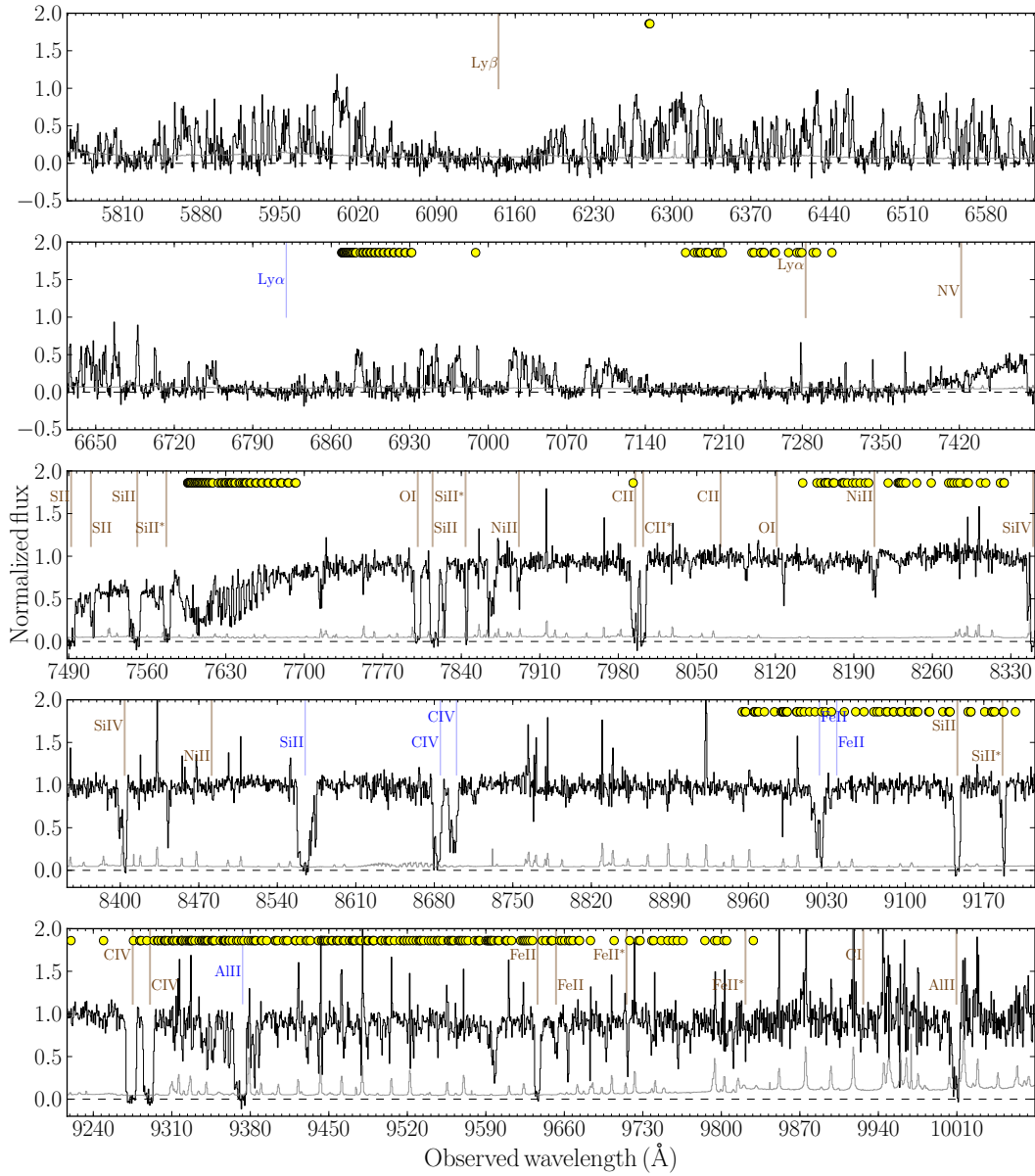


Figure 7.9: The VIS spectrum. The yellow circles mark telluric features, the brown marks show absorption lines from the GRB host galaxy, and the blue marks show absorption features from the intervening system at $z = 4.6$. The spectrum is shown in black, and the error spectrum is shown in gray.

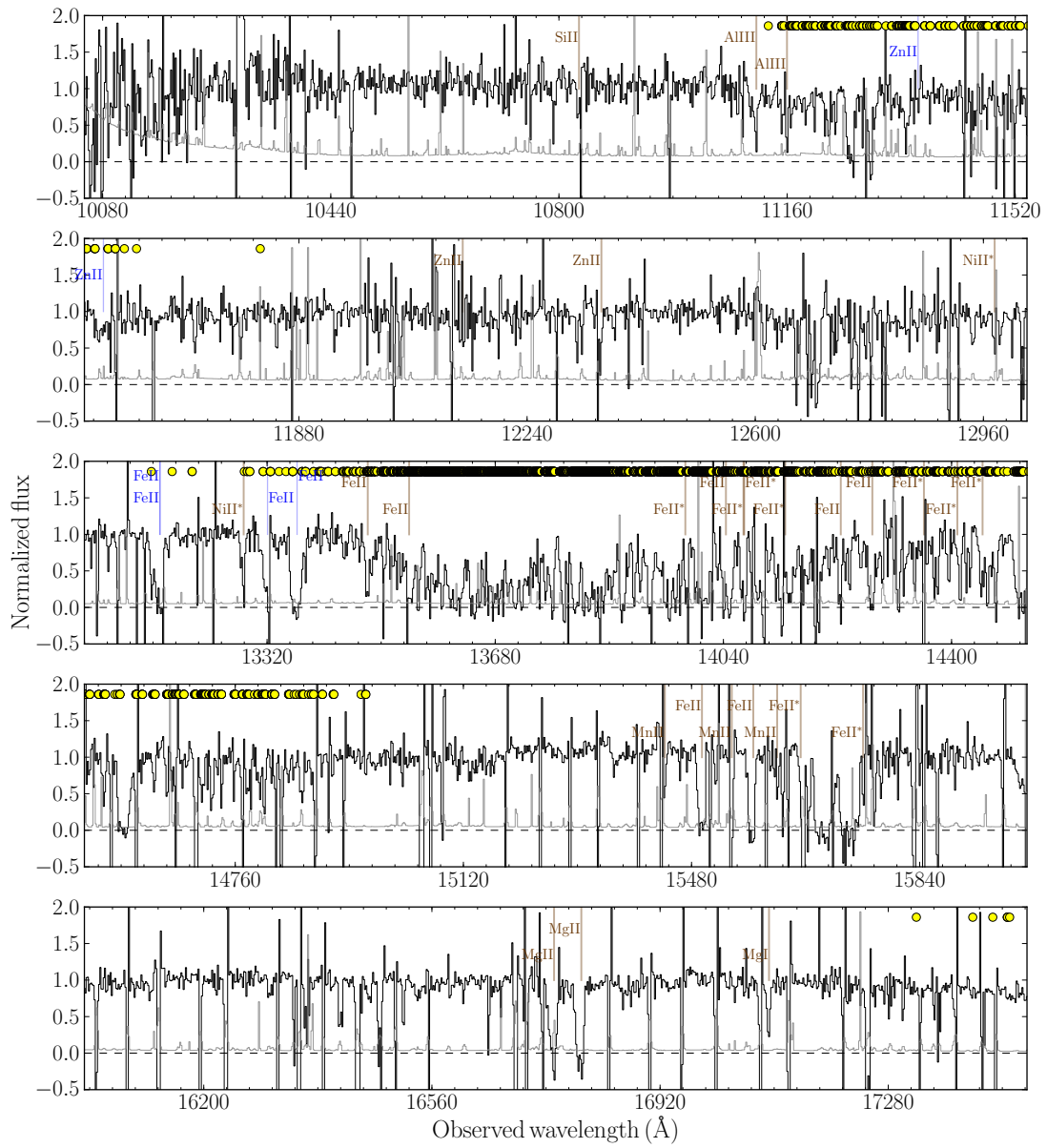


Figure 7.10: Same as Fig. 7.9, but for the NIR spectrum.

Chapter 8

Conclusions and perspectives for further research

In this thesis results from studies from several different fields have been presented. A selection of results is below:

- Chapter 2 and 3 studied computer simulations of the velocity distribution of dark matter particles in halo structures. Where baryonic particles usually have isotropic velocity dispersions, collisionless particles tend to have anisotropic distributions. The anisotropy of a velocity distributions is usually parametrized as,

$$\beta(r) = 1 - \frac{\sigma_{\text{tan}}^2}{2\sigma_{\text{rad}}^2}, \quad (8.1)$$

where σ_{rad} is the radial velocity dispersion and σ_{tan} is the tangential dispersion. With this definition a region with $\beta > 0$ has radially dominated anisotropy and $\beta < 0$ means tangentially dominated anisotropy. Hansen et al. (2010) claims that equilibrated structures exposed to perturbations follow an *attractor*, which relates β (at a given radius) to the density slope, $\gamma \equiv d \log \rho / d \log r$, and the slope of the radial velocity dispersion profile, $\kappa \equiv d \log \sigma_{\text{rad}}^2 / d \log r$. Chapter 2 and 3 study the behaviour of $\beta(r)$, $\gamma(r)$ and $\kappa(r)$ in various numerical simulations. One aim of these chapters is to study under what conditions structures end up following the attractor from Hansen et al. (2010). An important finding is that the merging of two halos produce a structure that does not follow the attractor. The reason for this is that mergers produce halos with β -profiles that are far from being spherically symmetric. Since mergers (and anisotropic accretion processes) are frequent in cosmological structure formation, halos in cosmological simulations are not expected to follow the attractor from Hansen et al. (2010). Furthermore, many other analytical models of the equilibrium of dark matter systems assuming spherically symmetric β -profiles (Hansen & Moore, 2006; Pontzen & Governato, 2013; Hjorth & Williams, 2010) give an incorrect description of cosmological halos, because these models assume spherically symmetric β -profiles.

- Chapter 4 studies the Illustris simulation, which is one of the largest hydrodynamical galaxy formation simulations ever made. One result worth pointing out is that the relation between star formation rate and stellar mass for the galaxies in Illustris agrees well with observations at $z = 0$ and $z = 4$. At $z = 2$ there are, however, too

low star formation rates in Illustris, and it is concluded that it is an important challenge for future galaxy formation models to reproduce the observed normalisation at $z = 2$. Another important limitation of the Illustris simulation is that it produces too few starbursts (starbursts are galaxies with a heavily enhanced star formation rate compared to the star formation rate – stellar mass relation).

- Chapter 5, 6 and 7 study long gamma-ray bursts and their host galaxies. An important result is the detection of a core-collapse supernova in the optical spectrum of a gamma-ray burst at $z = 0.55$. This is important partially because it confirms that long gamma-ray bursts can be produced by core-collapse supernovae, but especially because it establishes that supernovae associated with gamma-ray bursts can be observed at such high redshifts. Observations of such high- z supernovae associated with long GRBs have recently received a lot of attention because they can be used as cosmological standard candles (Li et al., 2014; Cano & Jakobsson, 2014). Chapter 7 studies the sight line towards a gamma-ray bursts at $z = 5$, and the dust extinction and metallicity from the host galaxy are measured. It is shown that the metallicity is significantly lower than solar metallicity, but the abundance pattern of the metals is very similar to the solar abundance pattern. This indicates that the metals in this $z = 5$ galaxy were formed by the same mechanism(s) as the metals in the Sun.

As seen, this thesis has presented results in both observational and numerical astrophysics. In the next couples of years I would like to focus on connecting properties of star formation in observations and simulations of galaxies. Specifically, I would like to investigate how star formation at high redshift can be constrained by combining observations of gamma-ray bursts with cosmological simulations. Another topic from this thesis I would like to investigate further is the issue of why there are too few starburst galaxies in the Illustris simulation. Two projects, which I have already started to work on, addressing these questions are:

- **Gamma-ray bursts in the Illustris simulation:** In this project I will study gamma-ray bursts in the Illustris simulation. To select a population of galaxies that mimic gamma-ray burst host galaxies I will sample star-forming galaxies, and pick out recently formed star particles (as also done in Pontzen et al., 2010). These star particles will like gamma-ray burst progenitors trace regions of recent star formation. An important aspect of this project is to see how a metallicity cutoff (GRBs mainly happen in low-metallicity galaxies, Vergani et al. 2014) affects e.g. the stellar mass function and UV-luminosity functions of the population of gamma-ray burst host galaxies. It is important to understand this question in order to relate the number counts of GRB host galaxies to the global star formation rate in the Universe at a given redshift (as done by e.g. Robertson & Ellis, 2012; Jakobsson et al., 2012).
- **Bursty star formation in the FIRE simulations:** In this project I will analyse properties of the star formation histories in the FIRE-simulations (Hopkins et al., 2013). The FIRE simulations are cosmological zoom-simulations of individual galaxies. A feature of the feedback model in these simulations is that the characteristic variability timescale of the star formation rate is $\simeq 10$ Myr, which is much lower than in Illustris. In this study it will be revealed whether such a model is able to produce starbursts (unlike the Illustris simulation). It will also be studied how SFRs derived

from different SFR-indicators deviate from each other: SFR-indicators have different sensitivity timescales (ranging from 10 to 100 Myr, see Kennicutt & Evans 2012), so if the SFR is variable on short timescales ($\simeq 10$ Myr), it is expected that indicators sensitive to the SFR in the last 100 Myr will over-estimate or under-estimate the true SFR of observed galaxies.

Bibliography

Cano Z., Jakobsson P., 2014, ArXiv: 1409.3570

Hansen S. H., Juncher D., Sparre M., 2010, ApJ, 718, L68

Hansen S. H., Moore B., 2006, New Astronomy, 11, 333

Hjorth J., Williams L. L. R., 2010, ApJ, 722, 851

Hopkins P. F., Keres D., Onorbe J., Faucher-Giguere C.-A., Quataert E., Murray N., Bullock J. S., 2013, ArXiv: 1311.2073

Jakobsson P., et al., 2012, ApJ, 752, 62

Kennicutt R. C., Evans N. J., 2012, ARA&A, 50, 531

Li X., Hjorth J., Wojtak R., 2014, ArXiv: 1409.3567

Pontzen A., Deason A., Governato F., Pettini M., Wadsley J., Quinn T., Brooks A., Bellovary J., Fynbo J. P. U., 2010, MNRAS, 402, 1523

Pontzen A., Governato F., 2013, MNRAS, 430, 121

Robertson B. E., Ellis R. S., 2012, ApJ, 744, 95

Vergani S. D., et al., 2014, ArXiv: 1409.7064

Appendix A

Author statements

The following pages contain author statements from the various papers.



3A. Co-authorship statement

All papers/manuscripts with multiple authors which is part of a PhD thesis should contain a co-author statement, stating the PhD student's contribution to the paper.

1. General information	
PhD student	Name Martin Sparre
	Civ.reg.no. (If not applicable, then birth date) 0312861097
	E-mail martinsparre@gmail.com
	Department Niels Bohr Institute, Dark Cosmology Centre
Principal supervisor	Name Johan P.U. Fynbo
	E-mail jfynbo@dark-cosmology.dk

2. Title of PhD thesis
Galaxy formation: observations and simulations of galaxies

3. This co-authorship declaration applies to the following paper/manuscript:
Title: Spectroscopic Evidence for SN 2010ma Associated with GRB 101219B Author(s): Sparre, M.; Sollerman, J.; Fynbo, J. P. U.; Malesani, D.; Goldoni, P.; de Ugarte Postigo, A.; Covino, S.; D'Elia, V.; Flores, H.; Hammer, F.; Hjorth, J.; Jakobsson, P.; Kaper, L.; Leloudas, G.; Levan, A. J.; Milvang-Jensen, B.; Schulze, S.; Tagliaferri, G.; Tanvir, N. R.; Watson, D. J.; Wiersema, K.; Wijers, R. A. M. J. Journal: ApJ Letters Vol./page: 2012, 735L, 24 DOI: 10.1088/2041-8205/735/1/L24

4. Contributions to the paper/manuscript made by the PhD student

What was the role of the PhD student in designing the study?

The initial idea of the paper came from a discussion between the PhD student, Prof. Jens Hjorth and Prof. Johan P.U. Fynbo.

How did the PhD student participate in data collection and/or development of theory?

The PhD student participated in the part of the collaboration was responsible for carrying out the observations. The following coauthors participated in carrying out the observations (sorted by contribution):

de Ugarte Postigo, A.; Goldoni, P.; Milvang-Jensen, B.; Malesani, D.; Sparre, M.; Fynbo, J. P. U.; Leloudas, G.; Covino, S.; Flores, H.; D'Elia, V.; Levan, A.

(List is taken from the initial circular, 2011, GCN, 11579, see <http://adsabs.harvard.edu/abs/2011GCN..11579...1D>)

Which part of the manuscript did the PhD student write or contribute to?

The PhD student drafted the initial paper. Prof. Johan P.U. Fynbo, Prof. Jesper Sollerman and Dr. Daniele Malesani subsequently edited and adjusted the paper in collaboration with the PhD student.

Dr. de Ugarte Postigo did the analysis behind Table 2.

Did the PhD student read and comment on the final manuscript?

Yes.

5. Material in the paper from another degree / thesis :

Articles/work published in connection with another degree/thesis must not form part of the PhD thesis. Data collected and preliminary work carried out as part of another degree/thesis may be part of the PhD thesis if further research, analysis and writing are carried out as part of the PhD study.

Does the paper contain data material, which has also formed part of a previous degree / thesis (e.g. your master's degree)


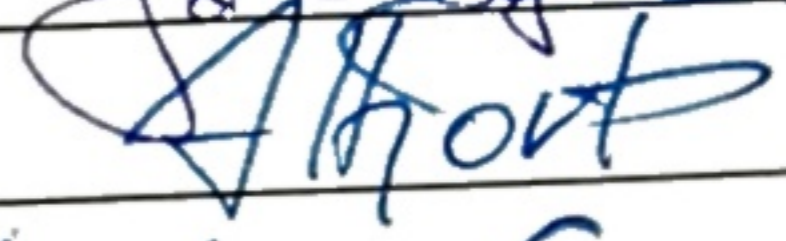
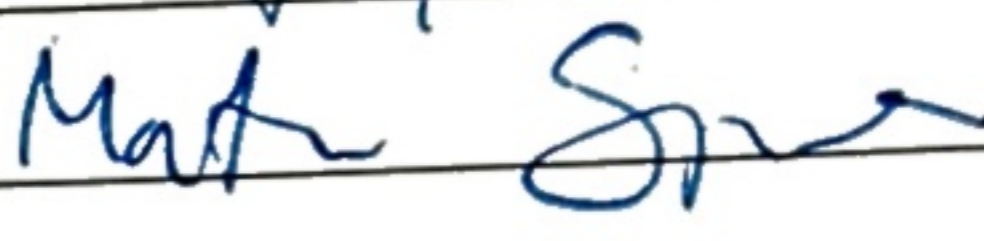
Yes:

Please indicate which degree / thesis: _____

No:

Please indicate which specific part(-s) of the paper that has been produced as part of the PhD study:

Everything.

6. Signatures of co-authors:		
Date	Name	Signature
17/9 - 2014	Prof. Johan P.U. Fynbo	
17/9 - 2014	Prof. Jens Hjorth	
17 September 2014	Martin Sparre	

When completed, please send the form to the PhD secretary at the department.

www.science.ku.dk/english/research/phd/student/contact/departments/



3A. Co-authorship statement

All papers/manuscripts with multiple authors which is part of a PhD thesis should contain a co-author statement, stating the PhD student's contribution to the paper.

1. General information	
PhD student	Name Martin Sparre
	Civ.reg.no. (If not applicable, then birth date) 0312861097
	E-mail martinsparre@gmail.com
	Department Niels Bohr Institute, Dark Cosmology Centre
Principal supervisor	Name Johan P.U. Fynbo
	E-mail jfynbo@dark-cosmology.dk

2. Title of PhD thesis
Galaxy formation: observations and simulations of galaxies

3. This co-authorship declaration applies to the following paper/manuscript:
Title: Asymmetric velocity anisotropies in remnants of collisionless mergers Author(s): Martin Sparre, Steen H. Hansen Journal: JCAP Vol./page: 2012, 07, 42 DOI: 10.1088/1475-7516/2012/07/042

4. Contributions to the paper/manuscript made by the PhD student

What was the role of the PhD student in designing the study?

The PhD student and Steen H. Hansen got the overall idea for the paper during discussions. The numerical setups were designed by the PhD student.

How did the PhD student participate in data collection and/or development of theory?

The PhD student did all the work, i.e. ran all the simulations, and did all the data analysis

Which part of the manuscript did the PhD student write or contribute to?

The PhD student wrote the entire paper. The supervisor commented on it before submission.

Did the PhD student read and comment on the final manuscript?

The PhD student wrote the final manuscript.

5. Material in the paper from another degree / thesis :

Articles/work published in connection with another degree/thesis must not form part of the PhD thesis.

Data collected and preliminary work carried out as part of another degree/thesis may be part of the PhD thesis if further research, analysis and writing are carried out as part of the PhD study.

Does the paper contain data material, which has also formed part of a previous degree / thesis (e.g. your master's degree)

Yes:

No:

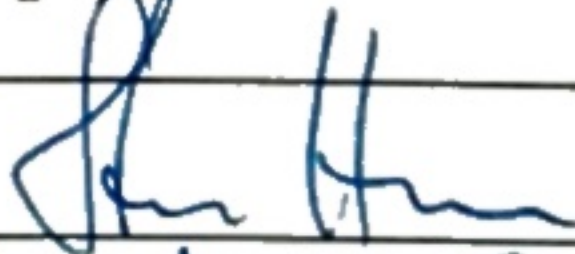

Please indicate which degree / thesis: _____

Please indicate which specific part(-s) of the paper that has been produced as part of the PhD study:

Everything

The co-author statement should always be signed by the first author, the corresponding-/senior author and the PhD student. If there are two or three authors the statement must always be signed by them all.

6. Signatures of co-authors:

<i>Date</i>	<i>Name</i>	<i>Signature</i>
17 Sep 2014	Dr. Steen H. Hansen	
17 September 2014	Martin Sparre	



3A. Co-authorship statement

All papers/manuscripts with multiple authors which is part of a PhD thesis should contain a co-author statement, stating the PhD student's contribution to the paper.

1. General information	
PhD student	Name Martin Sparre
	Civ.reg.no. (If not applicable, then birth date) 0312861097
	E-mail martinsparre@gmail.com
	Department Niels Bohr Institute, Dark Cosmology Centre
Principal supervisor	Name Johan P.U. Fynbo
	E-mail jfynbo@dark-cosmology.dk

2. Title of PhD thesis
Galaxy formation: observations and simulations of galaxies

3. This co-authorship declaration applies to the following paper/manuscript:
Title: The behaviour of shape and velocity anisotropy in dark matter haloes Author(s): Martin Sparre, Steen H. Hansen Journal: JCAP Vol./page: 2012, 10, 49 DOI: 10.1088/1475-7516/2012/10/049

4. Contributions to the paper/manuscript made by the PhD student

What was the role of the PhD student in designing the study?

The PhD student and Steen H. Hansen got the overall idea for the paper during discussions. The numerical setups were designed by the PhD student.

How did the PhD student participate in data collection and/or development of theory?

The PhD student did all the work, i.e. ran all the simulations, did all the data analysis, and created all figures.

Which part of the manuscript did the PhD student write or contribute to?

The PhD student wrote the entire paper. The supervisor commented on it before submission.

Did the PhD student read and comment on the final manuscript?

The PhD student wrote the final manuscript.

5. Material in the paper from another degree / thesis :

Articles/work published in connection with another degree/thesis must not form part of the PhD thesis. Data collected and preliminary work carried out as part of another degree/thesis may be part of the PhD thesis if further research, analysis and writing are carried out as part of the PhD study.

Does the paper contain data material, which has also formed part of a previous degree / thesis (e.g. your master's degree)

Yes:

Please indicate which degree / thesis: _____

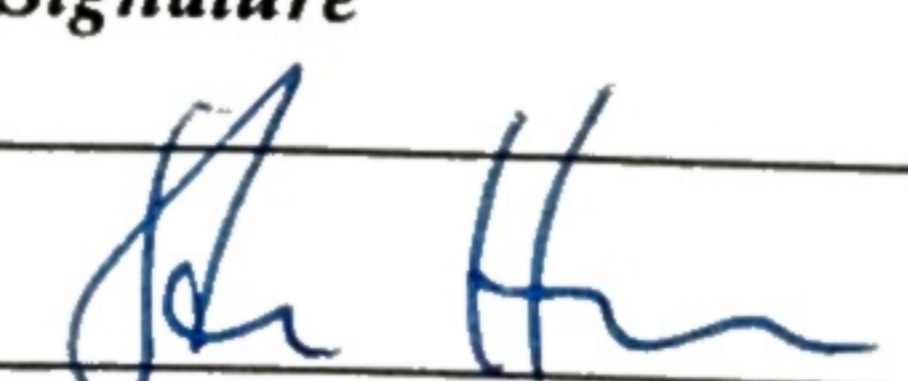
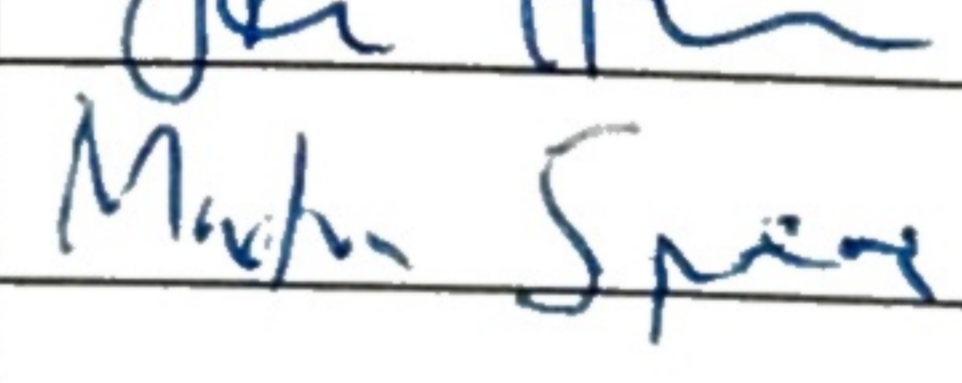
No:

Please indicate which specific part(-s) of the paper that has been produced as part of the PhD study:

Everything.

The co-author statement should always be signed by the first author, the corresponding-/senior author and the PhD student. If there are two or three authors the statement must always be signed by them all.

6. Signatures of co-authors:

Date	Name	Signature
17 Sep 2014	Dr. Steen H. Hansen	
17 September 2014	Martin Sparre	

3A. Co-authorship statement

All papers/manuscripts with multiple authors which is part of a PhD thesis should contain a co-author statement, stating the PhD student's contribution to the paper.

1. General information	
PhD student	Name Martin Sparre
	Civ.reg.no. (<i>If not applicable, then birth date</i>) 0312861097
	E-mail martinsparre@gmail.com
	Department Niels Bohr Institute, Dark Cosmology Centre
Principal supervisor	Name Johan P.U. Fynbo
	E-mail jfynbo@dark-cosmology.dk

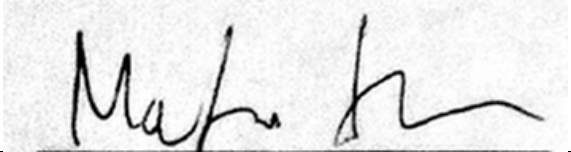
2. Title of PhD thesis
Galaxy formation: observations and simulations of galaxies

3. This co-authorship declaration applies to the following paper/manuscript:
Title: A search for thermal X-ray signatures in gamma-ray bursts - II. The Swift sample Author(s): Sparre, M.; R. L.C. Starling Journal: MNRAS Vol./page: 2012, 427, 2965 DOI: 10.1111/j.1365-2966.2012.21858.x

4. Contributions to the paper/manuscript made by the PhD student	
What was the role of the PhD student in designing the study?	Dr. Starling got the overall idea for the paper. The PhD student designed the analysis tools (with supervision from Dr. Starling), and designed the structure of the paper.
How did the PhD student participate in data collection and/or development of theory?	Public data was used for the analysis in this paper. Dr. Starling collected the public data, and Martin Sparre did the analysis.
Which part of the manuscript did the PhD student write or contribute to?	The PhD student created all the figures, in the paper, and wrote all sections except for Section 5.3, which was written by Dr. Starling. Dr. Starling commented on all sections, and also made some editions.
Did the PhD student read and comment on the final manuscript?	Yes.

5. Material in the paper from another degree / thesis :	
<i>Articles/work published in connection with another degree/thesis must <u>not</u> form part of the PhD thesis. Data collected and preliminary work carried out as part of another degree/thesis may be part of the PhD thesis if further research, analysis and writing are carried out as part of the PhD study.</i>	
Does the paper contain data material, which has also formed part of a previous degree / thesis (e.g. your master's degree) Please indicate which degree / thesis: _____	Yes: <input type="checkbox"/> No: <input checked="" type="checkbox"/>
Please indicate which specific part(-s) of the paper that has been produced as part of the PhD study: Everything.	

The co-author statement should always be signed by the first author, the corresponding-/senior author and the PhD student. If there are two or three authors the statement must always be signed by them all.

6. Signatures of co-authors:		
<i>Date</i>	<i>Name</i>	<i>Signature</i>
	Dr. Rhaana L. C. Starling	
27. September 2014	Martin Sparre	

When completed, please send the form to the PhD secretary at the department.

www.science.ku.dk/english/research/phd/student/contact/departments/



Martin Sparre <martinsparre@gmail.com>

Authorship statements for my thesis

Starling, Rhaana L.C. (Dr.) <rlcs1@leicester.ac.uk>

25. sep. 2014 kl. 11.20

Til: Martin Sparre <martinsparre@gmail.com>

Dear Martin,

Apologies for the delayed reply. I have been in Ecuador. Here is my statement of concurrence.

Rhaana

I have read the document and agree entirely with the statements written there. The work was almost all your own, apart from the stated section and some guidance from me.

Signed: Rhaana Starling

Date: 25/09/2014

From: Martin Sparre [martinsparre@gmail.com]

Sent: 17 September 2014 12:30

To: Rhaana Starling

Subject: Authorship statements for my thesis

[Citeret tekst er skjult]



3A. Co-authorship statement

All papers/manuscripts with multiple authors which is part of a PhD thesis should contain a co-author statement, stating the PhD student's contribution to the paper.

1. General information	
PhD student	Name Martin Sparre
	Civ.reg.no. (If not applicable, then birth date) 0312861097
	E-mail martinsparre@gmail.com
	Department Niels Bohr Institute, Dark Cosmology Centre
Principal supervisor	Name Johan P.U. Fynbo
	E-mail jfynbo@dark-cosmology.dk

2. Title of PhD thesis
Galaxy formation: observations and simulations of galaxies

3. This co-authorship declaration applies to the following paper/manuscript:
Title: The Metallicity and Dust Content of a Redshift 5 Gamma-Ray Burst Host Galaxy Author(s): Sparre, M.; Hartoog, O. E.; Krühler, T.; Fynbo, J. P. U.; Watson, D. J.; Wiersema, K.; D'Elia, V.; Zafar, T.; Afonso, P. M. J.; Covino, S.; de Ugarte Postigo, A.; Flores, H.; Goldoni, P.; Greiner, J.; Hjorth, J.; Jakobsson, P.; Kaper, L.; Klose, S.; Levan, A. J.; Malesani, D.; Milvang-Jensen, B.; Nardini, M.; Piranomonte, S.; Sollerman, J.; Sánchez-Ramírez, R.; Schulze, S.; Tanvir, N. R.; Vergani, S. D.; Wijers, R. A. M. J. Journal: ApJ Vol./page: 2014, 785, 150 DOI: 10.1088/0004-637X/785/2/150

4. Contributions to the paper/manuscript made by the PhD student

What was the role of the PhD student in designing the study?

Prof. Johan P.U. Fynbo got the initial idea for the paper. The PhD student designed the analysis and text behind Figure 2,7,8 and coordinated work and text among the remaining coauthors (see details below).

How did the PhD student participate in data collection and/or development of theory?

The PhD student was a part of the collaboration that did the data collection, but the PhD did not participate in the actual data-taking of the data for this paper.

Which part of the manuscript did the PhD student write or contribute to?

The PhD student drafted everything except: Section 2, 3.2, 4, 5, 6, 8. Section 3.2 and 5 are a part of Olga E. Hartoog's PhD thesis. Dr. Thomas Krühler drafted Section 4 and 6

The PhD student did all the analysis in the figures 2,7,8. Prof. J.P.U. Fynbo created figure 1, Dr. T. Krühler created Figures 3,9 and 10, O.E. Hartoog created Figure 4 and 6, Dr. T. Zafar created figure 5

Did the PhD student read and comment on the final manuscript?

Yes.

5. Material in the paper from another degree / thesis :

Articles/work published in connection with another degree/thesis must not form part of the PhD thesis.

Data collected and preliminary work carried out as part of another degree/thesis may be part of the PhD thesis if further research, analysis and writing are carried out as part of the PhD study.

Does the paper contain data material, which has also formed part of a previous degree / thesis (e.g. your master's degree)

Yes:


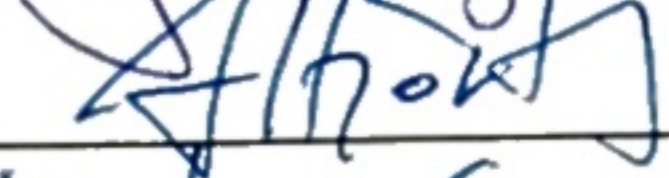
Please indicate which degree / thesis: _____

No:

Please indicate which specific part(-s) of the paper that has been produced as part of the PhD study:

Everything.

6. Signatures of co-authors:

<i>Date</i>	<i>Name</i>	<i>Signature</i>
17/9 - 2014	Prof. Johan P.U. Fynbo	
17/9 - 2014	Prof. Jens Hjorth	
17 September 2014	Martin Sparre	Martin Sparre

When completed, please send the form to the PhD secretary at the department.

www.science.ku.dk/english/research/phd/student/contact/departments/



3A. Co-authorship statement

All papers/manuscripts with multiple authors which is part of a PhD thesis should contain a co-author statement, stating the PhD student's contribution to the paper.

1. General information	
PhD student	Name Martin Sparre
	Civ.reg.no. (If not applicable, then birth date) 0312861097
	E-mail martinsparre@gmail.com
	Department Niels Bohr Institute, Dark Cosmology Centre
Principal supervisor	Name Johan P.U. Fynbo
	E-mail jfynbo@dark-cosmology.dk

2. Title of PhD thesis
Galaxy formation: observations and simulations of galaxies

3. This co-authorship declaration applies to the following paper/manuscript:
<p>Title: The star formation main sequence and stellar mass assembly of galaxies in the Illustris simulation Author(s): Sparre, Martin; Hayward, Christopher C.; Springel, Volker; Vogelsberger, Mark; Genel, Shy; Torrey, Paul; Nelson, Dylan; Sijacki, Debora; Hernquist, Lars Journal: Submitted to MNRAS, online at arXiv: 1409.0009 (http://arxiv.org/abs/1409.0009) Vol./page: - DOI: -</p>

4. Contributions to the paper/manuscript made by the PhD student

What was the role of the PhD student in designing the study?

The PhD student designed the study in collaboration with Prof. V. Springel and Dr. C. Hayward.

How did the PhD student participate in data collection and/or development of theory?

The Illustris simulation was run by coauthors of the paper. The PhD student did not participate in this.

The PhD student analysed the output of the simulation. The idea for the different sections came mainly from discussion between the PhD student, Prof. V. Springel and Dr. C. Hayward.

Which part of the manuscript did the PhD student write or contribute to?

The PhD student drafted Section 1-5. Prof. V. Springel and Dr. C. Hayward subsequently edited the text. Prof. V. Springel, Dr. C. Hayward and the PhD student all contributed to drafting section 6 and 7.

The PhD student created all the figures and did all the analysis presented in the manuscript.

Did the PhD student read and comment on the final manuscript?

Yes.

5. Material in the paper from another degree / thesis :

Articles/work published in connection with another degree/thesis must not form part of the PhD thesis.

Data collected and preliminary work carried out as part of another degree/thesis may be part of the PhD thesis if further research, analysis and writing are carried out as part of the PhD study.

Does the paper contain data material, which has also formed part of a previous degree / thesis (e.g. your master's degree)

Yes:

No:

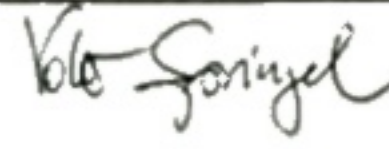

Please indicate which degree / thesis: _____

Please indicate which specific part(-s) of the paper that has been produced as part of the PhD study:

Everything.

The PhD School of SCIENCE

The co-author statement should always be signed by the first author, the corresponding-/senior author and the PhD student. If there are two or three authors the statement must always be signed by them all.

6. Signatures of co-authors:		
<i>Date</i>	<i>Name</i>	<i>Signature</i>
18.9.2014	Prof. Volker Springel	
18.9.2014	Martin Sparre	

When completed, please send the form to the PhD secretary at the department.

www.science.ku.dk/english/research/phd/student/contact/departments/